POLITECNICO DI TORINO

Doctor of Philosophy in Aerospace Engineering

Thesis

SIMULATION OF LOCAL EFFECTS, ENERGY ABSORPTION AND FAILURE MECHANISM IN MULTILAYERED AND SANDWICH STRUCTURES

(ING-IND/04)

Advisor:
Prof. Ugo Icardi

Author:
Federico Sola

MARCH 2016

Abstract

Over the last three decades, composites have been increasingly adopted in a lot of engineering fields due to their excellent specific properties. Thanks to this, many researches have been conducted in this field, which generally agree that composites:

    I.   need description of 3D stress fields, local effects and complex failure mechanisms with the minimum computational effort;

   II.   have low out-of-plane shear and transverse strengths;

Accordingly, in order to investigate these issues, the present dissertation describes the research work carried out towards:

    I.   developing of analytical and numerical models for accurate and efficient analysis of laminates and sandwiches under different loading conditions (static analyses, impulsive loading and low velocity impacts);

   II.   developing of techniques to improve structural performances of composites structures by tuning their energy absorption mechanism;

A higher order theory (AD-ZZ) including zig-zag effects, transverse shear continuity, variable transverse displacement and layerwise representation is presented for analysis of laminates and sandwiches. This theory is cast in such a way that the unknowns in the model will involve only five variables like equivalent single layer models: the three displacement components and the two shear rotations of the normals on the reference surface. It is advantageous to formulate the theory in this way, as it provides the opportunity to refine its through-the-thickness representation by adding computational layers in the thickness direction without increasing the number of unknowns. After extensive evaluation of the accuracy obtained by the above mentioned theory for a variety of structures, the AD-ZZ model is enriched by adding a set of continuity functions in order to treat laminates and structures with

in-plane discontinuities (e.g. bonded joints, two material wedge) under a unified approach without adding new unknowns.

Speaking of techniques to improve structural performances, two approaches are presented: **variable stiffness composites and stitching**. The former tool works on the strain energy of the structure computing fibre distributions that minimize unwanted energy contributions and maximize the wanted ones. The latter prescribes the insertions of transverse reinforcements in sandwich structures. The homogenized mechanical properties of this structure, required by the AD-ZZ model to perform the analysis, are evaluated through virtual material tests using a 3D FE model. The results obtained applying these techniques demonstrate that both are effective in reducing transverse stresses at critical interfaces and, in certain cases, in improving bending stiffness.

New C^0 **displacement-based and stress-based finite elements** for analysis of laminated and sandwich plates based on the AD-ZZ model are developed. To achieve this goal, a new technique that converts derivatives of functional degrees of freedom contained in the AD-ZZ is presented. Both the elements satisfy all the requirements of computationally efficient finite element models for analysis of multilayered structures, namely 1) the number of degrees of freedom is independent from the number of layers; 2) no shear correction factors or penalty number are added in the formulation. Consistent shear fields are obtained for the present finite element formulations. Numerical results demonstrate that these new elements are robust, accurate and computationally efficient for analysis of multilayered structures.

In order to study **structures subjected to impact loading** a new simulation procedure is developed. It is based on the AD-ZZ model and considers the crushing behaviour of soft-like media without performing each time a detailed 3D finite element analysis. Numerical results show that the response of composites undergoing low velocity impact is very accurately predicted with low computational effort. Overall, the present procedure holds great promise for analysis of laminated and sandwich structures undergoing low velocity impact.

This dissertation is organized in the form of eight chapters each of which is based on the papers published during the PhD:

- U Icardi and F Sola, "Development of an efficient zig-zag model with variable representation of displacement across the thickness," Journal of Eng. Mech., vol. 140, pp. 531-541, 2014.

- U Icardi and F Sola, "Analysis of bonded joints with laminated adherends by a variable kinematics layerwise model," International Journal of Adhesion and Adhesives, vol. 50, pp. 244 - 254, 2014.

- U Icardi and F Sola, "Response of sandwiches undergoing static and blast pulse loading with tailoring optimization and stitching," Aerospace Sci. & Tech., vol. 32, pp. 293 - 301, 2014.

- U Icardi and F Sola, "Recovering critical stresses in sandwiches using through-the-thickness reinforcement," Composites PartB: Engineering, vol. 54, pp. 269 - 277, 2013.

- U Icardi and F Sola, " C0 fixed degrees of freedom zigzag model with variable in-plane and out-of-plane kinematics and quadrilateral plate element," Journal of Aerospace Eng., vol. 28, pp. 040141351 - 0401413514, 2015.

- U Icardi and F Sola, " C0 mixed layerwise quadrilateral plate element with variable in and out-of-plane kinematics and fixed d.o.f.," Int. J. of Computational Engineering Research, vol. 5, pp. 6 - 26, 2015.

- U Icardi and F Sola, "Indentation of sandwiches using a plate model with variable kinematics and fixed degrees of freedom," Thin-Walled Structures, vol. 86, pp. 24 - 34, 2015.

Contents

Introduction

Over the last thirty years, composites have increasingly found applications in various engineering field (military and civil aircraft, aerospace vehicles, naval and civil structures) thanks to their high specific stiffness and strength. Accordingly, the present research study deals with composites in laminated and sandwich configurations. In particular, various aspects related to composite materials are examined in order to give a complete description of their critical aspects and their characteristic behaviour.

First, in order to put the present work in the right perspective, in **Chapter 1** the most recent analytical approaches adopted by researchers for modelling composite structures are discussed into details. In fact, composite materials require accurate description of their interlaminar stress field, since it completely differs from the one measured in classical materials; therefore, many theories have been developed in literature for obtaining meaningful results. Then, in **Chapter 2** it is presented a tool extensively used in the present research work due to its accuracy in the prediction of the interlaminar stress-field. It is an analytical physically based zig-zag model with fixed degrees of freedom and hierarchic representation, developed by Prof. Icardi and by the author. Thanks to this representation, the computational effort is kept as low as possible, since the model can be refined across the thickness in order to improve accuracy, without adding new unknowns as they are fixed. Accordingly, this model is here referred as adaptive model (AD-ZZ). As case studies, in **Chapter 3**, several laminated and sandwich structures are analysed in order to verify the accuracy of the present structural model. In particular, structures with extremely low length-to-thickness ratios are considered, as customarily in the reference literature, since they represent severe test cases, being characterized by strong layerwise effects. Different loading schemes are also considered, with the aim of verifying the accuracy of the AD-ZZ model also for structures with clamped edges, since structural models with the same functional degrees of freedom as the AD-ZZ model often fail with this kind of structures. Comparisons between the results by

the AD-ZZ model and by the most important theories discussed in Chapter 1 are also presented for laminates and sandwiches. Finally, as a preliminary application to dynamic analyses, three sandwich panels subjected to blast pulse are studied with the AD-ZZ model in order to test its accuracy for this kind of analyses.

As a next step, in **Chapter 4**, the AD-ZZ model is enriched with new contributions. Specifically, in order to analyse laminates and bonded joints under a unified approach, the AD-ZZ model incorporates new terms, which enables to satisfy the stress boundary conditions required when analysing structures with in-plane discontinuity, as in the overlap of bonded joints. More in general, thanks to these new contributions the AD-ZZ model is also made able to treat structures with in-plane variation of the mechanical properties with improved accuracy, as shown in Chapter 8. Similarly to its previous formulation, the model a priori satisfies the out-of-plane stress contact conditions at the interfaces of adjacent layers and the stress boundary conditions at the upper and lower faces of the structures. In order to show the capabilities of this model, applications to analyses of joints taken from the literature are presented, for which analytical or finite element results are available for comparisons. Single- and double-lap sample cases with isotropic or laminated adherents are investigated.

The next part of the present research focuses the attention on methods for improving structural performances of laminated and sandwich structures. Namely, in **Chapter 5** variable stiffness and textile composites are considered. The former tool takes advantage of the following condition: if each deformation process can be easily described in terms of its strain energy contributions, deformation modes responsible for unwanted behaviours can be identified and their energy contributions minimized; meanwhile, other deformation modes, not deleterious, could be maximized. In this way, an energy transfer process is induced between unwanted and preferred modes. On this basis, the law of variation for the mechanical properties of a single ply can be found as the ones able to minimize/maximize the contributions of interest. The plies with variable stiffness have properties that vary over the main plane (x-y plane), according to specific laws that can be satisfied by fibre distributions easy to be produced with current technologies. Once incorporated in multilayered structures or in the face-sheets of sandwich panels, these plies are able to transfer energy, reducing the transverse interlaminar stresses and, in specific configurations, the transverse deflection. The benefits that the layers with variable stiffness can bring to the dynamic response of the structures subjected to blast loading are also presented. In particular, it is shown that these

layers are able to reduce the transverse oscillations under impulsive loading. For what concerns textile composites, in accordance with the recent research results the attention is focused on specific applications such as stitching or tufting, which imply the insertions of transverse reinforcements in sandwich structures in order to reduce their typical difference between in-plane and transverse stiffness. This technique introduces the idea of 3D material, thus requiring developing specific techniques to treat the problem with the AD-ZZ model. Indeed, being a smeared model, it needs an evaluation of the homogenized mechanical properties due to the contribution of the through-the-thickness reinforcement. For doing this, virtual material tests are carried using a 3D FE model, thus obtaining all the constants of the 6-by-6 stiffness matrix. A full scale computation like this is expensive, but it is required only once for any specific case, therefore costs are affordable. The effects of the stitching spacing is taken into consideration, because, this parameter plays an important role in varying the stiffness of the structure. Once the homogenized mechanical properties of the reinforced sandwich have been determined, a global structural analysis is carried out. Applications are presented showing that virtual material tests provide results included in the natural dispersion of experiments and that stitching or tufting are effective in recovering critical stresses.

Chapter 6 faces one of the main drawbacks of the AD-ZZ model: the incorporation of derivatives of various orders of the functional d.o.f. in the displacement fields. This is due to the fact that expressions of zig-zag functions and of higher-order contributions are obtained once for all in a physically consistent way enforcing differential equations like the continuity of interlaminar stresses, the boundary conditions and indefinite equilibrium equations. Regrettably, derivatives are unwise contributions when finite elements are developed, since they should appear as nodal d.o.f. Consequently, computationally inefficient interpolation functions must be used. To overcome this drawback, in Chapter 6, it is developed a technique (SEUPT) that obtains a C^0 layerwise model with just five functional d.o.f. from a variable kinematics, physically-based zig-zag model. The objective is finding a priori corrections of displacements in closed form, which make the energy of the equivalent model with all the derivatives neglected equivalent to that of its initial counterpart model containing all the derivatives. This idea was already successfully applied in previous work by Prof. Icardi, where energy updating was developed as a post-processing technique to improve the predictive capability of shear deformable commercial finite plate elements. Here, the idea is adopted to eliminate the derivatives of the functional d.o.f. directly from the AD-ZZ model,

so to obtain a C^0 equivalent model with just five d.o.f. able to account for zig-zag and layerwise effects. Hermite's polynomial representations of the d.o.f. are used over the domain, whose order depends upon the order of derivatives appearing in the model. Accuracy and efficiency of the updating technique are assessed comparing the results of the AD-ZZ model to its equivalent counterpart free from derivatives and considering closed form solution of reference sample cases with intricate through-the-thickness displacement and stress distributions, for which exact elasticity solutions are available for comparisons.

In **Chapter 7**, taking advantage of SEUPT, two finite elements are developed. The former is an eight-node plate element with standard d.o.f. and serendipity interpolating functions. It is applied to compute stress and displacement fields of sample cases for which the exact solution is available in the literature. This demonstrates that, through energy balance considerations, an efficient and accurate C^0 element with standard features can be constructed even using as structural model a physically-based zig-zag one. The other finite element developed in Chapter 7 is a partial hybrid one, which only includes out-of-plane stresses as nodal d.o.f. In order to reduce the effort for developing the element without losing accuracy, displacement and stress interpolating functions all of the same order are considered. Accordingly, the same C^0 interpolation by standard serendipity polynomials is employed for all the nodal d.o.f. Accuracy, solvability and convergence behaviour of this element are assessed comparing its results for laminates and sandwiches with different boundary conditions and abruptly changing material properties with the exact solutions available in literature.

The last part of the present research deals with impact on composites structures, which is an application of practical engineering interest. In particular, in **Chapter 8**, a new simulation procedure for the analysis of low-velocity, low-energy impact is presented. It is based on the AD-ZZ model and uses a modified Hertzian contact law that forces the target to conform to the shape of the impactor. In order to describe core crushing, when dealing with sandwiches, the variable, apparent elastic moduli of the core while it collapses/buckles under transverse compressive loading are computed apart once for all through a detailed three-dimensional finite element analysis. Then, they are provided to the AD-ZZ model as variable properties at each load level. Furthermore, the damage analysis is integrated inside the dynamic analysis, thus stress-based criteria are applied for estimating the overall area of failure. Then, the damage analysis is repeated with the new stress-field and the relative property degradation is applied, as a consequence of the damage onset. Finally, the analysis goes on, while the time

folds, in an implicit time integration scheme. The results obtained by this new technique can be substantially collected in two classes: the prediction of the contact force and the damage analysis time after time. The results dealing with laminates and sandwiches, with various boundary conditions, impactor geometries, materials and impact energies, show the accuracy of the present technique and, what is important, its low computational effort.

Concluding, the present study focuses the attention on various aspects related to modelling of composite structures and offers theories, tools and techniques for accurate analyses. The most important topics related to the composite design are treated and new models proposed. Whenever possible, the results by the theories proposed are assessed through comparisons with experimental results. The matters opened by this study and the good results obtained by the tools implemented suggests to work further on these topics, thus future developments are currently in progress.

List of Tables

List of Figures

Chapter 1: Modelling of composite structures

1.1 State of the art

Laminates and sandwiches increasingly find use as primary structural components, since with respect to metals improved structural performances can be obtained with a lower mass using these materials (see, e.g., Sliseris and Rocens [1] and Khani et al. [2], Nik et al. [3]).

However, owing to their rather poor out-of-plane moduli and strengths compared to those in the in-plane direction, warping, shearing and straining deformations of the normal (zig-zag effect) and relevant out-of-plane stress concentrations (layerwise effect) rise. These effects can cause local micro-failures that lead to loss of strength and stiffness, which can be dangerous for structural integrity. They also affect vibration and buckling behavior, particularly in case of strong anisotropy and for thick structures (see, e.g. Liu and Islam [4] and Vachon et al. [5]). Since structures must carry the ultimate design load even when they are damaged, various technical skills have been developed to improve damage tolerance, strength and fatigue behaviour of composites (see, e.g., Potluri et al. [6], Judawisastra et al. [7], Wang et al. [8], Vaidya et al. [9], Nilanjan [10] and Cox and Flanagan [11]).

In order to enhance the effectiveness of these techniques, zig-zag and layerwise effects should be accurately described. Therefore, many multi-layered models based on different assumptions have been developed. Their basic requirement is that they produce continuous displacements across the thickness with appropriate discontinuous slope changes at the interfaces of constituent layer, which enables to obtain continuous interlaminar stresses as prescribed by the elasticity theory. Equivalent Single-Layer models (ESL) (e.g. FSDT [12] and HSDT [13]) still find many applications for predicting overall quantities being simple to handle and having low computational costs, but they are unable to provide realistic predictions of stress fields, as they disregard previous requirements.

The papers by Reddy [14], Bert [15], Noor and Burton [16], Reddy [17], Reddy and Robbins [18], Burton and Noor [19] and Noor, Burton and Bert [20] and more recently those by Chakrabarti et al. [21], Matsunaga [22], Chen and Wu [23], Kreja [24], Tahani [25], Noor and Malik [26], Carrera [27] give i) an extensive discussion of the various techniques employed to account for zig-zag and layerwise effects and ii) extensive assessments of their performances. Accuracy of finite element models for laminated and sandwich composites is assessed by To and Liu [28], Desai et al. [29], Ramtekkar et al. [30], Dau et al. [31], Carrera et al. [32], Shimpi and Ainapure [33], Elmalich and Rabinovitch [34], Zhen et al. [35], Cao et al. [36] and Dey at al. [37]. Further assessments are presented in the papers by Matsunaga [38], [39], [40], [41], [42], Mourad et al. [43], Versino et al. [44], Hu et al. [45], Kapuria and Nath [46], Oñate et al. [47], [48], [49], Vidal and Polit [50], Mashat et al. [51] and Carrera et al. [52], [53], [54], [55], [56], [57].

The most recent analytical models suitable for stress analyses are here classified in a broad outline as: (i) Discrete-Layer (DL) models with a separate representation across each computational/physical layer [58], [59]; (ii) High-Order Layerwise (HLW) plate models based on a combination of global higher-order terms and local layerwise functions of various type (see, e.g. [60] and [61]). These theories are further split into kinematic-based (ZZ-K) and physically-based zig-zag plate theories (ZZ-F) with displacement-based or mixed/hybrid formulation. The latter have the advantage of more easily enforcing stress interfacial and boundary constraints, but their stability, convergence and solvability are ruled by quite complex relations.

Of interest to this work are physically-based zig-zag plate theories with fixed degrees of freedom (d.o.f.) that *a priori* fulfil the stress continuity conditions [62]. They incorporate piecewise contributions to displacements that enable to meet these requirements, as prescribed by the elasticity theory. Thus, they change with the stacking sequence. On the contrary, kinematic-based zig-zag plate theories include piecewise contributions to displacements with a periodic change of the slope, as in the exact elasticity solution of laminates with periodical stack-up. Thus, this kind of models is not mechanical-properties dependent.

It is a common opinion that use of DL and 3D finite element analysis, though accurate, should be limited to local regions otherwise they could overwhelm the computational capacity having a too large number of variables. Instead, as shown by the cited reviews and in the papers by Giunta et al. [63], Vidal et al. [64], Shariyat [65], Lo et al. [66], Jun et al. [67], Zhen and

Wanji [**68**], [**69**], [**70**], [**71**], [**72**], Wanji et al. [**73**], Zhen et al. [**74**] HLW can be as accurate as 3D FEA and DL models at a much lower cost. Hence, a continuously increasing interest has been registered in the recent years towards these models. Among HLW, ZZ-F with a fixed number of variables pioneered by Di Sciuva in [**62**] and refined in [**75**], [**76**], [**77**], [**78**], [**79**], [**80**], [**81**] are of great interest, being accurate with the minimal computational effort

As a corroboration of this, ZZ-F based on Di Sciuva's ideas have found extensive application as structural models for solving various problems dealing with laminated and sandwich composites. As examples since earlier applications to present, the papers by Cho and Parmerter [**82**], Cho et al. [**83**], Cho and Kim [**84**], [**85**], [**86**], [**87**], Cho and Choi [**88**], Oh et al. [**89**], Kim et al. [**90**], Lee et al. [**91**], Kapuria et al. [**92**], [**93**], [**94**], [**95**], Li and Liu [**96**], Zhen and Wanji [**97**], Di Sciuva and Icardi [**98**], Gherlone and Di Sciuva [**99**], Di Sciuva, Gherlone, and Librescu [**100**], Averill [**101**], Averill and Yip [**102**], Aitharaju and Averill [**103**], Eby and Averill [**104**], Yip and Averill [**105**], Icardi [**106**], [**107**], [**108**], [**109**], Icardi and Ruotolo [**110**], Icardi, Di Sciuva and Librescu [**111**], Icardi and Di Sciuva [**112**], Icardi and Ferrero [**113**], [**114**], [**115**], [**116**], [**117**], [**118**], Icardi and Sola [**119**], [**120**], [**121**], [**122**], [**123**], Tessler et al. [**124**], [**125**], [**126**], [**127**], [**128**], [**129**], Gherlone et al. [**130**], Versino et al. [**131**] and Azhari et al. [**132**] are cited.

In the forthcoming sections, the kinematic assumptions of Di Sciuva's and of refined ZZ-F models, how and why they evolved till nowadays will be discussed into details.

1.2 Preliminaries and notations

Consider a multilayered plate made of n_l arbitrarily oriented, orthotropic layers and $n_i = n_l - 1$ interfaces. Each point of the plate is referred to a Cartesian coordinate system (x, y, z), with z as the thickness coordinate. The middle plane Ω is assumed as the reference plane, hence $z \in$ [-h/2, h/2], where h is the overall thickness. The principal material directions of each constituent lamina are indicated as 1, 2 and 3. The position of the upper⁺ and lower⁻ surfaces of the kth layer are indicated as $^{(k)}z^+$ and $^{(k)}z^-$; the quantities that belong to a generic layer k are denoted with the superscript$^{(k)}$ (see Figure 1.1). The applied transverse load is denoted with

the symbol p^0, the applied surface loads are indicated with τ_{ij} (ij indicate the surface over which they act).

It is assumed that sandwich plates can be analysed in homogenized form as laminated plates with a thick intermediate layer constituting the core, when the buckling of cell walls is considered outside the purpose of the analysis. Otherwise, a full three-dimensional description of the cellular structure should be employed (see Chapter 8).

The orthogonal components of the displacement vector in (x, y, z) are denoted as u, v and w. Linear relations between stresses and strains are assumed throughout this work, hence distinction between various measures of stresses and strains is unnecessary. The components of the strain tensor are ε_{xx}, ε_{yy}, ε_{zz}, ε_{xy}, ε_{xz} and ε_{yz} and the corresponding components of the stress tensor are σ_{xx}, σ_{yy}, σ_{zz}, σ_{xy}, σ_{xz} and σ_{yz} respectively.

According to [133], the generalized Hooke's law determines for each orthotropic layer with arbitrary orientation θ the following stress-strain relations:

$$\begin{Bmatrix} \sigma_{xx} \\ \sigma_{yy} \\ \sigma_{zz} \\ \sigma_{xz} \\ \sigma_{yz} \\ \sigma_{xy} \end{Bmatrix} = \begin{bmatrix} C_{11} & C_{12} & C_{13} & 0 & 0 & C_{16} \\ C_{12} & C_{22} & C_{23} & 0 & 0 & C_{26} \\ C_{13} & C_{23} & C_{33} & 0 & 0 & C_{36} \\ 0 & 0 & 0 & C_{44} & C_{45} & 0 \\ 0 & 0 & 0 & C_{45} & C_{55} & 0 \\ C_{16} & C_{26} & C_{36} & 0 & 0 & C_{66} \end{bmatrix} \begin{Bmatrix} \varepsilon_{xx} \\ \varepsilon_{yy} \\ \varepsilon_{zz} \\ \varepsilon_{xz} \\ \varepsilon_{yz} \\ \varepsilon_{xy} \end{Bmatrix} \qquad (1.1)$$

Where defining m= cos θ and n= sin θ:

$$C_{11} = m^4 C_{11}{}' + 2m^2 n^2 \left(C_{12}{}' + 2C_{66}{}' \right) + n^4 C_{22}{}'$$

$$C_{12} = m^2 n^2 \left(C_{11}{}' + C_{22}{}' - 4C_{66}{}' \right) + \left(m^4 + n^4 \right) C_{12}{}'$$

$$C_{13} = m^2 C_{13}{}' + n^2 C_{23}{}'$$

$$C_{16} = -mn \left[m^2 C_{11}{}' - n^2 C_{22}{}' - \left(m^2 - n^2 \right) \left(C_{12}{}' + 2C_{66}{}' \right) \right]$$

$$C_{22} = n^4 C_{11}{}' + 2m^2 n^2 \left(C_{12}{}' + 2C_{66}{}' \right) + m^4 C_{22}{}'$$

$$C_{23} = n^2 C_{13}{}' + m^2 C_{23}{}'$$

$$C_{26} = -mn \left[n^2 C_{11}{}' - m^2 C_{22}{}' - \left(m^2 - n^2 \right) \left(C_{12}{}' + 2C_{66}{}' \right) \right]$$

$$C_{33} = C_{33}{}'$$

$$C_{36} = mn \left(C_{23}{}' - C_{13}{}' \right)$$

$$C_{44} = m^2 C_{44}{}' + n^2 C_{55}{}'$$

$$C_{55} = n^2 C_{44}{}' + m^2 C_{55}{}'$$

$$C_{45} = mn \left(C_{44}{}' - C_{55}{}' \right)$$

$$C_{66} = m^2 n^2 \left(C_{11}{}' + C_{22}{}' - 2C_{12}{}' \right) + \left(m^2 - n^2 \right)^2 C_{66}{}' \tag{1.2}$$

The elastic coefficients $C_{ij}{}'$ in (1.2) are related to Young's moduli E_1, E_2, E_3 in 1, 2 and 3 directions, shear moduli G_{12}, G_{23}, G_{31} in the planes 1-2, 2-3, 3-1 and the Poisson's ratios $\nu_{ij} = -\varepsilon_j / \varepsilon_i$, which are the so-called engineering constants.
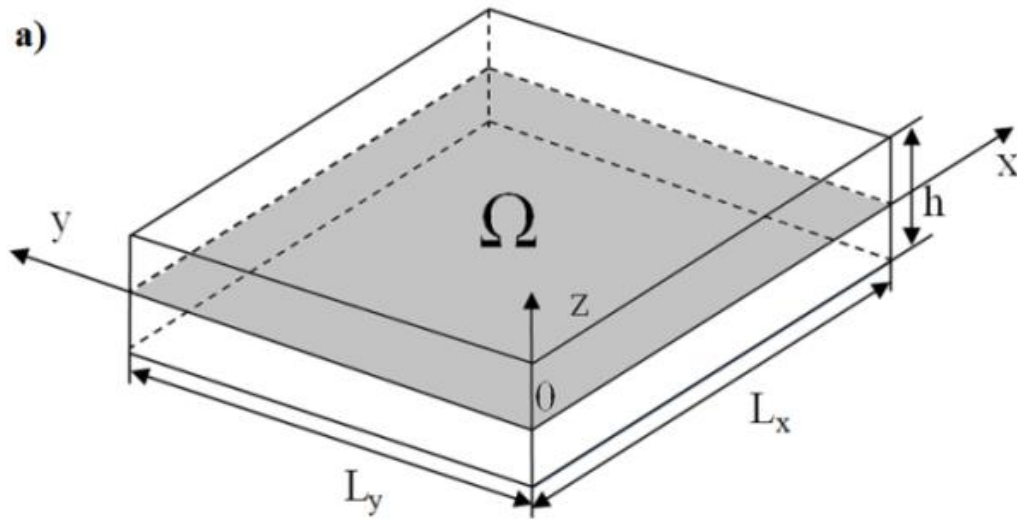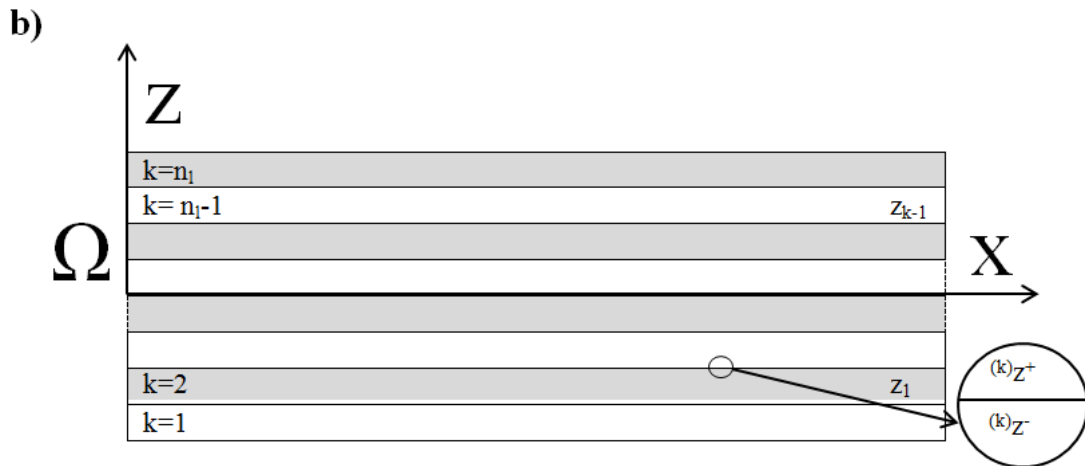
Figure 1.1 a) Reference system; b) criteria for numbering layers and interfaces.

Acronym	Definition
3D FEA	Three-dimensional Finite Element Analysis
DL	Discrete Layer models
d.o.f.	Degrees of freedom
ESL	Equivalent Single-Layer Models
FSDT	First-Order Shear Deformation Theory
GL-ST	Global-local superposition technique
HLW	High-order layerwise models
HSDT	Third-order shear deformation plate theory
RZT	Refined Zig-Zag Theory
TBT	Timoshenko Beam Theory
ZZ-F	Physically-based zig-zag models
ZZ-K	Cinematically-based zig-zag models
Symbol	**Definition**
u^0, v^0, w^0	Displacement of the points on the reference mid-plane
γ_x, γ_y	Transverse shear rotations of the normal of the points on the reference mid-plane
θ_x, θ_y	Rotations of the normal of the points on the reference mid-plane
$\Phi_x^k, \Phi_y^k, \Psi^k, \Omega^k$	Continuity constants (in Icardi's theories)
H_k	Heaviside unit step function
Ψ	Linear rotation of a layer above the reference surface (in

	Sublaminate theory)
β, η	Higher-order rotations of a layer above the reference surface (in Sublaminate theory)
ξ_i, ξ_j	Continuity coefficients (in Sublaminate theory)
$C_x, C_y, D_x, D_y, b,$ c, d, e	Higher-order terms to be computed by imposing conditions prescribed by the Elasticity Theory (in Icardi's theories)
u_G, v_G, w_G	Global contributions (in Global-local theory)
$\bar{u}_L^{\ k}, \hat{u}_L^{\ k}, \bar{v}_L^{\ k}, \hat{v}_L^{\ k},$ $\omega_z(x), u_{zz}(x)$	Local contributions (in Global-local theory)
Ψ_α	Zig-zag amplitude (in RZT theory)
$\varphi_\alpha^{(k)}$	Zig-zag function (in RZT theory)

Table 1.1 List of symbols and acronyms.

1.3 Di Sciuva's early ZZ-F models

The following piecewise representation of displacements is assumed in the Di Sciuva's zig-zag model [**80**]:

$$u(x,y,z) = u^0(x,y) + z\left[\ \gamma_x^0(x,y) - w^0_{,x}(x,y)\ \right] + A_{x3}(x,y)z^3 + \sum_{k=1}^{n_i} \Phi_x^k(x,y)(z-z_k)H_k$$

$$v(x,y,z) = v^0(x,y) + z\left[\ \gamma_y^0(x,y) - w^0_{,y}(x,y)\ \right] + A_{y3}(x,y)z^3 + \sum_{k=1}^{n_i} \Phi_y^k(x,y)(z-z_k)H_k \qquad (1.3)$$

$$w(x,y,z) = w^0(x,y)$$

that contains the piecewise linear model [**62**] as a particular case neglecting terms A_{x3} and A_{y3}.

As functional d.o.f. of the piecewise linear and cubic models, the orthogonal components of the elastic displacements u^0, v^0 and w^0 in the x, y, z directions of the points on the reference mid-plane and the transverse shear rotations γ_x and γ_y are assumed.

The characteristic feature of Di Sciuva's theory is the presence of piecewise functions Φ_x^k $=(a_k\ \gamma_x + c_k\ \gamma_y\ )$ and $\Phi_y^k =(b_k\ \gamma_x + d_k\ \gamma_y\ )$ the so-called zig-zag functions, whose purpose is to make continuous transverse shear stresses at the layer interfaces. Displacements (1.3) can be viewed as the sum of a polynomial representation in z whose representation is valid across the

whole thickness of the structure (i.e. global part) and a contribution varying among the layers constituting the local part of the model. The global contribution is continuous across the thickness and has a continuous gradient. The local contributions Φ_i^k provide appropriate discontinuous derivatives in z at the layer interfaces in order to make continuous transverse shear stresses. H_k is the Heaviside unit step function ($H_k=0$ for $z < z_k$, while $H_k=1$ for $z \geq z_k$). The expressions of the constants a_k, b_k, c_k, d_k are obtained in a straightforward way in a closed form for any lay-up by enforcing the continuity of transverse shear stresses at the interfaces:

$$\sigma_{xz}|_{(k)_{z^+}} = \sigma_{xz}|_{(k)_{z^-}}$$
$$\sigma_{yz}|_{(k)_{z^+}} = \sigma_{yz}|_{(k)_{z^-}}$$

(1.4)

These constraints only depend on the geometric and material properties of the structure. It is reminded that differently to other models they do not involve any additional d.o.f. and they identically vanish in homogeneous plates.

Coefficients A_{x3} and A_{y3} are incorporated in order to satisfy the traction-free boundary conditions at the upper and lower bounding faces:

$$\sigma_{xz}\left(z = \pm h/2\right) = 0 \quad \sigma_{yz}\left(z = \pm h/2\right) = 0$$

(1.5)

Many numerical assessments have been published by Di Sciuva (see, e.g. [77], [78], [134]) as closed-form solutions or finite element solutions. Comparisons with three-dimensional exact elasticity solutions and other approximate solutions demonstrated the significant influence of transverse shear deformations on the response of laminates, even when they are not extremely thick.

Displacement and stress fields are accurately predicted by Di Sciuva's models for structures with simply supported edges whenever the ratio of in-plane to transverse stiffness properties is not extremely high and the material properties of constituent layers do not abruptly change across the thickness.

Since no additional variables with respect to ESL theories are incorporated in the Di Sciuva's models for defining the zig-zag functions (and thus to satisfy the interlaminar stress continuity) they attracted many researchers aimed at obtaining accurate stress predictions with low processing time and memory storage dimension.

The pioneering model [80] found many applications. Based on this theory, Di Sciuva [78] develops a three-node, conforming, multilayered plate element of arbitrary triangular shape with a total of 30 nodal d.o.f., namely the two in-plane displacements, u^0, v^0 the two shear

rotations γ_x, γ_y, the transverse displacement w^0 and its first and second order derivatives $w^0{}_{,x}$, $w^0{}_{,y}$, $w^0{}_{,xx}$, $w^0{}_{,xy}$ and $w^0{}_{,yy}$ for a total of 10 d.o.f. at each node.

The third-order multi-layered zig-zag model with a constant transverse displacement and with interlayer transverse shear stress continuity fulfilment is applied by Icardi and Ruotolo [**110**] and Icardi [**135**] to analysis of symmetric and unsymmetric multi-layered shells. Curvature terms are incorporated into displacement fields and into the strain-displacements relations. Differently to plates, the comparison with exact solutions demonstrates that for shells integration of local equilibrium equations no longer obtains accurate stress predictions, owing to membrane-bending-twisting coupling effects. Indeed, in-plane stresses exploited to derive their out-of-plane counterparts by integrating the local equilibrium equations are no longer accurate for shells.

Averill [**101**] and Averill and Yip [**102**] develop zig-zag models where the continuity of the transverse shear stress across the laminate thickness is enforced using a penalty method in order to obtain a C^0 formulation. The standard form based on the bending rotation as primary kinematic variable in the expression for the axial displacement is adopted as in the Timoshenko Beam Theory (TBT). An additional kinematic variable associated with a zig-zag function is incorporated by introducing an ad hoc penalty term to the variational principle, enforcing continuity of the transverse shear stress across the cross-section in a limiting sense, as the penalty parameter approaches a large value. The through-the-thickness variation of the in-plane displacement is described by a cubic polynomial in the transverse coordinate with a piecewise linear function superposed upon it. The transverse displacement is assumed constant.

The displacement components of the kth layer can thus be written as:

$$\mathrm{u}(x,\mathrm{z}) = u^0(x) + z\Psi(x) + z^2\beta(x) + z^3\eta(x) + \sum_{i=1}^{k-1}\xi_i(x)(z-z_i) - \sum_{j=1}^{m}\xi_j(x)(z-z_j) \qquad (1.6)$$

$$w(x,z) = w^0(x)$$

where Ψ is the linear rotation of layer $m+1$ (the layer above the reference surface), β and η are higher-order rotations, which are computed by satisfying the transverse shear traction boundary conditions:

$$\sigma_{xz}\left(z = h/2\right) = \tau_{xz}\left(z = h/2\right) \quad \sigma_{xz}\left(z = -h/2\right) = \tau_{xz}\left(z = -h/2\right) \qquad (1.7)$$

ξ_i and ξ_j are continuity coefficients computed imposing conditions (1.4).

The model results in a four-variable, C^0- continuous beam theory suitable for formulation of efficient finite elements. But an anomaly is present since the methodology for defining the zig-zag function lacks invariance with respect to the choice of the fixed layer. Moreover, Averill's model still gives erroneous results at clamped ends. Tessler et al. [124], [125], [126], [127] overcome the shear-force inconsistency and difficulties in simulating clamped boundary conditions, proposing a zig-zag theory that constitutes a natural extension of TBT. This theory is based on a zig-zag function that i) vanishes at the top and bottom beam surfaces, ii) does not require full shear-stress continuity across the laminated-beam and iii) is C^0-continuous.

In the following section an approach for describing zig-zag and layerwise effects alternative to that proposed by Di Sciuva is presented, to give a complete view of the research in the field. Then, the most relevant contributions brought for improving zig-zag models based on Di Sciuva's ideas are discussed.

1.4 Murakami's zig-zag function

As an alternative to the approach suggested by Di Sciuva [62] - [80] and presented above, ZZ-K theories ([52], [53], [54], [55], [56], [57]) use

$$\mathrm{F}^k(z) = \left(-1\right)^k 2\frac{z - z_M^k}{h^k} \tag{1.8}$$

instead of the local contributions brought by the summations in Eq. (1.3). The meaning of symbols is as follows: $z_M^{\ k}$ is the thickness coordinate of the reference plane of the kth layer and h^k is the thickness of the kth layer. Eq. (1.8) is based on the Murakami's idea [136] of a priori assuming a slope variation of displacements at the interfaces as in laminates with periodic lay-up.

As discussed by Gherlone [137], the Murakami's zig-zag function obtains results in good agreement with exact 3D elasticity solution whenever periodical stack-ups are considered, while it is less accurate for arbitrary stacking sequences (see also Section 3.2.2).

ZZ-F models result into more accurate solutions with general lay-ups, in particular when asymmetrical sandwiches with high face-to-core stiffness ratios are considered, or when a weak layer is placed on the top or bottom of laminates to simulate a damaged face. Thus, to ensure always the maximal accuracy, physically-consistent zig-zag functions should be

considered. However, ZZ-K models are much easier to implement, require less effort than ZZ-F and can more easily produce an efficient C^0 formulation useful for the development of finite elements.

In light of these considerations, ZZ-F could help when solving practical problems, but techniques should be developed to manipulate the rather complex algebraic equations resulting from the enforcement of the physical contact conditions at the layer interfaces and for obtaining a C^0 formulation. This avoids development of inefficient finite elements with derivatives of the d.o.f. as nodal variables, which directly come from the fact that the unknown coefficients of the physically based zig-zag functions are computed through equations involving stresses.

Refined ZZ-F models developed to overcome the drawbacks of early Di Sciuva's ones are discussed in the next sections. Aims of these models developed by various researchers starting from the ideas by Di Sciuva are obtainment of accurate stress prediction from constitutive equations, consideration of general boundary conditions and incorporation of transverse normal deformability and stress, which are important when interlaminar bonding imperfections [138] and temperature gradients rise [139] and when cut-outs and delamination fronts are considered.

1.5 Sublaminate zig-zag models

Sublaminate zig-zag models by Averill and co-workers [101], [102], [103], [104], [105] extend the concept of local and global laminate modelling introduced by Pagano and Soni [140]. The idea is similar to Di Sciuva's model (1.3), but displacements at the top and bottom surfaces of computational layers are assumed as kinematic variables. Analyses are carried out using a single computational layer, stacking several computational layers or even subdividing a physical layer into one or more computational layers. As a consequence, a good compromise between accuracy and cost saving can be achieved in all cases. The representation can be refined in the regions with steep displacements and stress gradients, while a single computational layer can be used elsewhere. As important consequence, sublaminate models offer the possibility of obtaining accurate stress predictions from

constitutive equations, even with abruptly changing material properties of constituent layers, with a computational burden lower than DL models.

Averill and co-workers introduced the following zig-zag representation within each computational layer, i.e. within each sublaminate:

$$u(x,y,z) = u_b(x,y) + z\Psi_x(x,y) + \sum_{k=1}^{n_i} \xi_{xk}(x,y)(z - z_k)$$

$$v(x,y,z) = v_b(x,y) + z\Psi_y(x,y) + \sum_{k=1}^{n_i} \xi_{yk}(x,y)(z - z_k)$$
(1.9)

$$w(x,y,z) = w_b(x,y)\left(1 - \frac{z}{h_{sb}}\right) + w_t(x,y)\left(\frac{z}{h_{sb}}\right)$$

where h_{sb} is the thickness of the sublaminate; u_b and v_b are the axial displacements in x and y directions, respectively at z=0; Ψ_i is the rotations of the normal at z=0; w_t and w_b are the transverse deflections of the top and bottom surface of the kth sublaminate. ξ_{ik} are the continuity coefficients computed imposing conditions (1.4)

A modified sublaminate zig-zag beam theory is developed by Icardi [**107**] with a complete fulfilment of interfacial continuity. This model is developed from a previous one [**141**] constituting a refined version of the piecewise cubic zig-zag model by Di Sciuva, where a piecewise parabolic contribution is incorporated in the in-plane displacements of (1.3) in order to fulfil the stress-free boundary conditions (1.5) at the upper and lower free surfaces also for asymmetric structures. It could be noticed indeed that linear and cubic contributions give rise to parabolic, i.e. symmetric, transverse shear stress distributions, while the second order term enables the possibility to treat asymmetric stresses resulting from asymmetric lay-ups. The displacement field postulated in [**107**] is:

$$U(x,y,z) = u^0(x,y) + z\left[\gamma_x^0(x,y) - w_{,x}^0(x,y)\right] + C_x(x,y)z^2 + D_x(x,y)z^3 + \sum_{k=1}^{n_i} \Phi_x^k(x,y)(z - z_k)H_k$$

$$V(x,y,z) = v^0(x,y) + z\left[\gamma_y^0(x,y) - w_{,y}^0(x,y)\right] + C_y(x,y)z^2 + D_y(x,y)z^3 + \sum_{k=1}^{n_i} \Phi_y^k(x,y)(z - z_k)H_k$$
(1.10)

$$W(x,y,z) = w^0(x,y) + bz + cz^2 + dz^3 + ez^4 + \sum_{k=1}^{n_i} \Psi^k(x,y)(z - z_k)H_k + \sum_{k=1}^{n_i} \Omega^k(x,y)(z - z_k)^2 H_k$$

Based on this representation, the model [**107**] is developed with a piecewise variable transverse displacement. The d.o.f. are the same as in early Di Sciuva's theories. The continuity functions Φ_i^k are incorporated in order to fulfil the continuity of the interlaminar

shear stresses at the material interfaces (1.4) like in the Di Sciuva's theoretical models. The two contributions Ψ^k and Ω^k to the transverse displacement are incorporated in order to satisfy the continuity of the transverse normal stress at the interfaces $\sigma_{zz}|^{(k)\,+}_z = \sigma_{zz}|^{(k)\,-}_z$ and of related gradient in the thickness direction $\sigma_{zz,z}|^{(k)\,+}_z = \sigma_{zz,z}|^{(k)\,-}_z$, respectively, as discussed in Chapter 2. In light of these considerations, in [**107**] the displacement field of the sublaminate theory is as follows:

$$U_{(j)}(x,z) = \sum_{i=1}^{4} z^{i-1} U_j^i(x) + \sum_{k=1}^{n_i} \Phi_j^k(x)(z-z_k)H_k$$

$$W_{(j)}(x,z) = \sum_{i=1}^{5} z^{i-1} W_j^i(x) + \sum_{k=1}^{n_i} \Psi_j^k(x)(z-z_k)H_k + \sum_{k=1}^{n_i} \Omega_j^k(x)(z-z_k)^2 H_k \tag{1.11}$$

The d.o.f. in this case are the in-plane and transverse components of the displacements at the lower and upper bonding faces of the sublaminate, their thickness derivatives and the transverse displacement at the mid-plane of the sublaminate (the bottom plane of the sublaminate is assumed as reference plane).

Barboni and Gaudenzi in Ref. [**142**] develop a refined, physically-based three-dimensional zig-zag model with variable transverse displacement for analysis of multilayered composites with arbitrary lay-up capable of accurately capturing the warping of sections and the interlaminar stress fields. A class of C^0 finite element models based on this theory is developed by Gaudenzi et al. [**143**] and applied to bending and vibration problems of laminated plates, comparing results with the three-dimensional elasticity theory, classical laminate theory and other higher-order theories.

Numerical applications of sublaminate model [**108**], [**109**] and [**141**] demonstrate that accuracy is improved when laminates are very thick and/or the constituent layers have distinctly different elastic properties as shown by the comparison with the exact solutions [**144**], [**145**]. A fundamental advantage of the sublaminate solution is also the possibility to obtain accurate stress results from constitutive equations, because it is possible to refine the representation in the regions with steep gradients by stacking more sublaminates.

1.6 Global-Local zig-zag theories

Improved zig-zag models based on a global-local superposition technique (GL-ST) that obtain accurate stress from constitutive equations have been developed by Li and Liu [**96**] for analysis of plates considering 15 d.o.f. and, more recently, by Zhen and Wanji [**68**], [**69**], [**70**], [**71**], [**72**]. These models still assume a constant transverse displacement across the thickness, but refinements have been brought to the global-local superposition modelling technique over years by Zhen, Wanji and co-workers. A general formulation for this kind of models can be:

$$u^k(x, y, z) = u_G(x, y, z) + \bar{u}_L^k(x, y, z) + \hat{u}_L^k(x, y, z)$$

$$v^k(x, y, z) = v_G(x, y, z) + \bar{v}_L^k(x, y, z) + \hat{v}_L^k(x, y, z) \qquad (1.12)$$

$$w^k(x, y, z) = w_G(x, y, z)$$

where u_G, v_G and w_G are the global contributions to displacements; $\bar{u}_L{}^k$, $\hat{u}_L{}^k$, $\bar{v}_L{}^k$ and $\hat{v}_L{}^k$ are terms of local groups; the superscript k represents the number of layers. These terms are polynomials up to the third order in the thickness coordinate:

$$u_G(x, y, z) = u_0(x, y) + z u_1(x, y) + z^2 u_2(x, y) + z^3 u_3(x, y)$$

$$v_G(x, y, z) = v_0(x, y) + z v_1(x, y) + z^2 v_2(x, y) + z^3 v_3(x, y)$$

$$w_G(x, y, z) = w_0(x, y)$$

$$\bar{u}_L^k(x, y, z) = \left[\frac{2}{z_{k+1} - z_k} z - \frac{z_{k+1} + z_k}{z_{k+1} - z_k}\right] u_1^k(x, y) + \left[\frac{2}{z_{k+1} - z_k} z - \frac{z_{k+1} + z_k}{z_{k+1} - z_k}\right]^2 u_2^k(x, y)$$

$$\bar{v}_L^k(x, y, z) = \left[\frac{2}{z_{k+1} - z_k} z - \frac{z_{k+1} + z_k}{z_{k+1} - z_k}\right] v_1^k(x, y) + \left[\frac{2}{z_{k+1} - z_k} z - \frac{z_{k+1} + z_k}{z_{k+1} - z_k}\right]^2 v_2^k(x, y) \qquad (1.13)$$

$$\hat{u}_L^k(x, y, z) = \left[\frac{2}{z_{k+1} - z_k} z - \frac{z_{k+1} + z_k}{z_{k+1} - z_k}\right]^3 u_3^k(x, y)$$

$$\hat{v}_L^k(x, y, z) = \left[\frac{2}{z_{k+1} - z_k} z - \frac{z_{k+1} + z_k}{z_{k+1} - z_k}\right]^3 v_3^k(x, y)$$

By enforcing free conditions of the transverse shear stresses on the top and bottom surfaces, displacements and transverse shear stresses continuity conditions at the interfaces, terms u_i^k and v_i^k are computed. They are just functions of material constants and thickness of laminated plate, and their full expressions can be found in Ref. [**68**].

Numerical results (see, e.g. [**110**], [**141**]) show that the global-local superposition modelling technique is capable of accurately predicting the distributions of displacement and stress fields for laminates and shells, also for the cases where ZZ-F models by other researches fail

to be accurate. The global local ZZ-F theories [68], [69], [70], [71], [72] and [96] accurately predicts stress fields for laminates with general lamination configurations and for sandwiches under mechanical or thermal loading. C^0 triangular and quadrilateral multilayered plate elements are developed in [66], while C^1 finite elements are developed in [68], [69], [70] and [72]. In Ref. [146], Vidal and Polit propose the following displacement field:

$$u(x,\text{y},z) = u^0(x) - zw^0_{,x}(x) + \frac{h}{\pi}\sin\frac{\pi z}{h}\left(\omega_z(x) + w^0_{,x}(x)\right) + F^{(k)}(z)u_{ZZ}(x)$$

$$\text{w}(x,\text{y},z) = w^0(x)$$

(1.14)

where $\omega_z(x)$ and $u_{zz}(x)$ are additional d.o.f., which represent local contributions. A characteristic feature of this model is the use of sinus representation [147]. Sinus representation approximates the exact three-dimensional solution and furthermore the derivative of this function represents the transverse shear strain distribution due to bending. Therefore, the free boundary conditions at the top and bottom surfaces of the beam are automatically satisfied. Based on this model, in [148] a six d.o.f. global-local beam model with parabolic transverse displacement is developed.

Di Sciuva and Gherlone in Ref. [149] develop a third-order Hermitian zig-zag plate theory as a refinement of the cubic zig-zag one [78], [79], [80] and apply it to development of a finite element plate model able to capture also transverse normal deformability. In-plane displacements are represented across the thickness as the sum of a classical power expansion, a piecewise contribution that is continuous but with jumps in the first derivatives at interfaces (thus enforcing continuity of transverse shear stresses) and a contribution allowing in-plane displacement jumps at the interfaces, which simulate damaged interfaces (their detrimental effects are discussed in [100]). A linear variation of the transverse displacement is assumed across the thickness to account for the transverse normal deformability and the corresponding normal stress. Like in Refs. [150] and [151], a mixed approach is applied with the transverse normal stress as input and related strain as output. In [149], the transverse normal stress is supposed constant across the thickness. As functional d.o.f., transverse displacements and transverse normal stresses at the upper and lower faces are assumed to enable use of the sublaminate approach. The finite element is constructed adopting parabolic 2D interpolation functions of classical 8 node plate elements, assuming as nodal d.o.f. the three displacements, the derivatives of the transverse displacement and the transverse shear stresses at corner nodes

and the two in-plane displacements and transverse shear stresses at mid-side nodes. Further application and assessments of the Hermitian model are presented by Di Sciuva et al. in [**152**].

1.7 Refined Di Sciuva's zig-zag Theory RZT

Nevertheless Di Sciuva's early models satisfying the interlaminar transverse shear stress continuity accurately predict the through-the-thickness distribution of in-plane displacements and stresses of thin to thick laminated beams/plates, they are affected by three serious drawbacks. As highlighted in Tessler et al. [**125**], the shortcomings arisen are:

- the inconsistency of the transverse shear forces obtained integrating the transverse shear stresses, as they don't match their counterpart forces coming from the constitutive transverse shear stresses;
- the transverse shear forces incorrectly vanish at clamped edges;
- the C^1-continuity requirement for a finite element implementation.

To overcome these drawbacks, Tessler, Di Sciuva and Gherlone developed a refined version of Di Sciuva's piecewise linear zig-zag model [**62**], the Refined zig-zag Theory (RZT). In this theory, it is still assumed a piecewise linear distribution of the in-plane displacement and a constant transverse one, the displacements being postulated as:

$$U_\alpha^{(k)}(\mathbf{x}, z) = u_\alpha(\mathbf{x}) + z\theta_\alpha(\mathbf{x}) + \varphi_\alpha^{(k)}(z)\psi_\alpha(\mathbf{x})$$

$$U_z^{(k)}(\mathbf{x}, z) = w(\mathbf{x})$$

(1.15)

The meaning of symbols in (1.15) is as follows: the superscript k denotes the kth lamina and α represents the component of the displacement vector along the coordinate x_α. The variables u_α, θ_α and w represent the in-plane displacement, the rotation of the normal of points on the reference mid-plane and the transverse deflection, respectively. The first two contributions to the in-plane displacement $U_\alpha^{(k)}$ represent the global part, i.e. the coarse part of the model that repeats the kinematics of FSDT, while the latter one represents the local, i.e. the refined piecewise contribution, wherein Ψ_α is the zig-zag amplitude and $\varphi_\alpha^{(k)}$ is the zig-zag function. Thus the variable Ψ_α is added to kinematics.

For a plate, the RZT model results in seven kinematic variables, namely the five FSDT variables u_α, θ_α and w plus the two zig-zag amplitudes Ψ_α. Once the stacking sequence is defined along with the transverse shear moduli of constituent layers, the zig-zag function $\varphi_\alpha^{(k)}$ can be computed. For homogeneous plates $\varphi_\alpha^{(k)}$ still vanishes identically, like in the early Di Sciuva's zig-zag model.

To overcome the shortcomings of the Di Sciuva's early models mentioned above, in RZT the transverse shear stress continuity is only partially satisfied, a discontinuity being allowed at the layer interfaces. Relaxing the continuity conditions, the RZT model obtains a piecewise constant distribution of transverse shear stresses that is accurate in an average sense and that avoids the shear forces inconsistency (e.g., [98]- [100], [110]- [112], [153] - [154]). Namely, the transverse shear stress continuity condition is enforced only on the zig-zag dependent contribution.

RZT is revisited by Tessler, Di Sciuva and Gherlone in [127], [128] assuming the in-plane displacement field expressed as a superposition of coarse and fine contributions, within the framework of a multi-scale formalism that yields to four distinct sets of zig-zag functions, among which the best one is identified. Further studies are presented in Iurlaro et al. [155], Di Sciuva and Gherlone [156] and Di Sciuva et al. [157].

As RZT requires only C^0-continuous kinematic approximations, it is suitable for developing computationally efficient C^0-continuous finite elements. Gherlone, Tessler and Di Sciuva develop in [130] two- and three-node beam finite elements based on RZT for analysis of multilayered composite and sandwich beams accounting for stretching, bending, and transverse shear deformations. Anisoparametric interpolations are adopted to approximate the four independent kinematic variables of RZT so to avoid locking phenomena in thin cases. Different types of constraints are examined for obtaining two-node elements. The most accurate results are obtained for simply-supported and cantilever beams with a large range variation of lamination sequences and slenderness ratios and with heterogeneous material properties (including sandwiches). A variable transverse displacement is obtained from the constraint relations.

Versino, Mattone, Gherlone, Tessler and Di Sciuva in Ref. [131] develop C^0 three- and six-node triangular plate element based on RZT and still anisoparametric interpolations that ensure proper element behaviour even when plates are very thin. Continuous edge constraints

are enforced on transverse shear strains to derive coupled-field deflection shape functions also in this case.

Kim and Cho [**158**] obtains an accurate description of displacement and stress fields adopting a mixed variational formulation within the framework of the Reissner mixed variational theorem wherein the FSDT is adopted as kinematics, while the assumed transverse shear stress field derives from a higher-order zig-zag model by establishing a relation between the kinematic variables of the two models.

Oñate et al. [**47**] uses RZT as the basis for developing a two-node linear C^0 beam element named LRZ that was proven to accurately capture the stress fields of laminates, both for simply supported and clamped boundary conditions under different loads, and able to capture the relative displacement between layers occurring in a delamination process.

Iurlaro, Gherlone and Di Sciuva in [**159**] develop a mixed RZT model that assumes the RZT kinematics along with an independent transverse shear stress field that derives from the integration of local equilibrium equations as a generalization of the technique by Auricchio and Sacco [**160**]. In this formulation, originally developed for beams, the transverse shear stress satisfies exactly the axial equilibrium equation and it a priori satisfies the top and bottom stress boundary conditions on transverse shear stresses. As a result of the integration, the transverse shear stress is continuous at the layer interfaces. It is not used a polynomial thickness representation for transverse shear stresses, differently to many other mixed models, because Auricchio and Sacco highlighted a serious drawback for this kind of assumption: once stress variables increase according to the increase in the number of layers, the compatibility term in the Reissner's functional forces the assumed stresses to fit with those coming from kinematic assumptions yielding to no improvements (over fitting deficiency). So, it is better to simplify the expression of transverse shear stresses in terms of kinematic variables.

In order to extend the technique to plates and to prevent from over fitting deficiency, Iurlaro et al. [**159**] assumed the cylindrical bending hypothesis according to which the transverse shear stress is related only to second order derivatives of RZT kinematic variables u_α, θ_α and Ψ_α.

In thick laminates, the plane stress assumption $\sigma_{zz}=0$ ceases to be valid; hence a fully three-dimensional stress field takes place. Displacements cease to be piecewise linear across the thickness and assume a higher-order pattern. Hence, models suitable for analysis of these

cases should account for a non-linear piecewise distribution of in-plane displacements across the thickness and for the transverse normal deformability (see, e.g. Refs. [**107**], [**119**] and [**159**]). Accordingly, Barut et al. [**161**] incorporate a piece-wise parabolic contribution to in-plane displacements and assume a smeared parabolic distribution for the transverse displacement to enrich the RZT model. The transverse normal stress is independently assumed in the form of a smeared cubic polynomial in terms of two stress variables. Subsequently, the stress variables are expressed in terms of the kinematic ones by satisfying a least-square statement.

1.8 Zig-zag models with variable kinematics and fixed d.o.f

In order to limit computational burden, Icardi and Ferrero explore whether a model with the five classical middle surface functional d.o.f. and a hierarchic zig-zag representation that can adapt to the variation of solutions can obtain accurate stress predictions from constitutive equations. Initially, in [**116**] a sublaminate ZZ-F model with variable kinematics is developed as a mixed plate model with displacements and interlaminar stresses at the upper and lower faces as functional d.o.f. The following zig-zag representation of displacements is postulated across the thickness of each computational layer J:

$$U^J(x,y,z) = u^J(x,y) + \sum_{k=1}^{n_i} \Phi_x^k(x,y)\left(z^J - z_k\right)H_k$$

$$V^J(x,y,z) = v^J(x,y) + \sum_{k=1}^{n_i} \Phi_y^k(x,y)\left(z^J - z_k\right)H_k \qquad (1.16)$$

$$W^J(x,y,z) = w^J(x,y) + \sum_{k=1}^{n_i} \Psi^k(x,y)\left(z^J - z_k\right)H_k + \sum_{k=1}^{n_i} \Omega^k(x,y)\left(z^J - z_k\right)^2 H_k$$

Contributions u^J, v^J, w^J constitute the global part, which comprises hierarchic forms, while summations represent the local one. The continuity functions Φ_x^k, Φ_y^k are aimed at making continuous the interlaminar shear stresses at the interfaces of layers grouped in each computational layer J, while Ψ^k, Ω^k make the transverse normal stress and its gradient continuous at the interfaces as prescribed by the elasticity theory. Their expressions are

determined as a combination of unknown coefficients and derivatives of the generalized displacements u^J, v^J, w^J.

The generalised displacements u^J, v^J, w^J are assumed as polynomial expansions, across the thickness whose expansion order can be varied from region to region in order to adapt to the variation of solutions.

The goal of obtaining accurate stress predictions from constitutive equations without using a sublaminate representation is achieved by Icardi and Ferrero in [**113**]. Therein, a zig-zag displacement-based shell model is developed that incorporates the variable-expansion piecewise contributions (1.16) by assuming the mid-plane generalized displacements u^0, v^0 ,w^0, γ_x and γ_y as functional d.o.f. The in-plane displacements are postulated to vary across the thickness as follows:

$$u_\alpha(\alpha,\beta,\zeta) = \left(1+\frac{\zeta}{R_\alpha}\right)u_\alpha^0(\alpha,\beta) - \zeta\frac{u_{\zeta,\alpha}^0(\alpha,\beta)}{A_\alpha} + \zeta\left(1+\left(C_{2\alpha}(\alpha,\beta)\zeta + C_{3\alpha}(\alpha,\beta)\zeta^2\right)\right)\gamma_\alpha^0(\alpha,\beta) +$$

$$+(O\ \zeta^4) + \sum_{k=1}^{n_i}\Phi_\alpha^k(\alpha,\beta)(\zeta-\zeta_k)H_k$$

$$(1.17)$$

$$u_\beta(\alpha,\beta,\zeta) = \left(1+\frac{\zeta}{R_\beta}\right)u_\beta^0(\alpha,\beta) - \zeta\frac{u_{\zeta,\beta}^0(\alpha,\beta)}{A_\beta} + \zeta\left(1+\left(C_{2\beta}(\alpha,\beta)\zeta + C_{3\beta}(\alpha,\beta)\zeta^2\right)\right)\gamma_\beta^0(\alpha,\beta) +$$

$$+(O\ \zeta^4) + \sum_{k=1}^{n_i}\Phi_\beta^k(\alpha,\beta)(\zeta-\zeta_k)H_k$$

$$(1.18)$$

where α, β are the coordinate on the shell middle surface, ζ is the thickness coordinate and R_α, R_β are the radii. The coefficients $C_{2\alpha}$, $C_{3\alpha}$, $C_{2\beta}$ and $C_{3\beta}$ are expressed in terms of the functional d.o.f. and their derivatives by enforcing the stress-free boundary conditions for the transverse shear stresses (1.5).

The transverse displacement variation across the thickness is represented in the following form:

$$u_\zeta(\alpha,\beta,\zeta) = u_\zeta^0(\alpha,\beta) + \zeta b(\alpha,\beta) + \zeta^2 c(\alpha,\beta) + \zeta^3 d(\alpha,\beta) + \zeta^4 e(\alpha,\beta) +$$

$$+(O\ \zeta^5.....) + \sum_{k=1}^{n_i}\Psi_\zeta^k(\alpha,\beta)(\zeta-\zeta_k)H_k + \sum_{k=1}^{n_i}\Omega_\zeta^k(\alpha,\beta)(\zeta-\zeta_k)^2 H_k$$

$$(1.19)$$

The continuity functions have the same purpose as in (1.16). The still unknown coefficients b to e are determined by enforcing the stress boundary conditions:

$$\sigma_{\zeta\zeta}\left(\frac{h}{2}\right)= p^0\left(\frac{h}{2}\right); \quad \sigma_{\zeta\zeta}\left(-\frac{h}{2}\right)= p^0\left(-\frac{h}{2}\right); \quad \sigma_{\zeta\zeta,\varsigma}\left(\frac{h}{2}\right)=\sigma_{\zeta\zeta,\varsigma}\left(-\frac{h}{2}\right)=0; \qquad (1.20)$$

The displacement field fulfils the following kinematic contact conditions that hold for perfect bonding:

$$u_\alpha\big|_{k_{\zeta^+}} =u_\alpha\big|_{k_{\zeta^-}}; \quad u_\beta\big|_{k_{\zeta^+}} =u_\beta\big|_{k_{\zeta^-}}; \quad u_\zeta\big|_{k_{\zeta^+}} =u_\zeta\big|_{k_{\zeta^-}}; \qquad (1.21)$$

The higher-order terms $(O\zeta^4)$ and $(O\zeta^5)$ represent contributions whose expansion order can vary across the thickness as desired. This model provides accurate prediction of stress and displacement field directly from constitutive equations, as shown in the benchmark cases with exact solutions usually considered in literature and for variable-stiffness composites [114] - [115].

However, the model [113] requires adopting a too high order of expansion in each computational layer, which could be impractical in certain cases. Therefore, Icardi and Sola [119] recasts the approach of [113] in such a way that allows for reducing the expansion order of displacements across the thickness, as discussed in the next chapter, so to improve the computational efficiency.

Chapter 2: The present adaptive model (AD-ZZ)

In this chapter a high order theory including zig-zag effects, transverse shear continuity, variable transverse displacement and layerwise representation (AD-ZZ model) is presented for analysis of laminates and sandwiches. The dissertation is organized in such a way that explains how the author has reached the current version of this model. In particular, the path followed starts from basic Equivalent Single Layer theories ([**12**], [**13**]) and then, by adding new coefficients or varying the through-the-thickness interpolation, it refines the structural model and forces it to respect the conditions prescribed by the Elasticity Theory. The final result is a model that with low computational effort can represent the interlaminar shear stresses directly from constitutive equations even for thick laminated and sandwich structures also when the constituent plies have distinctly different properties across the thickness. These characteristics make this theory particularly suited for the analysis of highly iterative problems, such as non-linear analyses or impulsive dynamic studies, as discussed forward.

Generally speaking, the AD-ZZ model is a modified version of the zig-zag 3D one by Icardi and Ferrero [**113**]. In particular the AD-ZZ model differs from the theory of [**113**] mainly for two aspects:

- all the higher-order terms in the present model can vary between each layer, while in [**113**] the coefficients of second, third and fourth order in z are the same across all the structure. This new approach enables to reduce the coefficients to be determined, as shown next (see Section 2.2.3).

- a more intensive use of the symbolic calculus in the implementation that enable to compute apart once for all in closed form the expressions of high-order terms and continuity functions (see Figure 2.5). In this way, it is possible to overcome the drawbacks due to the rather complex algebraic manipulations required for an *a priori*

fulfilment of the stress continuity conditions at the interfaces and for deriving the expressions of the higher-order contributions. In addition, the use of the symbolic calculus avoids the simplifying assumptions that the theory [113] formulate to compute numerically high-order terms and continuity functions.

These aspects contribute to reduce the computational times of the present theory up to 10 % per each run with respect to [113].

2.1 Steps from FSDT to PWM4 models

In order make clearer the AD-ZZ model here presented, all the refinements brought through years till the present final version are recalled. This represents also the logical path followed when implementing the AD-ZZ model. As explained next, every refinement has been introduced in order to improve accuracy but keeping low computational burden.

For each model here recalled the displacement and stress fields are compared to the exact solution for a [0°/90°/0°] laminated beam.

The laminated beam, for which the exact solution is reported in Ref. [144], has three layers made of mat p (E_L/E_T=25; G_{LT}/E_T=0.5; G_{TT}/E_T=0.2; υ_{LT}=0.25), each h/3 high. In order to enhance the layerwise effects a length to thickness ratio of 4 is considered.

The beam is simply-supported and the acting loading on the upper face of the structure is sinusoidal:

$$p^0(x) = \sum_{m=1}^{M} P_m \sin\left(\frac{m\pi}{L_x} x\right) \tag{2.1}$$

The static problem is solved within the framework of the Rayleigh-Ritz method, assuming the in-plane variation of the functional d.o.f. as follows:

$$u^0(x) = \sum_{m=1}^{M} A_m \cos\left(\frac{m\pi}{L_x} x\right) \tag{2.2}$$

$$w^0(x) = \sum_{m=1}^{M} C_m \sin\left(\frac{m\pi}{L_x} x\right) \tag{2.3}$$

$$\gamma_x^0(x) = \sum_{m=1}^{M} D_m \cos\left(\frac{m\pi}{L_x} x\right) \tag{2.4}$$

The Rayleigh-Ritz method is chosen since, to obtain the governing equations, it requires writing only the strain energy, the kinetic energy and the work of external forces. In this way, it is not necessary deriving the Euler-Lagrange field equations and variationally consistent boundary conditions and it is easier using symbolic calculus within the solving procedure (see Section 2.2.2). Note that the use of the Rayleigh-Ritz method is allowed since always conservative systems are analysed.

The displacement and stress variations across the thickness reported in this section are normalized as follows [144]:

$$\bar{\sigma}_{xx} = \frac{\sigma_{xx}\left(\frac{L_x}{2}, z\right)}{p^0} \quad \bar{\sigma}_{zz} = \frac{\sigma_{zz}\left(\frac{L_x}{2}, z\right)}{p^0} \quad \bar{\sigma}_{xz} = \frac{\sigma_{xz}(0, z)}{p^0} \quad \bar{u} = \frac{E_2 u(0, z)}{hp^0} \tag{2.5}$$

Please notice that all results reported in this section are obtained without introducing any technique for improving results except integration of local equilibrium equations. No shear correction factors are used for FSDT in order to compare the results by elder models to those of most recent ones under the same hypotheses.

In order to put the results shown in this section in the right perspective, it is reminded that the elasticity theory prescribes the following requirements to be met:

$$\sigma_{xz}\left(z = \pm\frac{h}{2}\right) = \tau_{xz}\left(z = \pm\frac{h}{2}\right) \quad \sigma_{yz}\left(z = \pm\frac{h}{2}\right) = \tau_{yz}\left(z = \pm\frac{h}{2}\right) \tag{2.6}$$

$$\sigma_{zz}\left(z = \frac{h}{2}\right) = p^0\left(z = \frac{h}{2}\right) \quad \sigma_{zz}\left(z = -\frac{h}{2}\right) = p^0\left(z = -\frac{h}{2}\right) \tag{2.7}$$

$$\sigma_{xz}\big|_{(k)_{z^+}} = \sigma_{xz}\big|_{(k)_{z^-}} \quad \sigma_{yz}\big|_{(k)_{z^+}} = \sigma_{yz}\big|_{(k)_{z^-}} \tag{2.8}$$

$$\sigma_z\big|_{(k)_{z^+}} = \sigma_z\big|_{(k)_{z^-}} \tag{2.9}$$

Finally note that the notation adopted in this chapter is the same already explained in Section 1.2.

2.1.1 FSDT model

The First-Order Shear Deformation Theory (FSDT) [12] is the extension to multilayer laminates of previous theories available, as it allows a transverse shear deformation of the plate. The displacement field is:

$$u(x, y, z) = u^0(x, y) + z\left[\gamma_x^0(x, y) - w^0{}_{,x}(x, y)\right]$$

$$v(x, y, z) = v^0(x, y) + z\left[\gamma_y^0(x, y) - w^0{}_{,y}(x, y)\right] \tag{2.10}$$

$$\text{w}(x, y, z) = \text{w}^0(x, y)$$

The displacement and stress fields computed for the cross-ply beam described above are reported in Figure 2.1.
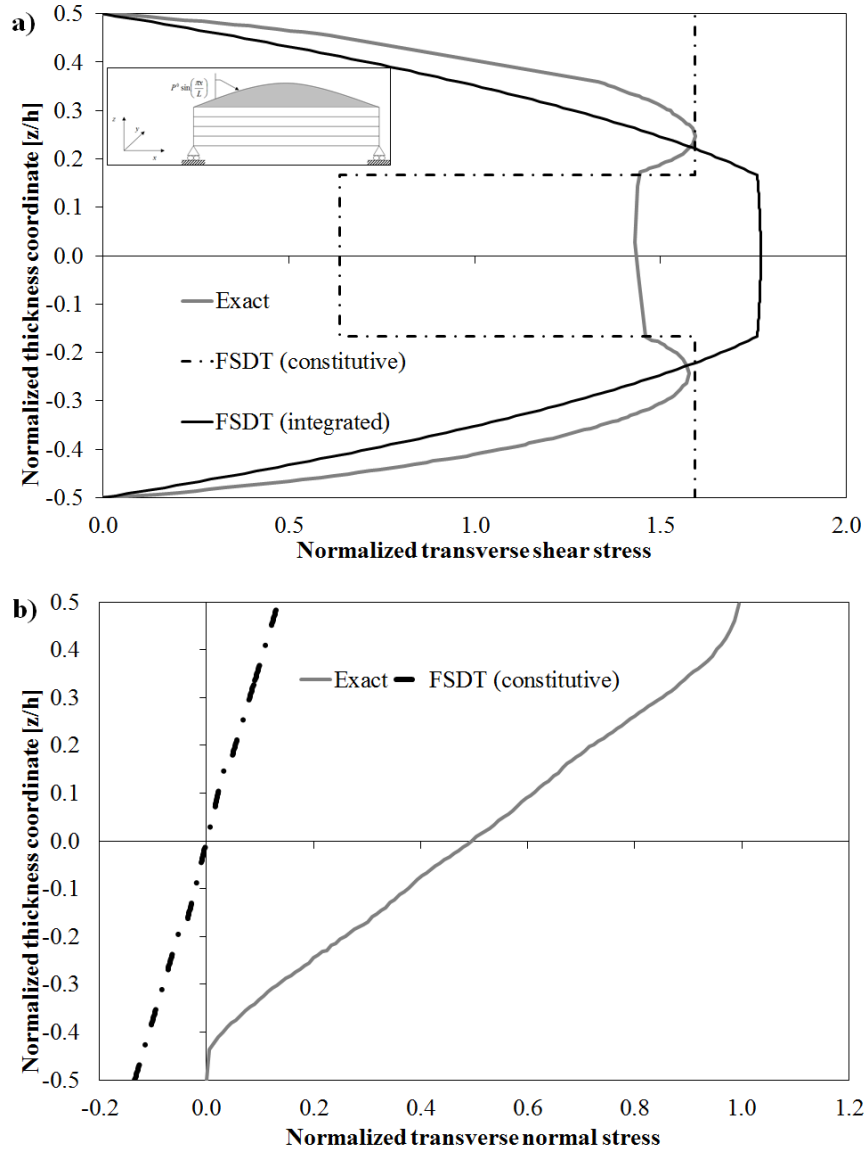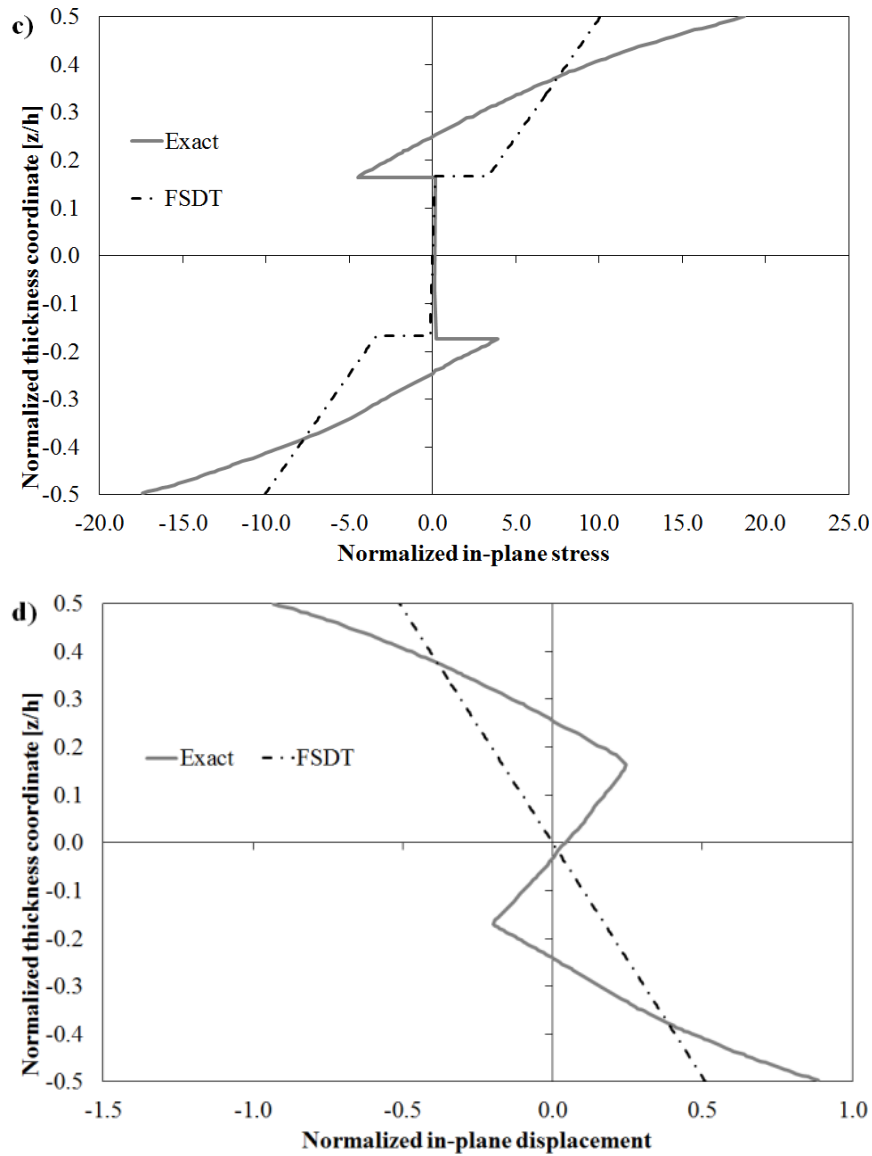
Figure 2.1 Comparison between stress and displacement fields by the FSDPT model [12] and the exact solution [144] for a [0°/90°/0°] laminated beam with L/h=4.

The FSDT model, which assumes the transverse shear strain constant across the thickness of the structure, yields to a piece-wise constant distribution of transverse shear stress that violates the continuity conditions at layer interfaces. Also the stress-free boundary conditions at the top and bottom surface are not satisfied, as shown by the shear stress computed from constitutive equations reported in Figure 2.1a. It is seen that the representation of in-plane displacement across the thickness is not adequate (Figure 2.1d) and also the distribution of the in-plane stress across the thickness is wrong (Figure 2.1c). As a consequence, integrating $\sigma_{xx,x} + \sigma_{xz,z} = 0$ does not bring a significant improvement in the prediction of the transverse shear

stress (Figure 2.1a). Note that in Figure 2.1b it is reported a quantity defined as transverse normal stress computed from constitutive equations. This means that this quantity is calculated applying Eq. (1.1). So, considering the structure analysed and the displacement field (2.10), it results that $\sigma_{zz} = C_{13}\, \varepsilon_{xx}$. This consideration holds also for the theory presented in Section 2.1.2 and 2.1.3.

2.1.2 HSDT model

In order to improve accuracy, Reddy [13] with the HSDT model postulates the addition of a term of third order in z to the in-plane displacements, whose aim is to meet the boundary conditions for the transverse shear stress at the upper and lower surfaces at least for symmetric lay-ups (Eq. 2.6):

$$
\begin{aligned}
\mathrm{u}(x,\mathrm{y},z) &= u^0(x,y) + z\left[\gamma_x^0(x,y) - w^0_{,x}(x,y)\right] + D_x(x,y)z^3 \\
v(x,\mathrm{y},z) &= v^0(x,y) + z\left[\gamma_y^0(x,y) - w^0_{,y}(x,y)\right] + D_y(x,y)z^3 \qquad (2.11)\\
\mathrm{w}(\mathrm{x},\mathrm{y},\mathrm{z}) &= \mathrm{w}^0(x,y)
\end{aligned}
$$

The stress and displacement fields by the HSDT model for the [0°/90°/0°] laminated beam are reported in Figure 2.2.

The results of Figure 2.2 show that HSDT still inaccurately evaluates and disregards the energy contributions of transverse normal strain and stress as well as those of the transverse shear stress (Figure 2.2a and c). Though fulfilling the boundary conditions of Eq. 2.6, the shear stress is not continuous and still inaccurate. The behaviour is different for the in-plane stress. Indeed, for this structure, the distribution computed by the HSDT model still remains inaccurate, but only close to the interfaces. As a consequence, integrating $\sigma_{xx,x} + \sigma_{xz,z} = 0$ allows for a good prediction of the transverse shear stress near the free faces (Figure 2.2a). An acceptable accuracy of the in-plane displacement is obtained at the upper and lower faces, while near the interfaces the through-the-thickness variation is inaccurate.

2.1.3 PWM3 model

As explained in Chapter 1, another constraint that the structural models tried to fulfil is the continuity of the transverse shear stress (Eq. 2.8). To reach this goal, as mentioned above two different solutions can be adopted using physically-based or cinematically-based zig-zag functions. For the development of the AD-ZZ model the former solution is adopted. Therefore, the displacement field (here named PWM3) discussed in this section, as in Ref. [**141**], adds one set of continuity functions to the in-plane displacement distribution of the HSDT model (2.11). These terms introduce a layerwise effect, aiming at restoring the through-the-thickness continuity of the transverse shear stress. In addition, also a parabolic contribution is incorporated in the in-plane displacements of (2.11) in order to fulfil the stress-free boundary conditions (2.6) at the upper and lower free surfaces also for asymmetric structures. Therefore, the displacement field for the PWM3 model is as follows:

$$\mathrm{u}(x,\mathrm{y},\mathrm{z}) = u^0(x,y) + z\left[\gamma_x^0(x,y) - w^0_{,x}(x,y)\right] + C_x(x,y)z^2 + D_x(x,y)z^3 + \sum_{k=1}^{n_i}\Phi_x^k(x,y)(z-z_k)H_k$$

$$\mathrm{v}(x,\mathrm{y},\mathrm{z}) = v^0(x,y) + z\left[\gamma_y^0(x,y) - w^0_{,y}(x,y)\right] + C_y(x,y)z^2 + D_y(x,y)z^3 + \sum_{k=1}^{n_i}\Phi_y^k(x,y)(z-z_k)H_k \qquad (2.12)$$

$$\mathrm{w}(x,\mathrm{y},\mathrm{z}) = w^0(x,y)$$

For the cross-ply beam, the stress and displacement fields predicted by the PWM3 model are reported in Figure 2.3.

a)

b)

c)
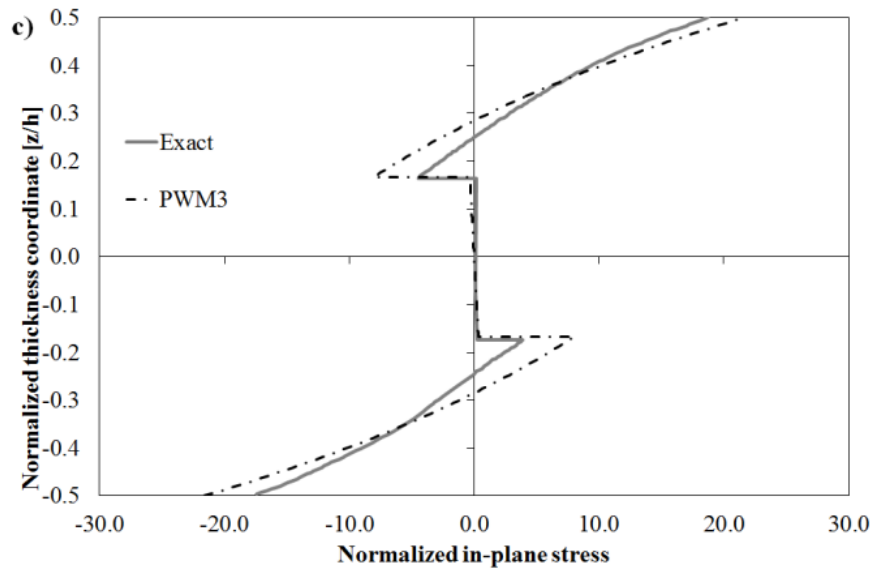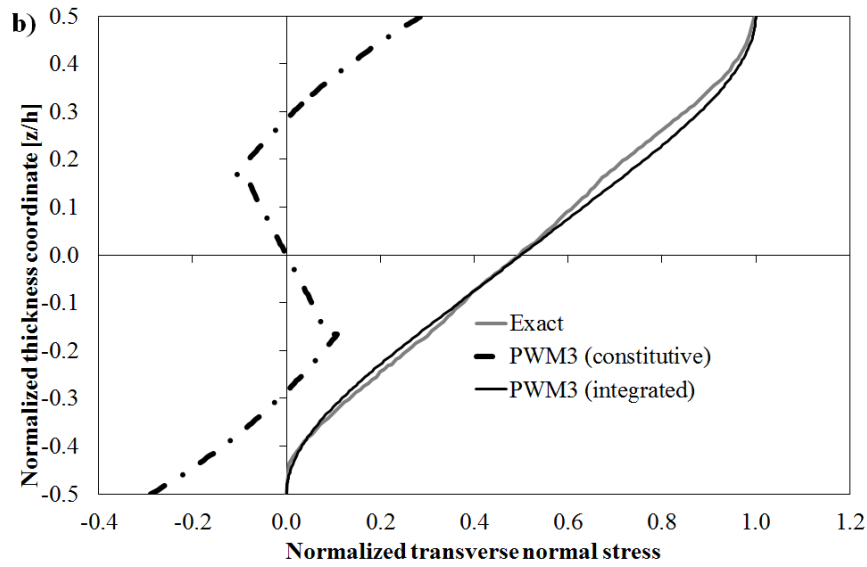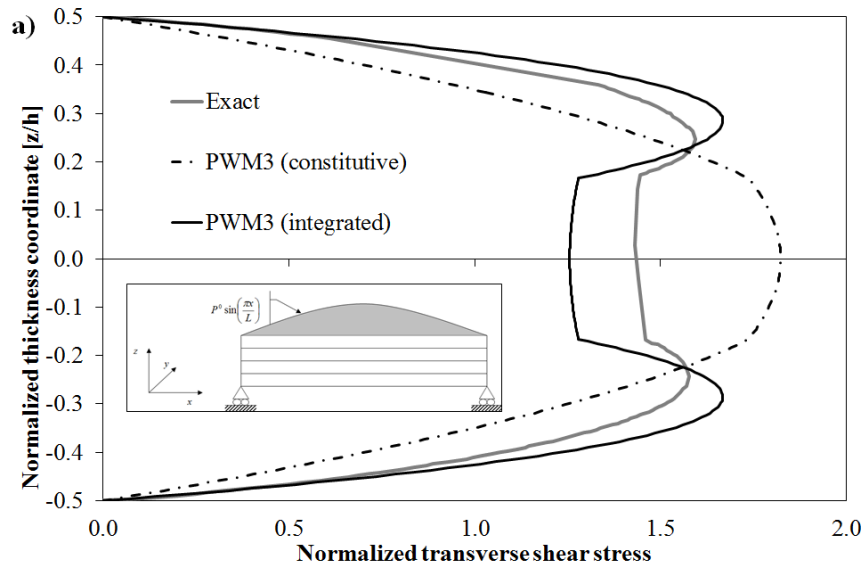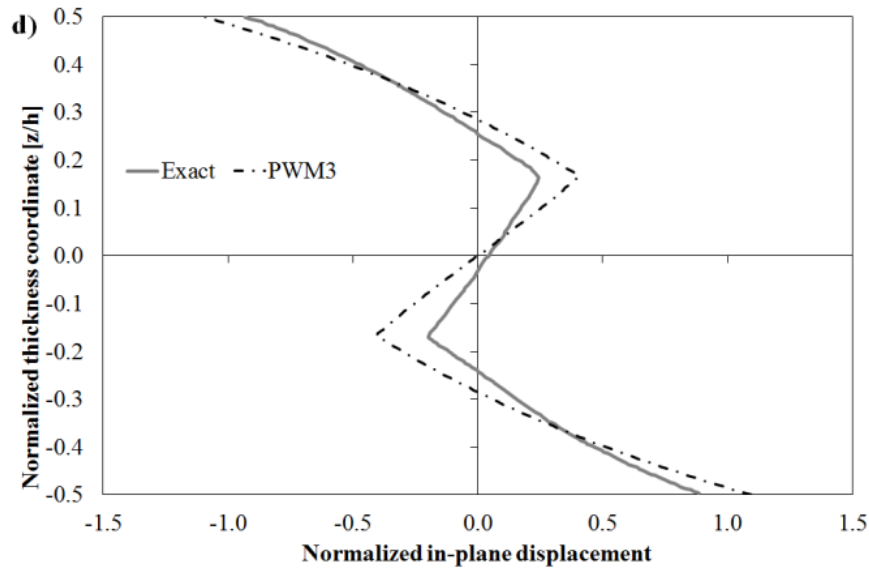
Figure 2.3 Comparison between stress and displacement fields by the Piecewise cubic model PWM3 (Eq. 2.12) and the exact solution [144] for a [0°/90°/0°] laminated beam with L/h=4.

In Figure 2.3a, the transverse shear stress predicted from constitutive equations is continuous and it respects the boundary conditions prescribed by the elasticity theory (2.6). Nevertheless, accuracy is not consistently improved as shown by the comparison with the exact solution. The situation does not improve integrating the equilibrium equation $\sigma_{xx,x} + \sigma_{xz,z} = 0$. Indeed, the layerwise effect is only partially captured and a coincidence with the exact solution is not still achieved. The difference between the exact solution and the one predicted by the PWM3 model is strongly evident close to the interfaces, which are the most critical regions when performing damage analysis. The incorrect result is a consequence of the inaccurate evaluation of the in-plane stress (Figure 2.3c) and of the in-plane displacement (Figure 2.3d). So, there is a lack in the theory. In fact, the energy due to the transverse normal stress is still disregarded. Despite this, the transverse normal stress computed integrating $\sigma_{xz,x} + \sigma_{zz,z} = 0$ (Figure 2.3b) is accurate.

The above mentioned lack of this theory becomes more evident when studying sandwiches, which have constituent layers with distinctly different mechanical properties and so claim for structural model with variable transverse displacement.

2.1.4 PWM4 model

In accordance with what discussed above, as explained in Chapter 1, Icardi [107] refines the PWM3 postulating also for the transverse displacement a variable representation up to the fourth order. In addition, the PWM4 model adds two set of layerwise terms to the transverse displacement in order to satisfy the continuity conditions on the transverse normal stress (Eq. 2.9) and its through-the-thickness gradient. Thus, the following displacement field is postulated:

$$\mathrm{u}(x,y,\mathrm{z}) = u^0(x,y) + z\left[\gamma_x^0(x,y) - w^0{}_{,x}(x,y)\right] + C_x(x,y)z^2 + D_x(x,y)z^3 + \sum_{k=1}^{n_i}\Phi_x^k(x,y)(z-z_k)H_k$$

$$v(x,y,\mathrm{z}) = v^0(x,y) + z\left[\gamma_y^0(x,y) - w^0{}_{,y}(x,y)\right] + C_y(x,y)z^2 + D_y(x,y)z^3 + \sum_{k=1}^{n_i}\Phi_y^k(x,y)(z-z_k)H_k \qquad (2.13)$$

$$\mathrm{w}(x,y,\mathrm{z}) = w^0(x,y) + b(x,y)z + c(x,y)z^2 + d(x,y)z^3 + e(x,y)z^4 + \sum_{k=1}^{n_i}\Psi_x^k(x,y)(z-z_k)H_k +$$

$$+ \sum_{k=1}^{n_i}\Omega_x^k(x,y)(z-z_k)^2 H_k$$

As shown by Figure 2.4a, the addition of these terms does not bring to significant improvement in the evaluation of the transverse shear stress both from constitutive equations and from integration. The same consideration holds for in-plane stress and displacement, whose accuracy is not changed with respect to that of Figure 2.3 (see Figure 2.4 c and d). Instead, an improvement is obtained for the transverse normal stress (Figure 2.4b), which now, also when computed from constitutive equations, fulfils all the conditions prescribed by the elasticity theory (Eq. 2.7) and quite well describes the through-the-thickness distribution of the exact solution.
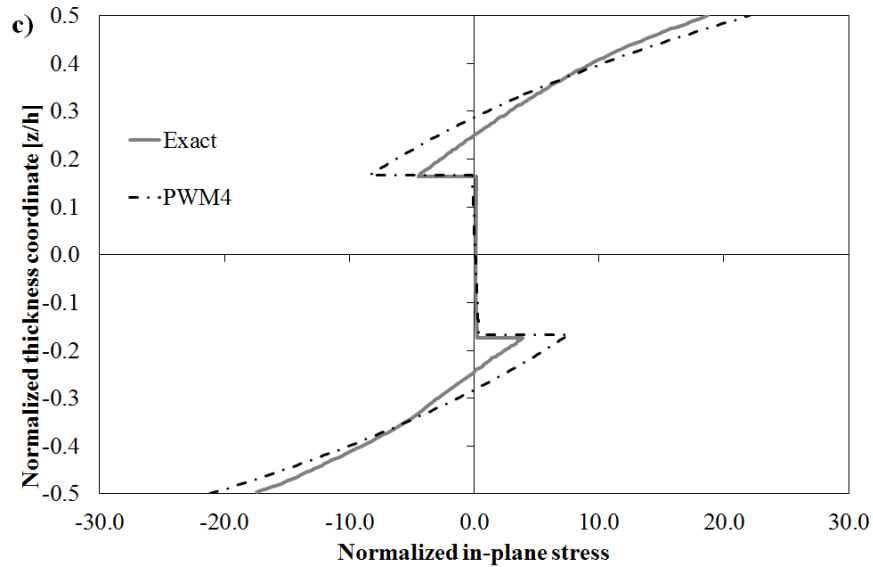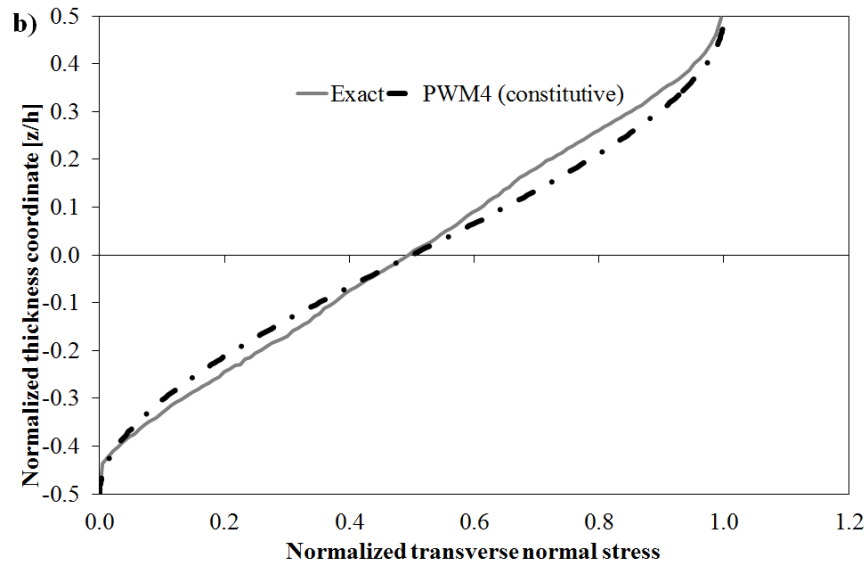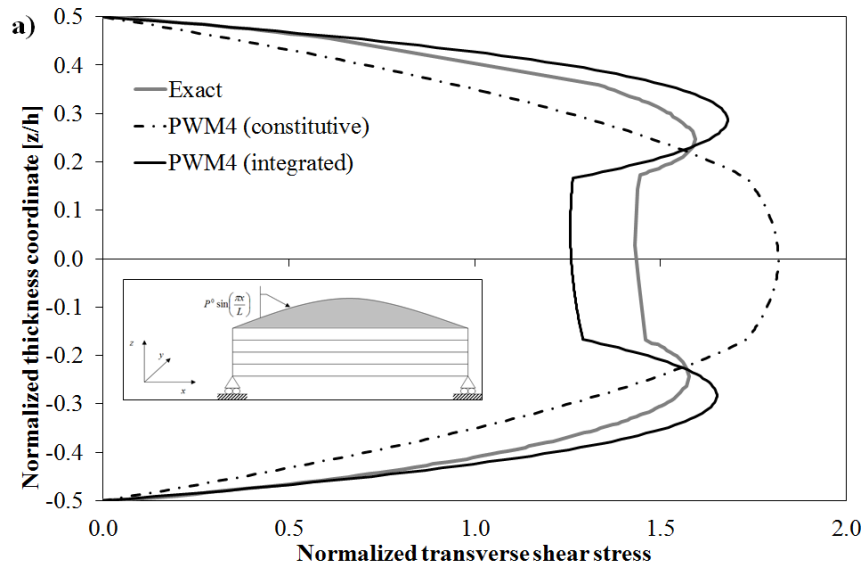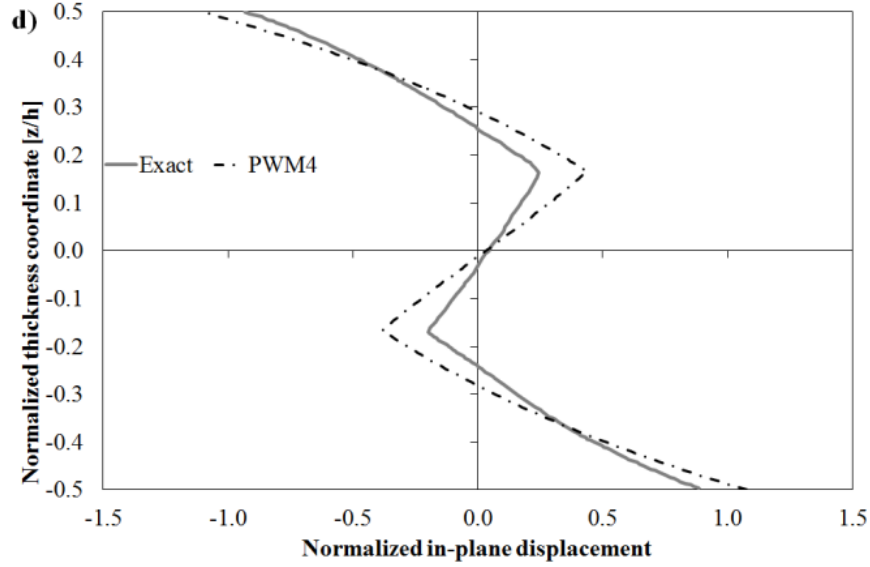
Figure 2.4 Comparison between stress and displacement fields by the Piecewise quartic model PWM4 (Eq. 2.13) and the exact solution [144] for a [0°/90°/0°] laminated beam with L/h=4.

2.2 Development of the AD-ZZ model

A further improvement of model [**107**] is difficult to obtain by simply adding terms of higher order in z. To overcome this problem, the author developed the AD-ZZ model [**119**] by exploiting a different version of the idea of refining the local interpolation already pursued by sublaminate and global local models discussed in Section 1.5 and 1.6. Accordingly, the following representation of the in-plane displacements is postulated across the thickness:

$$u(x, y, z) = u^0(x, y) + z(\gamma_x^0(x, y) - w^0_{,x}) + C_x^i(x, y)z^2 + D_x^i(x, y)z^3 + (Oz^4) +$$
$$+ \sum_{k=1}^{n_i} \Phi_x^k(x, y)(z - z_k)H_k + \sum_{k=1}^{n_i} C_u^k(x, y)H_k \tag{2.14}$$

$$v(x, y, z) = v^0(x, y) + z(\gamma_y^0(x, y) - w^0_{,y}) + C_y^i(x, y)z^2 + D_y^i(x, y)z^3 + (Oz^4) +$$
$$+ \sum_{k=1}^{n_i} \Phi_y^k(x, y)(z - z_k)H_k + \sum_{k=1}^{n_i} C_v^k(x, y)H_k \tag{2.15}$$

To have the minimal number of unknowns, the three displacement components and the two shear rotations of the normals on the reference surface are assumed as functional d.o.f. The superscripts i mean that these terms vary from point to point across the thickness. From the theoretical viewpoint, this aspect and the addition of the continuity functions C_u^k and C_v^k

34

represent the new contributions with respect to the model by Icardi and Ferrero [**113**] with the same d.o.f. Indeed, in [**113**] the third and four order expansion is considered fixed across the thickness, while just the higher-order terms are assumed to vary with position.

As for the other zig-zag models, the terms in the summations represent contributions that are continuous across the thickness, but with discontinuous derivatives at the layer interfaces. The expressions of the continuity functions $\Phi_x^{\,k}$, $\Phi_y^{\,k}$, $C_u^{\,k}$ and $C_v^{\,k}$ are determined enforcing an *a priori* fulfilment of the transverse shear stress (Eq. 2.8) and of the displacement contact conditions at the interfaces:

$$u(z={}^{(k)}z^+) = u(z={}^{(k+1)}z^-) \tag{2.16}$$

$$v(z={}^{(k)}z^+) = v(z={}^{(k+1)}z^-) \tag{2.17}$$

The coefficients $C_x^{\,i}$, $C_y^{\,i}$, $D_x^{\,i}$ and $D_y^{\,i}$ as well as the other high order coefficients are determined by enforcing the stress-free boundary conditions for the transverse shear stresses at the upper $|^u$ and lower $|_l$ free surfaces (Eq. 2.6) and also by enforcing equilibrium conditions at discrete points across the thickness:

$$\sigma_{xx,x} + \sigma_{xy,y} + \sigma_{xz,z} = b_x$$
$$\sigma_{xy,x} + \sigma_{yy,y} + \sigma_{yz,z} = b_y \tag{2.18}$$
$$\sigma_{xz,x} + \sigma_{yz,y} + \sigma_{zz,z} = b_z$$

where b_i are the body forces.

In this work, as explained forward, these cumbersome algebraic operations are carried out once for all with a symbolic calculus tool, thus speeding up the analysis.

As already discussed, the transverse displacement has a significant role for describing core's crushing in sandwich structure as well as for keeping equilibrium when thermal stresses are applied. Accordingly, a variable representation across the thickness is postulated:

$$w(x,y,z) = w^0(x,y) + b^i(x,y)z + c^i(x,y)z^2 + d^i(x,y)z^3 + e^i(x,y)z^4 + (Oz^5) +$$
$$+ \sum_{k=1}^{n_i} \Psi^k(x,y)(z-z_k)H_k + \sum_{k=1}^{n_i} \Omega^k(x,y)(z-z_k)^2 H_k + \sum_{k=1}^{n_i} C_w^k(x,y)H_k \tag{2.19}$$

From the formal point of view, this expression is similar to the one proposed in Ref. [**113**], but here, though the functional d.o.f. are fixed, the expression holds in a single layer. This aspect and the addition of the continuity function $C_w^{\,k}$ represent the new contributions with respect to the model Icardi and Ferrero [**113**].

The two zig-zag contributions Ψ^k and Ω^k in the summations are incorporated in order to *a priori* fulfil the stress contact conditions on the transverse normal stress (Eq. 2.9) and its gradient (as it can be noticed analysing the local equilibrium equations (2.18)):

$$\sigma_{z,z}(z={}^{(k)}z^+) = \sigma_{z,z}(z={}^{(k+1)}z^-) \tag{2.20}$$

The continuity function C_w^k, enable an *a priori* fulfilment of the displacement contact conditions, by imposing:

$$w(z={}^{(k)}z^+) = w(z={}^{(k+1)}z^-) \tag{2.21}$$

The still unknown coefficients b^i to e^i are determined by enforcing equilibrium conditions (2.18) at discrete points across the thickness, as well as by enforcing the fulfilment of the boundary conditions on the transverse normal stress (Eq. 2.7) and its gradient at the upper and lower bounding surfaces:

$$\sigma_{z,z}\left(\pm\frac{h}{2}\right) = 0 \tag{2.22}$$

This last condition directly derives from Eq. (2.18), from which, it is possible to obtain:

$$\sigma_{zz,z} = b_z - \sigma_{xz,x} - \sigma_{yz,y} \tag{2.23}$$

By assuming $b_i=0$, Eq. (2.23) at the free surfaces of the structures turns into (2.22).

From the practical viewpoint, the new contribution with respect to the model of Ref. [113] is that continuity functions and high-order terms are computed in a fully closed exact form using a symbolic calculus tool, as explained next.

2.2.1 Continuity functions

In order to get the expressions of continuity functions, the displacement field is split into fixed contributes, layer's contributes and summations' contributes, as follows:

$$u(x,y,z) = U^0\left(x,y,z\right) + U^i\left(x,y,z\right) + \sum_{k=1}^{n_i}\Phi_x^k(x,y)(z-z_k)H_k + \sum_{k=1}^{n_i}C_u^k(x,y)H_k$$

$$v(x,y,z) = V^0\left(x,y,z\right) + V^i\left(x,y,z\right) + \sum_{k=1}^{n_i}\Phi_y^k(x,y)(z-z_k)H_k + \sum_{k=1}^{n_i}C_v^k(x,y)H_k \tag{2.24}$$

$$w(x,y,z) = W^0\left(x,y,z\right) + W^i\left(x,y,z\right) + \sum_{k=1}^{n_i}\Psi^k(x,y)(z-z_k)H_k +$$

$$+\sum_{k=1}^{n_i}\Omega^k(x,y)(z-z_k)^2H_k + \sum_{k=1}^{n_i}C_w^k(x,y)H_k$$

As it can be seen in a straightforward way, the interfacial displacement contact conditions do not involve derivatives of the functional d.o.f. of any order. As example, the explicit expressions of (2.16) and (2.21) at the generic interface $\Im$ are reported:

$$
U^0\left(x,y,z_\Im\right)+U^i\left(x,y,z_\Im\right)+\sum_{k=1}^{\Im}\Phi_x^k(x,y)(z_\Im-z_k)H_k+\sum_{k=1}^{\Im}C_u^k(x,y)H_k=
$$
$$
=U^0\left(x,y,z_\Im\right)+U^{i+1}\left(x,y,z_\Im\right)+\sum_{k=1}^{\Im+1}\Phi_x^k(x,y)(z_\Im-z_k)H_k+\sum_{k=1}^{\Im+1}C_u^k(x,y)H_k
$$
(2.25)

$$
W^0\left(x,y,z_\Im\right)+W^i\left(x,y,z_\Im\right)+\sum_{k=1}^{\Im}\Psi^k(x,y)(z_\Im-z_k)H_k+\sum_{k=1}^{\Im}\Omega^k(x,y)(z_\Im-z_k)^2H_k+\sum_{k=1}^{\Im}C_w^k(x,y)H_k=
$$
$$
=W^0\left(x,y,z_\Im\right)+W^i\left(x,y,z_\Im\right)+\sum_{k=1}^{\Im+1}\Psi^k(x,y)(z_\Im-z_k)H_k+\sum_{k=1}^{\Im+1}\Omega^k(x,y)(z_\Im-z_k)^2H_k+\sum_{k=1}^{\Im+1}C_w^k(x,y)H_k
$$
(2.26)

From Eqs. (2.25) and (2.26) it is possible to easily notice that the expressions of the displacement continuity functions C_u^k, C_v^k and C_w^k at a generic interface $\Im$ are represented by the difference between the layer's contributes of adjacent plies:

$$
C_u^k(x,y)=U^i\left(x,y,z_\Im\right)-U^{i+1}\left(x,y,z_\Im\right)
$$
(2.27)

$$
C_v^k(x,y)=V^i\left(x,y,z_\Im\right)-V^{i+1}\left(x,y,z_\Im\right)
$$
(2.28)

$$
C_w^k(x,y)=W^i\left(x,y,z_\Im\right)-W^{i+1}\left(x,y,z_\Im\right)
$$
(2.29)

The expressions of the other continuity functions are more intricate, however it is possible to notice that Φ_x^k, Φ_y^k and Ψ^k involve first order derivatives of the functional d.o.f., whereas Ω^k involves also second order derivatives of the functional d.o.f. Their expressions should be assumed in the following form as function of unknown coefficients (here named continuity constants) and of derivatives of various order of the functional d.o.f.:

$$
\Phi_x^k=\Phi_{u1}^{(k)}\left(U^0+U^i\right)_{,x}+\Phi_{u2}^{(k)}\left(U^0+U^i\right)_{,y}+\Phi_{u3}^{(k)}\left(U^0+U^i\right)_{,z}+\Phi_{u4}^{(k)}\left(V^0+V^i\right)_{,x}+
$$
$$
+\Phi_{u5}^{(k)}\left(V^0+V^i\right)_{,y}+\Phi_{u6}^{(k)}\left(V^0+V^i\right)_{,z}+\Phi_{u7}^{(k)}\left(W^0+W^i\right)_{,x}+\Phi_{u8}^{(k)}\left(W^0+W^i\right)_{,y}+
$$
$$
+\Phi_{u9}^{(k)}\left(W^0+W^i\right)_{,z}
$$
(2.30)

$$
\Phi_y^k=\Phi_{v1}^{(k)}\left(U^0+U^i\right)_{,x}+\Phi_{v2}^{(k)}\left(U^0+U^i\right)_{,y}+\Phi_{v3}^{(k)}\left(U^0+U^i\right)_{,z}+\Phi_{v4}^{(k)}\left(V^0+V^i\right)_{,x}+
$$
$$
+\Phi_{v5}^{(k)}\left(V^0+V^i\right)_{,y}+\Phi_{v6}^{(k)}\left(V^0+V^i\right)_{,z}+\Phi_{v7}^{(k)}\left(W^0+W^i\right)_{,x}+\Phi_{v8}^{(k)}\left(W^0+W^i\right)_{,y}+
$$
$$
+\Phi_{v9}^{(k)}\left(W^0+W^i\right)_{,z}
$$
(2.31)

$$\Psi^k = \Psi_1^{(k)}\left(U^0 + U^i\right)_{,x} + \Psi_2^{(k)}\left(U^0 + U^i\right)_{,y} + \Psi_3^{(k)}\left(U^0 + U^i\right)_{,z} + \Psi_4^{(k)}\left(V^0 + V^i\right)_{,x} +$$
$$+ \Psi_5^{(k)}\left(V^0 + V^i\right)_{,y} + \Psi_6^{(k)}\left(V^0 + V^i\right)_{,z} + \Psi_7^{(k)}\left(W^0 + W^i\right)_{,x} + \Psi_8^{(k)}\left(W^0 + W^i\right)_{,y} + \qquad (2.32)$$
$$+ \Psi_9^{(k)}\left(W^0 + W^i\right)_{,z}$$

$$\Omega^k = \Omega_1^{(k)}\left(U^0 + U^i\right)_{,xx} + \Omega_2^{(k)}\left(U^0 + U^i\right)_{,xy} + \Omega_3^{(k)}\left(U^0 + U^i\right)_{,xz} + \Omega_4^{(k)}\left(U^0 + U^i\right)_{,yy} +$$
$$+ \Omega_5^{(k)}\left(U^0 + U^i\right)_{,yz} + \Omega_6^{(k)}\left(U^0 + U^i\right)_{,zz} + \Omega_7^{(k)}\left(V^0 + V^i\right)_{,xx} + \Omega_8^{(k)}\left(V^0 + V^i\right)_{,xy} +$$
$$+ \Omega_9^{(k)}\left(V^0 + V^i\right)_{,xz} + \Omega_{10}^{(k)}\left(V^0 + V^i\right)_{,yy} + \Omega_{11}^{(k)}\left(V^0 + V^i\right)_{,yz} + \Omega_{12}^{(k)}\left(V^0 + V^i\right)_{,zz} + \qquad (2.33)$$
$$+ \Omega_{13}^{(k)}\left(W^0 + W^i\right)_{,xx} + \Omega_{14}^{(k)}\left(W^0 + W^i\right)_{,xy} + \Omega_{15}^{(k)}\left(W^0 + W^i\right)_{,xz} + \Omega_{16}^{(k)}\left(W^0 + W^i\right)_{,yy} +$$
$$+ \Omega_{17}^{(k)}\left(W^0 + W^i\right)_{,yz} + \Omega_{18}^{(k)}\left(W^0 + W^i\right)_{,zz}$$

Thus, at every interface, 45 unknowns should be computed $\Phi_{u1}^{(k)}$, …., $\Phi_{u9}^{(k)}$, $\Phi_{v1}^{(k)}$, …., $\Phi_{v9}^{(k)}$, $\Psi_1^{(k)}$, …., $\Psi_9^{(k)}$, $\Omega_1^{(k)}$, …., $\Omega_{18}^{(k)}$. For doing this, based on the assumption of Eqs. (2.24), the strain field becomes:

$$\varepsilon_{xx}(x,y,z) = U_{,x}^0 + U_{,x}^i + \sum_{k=1}^{n_i} \Phi_{x,x}^k(z - z_k)H_k + \sum_{k=1}^{n_i} C_{u,x}^k H_k$$

$$\varepsilon_{yy}(x,y,z) = V_{,y}^0 + V_{,y}^i + \sum_{k=1}^{n_i} \Phi_{y,y}^k(z - z_k)H_k + \sum_{k=1}^{n_i} C_{v,y}^k H_k$$

$$\varepsilon_{zz}(x,y,z) = W_{,z}^i + \sum_{k=1}^{n_i} \Psi^k H_k + 2\sum_{k=1}^{n_i} \Omega^k(z - z_k)H_k$$

$$\varepsilon_{xz}(x,y,z) = U_{,z}^0 + U_{,z}^i + \sum_{k=1}^{n_i} \Phi_x^k H_k + W_{,x}^0 + W_{,x}^i + \sum_{k=1}^{n_i} \Psi_{,x}^k(z - z_k)H_k +$$

$$+ \sum_{k=1}^{n_i} \Omega_{,x}^k(z - z_k)^2 H_k + \sum_{k=1}^{n_i} C_{w,x}^k H_k$$

$$\varepsilon_{yz}(x,y,z) = V_{,z}^0 + V_{,z}^i + \sum_{k=1}^{n_i} \Phi_y^k H_k + W_{,y}^0 + W_{,y}^i + \sum_{k=1}^{n_i} \Psi_{,y}^k(z - z_k)H_k + \qquad (2.34)$$

$$+ \sum_{k=1}^{n_i} \Omega_{,y}^k(z - z_k)^2 H_k + \sum_{k=1}^{n_i} C_{w,y}^k H_k$$

$$\varepsilon_{xy}(x,y,z) = U_{,y}^0 + U_{,y}^i + \sum_{k=1}^{n_i} \Phi_{x,y}^k(z - z_k)H_k + \sum_{k=1}^{n_i} C_{u,y}^k H_k +$$

$$+ V_{,x}^0 + V_{,x}^i + \sum_{k=1}^{n_i} \Phi_{y,x}^k(z - z_k)H_k + \sum_{k=1}^{n_i} C_{v,x}^k H_k$$

By applying the strain-stress relations (Hooke Law (1.1)) it is possible to write stresses σ_{xz}, σ_{yz}, σ_{zz}, and the gradient $\sigma_{zz,z}$ in the generic layer j as follows:

$$\sigma_{xz}^{j}(x,y,z) = C_{44}^{j}\left[U_{,z}^{0} + U_{,z}^{i} + \sum_{k=1}^{j-1}\Phi_{x}^{k}H_{k} + W_{,x}^{0} + W_{,x}^{i} + \sum_{k=1}^{j-1}\Psi_{,x}^{k}(z-z_{k})H_{k} + \right.$$

$$\left. +\sum_{k=1}^{j-1}\Omega_{,x}^{k}(z-z_{k})^{2}H_{k} + \sum_{k=1}^{j-1}C_{w,x}^{k}H_{k} \right] + C_{45}^{j}\left[V_{,z}^{0} + V_{,z}^{i} + \sum_{k=1}^{j-1}\Phi_{y}^{k}H_{k} + W_{,y}^{0} + W_{,y}^{i} + \right. \qquad (2.35)$$

$$\left. +\sum_{k=1}^{j-1}\Psi_{,y}^{k}(z-z_{k})H_{k} + \sum_{k=1}^{j-1}\Omega_{,y}^{k}(z-z_{k})^{2}H_{k} + \sum_{k=1}^{j-1}C_{w,y}^{k}H_{k} \right]$$

$$\sigma_{yz}^{j}(x,y,z) = C_{45}^{j}\left[U_{,z}^{0} + U_{,z}^{i} + \sum_{k=1}^{j-1}\Phi_{x}^{k}H_{k} + W_{,x}^{0} + W_{,x}^{i} + \sum_{k=1}^{j-1}\Psi_{,x}^{k}(z-z_{k})H_{k} + \right.$$

$$\left. +\sum_{k=1}^{j-1}\Omega_{,x}^{k}(z-z_{k})^{2}H_{k} + \sum_{k=1}^{j-1}C_{w,x}^{k}H_{k} \right] + C_{55}^{j}\left[V_{,z}^{0} + V_{,z}^{i} + \sum_{k=1}^{j-1}\Phi_{y}^{k}H_{k} + W_{,y}^{0} + W_{,y}^{i} + \right. \qquad (2.36)$$

$$\left. +\sum_{k=1}^{j-1}\Psi_{,y}^{k}(z-z_{k})H_{k} + \sum_{k=1}^{j-1}\Omega_{,y}^{k}(z-z_{k})^{2}H_{k} + \sum_{k=1}^{j-1}C_{w,y}^{k}H_{k} \right]$$

$$\sigma_{zz}^{j}(x,y,z) = C_{13}^{j}\left[U_{,x}^{0} + U_{,x}^{i} + \sum_{k=1}^{j-1}\Phi_{x,x}^{k}(z-z_{k})H_{k} + \sum_{k=1}^{j-1}C_{u,x}^{k}H_{k} \right] +$$

$$C_{23}^{j}\left[V_{,y}^{0} + V_{,y}^{i} + \sum_{k=1}^{j-1}\Phi_{y,y}^{k}(z-z_{k})H_{k} + \sum_{k=1}^{j-1}C_{v,y}^{k}H_{k} \right] + C_{33}^{j}\left[W_{,z}^{i} + \sum_{k=1}^{j-1}\Psi^{k}H_{k} + \right.$$

$$\left. +2\sum_{k=1}^{j-1}\Omega^{k}(z-z_{k})H_{k} \right] + C_{36}^{j}\left[U_{,y}^{0} + U_{,y}^{i} + \sum_{k=1}^{j-1}\Phi_{x,y}^{k}(z-z_{k})H_{k} + \sum_{k=1}^{j-1}C_{u,y}^{k}H_{k} + \right. \qquad (2.37)$$

$$\left. +V_{,x}^{0} + V_{,x}^{i} + \sum_{k=1}^{j-1}\Phi_{y,x}^{k}(z-z_{k})H_{k} + \sum_{k=1}^{j-1}C_{v,x}^{k}H_{k} \right]$$

$$\sigma_{zz,z}^{j}(x,y,z) = C_{13}^{j}\left[U_{,xz}^{0} + U_{,xz}^{i} + \sum_{k=1}^{j-1}\Phi_{x,x}^{k}H_{k} \right] + C_{23}^{j}\left[V_{,yz}^{0} + V_{,yz}^{i} + \sum_{k=1}^{j-1}\Phi_{y,y}^{k}H_{k} \right] +$$

$$+C_{33}^{j}\left[W_{,z}^{i} + 2\sum_{k=1}^{j-1}\Omega^{k}H_{k} \right] + C_{36}^{j}\left[U_{,yz}^{0} + U_{,yz}^{i} + \sum_{k=1}^{j-1}\Phi_{x,y}^{k}H_{k} + V_{,xz}^{0} + V_{,xz}^{i} + \sum_{k=1}^{j-1}\Phi_{y,x}^{k}H_{k} \right] \qquad (2.38)$$

By imposing the continuity conditions (2.8), (2.9) and (2.20) at the interface between the layers j and j+1 one can obtain:

$$
\sigma_{xz}^{j}(x,y,z) = C_{44}^{j}\left[U_{,z}^{0} + U_{,z}^{i} + \sum_{k=1}^{j-1}\Phi_{x}^{k}H_{k} + W_{,x}^{0} + W_{,x}^{i} + \sum_{k=1}^{j-1}\Psi_{,x}^{k}(z-z_{k})H_{k} + \right.
$$

$$
\left. + \sum_{k=1}^{j-1}\Omega_{,x}^{k}(z-z_{k})^{2}H_{k} + \sum_{k=1}^{j-1}C_{w,x}^{k}H_{k} \right] + C_{45}^{j}\left[V_{,z}^{0} + V_{,z}^{i} + \sum_{k=1}^{j-1}\Phi_{y}^{k}H_{k} + W_{,y}^{0} + W_{,y}^{i} + \right.
$$

$$
\left. + \sum_{k=1}^{j-1}\Psi_{,y}^{k}(z-z_{k})H_{k} + \sum_{k=1}^{j-1}\Omega_{,y}^{k}(z-z_{k})^{2}H_{k} + \sum_{k=1}^{j-1}C_{w,y}^{k}H_{k} \right] = \sigma_{xz}^{j+1}(x,y,z) =
$$

$$
= C_{44}^{j+1}\left[U_{,z}^{0} + U_{,z}^{i} + \sum_{k=1}^{j}\Phi_{x}^{k}H_{k} + W_{,x}^{0} + W_{,x}^{i} + \sum_{k=1}^{j}\Psi_{,x}^{k}(z-z_{k})H_{k} + \right. \tag{2.39}
$$

$$
\left. + \sum_{k=1}^{j}\Omega_{,x}^{k}(z-z_{k})^{2}H_{k} + \sum_{k=1}^{j}C_{w,x}^{k}H_{k} \right] + C_{45}^{j+1}\left[V_{,z}^{0} + V_{,z}^{i} + \sum_{k=1}^{j}\Phi_{y}^{k}H_{k} + W_{,y}^{0} + W_{,y}^{i} + \right.
$$

$$
\left. + \sum_{k=1}^{j}\Psi_{,y}^{k}(z-z_{k})H_{k} + \sum_{k=1}^{j}\Omega_{,y}^{k}(z-z_{k})^{2}H_{k} + \sum_{k=1}^{j}C_{w,y}^{k}H_{k} \right]
$$

$$
\sigma_{yz}^{j}(x,y,z) = C_{45}^{j}\left[U_{,z}^{0} + U_{,z}^{i} + \sum_{k=1}^{j-1}\Phi_{x}^{k}H_{k} + W_{,x}^{0} + W_{,x}^{i} + \sum_{k=1}^{j-1}\Psi_{,x}^{k}(z-z_{k})H_{k} + \right.
$$

$$
\left. + \sum_{k=1}^{j-1}\Omega_{,x}^{k}(z-z_{k})^{2}H_{k} + \sum_{k=1}^{j-1}C_{w,x}^{k}H_{k} \right] + C_{55}^{j}\left[V_{,z}^{0} + V_{,z}^{i} + \sum_{k=1}^{j-1}\Phi_{y}^{k}H_{k} + W_{,y}^{0} + W_{,y}^{i} + \right.
$$

$$
\left. + \sum_{k=1}^{j-1}\Psi_{,y}^{k}(z-z_{k})H_{k} + \sum_{k=1}^{j-1}\Omega_{,y}^{k}(z-z_{k})^{2}H_{k} + \sum_{k=1}^{j-1}C_{w,y}^{k}H_{k} \right] = \sigma_{yz}^{j+1}(x,y,z) =
$$

$$
\tag{2.40}
$$

$$
= C_{45}^{j+1}\left[U_{,z}^{0} + U_{,z}^{i} + \sum_{k=1}^{j}\Phi_{x}^{k}H_{k} + W_{,x}^{0} + W_{,x}^{i} + \sum_{k=1}^{j}\Psi_{,x}^{k}(z-z_{k})H_{k} + \right.
$$

$$
\left. + \sum_{k=1}^{j}\Omega_{,x}^{k}(z-z_{k})^{2}H_{k} + \sum_{k=1}^{j}C_{w,x}^{k}H_{k} \right] + C_{55}^{j+1}\left[V_{,z}^{0} + V_{,z}^{i} + \sum_{k=1}^{j}\Phi_{y}^{k}H_{k} + W_{,y}^{0} + W_{,y}^{i} + \right.
$$

$$
\left. + \sum_{k=1}^{j}\Psi_{,y}^{k}(z-z_{k})H_{k} + \sum_{k=1}^{j}\Omega_{,y}^{k}(z-z_{k})^{2}H_{k} + \sum_{k=1}^{j}C_{w,y}^{k}H_{k} \right]
$$

$$\sigma_{zz}^j(x,y,z) = C_{13}^j \left[U_{,x}^0 + U_{,x}^i + \sum_{k=1}^{j-1} \Phi_{x,x}^k (z-z_k) H_k + \sum_{k=1}^{j-1} C_{u,x}^k H_k \right] +$$

$$C_{23}^j \left[V_{,y}^0 + V_{,y}^i + \sum_{k=1}^{j-1} \Phi_{y,y}^k (z-z_k) H_k + \sum_{k=1}^{j-1} C_{v,y}^k H_k \right] + C_{33}^j \left[W_{,z}^i + \sum_{k=1}^{j-1} \Psi^k H_k + \right.$$

$$\left. +2\sum_{k=1}^{j-1} \Omega^k (z-z_k) H_k \right] + C_{36}^j \left[U_{,y}^0 + U_{,y}^i + \sum_{k=1}^{j-1} \Phi_{x,y}^k (z-z_k) H_k + \sum_{k=1}^{j-1} C_{u,y}^k H_k + \right.$$

$$\left. + V_{,x}^0 + V_{,x}^i + \sum_{k=1}^{j-1} \Phi_{y,x}^k (z-z_k) H_k + \sum_{k=1}^{j-1} C_{v,x}^k H_k \right] = \sigma_{zz}^{j+1}(x,y,z) =$$

$$= C_{13}^{j+1} \left[U_{,x}^0 + U_{,x}^i + \sum_{k=1}^{j} \Phi_{x,x}^k (z-z_k) H_k + \sum_{k=1}^{j} C_{u,x}^k H_k \right] +$$

$$C_{23}^{j+1} \left[V_{,y}^0 + V_{,y}^i + \sum_{k=1}^{j} \Phi_{y,y}^k (z-z_k) H_k + \sum_{k=1}^{j} C_{v,y}^k H_k \right] + C_{33}^{j+1} \left[W_{,z}^i + \sum_{k=1}^{j} \Psi^k H_k + \right.$$

$$\left. +2\sum_{k=1}^{j} \Omega^k (z-z_k) H_k \right] + C_{36}^{j+1} \left[U_{,y}^0 + U_{,y}^i + \sum_{k=1}^{j} \Phi_{x,y}^k (z-z_k) H_k + \sum_{k=1}^{j} C_{u,y}^k H_k + \right.$$

$$\left. + V_{,x}^0 + V_{,x}^i + \sum_{k=1}^{j} \Phi_{y,x}^k (z-z_k) H_k + \sum_{k=1}^{j} C_{v,x}^k H_k \right] \qquad (2.41)$$

$$\sigma_{zz,z}^j(x,y,z) = C_{13}^j \left[U_{,xz}^0 + U_{,xz}^i + \sum_{k=1}^{j-1} \Phi_{x,x}^k H_k \right] + C_{23}^j \left[V_{,yz}^0 + V_{,yz}^i + \sum_{k=1}^{j-1} \Phi_{y,y}^k H_k \right] +$$

$$+C_{33}^j \left[W_{,z}^i + 2\sum_{k=1}^{j-1} \Omega^k H_k \right] + C_{36}^j \left[U_{,yz}^0 + U_{,yz}^i + \sum_{k=1}^{j-1} \Phi_{x,y}^k H_k + V_{,xz}^0 + V_{,xz}^i + \sum_{k=1}^{j-1} \Phi_{y,x}^k H_k \right] =$$

$$= \sigma_{zz,z}^{j+1}(x,y,z) = C_{13}^{j+1} \left[U_{,xz}^0 + U_{,xz}^i + \sum_{k=1}^{j} \Phi_{x,x}^k H_k \right] + C_{23}^{j+1} \left[V_{,yz}^0 + V_{,yz}^i + \sum_{k=1}^{j} \Phi_{y,y}^k H_k \right] + \qquad (2.42)$$

$$+C_{33}^{j+1} \left[W_{,z}^i + 2\sum_{k=1}^{j} \Omega^k H_k \right] + C_{36}^{j+1} \left[U_{,yz}^0 + U_{,yz}^i + \sum_{k=1}^{j} \Phi_{x,y}^k H_k + V_{,xz}^0 + V_{,xz}^i + \sum_{k=1}^{j} \Phi_{y,x}^k H_k \right]$$

Eqs. (2.39) - (2.42) are solved with the symbolic calculus tool of MatLab® without introducing any simplifying assumption differently to Ref. [**113**]. By solving this system, it is possible to obtain in closed form the expressions of the continuity functions at any constituent or computational layers (see Figure 2.5). The arbitrary nature of displacements enables the decomposition of the system (2.39) - (2.42) into 45 independent conditions at each interface, since the homologous displacements and displacement derivatives have to be collected separately at both hands as an independent condition to be fulfilled.

2.2.2 Hierarchic terms

The high order coefficients of Eqs. (2.14), (2.15) and (2.19) are computed in a similar way. These terms are here referred as hierarchical terms, as they enable a variable representation in different regions across the thickness.

The unknown coefficients are determined with a system of independent equations, obtained by enforcing the fulfilment of the boundary conditions of Eqs. (2.6), (2.7) and (2.22), as well as by imposing the fulfilment of the local differential equilibrium equations (2.18).

Considering the displacement field of Eqs. (2.14), (2.15) and (2.19) with through-the-thickness representation up to the third order for u and v and up to the fourth order for w, Eqs. (2.6), (2.7) and (2.22) determine the following solving system:

$$
C_{44}^{n_l}\left[\gamma_x^0 + 2C_x^i \frac{h}{2} + 3D_x^i \left(\frac{h}{2}\right)^2 + \sum_{k=1}^{n_i} \Phi_x^k H_k + b_{,x}^i \frac{h}{2} + c_{,x}^i \left(\frac{h}{2}\right)^2 + d_{,x}^i \left(\frac{h}{2}\right)^3 + e_{,x}^i \left(\frac{h}{2}\right)^4 + \right.
$$

$$
\left. + \sum_{k=1}^{n_i} \Psi_{,x}^k(x,y)\left(\frac{h}{2} - z_k\right)H_k + \sum_{k=1}^{n_i} \Omega_{,x}^k \left(\frac{h}{2} - z_k\right)^2 H_k + \sum_{k=1}^{n_i} C_{w,x}^k H_k \right] +
$$

$$
+ C_{45}^{n_l}\left[\gamma_y^0 + 2C_y^i \frac{h}{2} + 3D_y^i \left(\frac{h}{2}\right)^2 + \sum_{k=1}^{n_i} \Phi_y^k H_k + b_{,y}^i \frac{h}{2} + c_{,y}^i \left(\frac{h}{2}\right)^2 + d_{,y}^i \left(\frac{h}{2}\right)^3 + e_{,y}^i \left(\frac{h}{2}\right)^4 + \right.
$$

$$
\left. + \sum_{k=1}^{n_i} \Psi_{,y}^k(x,y)\left(\frac{h}{2} - z_k\right)H_k + \sum_{k=1}^{n_i} \Omega_{,y}^k \left(\frac{h}{2} - z_k\right)^2 H_k + \sum_{k=1}^{n_i} C_{w,y}^k H_k \right] = 0
$$

$$(2.43)$$

$$
C_{44}^{1}\left[\gamma_x^0 - 2C_x^i \frac{h}{2} + 3D_x^i \left(\frac{h}{2}\right)^2 - b_{,x}^i \frac{h}{2} + c_{,x}^i \left(\frac{h}{2}\right)^2 + d_{,x}^i \left(-\frac{h}{2}\right)^3 + e_{,x}^i \left(\frac{h}{2}\right)^4 \right] +
$$

$$
+ C_{45}^{1}\left[\gamma_y^0 - 2C_y^i \frac{h}{2} + 3D_y^i \left(\frac{h}{2}\right)^2 + b_{,y}^i \frac{h}{2} + c_{,y}^i \left(\frac{h}{2}\right)^2 + d_{,y}^i \left(\frac{h}{2}\right)^3 + e_{,y}^i \left(\frac{h}{2}\right)^4 \right] = 0
$$

$$C_{45}^{n_l}\left[\gamma_x^0 + 2C_x^i\frac{h}{2} + 3D_x^i\left(\frac{h}{2}\right)^2 + \sum_{k=1}^{n_i}\Phi_x^k H_k + b_{,x}^i\frac{h}{2} + c_{,x}^i\left(\frac{h}{2}\right)^2 + d_{,x}^i\left(\frac{h}{2}\right)^3 + e_{,x}^i\left(\frac{h}{2}\right)^4 + \right.$$

$$\left. + \sum_{k=1}^{n_i}\Psi_{,x}^k(x,y)\left(\frac{h}{2} - z_k\right)H_k + \sum_{k=1}^{n_i}\Omega_{,x}^k\left(\frac{h}{2} - z_k\right)^2 H_k + \sum_{k=1}^{n_i}C_{w,x}^k H_k\right] +$$

$$+ C_{55}^{n_l}\left[\gamma_y^0 + 2C_y^i\frac{h}{2} + 3D_y^i\left(\frac{h}{2}\right)^2 + \sum_{k=1}^{n_i}\Phi_y^k H_k + b_{,y}^i\frac{h}{2} + c_{,y}^i\left(\frac{h}{2}\right)^2 + d_{,y}^i\left(\frac{h}{2}\right)^3 + e_{,y}^i\left(\frac{h}{2}\right)^4 + \right.$$

$$\left. + \sum_{k=1}^{n_i}\Psi_{,y}^k(x,y)\left(\frac{h}{2} - z_k\right)H_k + \sum_{k=1}^{n_i}\Omega_{,y}^k\left(\frac{h}{2} - z_k\right)^2 H_k + \sum_{k=1}^{n_i}C_{w,y}^k H_k\right] = 0$$

$$(2.44)$$

$$C_{45}^1\left[\gamma_x^0 - 2C_x^i\frac{h}{2} + 3D_x^i\left(\frac{h}{2}\right)^2 - b_{,x}^i\frac{h}{2} + c_{,x}^i\left(\frac{h}{2}\right)^2 + d_{,x}^i\left(-\frac{h}{2}\right)^3 + e_{,x}^i\left(\frac{h}{2}\right)^4\right] +$$

$$+ C_{55}^1\left[\gamma_y^0 - 2C_y^i\frac{h}{2} + 3D_y^i\left(\frac{h}{2}\right)^2 + b_{,y}^i\frac{h}{2} + c_{,y}^i\left(\frac{h}{2}\right)^2 + d_{,y}^i\left(\frac{h}{2}\right)^3 + e_{,y}^i\left(\frac{h}{2}\right)^4\right] = 0$$

$$C_{13}^{n_l}\left[u_{,x}^0 + \frac{h}{2}(\gamma_{x,x}^0 - w_{,xx}^0) + C_{x,x}^i\left(\frac{h}{2}\right)^2 + D_{x,x}^i\left(\frac{h}{2}\right)^3 + \sum_{k=1}^{n_i}\Phi_{x,x}^k\left(\frac{h}{2} - z_k\right)H_k + \sum_{k=1}^{n_i}C_{u,x}^k H_k\right] +$$

$$+ C_{23}^{n_l}\left[v_{,y}^0 + \frac{h}{2}(\gamma_{y,y}^0 - w_{,yy}^0) + C_{y,y}^i\left(\frac{h}{2}\right)^2 + D_{y,y}^i\left(\frac{h}{2}\right)^3 + \sum_{k=1}^{n_i}\Phi_{y,y}^k\left(\frac{h}{2} - z_k\right)H_k + \sum_{k=1}^{n_i}C_{v,y}^k H_k\right] +$$

$$+ C_{33}^{n_l}\left[b^i + 2c^i\frac{h}{2} + 3d^i\left(\frac{h}{2}\right)^2 + 4e^i\left(\frac{h}{2}\right)^3 + \sum_{k=1}^{n_i}\Psi^k H_k + 2\sum_{k=1}^{n_i}\Omega^k\left(\frac{h}{2} - z_k\right)H_k\right] + \quad(2.45a)$$

$$+ C_{36}^{n_l}\left[u_{,y}^0 + \frac{h}{2}(\gamma_{x,y}^0 - w_{,xy}^0) + C_{x,y}^i\left(\frac{h}{2}\right)^2 + D_{x,y}^i\left(\frac{h}{2}\right)^3 + \sum_{k=1}^{n_i}\Phi_{x,y}^k\left(\frac{h}{2} - z_k\right)H_k + \sum_{k=1}^{n_i}C_{u,y}^k H_k + \right.$$

$$\left. + v_{,x}^0 + \frac{h}{2}(\gamma_{y,x}^0 - w_{,yx}^0) + C_{y,x}^i\left(\frac{h}{2}\right)^2 + D_{y,x}^i\left(\frac{h}{2}\right)^3 + \sum_{k=1}^{n_i}\Phi_{y,x}^k\left(\frac{h}{2} - z_k\right)H_k + \sum_{k=1}^{n_i}C_{v,x}^k H_k\right] = p^0\left(\frac{h}{2}\right)$$

$$C_{13}^1\left[u_{,x}^0-\frac{h}{2}(\gamma_{x,x}^0-w_{,xx}^0)+C_{x,x}^i\left(\frac{h}{2}\right)^2+D_{x,x}^i\left(-\frac{h}{2}\right)^3\right]+$$

$$+C_{23}^1\left[v_{,y}^0-\frac{h}{2}(\gamma_{y,y}^0-w_{,yy}^0)+C_{y,y}^i\left(\frac{h}{2}\right)^2+D_{y,y}^i\left(\frac{h}{2}\right)^3\right]+$$

$$+C_{33}^1\left[b^i-2c^i\frac{h}{2}+3d^i\left(\frac{h}{2}\right)^2+4e^i\left(-\frac{h}{2}\right)^3\right]+ \qquad (2.45b)$$

$$+C_{36}^1\left[u_{,y}^0-\frac{h}{2}(\gamma_{x,y}^0-w_{,xy}^0)+C_{x,y}^i\left(\frac{h}{2}\right)^2+D_{x,y}^i\left(-\frac{h}{2}\right)^3+\right.$$

$$\left.+v_{,x}^0-\frac{h}{2}(\gamma_{y,x}^0-w_{,yx}^0)+C_{y,x}^i\left(\frac{h}{2}\right)^2+D_{y,x}^i\left(-\frac{h}{2}\right)^3\right]=p^0\left(-\frac{h}{2}\right)$$

$$C_{13}^1\left[(\gamma_{x,x}^0-w_{,xx}^0)-2C_{x,x}^i\frac{h}{2}+3D_{x,x}^i\left(\frac{h}{2}\right)^2\right]+C_{23}^1\left[(\gamma_{y,y}^0-w_{,yy}^0)-C_{y,y}^i\frac{h}{2}+3D_{y,y}^i\left(\frac{h}{2}\right)^2\right]+$$

$$+C_{33}^1\left[2c^i-6d^i\frac{h}{2}+12e^i\left(\frac{h}{2}\right)^2\right]+C_{36}^1\left[(\gamma_{x,y}^0-w_{,xy}^0)-2C_{x,y}^i\frac{h}{2}+3D_{x,y}^i\left(\frac{h}{2}\right)^2+\right.$$

$$\left.+(\gamma_{y,x}^0-w_{,yx}^0)-2C_{y,x}^i\frac{h}{2}+3D_{y,x}^i\left(\frac{h}{2}\right)^2\right]=0$$

$$(2.46)$$

$$C_{13}^{n_l}\left[(\gamma_{x,x}^0-w_{,xx}^0)+2C_{x,x}^i\frac{h}{2}+3D_{x,x}^i\left(\frac{h}{2}\right)^2+\sum_{k=1}^{n_i}\Phi_{x,x}^kH_k\right]+$$

$$+C_{23}^{n_l}\left[(\gamma_{y,y}^0-w_{,yy}^0)+2C_{y,y}^i\frac{h}{2}+3D_{y,y}^i\left(\frac{h}{2}\right)^2+\sum_{k=1}^{n_i}\Phi_{y,y}^kH_k\right]+$$

$$+C_{33}^{n_l}\left[2c^i+6d^i\frac{h}{2}+12e^i\left(\frac{h}{2}\right)^2+2\sum_{k=1}^{n_i}\Omega^kH_k\right]+$$

$$+C_{36}^{n_l}\left[(\gamma_{x,y}^0-w_{,xy}^0)+2C_{x,y}^i\frac{h}{2}+3D_{x,y}^i\left(\frac{h}{2}\right)^2+\sum_{k=1}^{n_i}\Phi_{x,y}^kH_k+\right.$$

$$\left.+(\gamma_{y,x}^0-w_{,yx}^0)+2C_{y,x}^i\frac{h}{2}+3D_{y,x}^i\left(\frac{h}{2}\right)^2+\sum_{k=1}^{n_i}\Phi_{y,x}^kH_k\right]=0$$

Finally, the constraint of Eq. (2.18) should be imposed at $n_p=N_{lay}\cdot ord\_u-2$ points across the thickness, where N_{lay} is the number of computational layers, while ord_u is the order of the

expansion chosen for the in-plane displacements. The location of the n_p points is arbitrary and it is determined trying to fulfil the equilibrium condition (2.18) in all the points across the thickness of the structure. From the practical point of view, in order to verify the fulfilment of the equilibrium (2.18) across all the thickness of the structure, the through-the-thickness variations of the three components of Eq. (2.18) are plotted on separate graphs. If these variations are equal to b_i (or 0 as in the cases here considered) the points chosen are correct, otherwise they should be changed placing the points where errors are bigger. This procedure can be carried out by hands (as in the cases here considered) or it can be automated by defining error indices.

However, in order to avoid numerical problems (i.e. singular or badly scaled matrix) the n_p points should not be placed excessively near to the layers' interfaces, since, as explained before continuity conditions derive from equilibrium.

In details, considering the displacement fields in compact form as in Eqs. (2.24), Eqs (2.47) and (2.48) represent the explicit form of Eq. (2.18) for the evaluation of the generic higher order terms of a beam at the generic point z_p in the layer j:

$$
\begin{aligned}
C_{11}^j U,_{xx}^i + C_{44}^j U,_{zz}^i + \left(C_{13}^j + C_{44}^j \right) W,_{xz}^i &= -C_{11}^j \left(U,_{xx}^0 + \sum_{k=1}^{j-1} \Phi,_{xx}^k \left(z_p - z_k \right) + \sum_{k=1}^{j} C_u,_{xx}^k \right) + \\
&\quad - \left(C_{13}^j + C_{44}^j \right) \left(\sum_{k=1}^{j-1} \Psi,_x^k + 2\sum_{k=1}^{j-1} \Omega,_x^k \left(z_p - z_k \right) \right) - C_{44}^j U,_{zz}^0
\end{aligned} \tag{2.47}
$$

$$
\begin{aligned}
C_{44}^j \left(U,_{zz}^i + W,_{xz}^i \right) + C_{13}^j U,_{xz}^i + C_{33}^j W,_{zz}^i &= -C_{44}^j \left(U,_{zz}^0 + \sum_{k=1}^{q} \Psi,_x^k + 2\sum_{k=1}^{q} \Omega,_x^k \left(z_p - z_k \right) \right) + \\
&\quad - C_{13}^j \left(U,_{xz}^0 + \sum_{k=1}^{q} \Phi_x,_x^k \right) - 2C_{33}^j \sum_{k=1}^{q} \Omega^k
\end{aligned} \tag{2.48}
$$

As already done for the computations of the continuity functions, the solving system obtained by Eqs. (2.43) – (2.48) is implemented in a symbolic MatLab® code. Please note that, the solution is obtained starting from the bottom layer of the structure and then moving up across the thickness.

It is remarked that all the algebraic operations required for determining the expressions of the coefficients of displacements and the expression of the continuity functions are carried out once for all in analytic form after having defined loading and boundary conditions (see Figure 2.5). Note that, the procedure needs to know the boundary conditions applied because if a structure with the same boundary conditions of that analysed has been already solved, the

symbolic calculus is not performed since the closed-form expressions of higher order terms and continuity functions are already known. Therefore, they are just recalled in order to save computational effort.

Owing to this, the present model obtains accurate results with a low computational effort, because many computations are carried apart once for all outside the solution process. Also the governing equations are computed with symbolic calculus by applying the Rayleigh-Ritz method. In particular, the procedure requires writing the strain energy of the structure (U), its kinetic energy (K) and the work of external forces (W). These quantities, according to the notation of Section 1.2, are defined as follows:

$$U = \frac{1}{2}\int_V \{\sigma\}^T \{\varepsilon\} dV = \frac{1}{2}\int_V \{\varepsilon\}^T [C]^T \{\varepsilon\} dV \qquad (2.49)$$

$$W = \int_V \{b\}\{u\} dV + \int_S \{t\}\{u\} dS \qquad (2.50)$$

$$K = \frac{1}{2}\int_V \rho\{\dot{u}\}^T \{\dot{u}\} dV \qquad (2.51)$$

The symbols {b} and {t} are the body and surface forces, ρ is the density and {u} the vector of displacements.

Actions performed apart with symbolic calculus
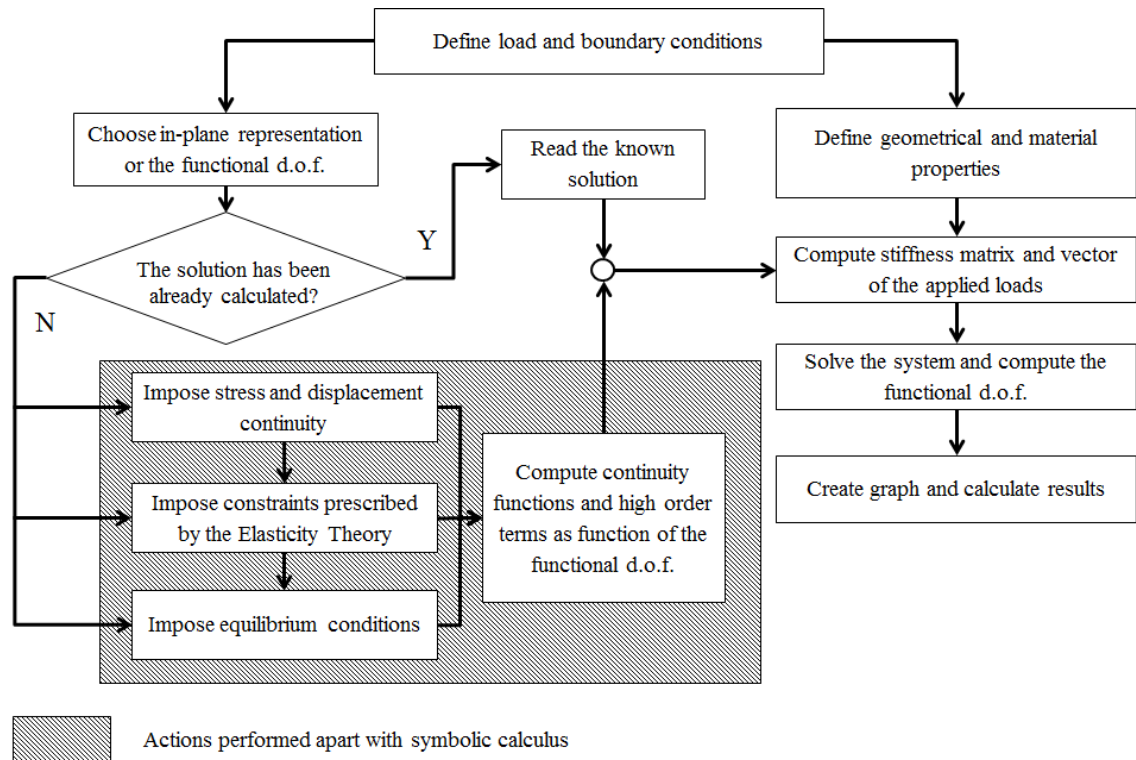
Figure 2.5 Steps for applying the AD-ZZ for a static analysis

2.2.3 Remarks on the AD-ZZ model

The present model avoids the poor behaviour of the models with displacements and shear rotations as functional d.o.f. that often fail in the prediction of deflection and stresses of clamped components. Indeed, when computing higher order terms during the symbolic procedure, it is sufficient to enforce as additional constraint a non-vanishing transverse shear at clamped edges..

The present model is compatible with cohesive models, as specific laws for the displacements contact conditions can be enforced instead of Eqs. (2.16), (2.17) and (2.21).

Finally note that the present model can treat sandwiches, since HLW models have this capability as shown by numerical results of Chapter 3 and by Elmalich and Rabinovitch [34], Giunta et al. [63], Plagianakos and Saravanos [162], Moreira and Rodrigues [163], Chrysochoidis and Saravanos [164], Hohe and Librescu [165] and Shariyat [166].

As mentioned above, the AD-ZZ model, which is used in the present numerical illustrations, requires computing a lower number of unknowns than its pioneering model [113], thus allowing a significant reduction of the computational burden though it is equally accurate. For instance, let us consider the case of a three layer structure: the AD-ZZ model generates 18 higher order terms, while the one by Icardi and Ferrero [113], in order to obtain the same accuracy as the AD-ZZ, requires computing 20 higher order terms. This results in a reduction of the overall computational processing time up to 10 % of the memory storage dimension per each run. This reduction determines a consistent advantage, for instance, when progressive failure analyses are carried out. Of course, the greater is the number of constituent layers, the bigger is the advantage of the AD-ZZ model over the model [113].

2.2.4 Application of AD-ZZ to [0°/90°/0°] laminated beam

The stress and displacement fields predicted by the AD-ZZ model for the [0°/90°/0°] cross-ply beam are reported in Figure 2.6.

a)

b)

c)
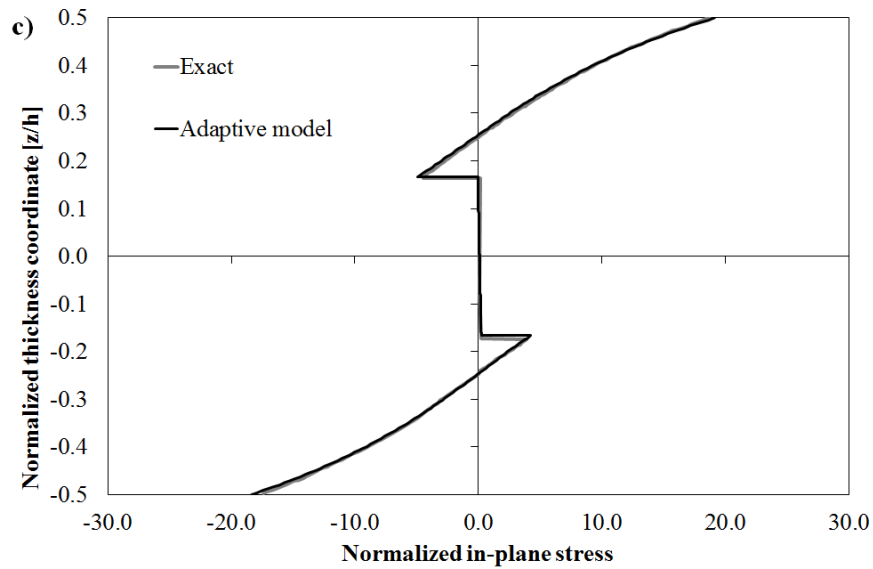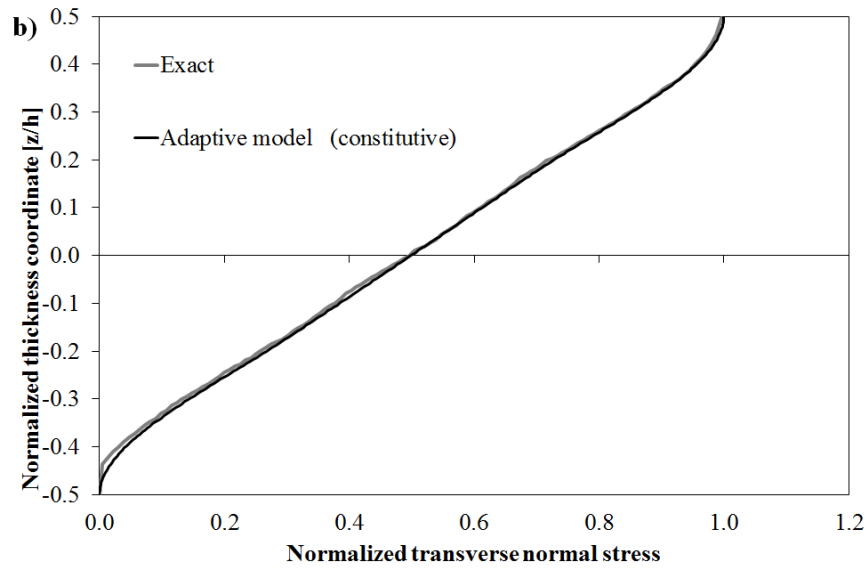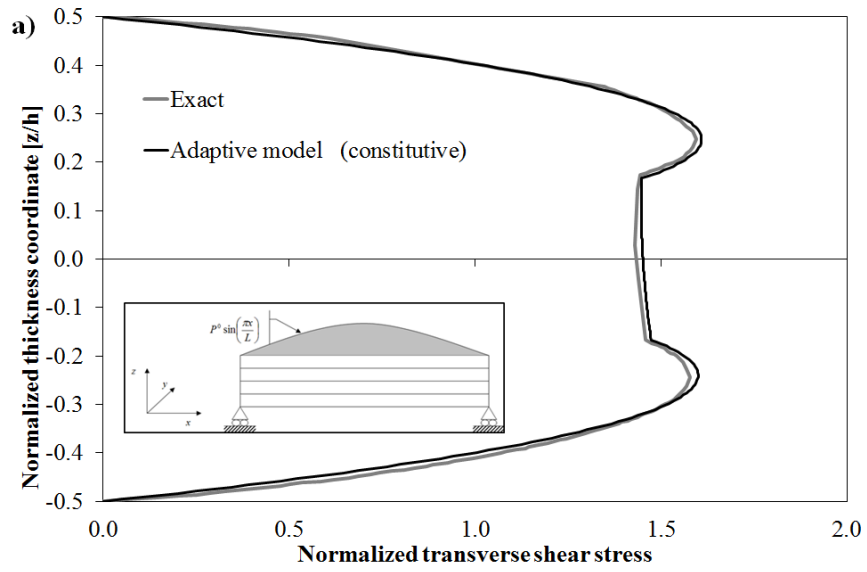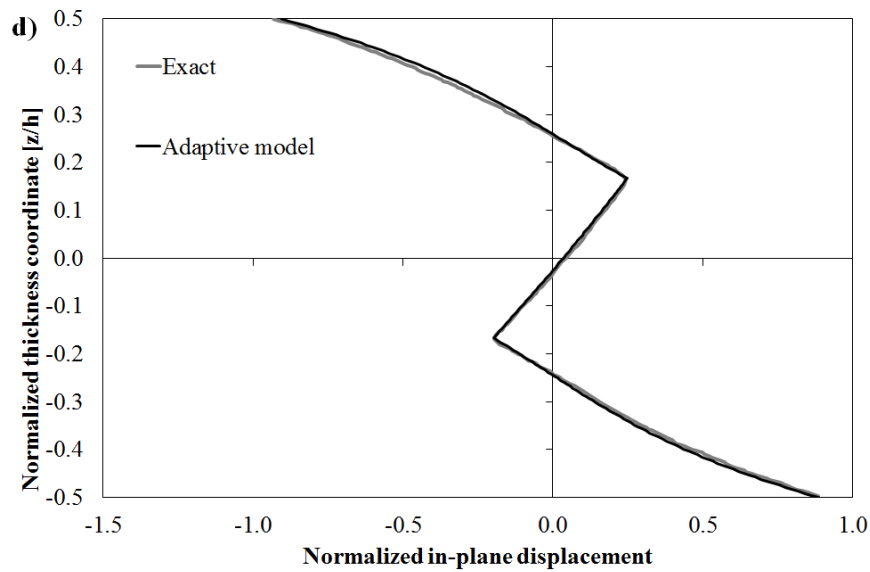
Figure 2.6 Comparison between stress and displacement fields by the AD-ZZ model and the exact solution [144] for a [0°/90°/0°] laminated beam with L/h=4.

From the results of Figure 2.6 it could be noticed that the AD-ZZ model is able to predict stress and displacement fields as accurate as the exact 3D solution from constitutive equations.

Note that both the transverse normal stress and the shear stress are obtained directly from constitutive equations. For what concerns the computational times, the results by the theories discussed in this session are not largely variable.

Indeed, processing times ranging from 0.79 s for the FSDT to 0.90 s for the AD-ZZ model are required on a laptop computer with an 1.80 GHz double-core processor and 4 GB RAM. This confirms that, thanks to an a priori evaluation of high-order terms, the AD-ZZ model has a low computational burden even if it can be refined locally. Note that the computational time reported above for the AD-ZZ does not include the time required by the symbolic procedure to compute higher order terms and continuity functions. This time for the structure considered here is 600 s.

After this preliminary assessment, in the next Chapter accuracy and efficiency of the AD-ZZ will be analysed in details considering both laminates and sandwiches with different boundary conditions.

Chapter 3: Assessment of the AD-ZZ model

In the present section, the AD-ZZ model explained above will be tested comparing its results with those by other theories discussed in Chapter 1 and with exact solutions available in literature for laminated and sandwich structures. The goal is to verify the accuracy of the model for a variety of structures.

	MAT p	MAT c	MAT bc	MAT bl	MAT g	MAT 1	MAT 2	MAT 3	MAT 4	Carbon-Epoxy	PVC foam
E1 [GPa]	172.4	0.1	$1.72 \ 10^{-3}$	137.92	5.9	1	33	25	0.05	157.9	0.104
E2 [GPa]	6.89	0.1	$6.89 \ 10^{-5}$	5.512	10	1	1	1	0.05	9.584	0.104
E3 [GPa]	6.89	0.1	$6.89 \ 10^{-5}$	5.512	10	1	1	1	0.05	9.584	0.104
G12 [GPa]	3.45	0.04	$3.45 \ 10^{-5}$	2.76	5.9	0.2	0.8	0.5	0.0217	5.93	0.04
G13 [GPa]	3.45	0.04	$3.45 \ 10^{-5}$	2.76	0.2	0.2	0.8	0.5	0.0217	5.93	0.04
G23 [GPa]	1.378	0.04	$1.38 \ 10^{-5}$	1.1024	0.7	0.2	0.8	0.5	0.0217	3.227	0.04
$\upsilon 12$	0.25	0.25	0.25	0.25	0.25	0.25	0.25	0.25	0.15	0.32	0.3
$\upsilon 13$	0.25	0.25	0.25	0.25	0.25	0.25	0.25	0.25	0.15	0.32	0.3
$\upsilon 23$	0.25	0.25	0.25	0.25	0.25	0.25	0.25	0.25	0.15	0.49	0.3

Table 3.1 Mechanical properties of the materials constituting the structures considered in static analyses of Section 3.1 and 3.2.

3.1 Validation of the AD-ZZ model for static analyses

Numerical applications are presented for laminated plates and beams in order to demonstrate that the present model is accurate, efficient and able to predict interlaminar stresses without post-processing techniques. Results for sandwiches undamaged or with damaged faces or with a damaged core are also presented since, owing to their abruptly changing material properties across the thickness, they represent very severe tests cases for the model.

Structures with simply-supported edges under sinusoidal distributed loading are considered first, since they are the test cases initially considered by the researchers, then applications are presented to structures with other boundary conditions that are proven to be critical for the models in the literature.

Even if unrealistic for engineering applications, all the results refer to extremely low values of the thickness ratio S=L/h, in order to enhance the layerwise effects.

The static problem is solved within the framework of the Rayleigh-Ritz method assuming the in-plane variation of the functional d.o.f. as series expansion able to fulfil the imposed boundary conditions.

After substitution of this representation into the governing equations, a set of linear algebraic equations is obtained that allows determining the unknown amplitudes.

3.1.1 [0°/90°] laminated beam

First a cross-ply [0°/90°] beam is considered. This lay-up gives rise to strongly asymmetric stress field across the thickness and thus it well puts in evidence the importance of high-order hierarchic terms. Displacements and stresses are reported at $x=L_x/2$ or at $x=0$, where they assume their maximum, in the following normalized form, according to Pagano [144], which computes the exact solution for this case:

$$\bar{\sigma}_{xx} = \frac{\sigma_{xx}\left(\frac{L_x}{2},z\right)}{p^0} \quad \bar{\sigma}_{zz} = \frac{\sigma_{zz}\left(\frac{L_x}{2},z\right)}{p^0} \quad \bar{\sigma}_{xz} = \frac{\sigma_{xz}(0,z)}{p^0} \quad \bar{u} = \frac{E_2 u(0,z)}{hp^0} \tag{3.1}$$

The beam is in mat-p (see Table 3.1), with each layer h/2 thick, it is simply supported and the acting load is sinusoidal:

$$p^0(x) = \sum_{m=1}^{M} P_m \sin\left(\frac{m\pi}{L_x}x\right) \tag{3.2}$$

A length-to-thickness ratio of 4 is considered. According to the boundary conditions imposed the in-plane variation of the functional d.o.f. is chosen as follows:

$$u^0(x) = \sum_{m=1}^{M} A_m \cos\left(\frac{m\pi}{L_x}x\right) \tag{3.3}$$

$$w^0(x) = \sum_{m=1}^{M} C_m \sin\left(\frac{m\pi}{L_x}x\right) \tag{3.4}$$

$$\gamma_x^{\,0}(x) = \sum_{m=1}^{M} D_m \cos\left(\frac{m\pi}{L_x}x\right) \tag{3.5}$$

All the results by the AD-ZZ model appearing in the Figure 3.1 are obtained considering M=1, a third order expansion of the in-plane displacement u and a fourth order expansion for the transverse displacement w in Eqs. (2.14) and (2.19) in each constituent layers (i.e. the terms (Oz^4) and (Oz^5) are disregarded), while the points where the equilibrium constraint (2.18) has been imposed are located at: (-0.412 h; -0.10 h; 0.075 h; 0.2 h), where h is thickness of the beam.
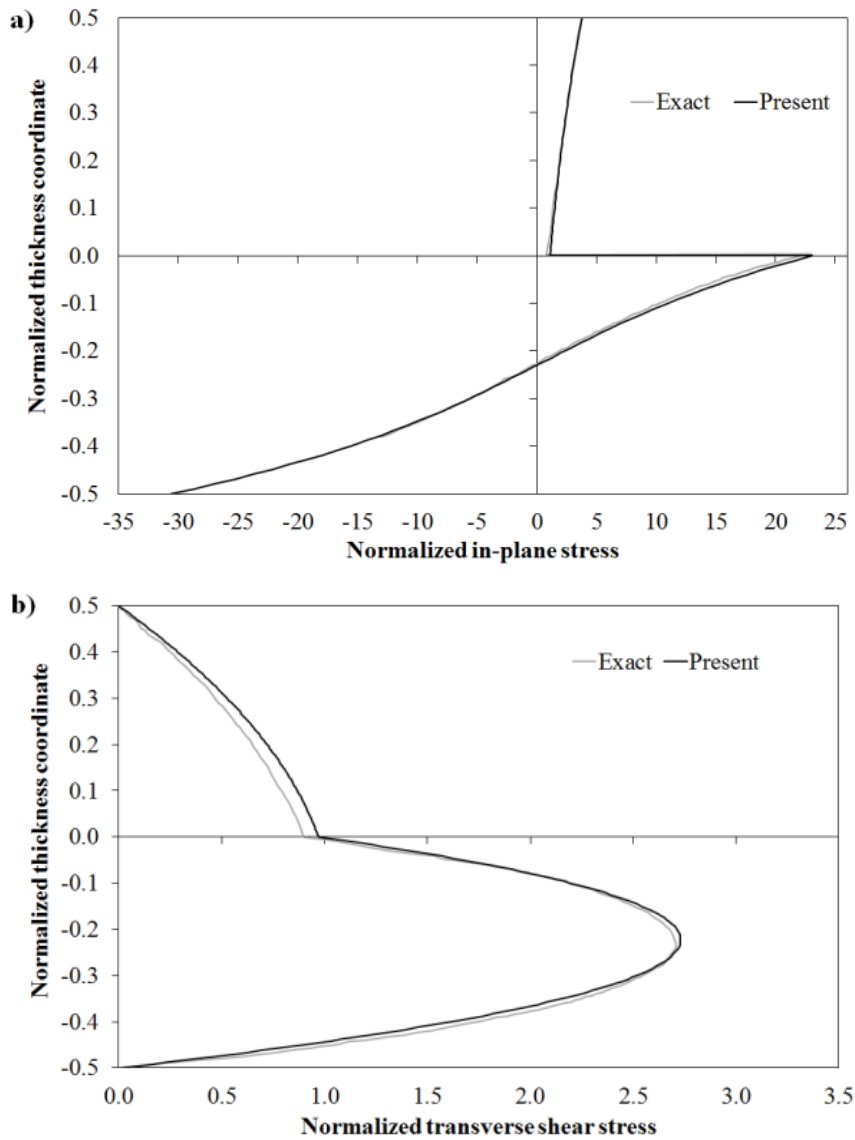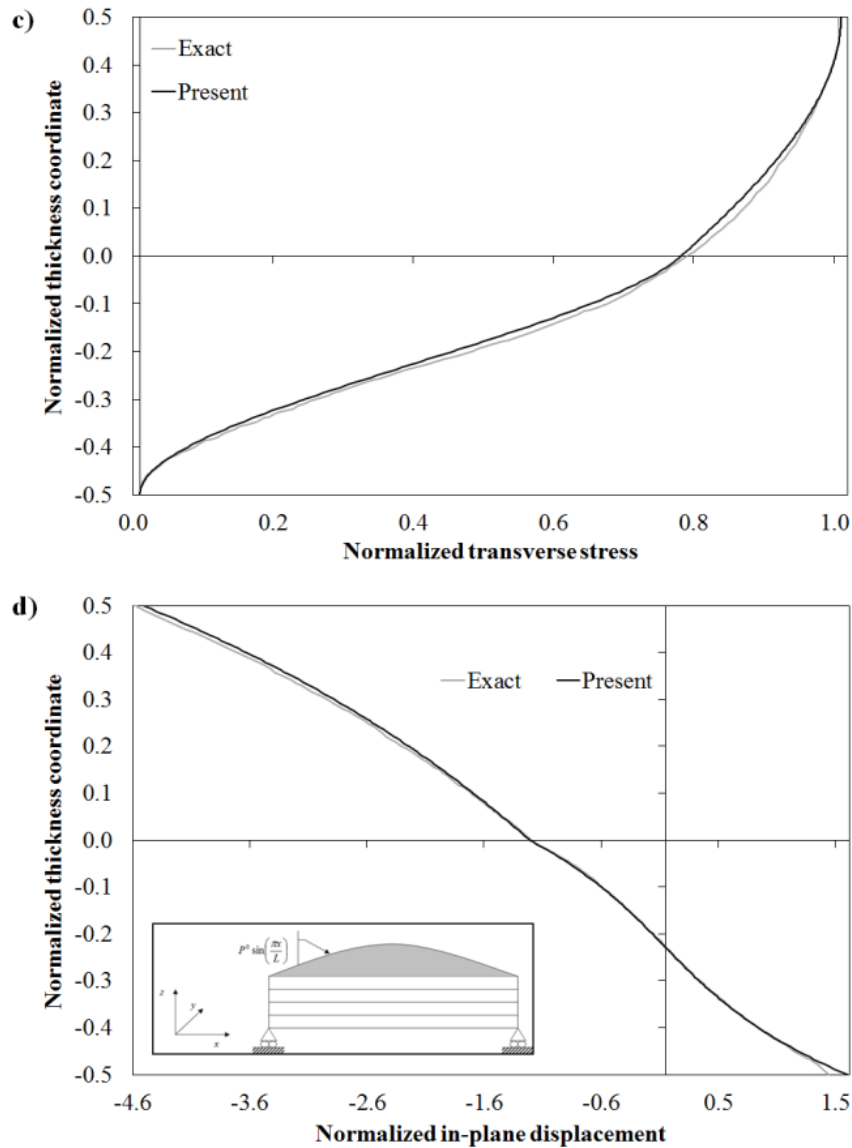
Figure 3.1 Through-the-thickness distribution of a) in-plane stress $\overline{\sigma}_{xx}$, b) transverse shear stress $\overline{\sigma}_{xz}$, c) transverse normal stress $\overline{\sigma}_{zz}$ and d) in-plane displacement $\overline{u}$ for the [0°/90°] beam by the AD-ZZ model and exact solution [144].

Figure 3.1a represents the through-the-thickness variation of the in-plane stress $\overline{\sigma}_{xx}$ by the AD-ZZ model compared to the exact solution. While Figure 3.1b and Figure 3.1c represent respectively $\overline{\sigma}_{xz}$ and $\overline{\sigma}_{zz}$, and Figure 3.1d represents the through-the-thickness variation of the in-plane displacement $\overline{u}$.

From the reported numerical results, it appears that the AD-ZZ model accurately predicts the stress and displacement fields for this structure, the numerical results being the same as the exact solutions by Pagano [**144**]. Note that the results by the AD-ZZ model reported in Figure 3.1 are obtained directly from constitutive equations, thus determining a very low

computational time, which is just 0.88 s on a laptop computer with an 1.80 GHz double-core processor and 4 GB RAM.

3.1.2 [0°/90°/0°] laminated plate

Now a cross-ply [0°/90°/0°] square plate is examined. The length-to-thickness ratio is again 4, each of the three layers is in mat-p and h/3 thick. The plate is simply supported and a bisinusoidal loading acts on its upper surface:

$$p^0(x,y) = \sum_{m=1}^{M}\sum_{n=1}^{N} P_{mn} \sin\left(\frac{m\pi}{L_x}x\right)\sin\left(\frac{n\pi}{L_y}y\right) \tag{3.6}$$

The in-plane variation of the functional d.o.f. is chosen as follows:

$$u^0(x,y) = \sum_{m=1}^{M}\sum_{n=1}^{N} A_{mn} \cos\left(\frac{m\pi}{L_x}x\right)\sin\left(\frac{n\pi}{L_y}y\right) \tag{3.7}$$

$$v^0(x,y) = \sum_{m=1}^{M}\sum_{n=1}^{N} B_{mn} \sin\left(\frac{m\pi}{L_x}x\right)\cos\left(\frac{n\pi}{L_y}y\right) \tag{3.8}$$

$$w^0(x,y) = \sum_{m=1}^{M}\sum_{n=1}^{N} C_{mn} \sin\left(\frac{m\pi}{L_x}x\right)\sin\left(\frac{n\pi}{L_y}y\right) \tag{3.9}$$

$$\gamma_x^{\,0}(x,y) = \sum_{m=1}^{M}\sum_{n=1}^{N} D_{mn} \cos\left(\frac{m\pi}{L_x}x\right)\sin\left(\frac{n\pi}{L_y}y\right) \tag{3.10}$$

$$\gamma_y^{\,0}(x,y) = \sum_{m=1}^{M}\sum_{n=1}^{N} B_{mn} \sin\left(\frac{m\pi}{L_x}x\right)\cos\left(\frac{n\pi}{L_y}y\right) \tag{3.11}$$

All results presented for this case are obtained considering M=N=1. According to Pagano [145], displacements and stresses in Figure 3.2 are reported in the following normalized form:

$$\overline{\sigma}_{xz} = \frac{\sigma_{xz}\left(0,\frac{L_y}{2},z\right)}{p^0 S} \qquad \overline{\sigma}_{yz} = \frac{\sigma_{yz}\left(\frac{L_x}{2},0,z\right)}{p^0 S} \qquad \overline{u} = \frac{E_2 u\left(0,\frac{L_y}{2},z\right)}{h p^0 S^3} \tag{3.12}$$

All the next results refer to a third order expansion of the in-plane displacement u and v, and a fourth order expansion for the transverse displacement w in Eqs. (2.14), (2.15) and (2.19). Every expansion is valid within the thickness of the three layers, while the points where the constraint (2.18) has been imposed are: (-0.45 h;-0.3 h;-0.15 h; 0 h; 0.05 h; 0.25 h; 0.45 h),

where h is thickness of the plate. Figure 3.2a and 3.2b represent the through-the-thickness variation of the shear stresses $\bar{\sigma}_{xz}$ and $\bar{\sigma}_{yz}$, while Figure 3.2c represents the through-the-thickness variation of the in-plane displacement $\bar{u}$.
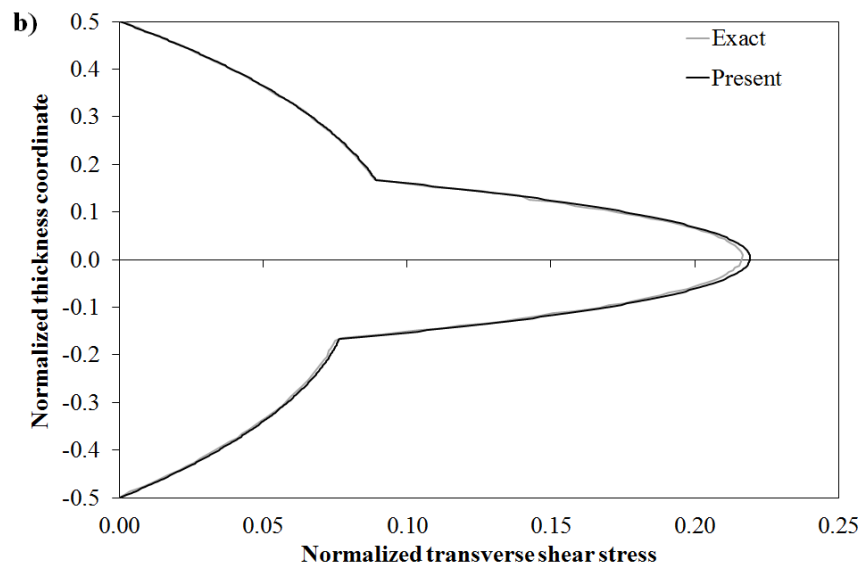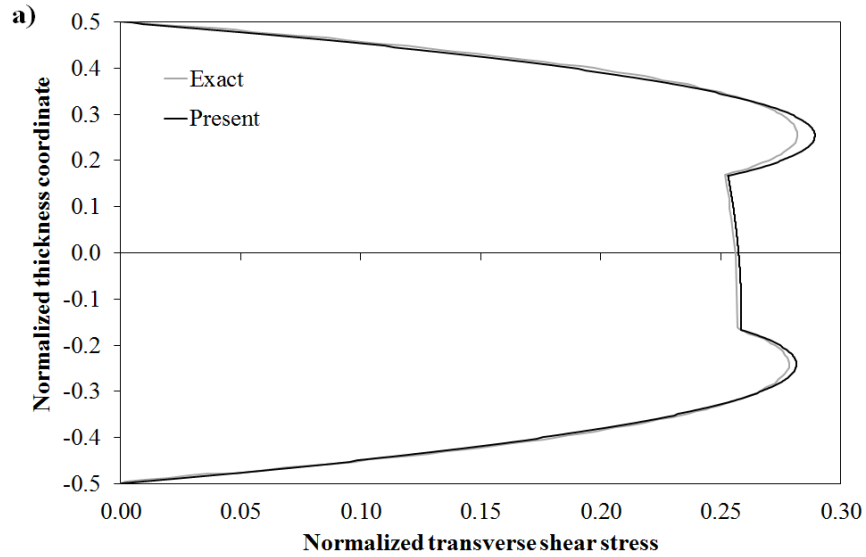
Figure 3.2 Through-the-thickness distribution of a) transverse shear stress $\bar{\sigma}_{xz}$, b) transverse shear stress $\bar{\sigma}_{yz}$ and c) in-plane displacement $\bar{u}$ for the [0°/90°/0°] plate by the AD-ZZ model and exact solution [145].

The results of Figure 3.2 show that the AD-ZZ model accurately describes the in-plane displacement $\bar{u}$ and the shear stresses $\bar{\sigma}_{xz}$ and $\bar{\sigma}_{yz}$ also for this case. Note that both the shear stresses reported in Figure 3.2 are computed from constitutive equations. For what concerns the processing times, 0.96 s are required to perform the analysis on a laptop computer with an 1.80 GHz double-core processor and 4 GB RAM.

3.1.3 [0°/90°/0°] laminated plate with clamped edges

To assess whether a non-vanishing transverse shear can be enforced with displacements and shear rotations that vanish, the result by the present model are compared to those by Vel and Batra [167], who studies the effects of various boundary conditions. This serves also as a test of the capability of the AD-ZZ model to treat general boundary conditions.

The case of a square plate that is simply supported on two opposite edges and clamped on the other two is considered, whose top surface is subjected to a bi-sinusoidal normal load (Eq. (3.6)), whereas the bottom surface is traction free. Vel and Batra [167] solves the governing equations using a three-dimensional generalization of the Eshelby-Stroh formalism that determines an infinite system of equations in infinite unknowns. The boundary conditions at the edges and the continuity conditions at the interfaces are exploited to define constants in

the general solution, which are determined by the Fourier series method. Truncations of the set of infinite equations introduce errors that are minimized by increasing the number of the terms in the series.

Figure 3.3a reports the variation of the transverse shear stress across the thickness predicted by the present model and by Vel and Batra [167] with 250 terms in the series. This case corresponds to a length-to-thickness ratio of 5, assuming that each lamina is in mat-p and h/3 thick. The stacking sequence is [0°/ 90°/ 0°].

The through-the-thickness variation of the transverse displacement component at the centre of the plate $\bar{w}$ and the transverse shear stress $\bar{\sigma}_{xz}$ at the clamped edge are presented in normalized form as follows, according to [167]:

$$\bar{\sigma}_{xz} = \frac{10 \cdot h \cdot \sigma_{xz}\left(\dfrac{L_x}{8}, \dfrac{L_y}{2}, z\right)}{p^0 L_x}; \quad \bar{w} = \frac{100 E_T \cdot h^3}{p^0 L_x^4} w\left(\dfrac{L_x}{2}, \dfrac{L_y}{2}, z\right) \tag{3.13}$$

L_x being the side length, h the thickness of the plate and p^0 the amplitude of the bi-sinusidal load.

Figure 3.3b shows how the transverse displacement varies across the thickness. In this case, the comparison results are obtained from those presented in Ref. [167] in tabular form. The results by the present model reported in Figures 3.3a and 3.3b are computed whitihn the framework of the Rayleigh-Ritz method assuming the following in-plane representation of the functional d.o.f.

$$u^0(x, y) = \sum_{m=2,4}^{M} \sum_{n=1,3}^{N} A_{mn} \sin\left(\frac{m\pi}{L_x} x\right) \cos\left(\frac{n\pi}{L_y} y\right) \tag{3.14}$$

$$v^0(x, y) = \sum_{m=1,3}^{M} \sum_{n=2,4}^{N} B_{mn} \cos\left(\frac{m\pi}{L_x} x\right) \sin\left(\frac{n\pi}{L_y} y\right) \tag{3.15}$$

$$w^0(x, y) = \sum_{m=2,4}^{M} \sum_{n=2,4}^{N} C_{mn} \left[\cos\left(\frac{m\pi}{L_x} x\right) - (-1)^{m/2}\right]\left[\cos\left(\frac{n\pi}{L_y} y\right) - (-1)^{n/2}\right] \tag{3.16}$$

$$\gamma_x^0(x, y) = \sum_{m=2,4}^{M} \sum_{n=1,3}^{N} D_{mn} \sin\left(\frac{m\pi}{L_x} x\right) \cos\left(\frac{n\pi}{L_y} y\right) \tag{3.17}$$

$$\gamma_y^0(x, y) = \sum_{m=1,3}^{M} \sum_{n=2,4}^{N} E_{mn} \cos\left(\frac{m\pi}{L_x} x\right) \sin\left(\frac{n\pi}{L_y} y\right) \tag{3.18}$$

The results with dashed lines are computed considering 200 terms in the series, while the ones with a solid line are obtained considering just a single component in the series expansion, i.e. M=N=1.

For what concerns the through-the-thickness representation, the results of Figure 3.3 are obtained considering a third order expansion of the in-plane displacement u and v, and a fourth order expansion for the transverse displacement w in Eqs. (2.14), (2.15) and (2.19). Every expansion is valid within the thickness of the three layers, while the points where the constraint (2.18) has been imposed are: (-0.47 h;-0.3 h;-0.1 h; 0 h; 0.05 h; 0.26 h; 0.45 h), where h is thickness of the plate
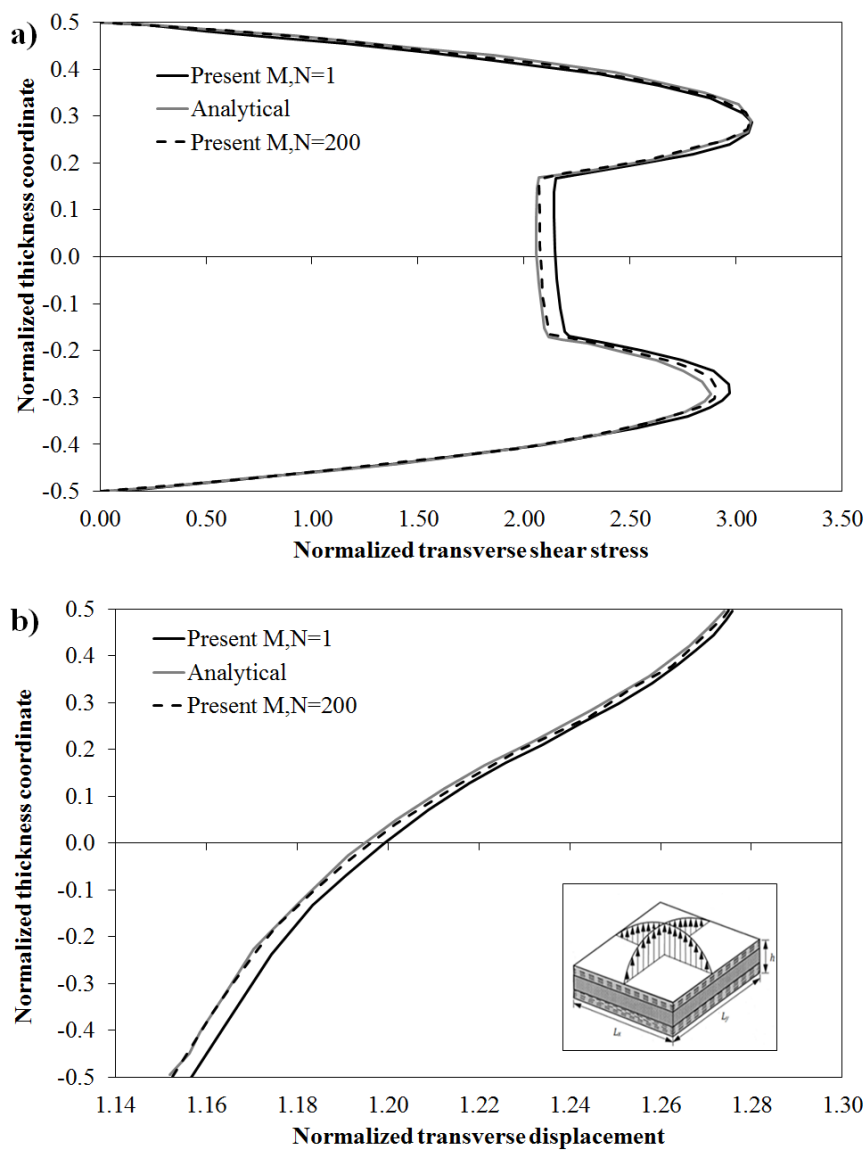
Figure 3.3 Through-the-thickness distribution of a) transverse shear stress $\bar{\sigma}_{xz}$ and b) transverse displacement $\bar{w}$ for the [0°/90°/0°] plate with clamped edges by the AD-ZZ model and analytical solution [167].

It could be seen that the present model accurately predicts the through-the-thickness variation of solutions even when just a single terms representation is adopted, so with the minimal computational effort. This is due to the *a priori* fulfilment of the stress and displacement boundary conditions and of the interfacial stress contact conditions obtained determining expressions in closed form for the coefficients of displacements. The computation of these coefficients, which is required just once at a time, takes about a minute, while the solution of governing equations takes four minutes with M=N=200 and 1.3 s with M=N=1. So, it could be noticed the capability of the model of being accurate with a low expansion order, which gives a considerable practical advantage when repeated computations are required.

3.1.4 Sandwich beam

Sandwich structures are more critical since they are characterized by abruptly changing material properties across the thickness.

Simply supported sandwich beams undergoing sinusoidal loading with S=4 already studied by Aitharaju and Averill [103] and Icardi [107] are here considered. The face layers are made of materials MAT1, MAT2 and MAT3, while the core is made of material MAT4, whose mechanical properties are reported in Table 3.1. As it can be seen from the data reported in Table 3.1, MAT1 is a rather compliant material, as compared to others, having weak properties in tension, compression and shear, MAT2 has high stiffness properties, MAT3 is stiff in tension and compression, but rather compliant in shear, while MAT4 is very compliant, as usual for core.

The sandwich beam is simulated as a multilayered beam with a (MAT 1/2/3/1/3/4)$_s$ stacking sequence and the following thickness ratios of the constituent layers (0.010/0.025 /0.015/0.020/0.030/0.4)$_s$. As shown in Aitharaju and Averill [103] and Icardi [107], this combination of materials and the lay-up determines rather intricate displacement and stress distributions across the thickness, which are more difficult to capture from constitutive equations than those of laminates.

The exact three dimensional solution for the present cases has been computed in Icardi [107] with the technique of Pagano [144], since results were not available in literature in the presence of damage. To simulate the damage, a degradation of the elastic properties is considered according to the ply-discount theory.

More realistic damage models are not considered, because here the purpose is to consider just abruptly changing material properties. In light of the boundary conditions of the beam, the in-plane variation of the functional d.o.f. of Eqs. (3.3) – (3.5) is chosen.

The numerical results are reported in the following normalized form ([107]):

$$\overline{\sigma}_{xz} = \frac{\sigma_{xz}(0,z)}{p^0} \quad \overline{\sigma}_z = \frac{\sigma_z\left(\frac{L_x}{2},z\right)}{p^0} \quad \overline{u} = \frac{E_2 u(0,z)}{hp^0} \quad \overline{w} = \frac{E_2 w\left(\frac{L_x}{2},z\right)}{hp^0} \quad (3.19)$$

Like in the previous cases, the results by the present model refer to a third order expansion of the in-plane displacement u and a fourth order expansion for the transverse displacement w in Eqs. (2.14) and (2.19), as higher order representations do not considerably improve accuracy. This expansion order is valid within the thickness of the eleven constituent layers. The points where the constraint (2.18) has been imposed are: (-0.4975 h; -0.4925 h; -0.48375 h; -0.4775 h; -0.47125 h; -0.46125 h; -0.4575 h; -0.45375 h; -0.445 h; -0.44 h; -0.435 h; -0.4225 h; -0.415 h; -0.4075 h; -0.2 h; 0 h; 0.2 h; 0.4075 h; 0.415 h; 0.4225 h; 0.435 h; 0.44 h; 0.445 h; 0.45375 h; 0.4575 h; 0.46125 h; 0.47125 h; 0.4775 h; 0.48375 h; 0.4925 h; 0.4975 h), where h is thickness of the beam.

Undamaged case - Figure 3.4 compares the results by the present model to the exact solution by Icardi [107]. It could be noticed that the AD-ZZ model provides an accurate representation of interlaminar stress directly from the constitutive equations. Also note that, thanks to a variable representation of the transverse displacement, the AD-ZZ model is able to describe the variable transverse displacement that is typical for sandwich structures. At the same time, also for this case the computational effort is low, since only 1.15 s are required to perform the analysis.

a)

b)

c)
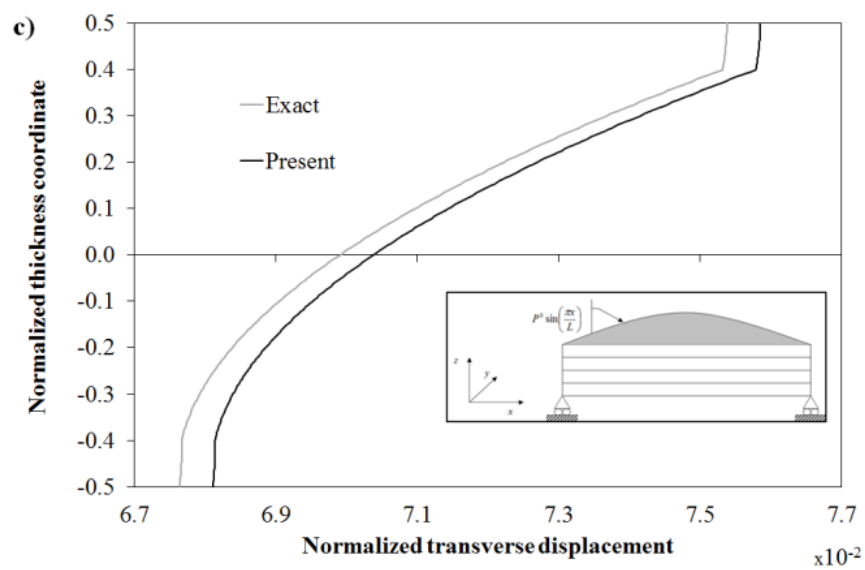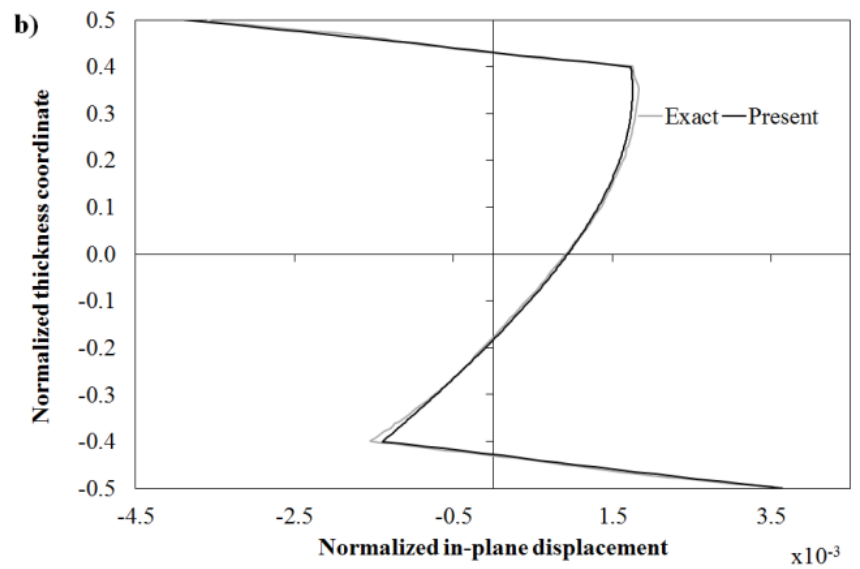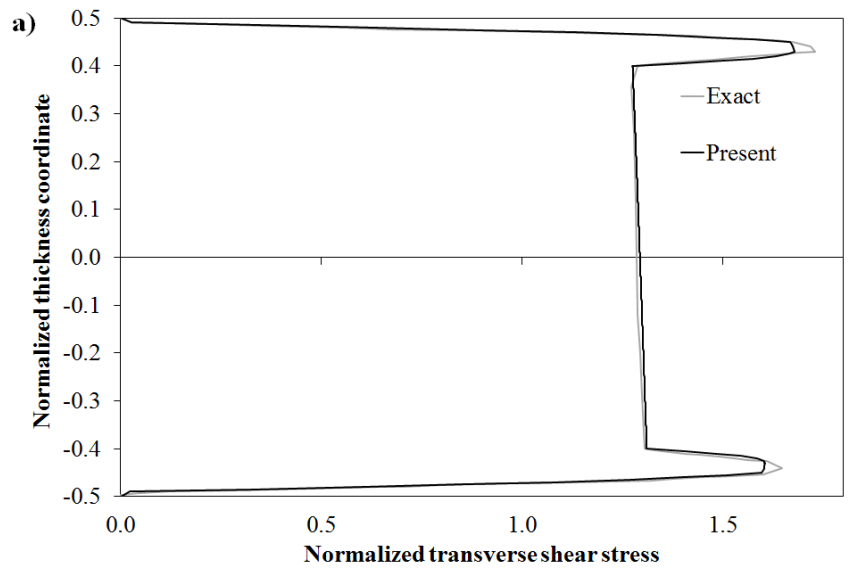
Figure 3.4 Through-the-thickness distribution of a) transverse shear stress $\bar{\sigma}_{xz}$, b) in-plane displacement $\bar{u}$ and c) transverse displacement $\bar{w}$ for the sandwich beam by the AD-ZZ model and exact solution [107].

Damaged core - The damage is simulated reducing G_{13} of the core's material of a 10^2 factor. Figure 3.5 compares the results by the present model to the exact solution of Ref. [**107**]. As a general observation, it could be noticed that the damage does not vary the symmetry of the stress and displacement fields, but it enhances the differences between core and faces. Despite this, the AD-ZZ model is still able to correctly predict displacements and stresses across the thickness without post-processing. In particular, the model can accurately capture $\bar{\sigma}_{xz}$ and $\bar{\sigma}_{zz}$ from constitutive equations, even with abruptly changing material properties across the thickness. For this case the computational time is 1.28 s.
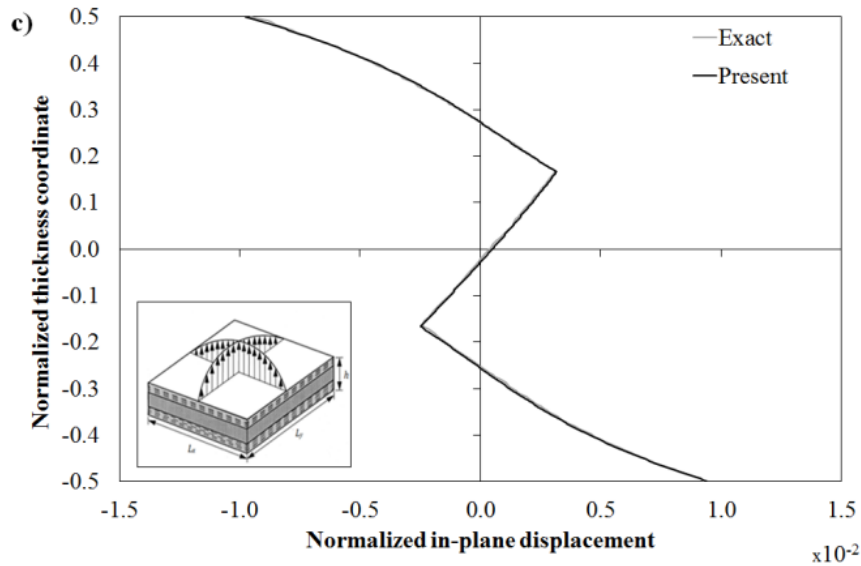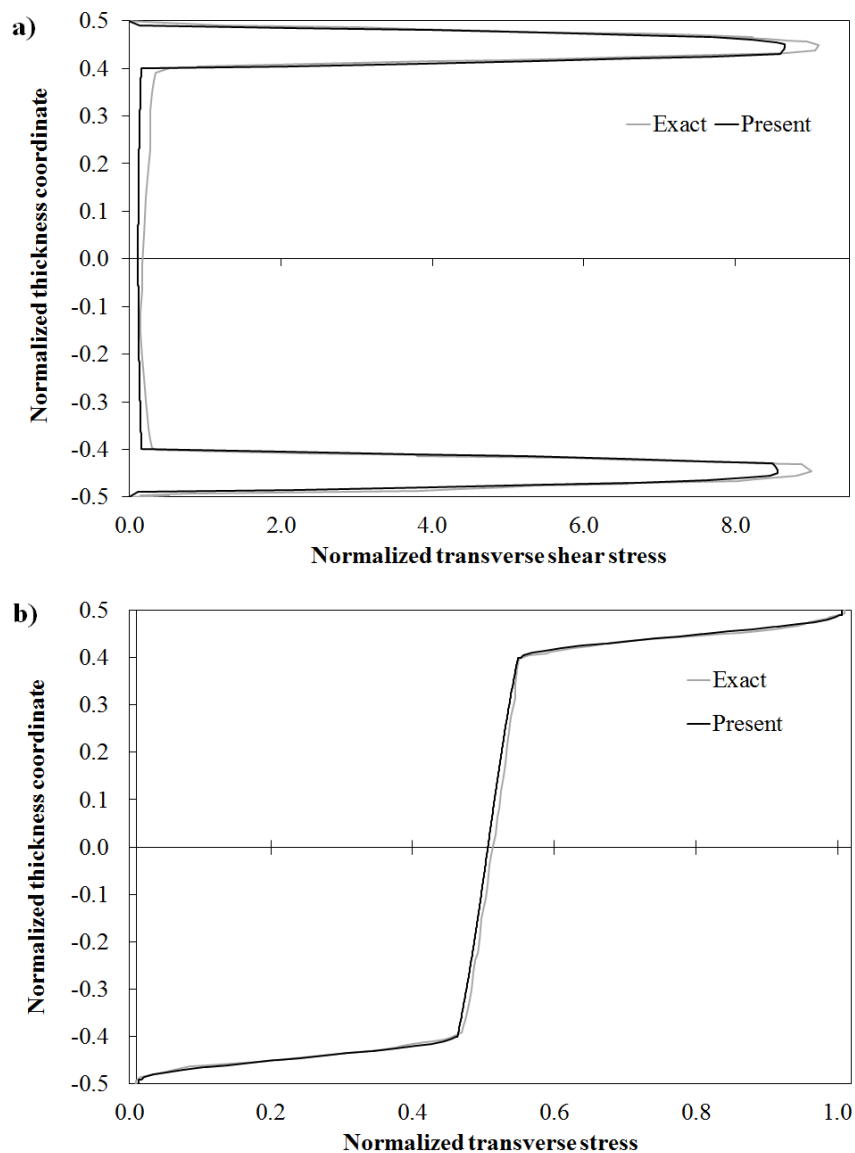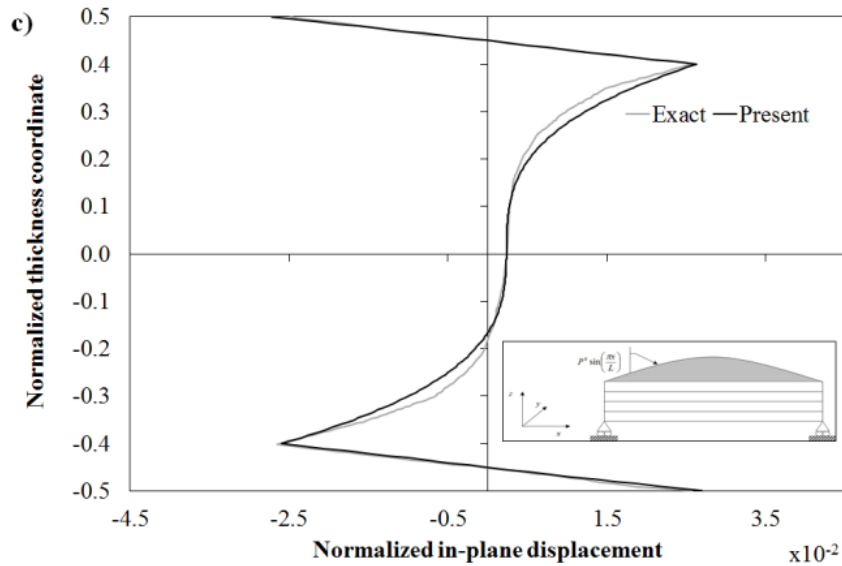
Figure 3.5 Through-the-thickness distribution of a) transverse shear stress $\bar{\sigma}_{xz}$, b) transverse normal stress $\bar{\sigma}_{zz}$ and c) in-plane displacement $\bar{u}$ for the sandwich beam with damaged core by the AD-ZZ model and exact solution [107].

Damaged upper face - The damage is simulated considering the elastic moduli E_3 of the core and of the upper face layers reduced of a 10^2 factor. Figure 3.6a represents the through-the-thickness variation of the shear stress $\bar{\sigma}_{xz}$, while Figure 3.6b represents $\bar{\sigma}_{zz}$ and Figure 3.6c and 3.6d represent, respectively, the through-the-thickness variation of the in-plane displacement $\bar{u}$, and of the transverse displacement $\bar{w}$.

Exact solution [107] demonstrates that if the elastic moduli E_3 of the core and of the upper face layers are reduced by a factor 10^2, strong layerwise effects rise due to asymmetry of properties and different moduli of adjacent constituent layers. This makes the out-of-plane stresses of this sample case difficult to capture. In particular, $\bar{\sigma}_{xz}$ shows nearly an opposite behaviour between the upper and lower face, which can be captured only if the models can be locally refined, e.g. by changing their representation across the thickness. Indeed, reduction of E_3 implies a relevant increase of $\bar{\sigma}_{xz}$ in the upper face and in a region of the core close to it, while it decreases and changes sign at the lower face. Thus, in order to treat this case, the models should be able to capture sudden variations.

The results of Figure 3.6d, showing a strong variation across the thickness of $\bar{w}$, point out again that sandwiches require an accurate modelling of the transverse normal stress and deformation through a detailed description of the piecewise variation of the transverse displacement. The displacement of Figure 3.6c also shows that the Murakami's zig-zag

function [**136**] based upon kinematic assumptions cannot appropriately represent the solution for this case, as the slope does not necessarily reverse at each interface, as shown by the exact solution. Thus, this could represent a further case where a physically based zig-zag function should give better estimates, in addition to those discussed next and in Ref. [**137**].

The AD-ZZ model still confirms its efficiency also for this case, as it requires only 1.35 s to perform the analysis.
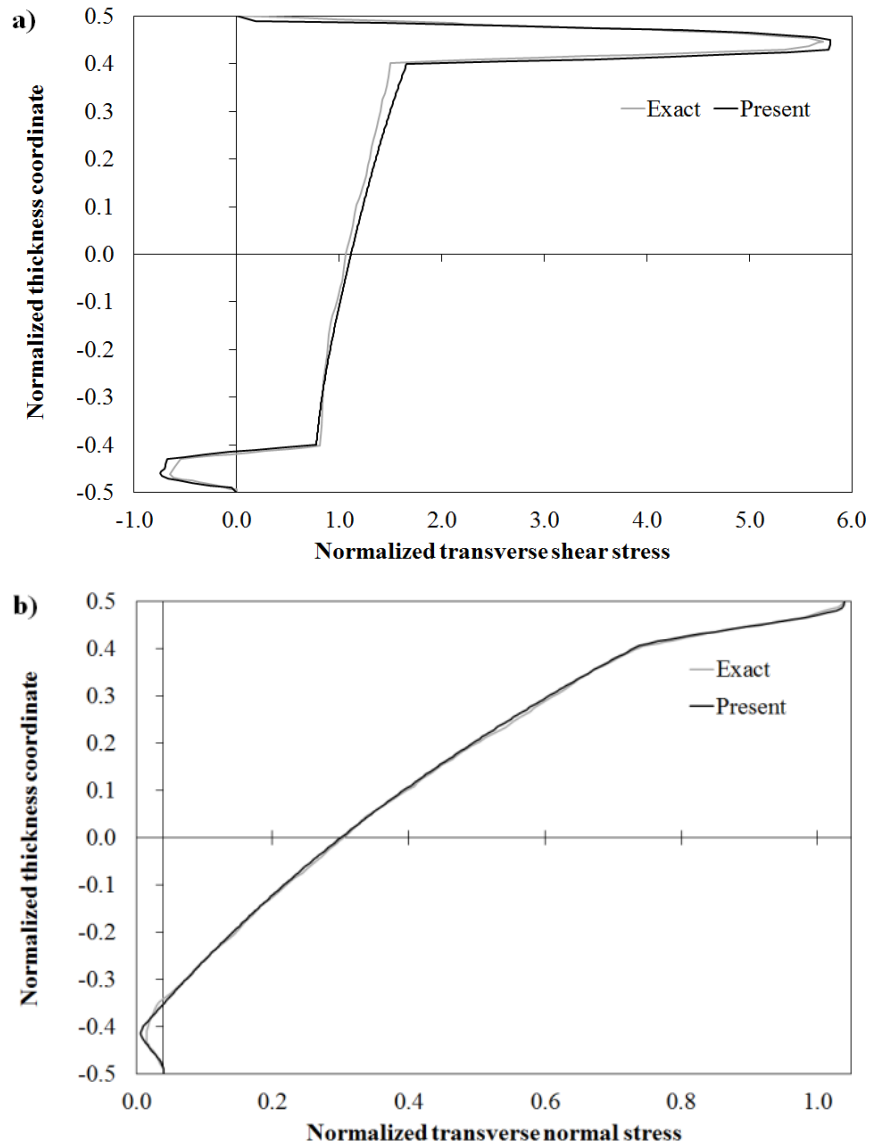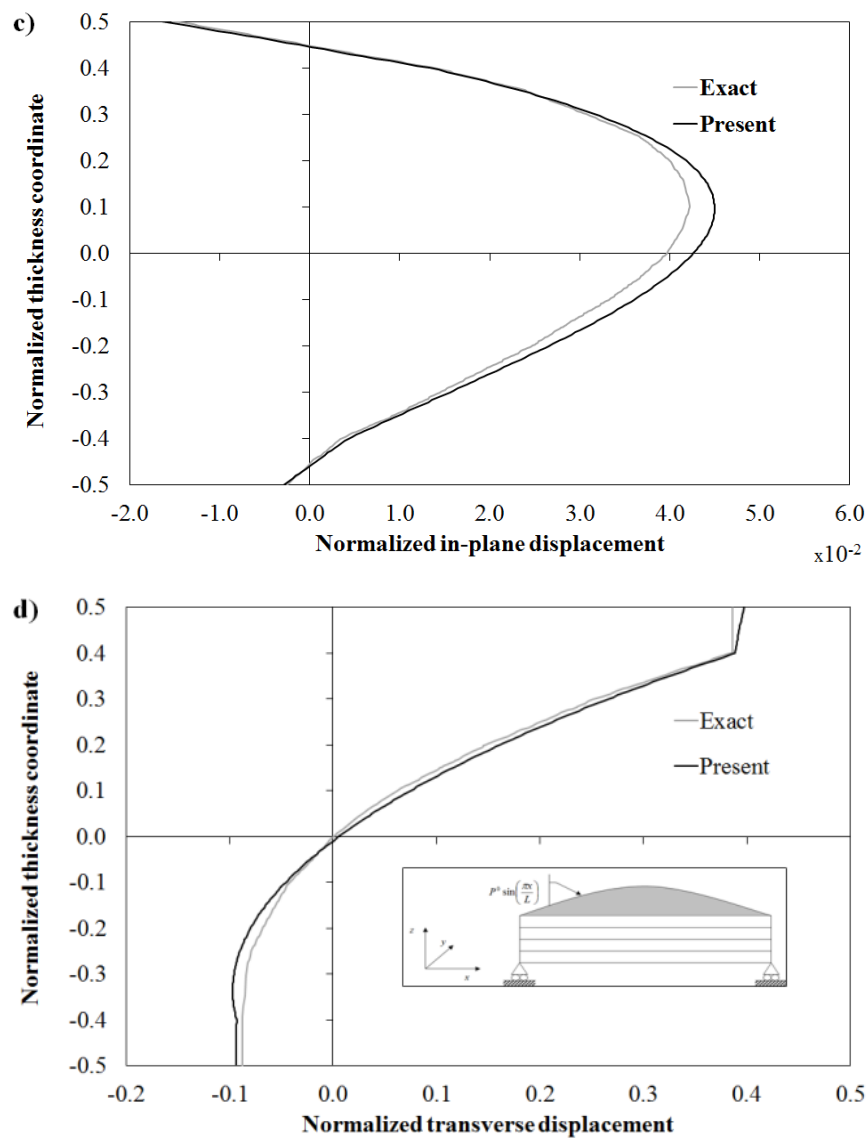
Figure 3.6 Through-the-thickness distribution of a) transverse shear stress $\bar{\sigma}_{xz}$, b) transverse normal stress $\bar{\sigma}_{zz}$, c) in-plane displacement $\bar{u}$ and d) transverse displacement $\bar{w}$ for the sandwich beam with damaged face by the AD-ZZ model and exact solution [107].

3.1.5 Cantilever sandwich beam

Now a cantilever sandwich beam formerly considered by Tessler et al. [**129**] that is subjected to a uniform transverse loading acting on the upper face is considered. The aim is to discuss a sample case for which zig-zag theories based on the same d.o.f. of the present AD-ZZ model failed the prediction of displacement and stress fields at the clamped edge, as discussed in

Chapter 1. Since for this case no exact solution is known, the comparison is made with the 3D finite element results of Ref. [129].

The beam has the faces made of unidirectional Carbon-Epoxy laminates and a PVC foam core (See Table 3.1). The length-to-thickness ratio is 10, while the thickness ratios of the constituent layers are [0.1h/0.8h/0.1h]. For this sample case, the results by the present model are again obtained considering a third order expansion of the in-plane displacements u, v and a fourth order expansion for the transverse displacement w in Eqs. (2.14), (2.15) and (2.19). This expansion order is valid within the thickness of each constituent layer. The points where the constraint (2.18) has been imposed are: (-0.47 h;-0.425 h;-0.35 h; 0.1 h; 0.25 h; 0.42 h; 0.45 h), where h is thickness of the beam.

Figure 3.7 reports the comparison between the through-the-thickness distribution of the transverse shear stress and of the in-plane stress predicted by the AD-ZZ model and by the 3D FEM analysis by Tessler et al. [129]. The normalization is as follows, according to Ref. [129]:

$$\overline{\sigma}_{xz} = \frac{h}{L_x p^0} \sigma_{xz}\left(\frac{L_x}{5}, \frac{L_y}{2}, z\right) \quad \overline{\sigma}_{xx} = \frac{h^2}{L_x^2 p^0} \sigma_{xx}\left(\frac{L_x}{5}, \frac{L_y}{2}, z\right) \tag{3.20}$$

Differently to other cases discussed, here the in-plane variation of the functional d.o.f. within the Rayleigh-Ritz method is described as a product of orthogonal one-dimensional Gram–Schmidt polynomial in the *x* and *y* directions:

$$\mathrm{d}(x, y) = \sum_{m=1}^{M}\sum_{n=1}^{N} P_{mn}\chi_m(x)\aleph_n(\mathrm{y}) \tag{3.21}$$

where d is the generic d.o.f. (i.e. $\{d\}=\{u^0, v^0, w^0, \gamma_x^0, \gamma_y^0\}$), while the polynomials are as follow:

$$\chi_1(x) = x$$

$$\chi_2(x) = x^2 - \frac{3}{4}x$$

$$\chi_3(x) = x^3 - \frac{4}{3}x^2 + \frac{2}{5}x$$

$$\chi_4(x) = x^4 - \frac{15}{8}x^3 + \frac{15}{14}x^2 - \frac{5}{28}x \qquad (3.22)$$

$$\chi_5(x) = x^5 - \frac{12}{5}x^4 + 2x^3 - \frac{2}{3}x^2 + \frac{1}{14}x$$

$$\chi_6(x) = x^6 - \frac{35}{12}x^5 + \frac{35}{11}x^4 - \frac{35}{22}x^3 + \frac{35}{99}x^2 - \frac{7}{264}x$$

$$\chi_7(x) = x^7 - \frac{24}{7}x^6 + \frac{60}{13}x^5 - \frac{40}{13}x^4 + \frac{150}{143}x^3 - \frac{24}{143}x^2 + \frac{4}{429}x$$

$$\aleph_1(y) = 1$$

$$\aleph_2(y) = y - \frac{1}{2}$$

$$\aleph_3(y) = y^2 - y + \frac{1}{6} \qquad (3.23)$$

$$\aleph_4(y) = y^3 - \frac{3}{2}y^2 + \frac{3}{5}y - \frac{1}{20}$$

$$\aleph_5(y) = y^4 - 2y^3 + \frac{9}{7}y^2 - \frac{2}{7}y + \frac{1}{70}$$

Results of Figure 3.7 show that the AD-ZZ model achieves a high level of accuracy. It is reminded that this achievement is not so obvious for structural models, since when the d.o.f. vanish at the clamped edge, the transverse shear stress resultant also incorrectly vanishes. The present model prevents from this drawback by enforcing as additional constraint a non-vanishing transverse shear at clamped edges when computing higher order terms with symbolic.
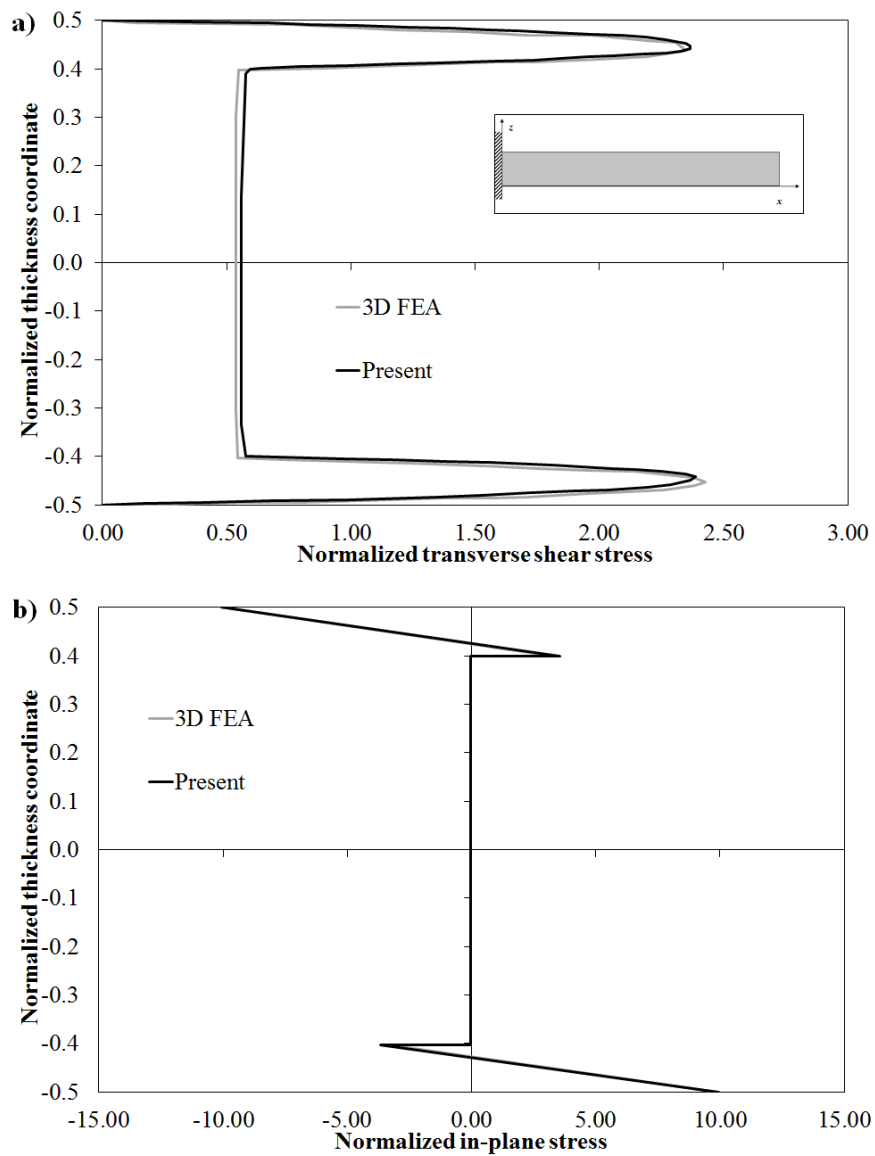
Figure 3.7 Through-the-thickness distribution of a) transverse shear stress $\bar{\sigma}_{xz}$ and b) in-plane stress $\bar{\sigma}_{xx}$ for the cantilever sandwich beam by the AD-ZZ model and 3D FEA [129].

3.2 Comparison with other theories

As a further assessment of the accuracy of the AD-ZZ model for static analysis, in the present section its results are compared to those by some of the theories discussed in Chapter 1, considering laminates or sandwiches.

3.2.1 Sandwich plate by global-local theory and AD-ZZ model

First, the sample case by Zhen and Wanji [72] is analysed, which refers to a simply supported sandwich plate undergoing a sinusoidal loading with faces in MAT p and core in MAT c. The length to thickness ratio is 4, faces are 0.1h thick and core is 0.8h thick. Transverse shear stresses by the global − local approach of Ref. [72] and by the AD-ZZ model [119] are compared to the exact solution [72] in Figure 3.8, where they are normalized according to Eq. (3.12).

The in-plane variation of the functional d.o.f. given in Eqs. (3.7)-(3.11) is adopted. The equilibrium condition of Eq. (2.18) is imposed in [-0.45h; -0.41h; -0.2h; 0.1h; 0.36h; 0.41h; 0.45h].

The results of Figure 3.8 show that both models [72] and [119] obtain results in good agreement with the exact solution. This is a consequence of the possibility both models offer of refining locally their solution. However, while the global-local approach [72] only gives a hint of the asymmetry in $\bar{\sigma}_{yz}$ due to the loading acting on the upper face of the structure, the AD-ZZ model is able to precisely describe this aspect because equilibrium is enforced at several points across the thickness. It could be noticed that asymmetry is enhanced by the rather poor properties of the core as compared to faces, which amplifies the fact that loading is applied only on the upper face.
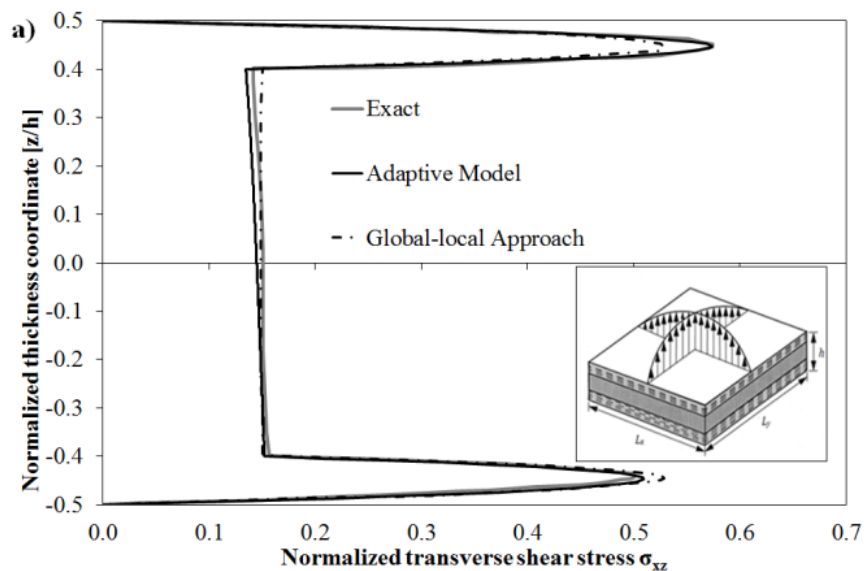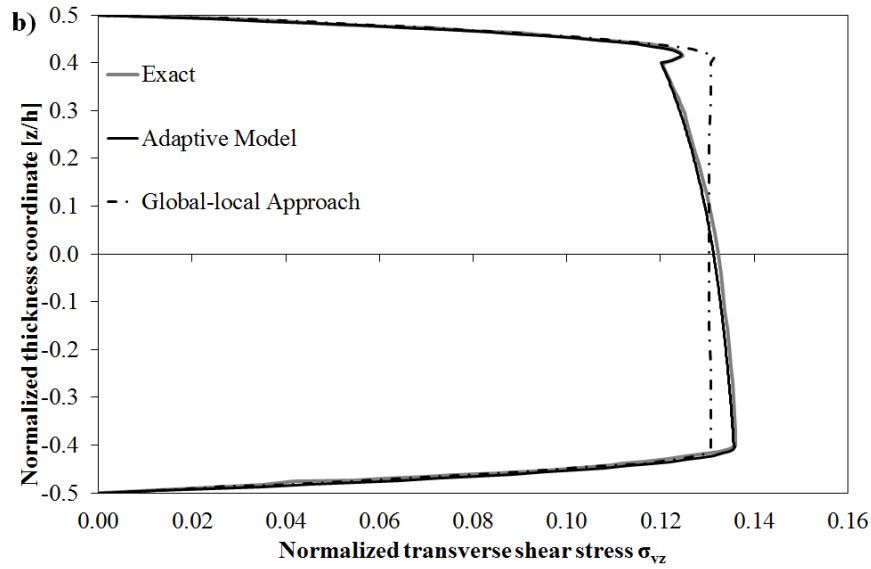
Figure 3.8 Comparison between transverse shear stresses by the AD-ZZ model [119], the global-local approach by Zhen and Wanji [72] and the exact solution [72] for a sandwich plate with L/h=4.

3.2.2 Sandwich plate by AD-ZZ model and HLW theory with ZZ-K function

It is now considered the simply supported rectangular sandwich plate under bi-sinusoidal loading analysed by Brischetto et al. [**168**]. It has a length to thickness ratio of $L_x/h=4$ and a length-side ratio of $L_y/L_x=3$. A geometrical asymmetry due to the difference between the thickness of the upper and lower faces characterizes this case, as the thickness ratios of the constituent layers are [2h/10; 7h/10; h/10]. There is also an asymmetry in the material properties, the lay-up being [MAT bl/ MAT bc/ MAT p]. Figure 3.9 reports the comparison between the exact solutions and the numerical results by the AD-ZZ model [**119**] and by the model [**168**]. This ZZ-K layerwise model describes the through-the-thickness variation of displacements using a seventh order representation and the Murakami's zig-zag function. The quantities reported in Figure 3.9 are normalized as follows, according to [**168**]:

$$\overline{\sigma}_{xz} = \frac{\sigma_{xz}\left(0,\dfrac{L_y}{2},z\right)h}{q^0 L_x} \qquad \overline{u} = \frac{u\left(0,\dfrac{L_y}{2},z\right)E_{1MATbc}h^2}{q^0 L_x^3} \qquad (3.24)$$

70

The results by the AD-ZZ model [**119**] have been obtained imposing the equilibrium condition (2.18) in [-0.45h; -0.35h; -0.25h; 0.1h; 0.3h; 0.42h; 0.47h]. Nevertheless this case is a very challenging stacking sequence due to the unsymmetric lay-up, both the approaches considered are accurate for what concerns transverse shear stress. However Figure 3.9b shows the limit of using Murakami zig-zag function for structure with asymmetric lay-up. As a matter of fact, the AD-ZZ model, which uses a physically-based zig-zag function, is dramatically more accurate in describing the through-the-thickness distribution of the in-plane displacement. Thus, it can better approximate the in-plane stress and strain, and consequently their contribution to strain energy for general lay-up.
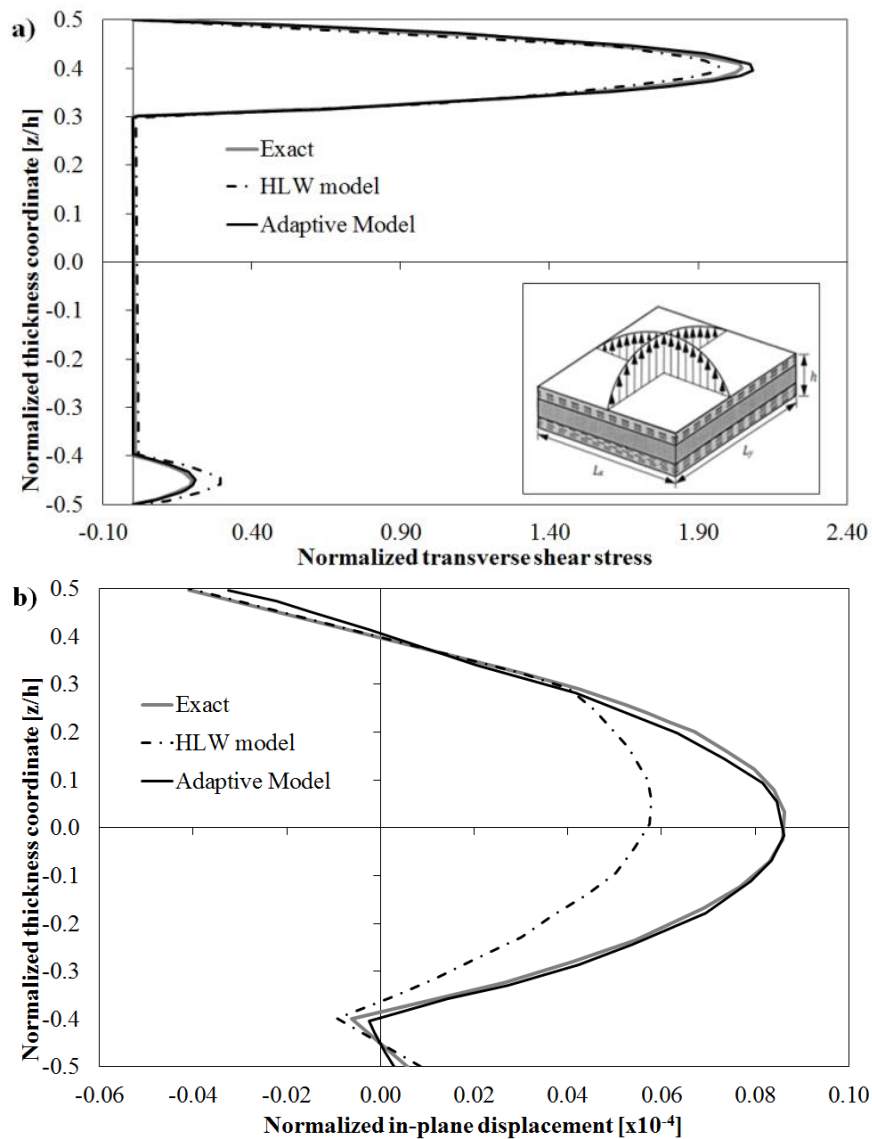
Figure 3.9 Comparison between transverse shear stress and in-plane displacement by the AD-ZZ model [119], the HLW model [168] and the exact solution [168] for a sandwich plate with L/h=4.

3.2.3 [0°/90°/0°/90°] laminated beam by sublaminate theory and AD-ZZ model

This case considers the simply supported laminated [0°/90°/0°/90°] beam undergoing sinusoidal loading analysed by Averill and Yip [102]. The beam has four layers each h/4 thick and made of MAT p. The length to thickness ratio of the beam is 4. Figure 3.10 reports the exact elasticity solution for this case compared to the numerical ones by the sublaminate approach of Ref. [102] and by the AD-ZZ model [119]. The quantities reported in Figure 3.10 are normalized as in Eq. (3.1). For the AD-ZZ model, equilibrium conditions (2.18) have been imposed in the following points [-0.45h; -0.4h; -0.2h; -0.15h; -0.1h; 0.05h; 0.1h; 0.2h; 0.27h; 0.45h].

Numerical results show that both the approaches considered obtain accurate results, especially for the in-plane stress and displacement. Instead, the sublaminate approach [102] is less accurate in describing the through the thickness distribution of the transverse shear stress. Perhaps, an improved accuracy could be obtained further refining the discretization in [102]. The superior accuracy of model [119] with fewer unknowns is the results of equilibria enforced at points across the thickness.

b)

c)
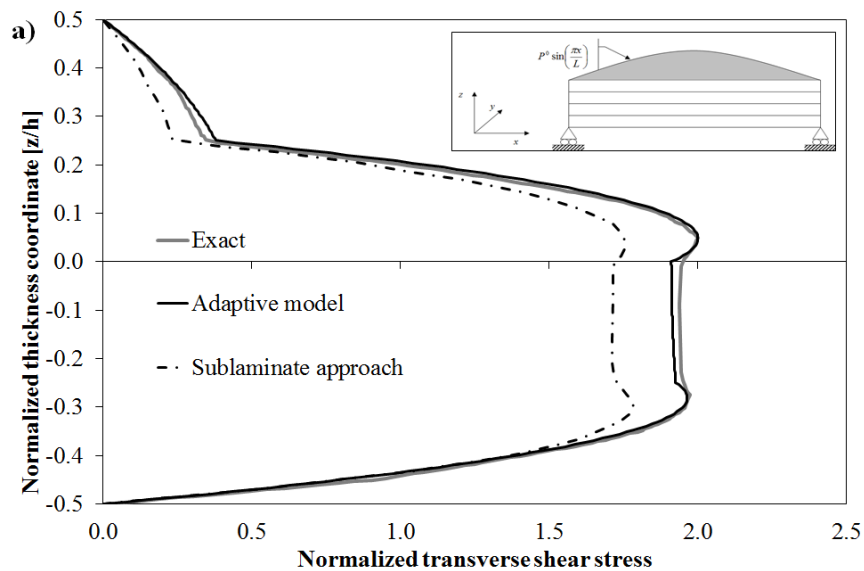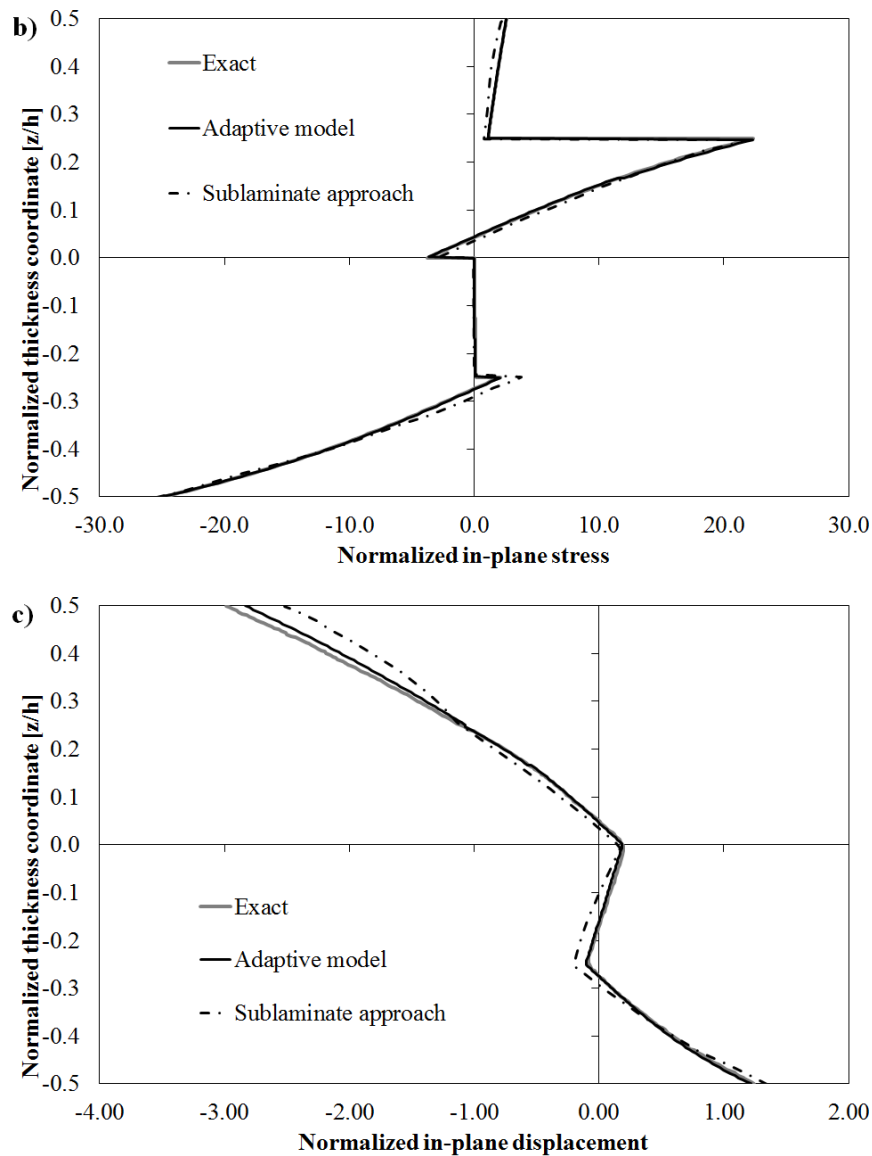
Figure 3.10 Comparison between transverse shear stress, in-plane stress and in-plane displacement by the AD-ZZ model [119], the sublaminate approach [102] and the exact solution [102] for a [0°/90°/0°/90°] laminated beam with L/h=4.

3.2.4 [0°/90°/0°] laminated plate by cubic-parabolic RZT model and AD-ZZ model

In thick laminates with different properties of layers and thickness, displacements cease to be piecewise linear across the thickness, assuming a higher-order pattern. In order to show this, here a [0°/90°/0°] simply supported rectangular ($L_y=3L_x$) plate, with a length-to-thickness ratio of 5, subjected to bi-sinusoidal transverse loading is considered. All three constituent

layers are made of MAT g. The outer ones have thickness 0.25h, the inner one has thickness 0.5h.

In order to treat this case, Iurlaro et al. in [159] enrich the RZT model [62] with a higher-order kinematic assumptions for the in-plane displacements and with a through-the-thickness parabolic distribution of the transverse displacement (here referred as the cubic-parabolic RZT). In Figure 3.11, the results by this formulation are compared to the exact 3D solution computed using the Pagano technique [145] and the results by the AD-ZZ model. Stresses and displacements are reported in normalized form as prescribed in Ref. [159]:

$$\left\{ \overline{\sigma}_{xz}; \overline{\sigma}_{yz} \right\} = \frac{h}{L_x^2 p^0} \left\{ \sigma_{xz} \left(0, \frac{L_y}{2}, z \right); \sigma_{yz} \left(\frac{L_x}{2}, 0, z \right) \right\}$$

$$\left\{ \overline{\sigma}_{xx}; \overline{\sigma}_{yy}; \overline{\sigma}_{zz} \right\} = \frac{h^2}{L_x^2 p^0} \left\{ \sigma_{xx} \left(\frac{L_x}{2}, \frac{L_y}{2}, z \right); \sigma_{yy} \left(\frac{L_x}{2}, \frac{L_y}{2}, z \right); \sigma_{zz} \left(\frac{L_x}{2}, \frac{L_y}{2}, z \right) \right\} \qquad (3.25)$$

$$\left\{ \overline{u}; \overline{w} \right\} = 10^4 \frac{D_{11}}{L_x^4 p^0} \left\{ u \left(0, \frac{L_y}{2}, z \right); w \left(\frac{L_x}{2}, \frac{L_y}{2}, z \right) \right\}$$

Where D_{11} is the bending stiffness defined according to [159] as:

$$D_{11} = \frac{1}{3} \sum_{k=1}^{n_l} \left(Q_{11} \right)_k \left(z_k^3 - z_{k-1}^3 \right) \qquad (3.26)$$

These results show the importance of assuming a high-order through-the-thickness representation of displacements, because cases exists for which a piecewise linear representation cannot achieve the maximal accuracy.

Indeed, nevertheless the material properties of constituent layers and the lay-up are not dissimilar to those of previous cases, here a piecewise linear representation with a constant w cannot be accurate. From Figure 3.11, it could be noticed that both the AD-ZZ model [119] and cubic-parabolic RZT [159] models obtain the fulfilment of the boundary conditions prescribed by the elasticity theory for shear and transverse normal stresses (2.6) − (2.7) and (2.22). Both models show an accurate predictive capability accounting for the idea pioneered by Di Sciuva in Ref. [62] of a priori fulfilling the interlaminar stress continuity with a fixed number of d.o.f.

d)

e)

f)
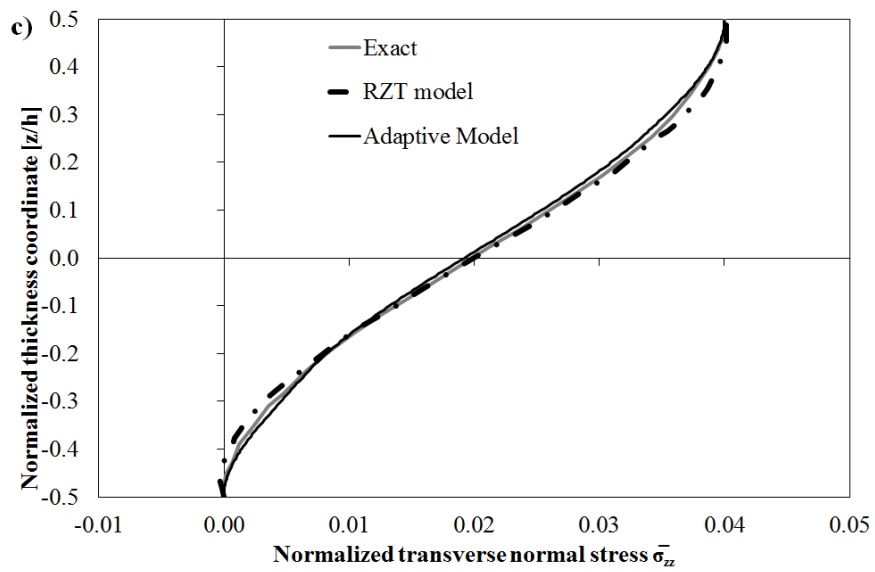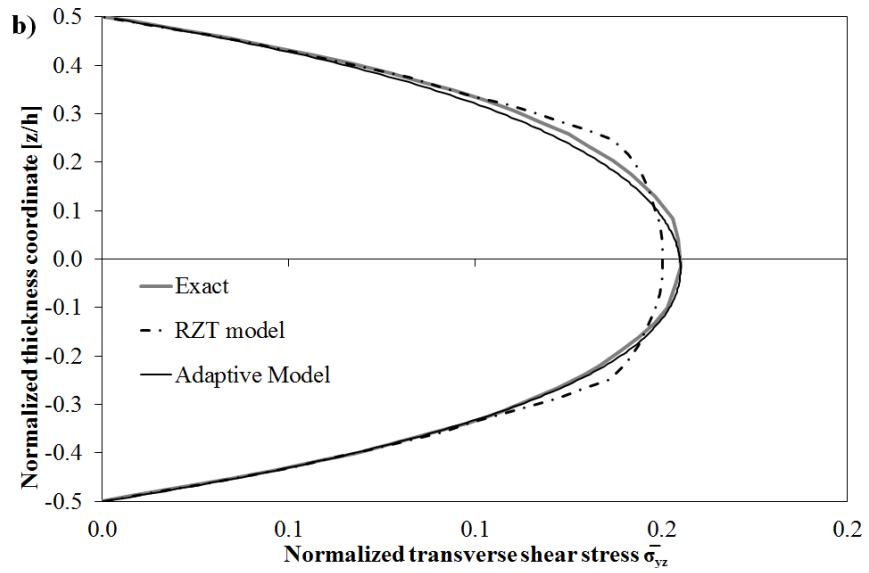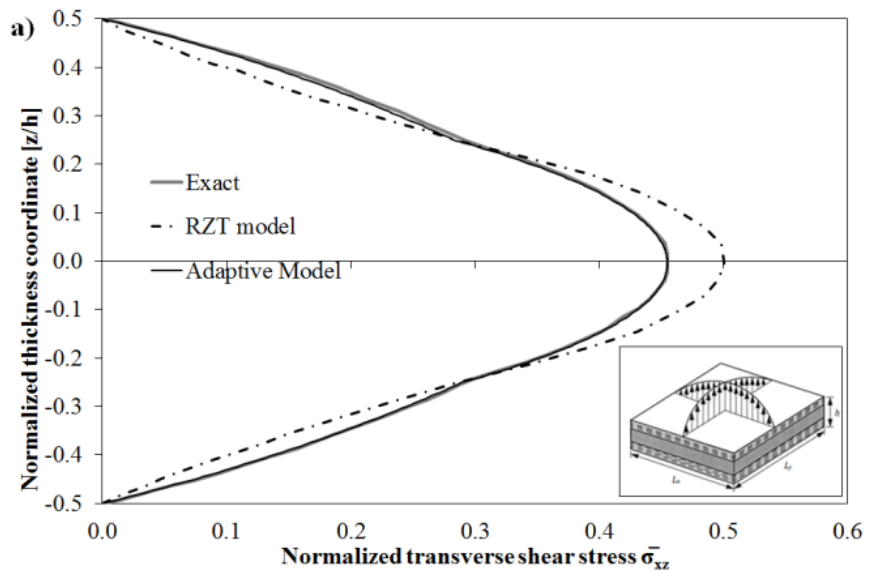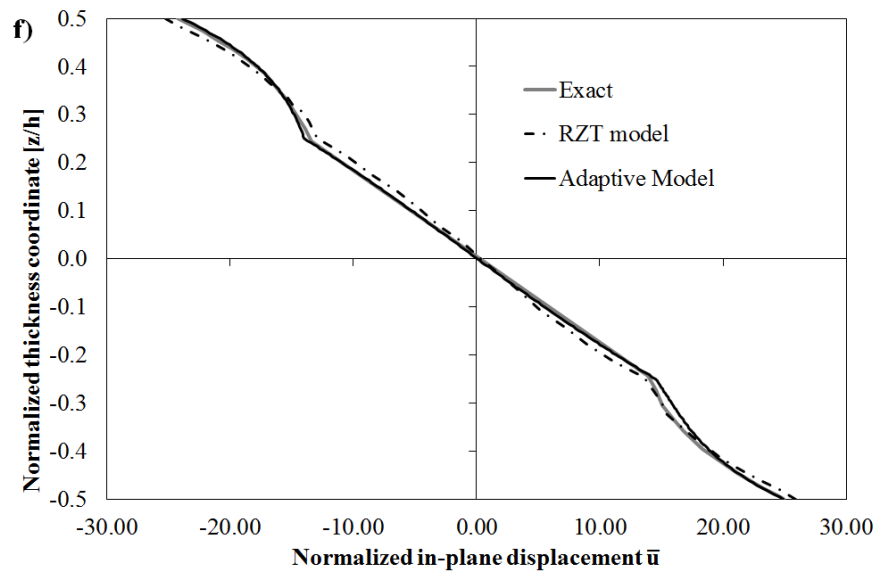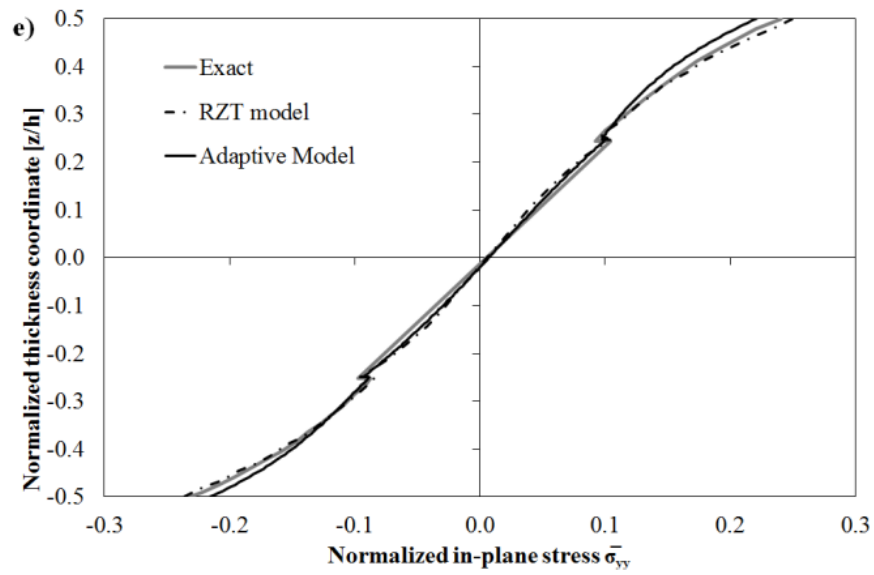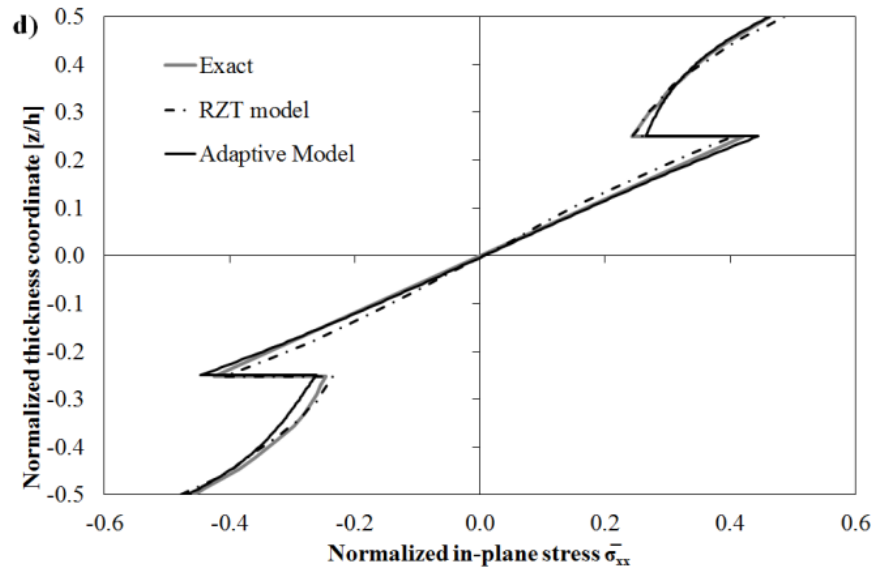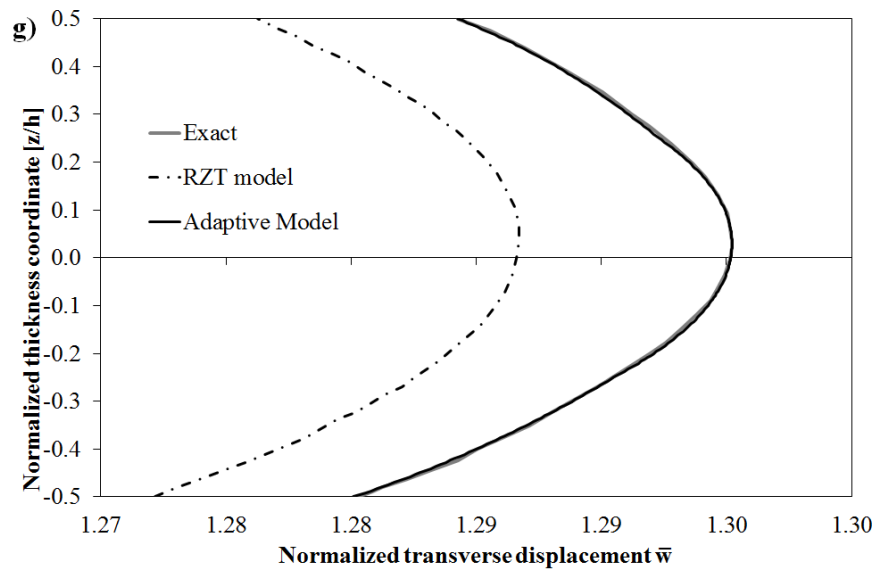
Figure 3.11 Comparison between stress and displacement fields by the AD-ZZ model [119], the RZT approach [159] and the exact solution [159] for a laminated plate with length-to-thickness ratio 5.

3.3 Validation of the AD-ZZ model for dynamic analyses

Now attention is focused on dynamic analyses. In particular the validation of the AD-ZZ model for this kind of analysis is done considering three sandwiches undergoing blast loading. The choice of performing validation of the structural model considering pulse loading and not evaluation of natural frequencies is done because the natural frequencies are global quantities (see Ref. [155]) that don't enhance the quality of the AD-ZZ in describing local effects.

3.3.1 Impulsive loading

Blast pulse loading represents a major hazard responsible for catastrophic failure of structures, as evidenced by research works dealing with explosive pressure pulses, which look for configurations able to reduce their detrimental effects (see e.g. Librescu et al. [169], [170] and [171] and Hause and Librescu [172] and [173]).

Once a pressure pulse is generated, a shock wave is transmitted in all directions. When this wave reaches a structure, it can be noticed an instantaneous pressure peak, followed by a decrease. Various expressions have been suggested in literature, either of theoretical or

numerical nature, to describe the overpressure time history. In particular, the modified Friedlander exponential decay equation is generally adopted as blast-type loading (see e.g. Librescu et al. [169] and [171], Hause and Librescu [172], Gupta [174], Gupta et al. [175] and Song et al. [176]):

$$P(t) = P_m \left(1 - \frac{t}{t_p} \right) e^{-a't/t_p} \tag{3.27}$$

P_m being the peak pressure in excess of the ambient one, t_p the positive phase duration measured from the time of arrival of the blast and a' a decay parameter that can be adjusted in order to approximate the result of an experimental test. Customarily, the pressure is assumed to be uniformly distributed over the entire panel and the impact is assumed to occur with a normal incidence. This is not the case of gun blast pressure pulses, which require the spatial distribution of the pressure pulse to be considered; the readers find a study about gun blast in the paper by Kim and Han [177].

Assuming a'/t_p equal to zero, the limiting case of the triangular loading is featured. As other special cases, the rectangular, step and sine pressure pulses have been considered in literature. The sonic boom-type loading is customarily modelled as an N-shaped pressure pulse corresponding to an idealized far-field pulse impacting at a normal incidence:

$$P(t) = \begin{cases} P_m \left(1 - \dfrac{t}{t_p} \right) & \text{for } 0 < t < rt_p \\ 0 & \text{for } t < 0 \text{ and } t > rt_p \end{cases} \tag{3.28}$$

where r denotes the shock pulse length factor and the other symbols are as in (3.27). For the case r = 1, the N-shaped pulse degenerates into a triangular distribution, while for r = 2 a symmetric pulse is obtained.

The solving system for the dynamic problem due to this kind of loading is as follows:

$$\begin{cases} [M]\{\ddot{D}\} + [K]\{D\} = \{P(t)\} \\ \{D\}(0) = 0 \\ \{\dot{D}\}(0) = 0 \end{cases} \tag{3.29}$$

Where [M] is the mass matrix of the structure, [K] is the stiffness matrix, {D} is the column vector of the functional d.o.f. and {P(t)} is the column vector of the applied load. To solve the equation system (3.29) a step by step procedure is used, discretising the equation in time. More precisely the Newmark implicit time integration scheme is adopted, since alternative

explicit time integration schemes need extremely small time steps to be stable. It is worthwhile to mention that all the numerical results here considered disregard geometrical and material non-linearity, therefore, at any time step the solving system is a linear system with constant coefficients, thus the main drawback of the implicit integration schemes (i.e. inverting a stiffness matrix with coefficients that depend on the displacement) is avoided. Using the Newmark algorithm the velocity and the acceleration vectors after a time step Δt are:

$$\left\{\dot{D}\right\}_{n+1} = \frac{\gamma}{\beta\Delta t}\left(\left\{D\right\}_{n+1}-\left\{D\right\}_{n}\right)+\left(1-\frac{\gamma}{\beta}\right)\left\{\dot{D}\right\}_{n}+\left(1-\frac{\gamma}{2\beta}\right)\Delta t\left\{\ddot{D}\right\}_{n}$$

$$\left\{\ddot{D}\right\}_{n+1} = \frac{1}{\beta\Delta t^2}\left(\left\{D\right\}_{n+1}-\left\{D\right\}_{n}\right)-\frac{1}{\beta\Delta t}\left\{\dot{D}\right\}_{n}+\left(1-\frac{1}{2\beta}\right)\left\{\ddot{D}\right\}_{n}$$

(3.30)

By setting $2\beta \geq \gamma \geq 0.5$ the method is unconditionally stable (see, e.g. Ref. [178]). In the present work, aiming at meeting stability requirements, all the calculations are carried out considering $\beta=1/4$ and $\gamma=1/2$. However, in order to limit convergence and rounding errors, relatively small time-steps are considered. By substituting the expressions of Eq. (3.30) into Eq. (3.29), a linear algebraic solving system of the type $F(D_{n+1}) = 0$ is obtained.

The Rayleigh Ritz method is employed to solve the static equations, i.e. the spatial part of the problem. In details, since all the structures analysed in this sections are simply supported, the trial functions of Eqs. (3.7) – (3.11) are employed to describe the in-plane variation of the functional d.o.f.
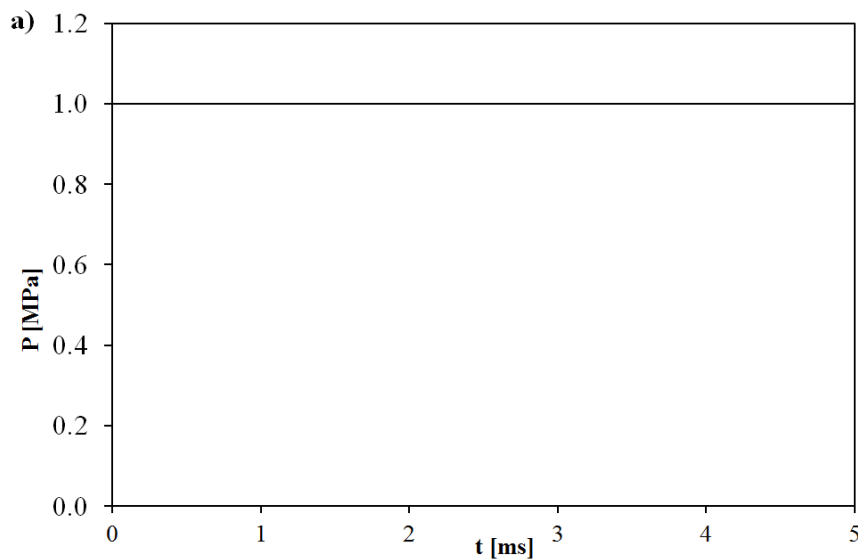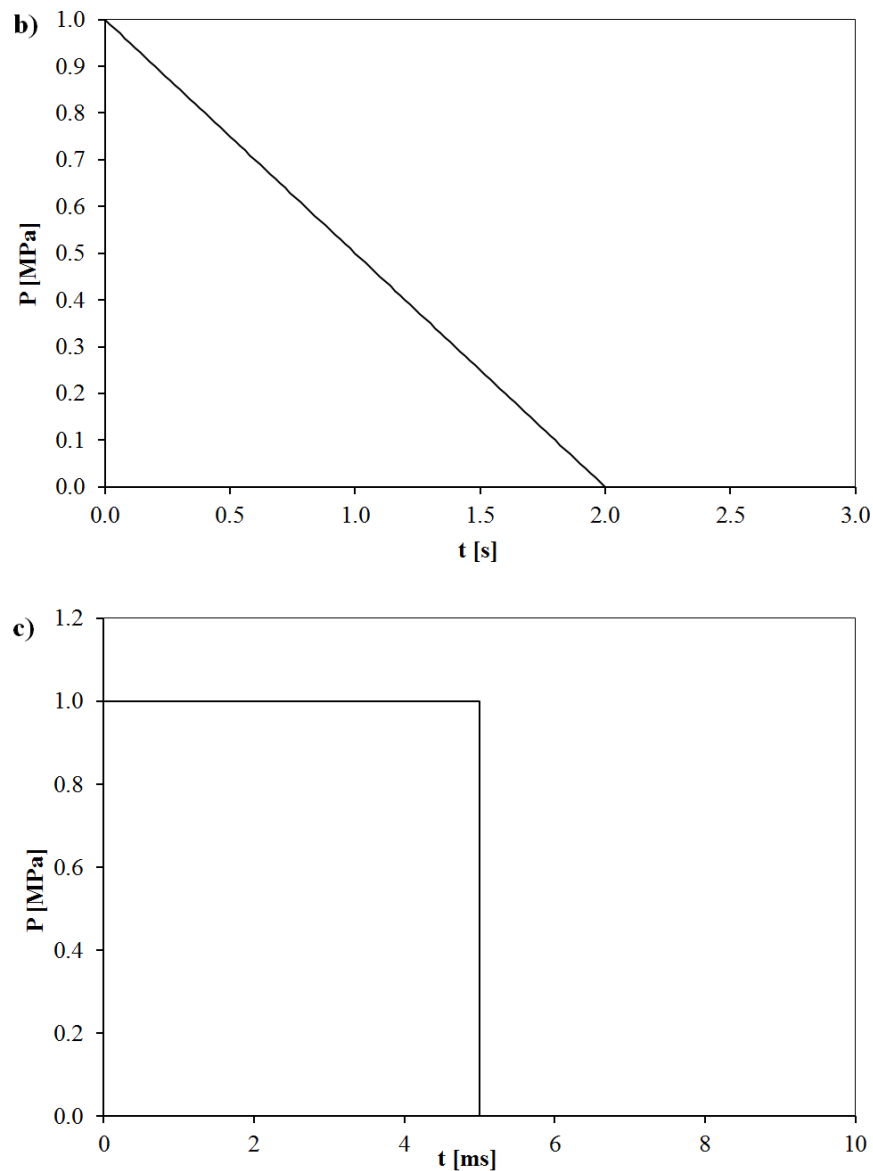
Figure 3.12 Time history for a) constant blast pulse, b) triangular blast pulse and c) step blast pulse.

3.3.2 Study of sandwiches undergoing blast pulse loading

Three sample test cases concerning simply-supported sandwich panels subjected to blast pulse loading are considered in order to assess the accuracy of the model in case of dynamic analyses.

In all the cases, according to [172], which analytically solves the problem by applying the extended Galerkin method (EGM) coupled with the Laplace Transform, the material properties of faces are chosen as: $E_1=206.84$ GPa, $E_2= E_3=5.171$ GPa, $G_{12}= G_{13}= G_{23}=2.551$

GPa, υ_{12}= υ_{23} =0.25, υ_{13}=0.22, density 1558.35 Kg/m^3. Those of core are: E_1=E_2=E_3=0.138 GPa, G_{12}= G_{13}= 0.1027 GPa, G_{23}=0.06205 GPa; υ_{ij} follows from E_{ij} and G_{ij} according to the rule for transversely orthotropic media; the density is 16.3136 Kg/m^3. The panels are plate, square (L_x= L_y= 0.6096 m) and have a core 25.4 mm thick, each of the faces is 1.905 mm thick and the lay-up is [45°/-45°/45°/-45°/45°/core/45°/-45°/45°/-45°/45°].

Figure 3.13a represents the central deflection of the sandwich panel normalized to the static one under a triangular pulse loading, Figure 3.13b and 3.13c respectively represent the normalized central deflection of the plate under a step pulse loading and a constant pulse loading. Note that for Figure 3.13b, the differences between the analytical solution by Hause and Librescu [172] and that computed by the present AD-ZZ model are due to the fact that the latter considers a variable transverse displacement differently to [172]. This implies a different behaviour of the two theories that is evident just for the case with step blast loading.

The results of Figures 3.13a, 3.13b and 3.13c are obtained considering M=N=1 in Eqs. (3.7) − (3.11) similarly to what done by Hause and Librescu [172]. Therefore, in order to better evaluate the effect of these parameters on the structural response, the central deflections for different values of M and N for the sandwich panel subjected to a constant pulse loading are reported in Figure 3.13d.

From this figure, it could be noticed that the mean value of the deflection varies. Indeed, the minimum and the maximum deflections translate upwards as M and N grow because the stiffness of the structure decreases a little as a result of an increase in the number of components of the displacements' representation. In addition, even if it is less evident, it could also be noticed a small increase in the frequency of the dynamic response due to the same reason.
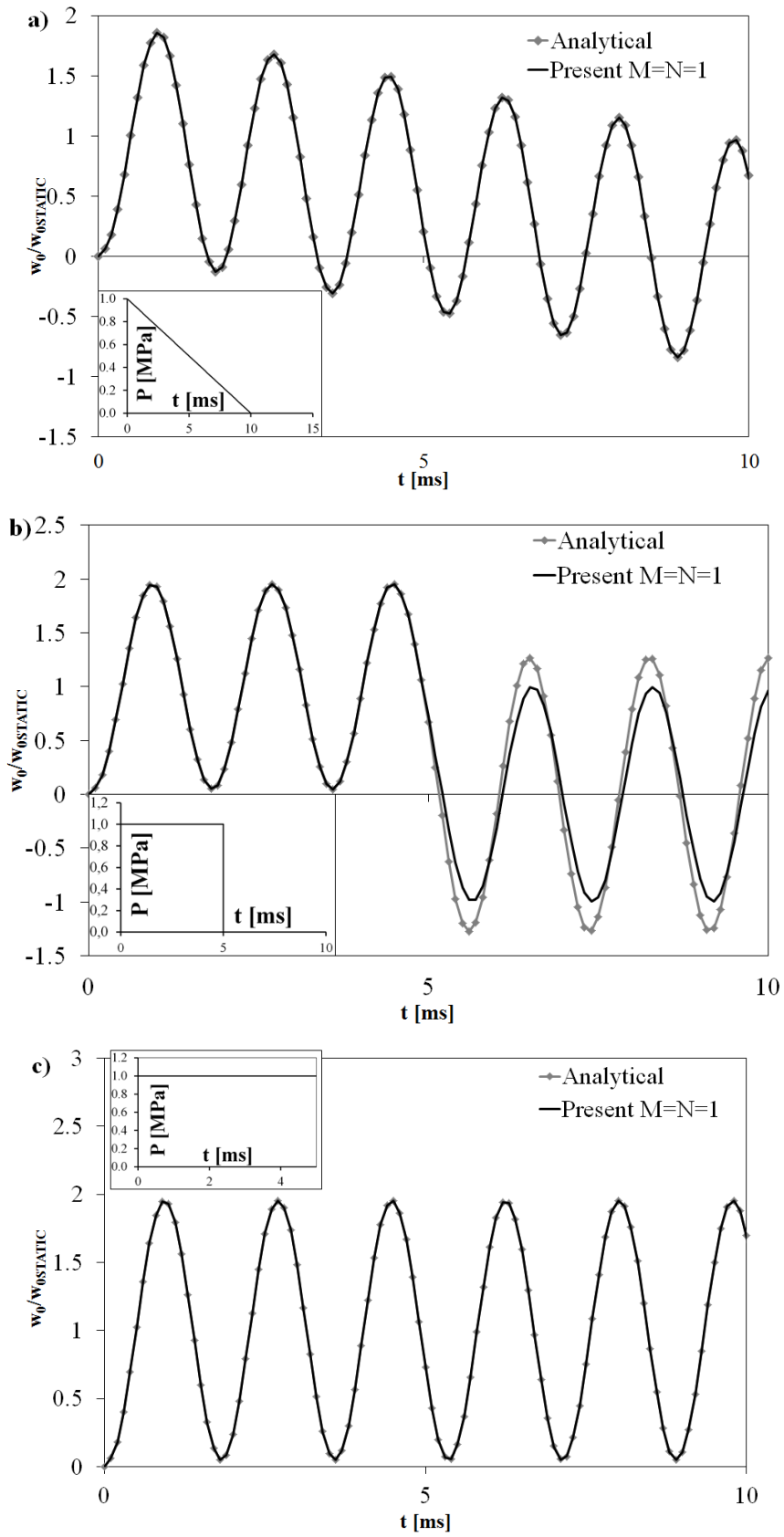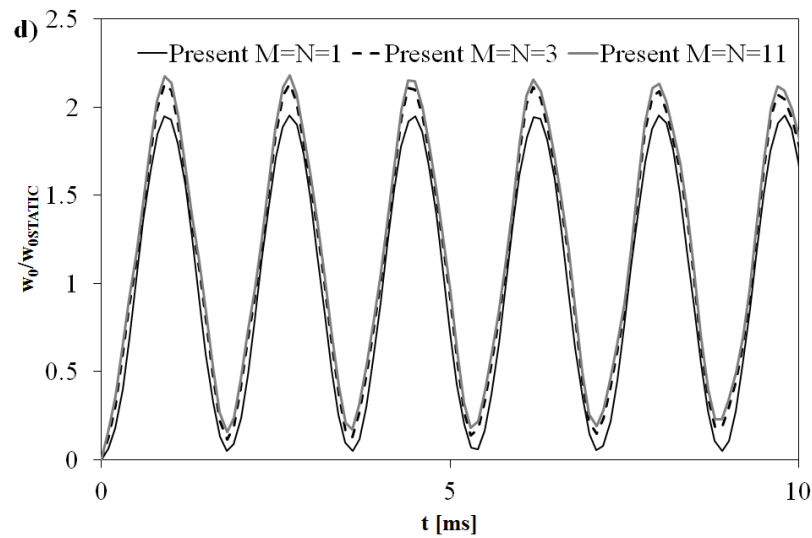
Figure 3.13 Non dimensional deflection time history for a simply-supported sandwich plate (L_x= L_y= 0.6096 m, h= 29.21 mm) subjected to a) triangular pulse loading, b) step pulse loading and c) constant pulse loading. d) Non dimensional deflection time history for different order of expansion (constant pulse loading).

Another important effect to be remarked is that related to the variation of the length to thickness ratio. As well known, the lower is this ratio, the higher are the layerwise effects, and in particular those due to transverse shear deformation. In order to study these effects on the response, once again, the sandwich panel subjected to a constant pulse loading is considered. Figure 3.14 represents the central deflection of the sandwich panel normalized to the static one considering different values of the length to thickness ratio. Reducing the length to thickness ratio it could be noticed a strong reduction in the amplitude of the oscillation, together with an increase in the frequency of the response due to the fact that a thick structure is considerably stiffer than a thin one.
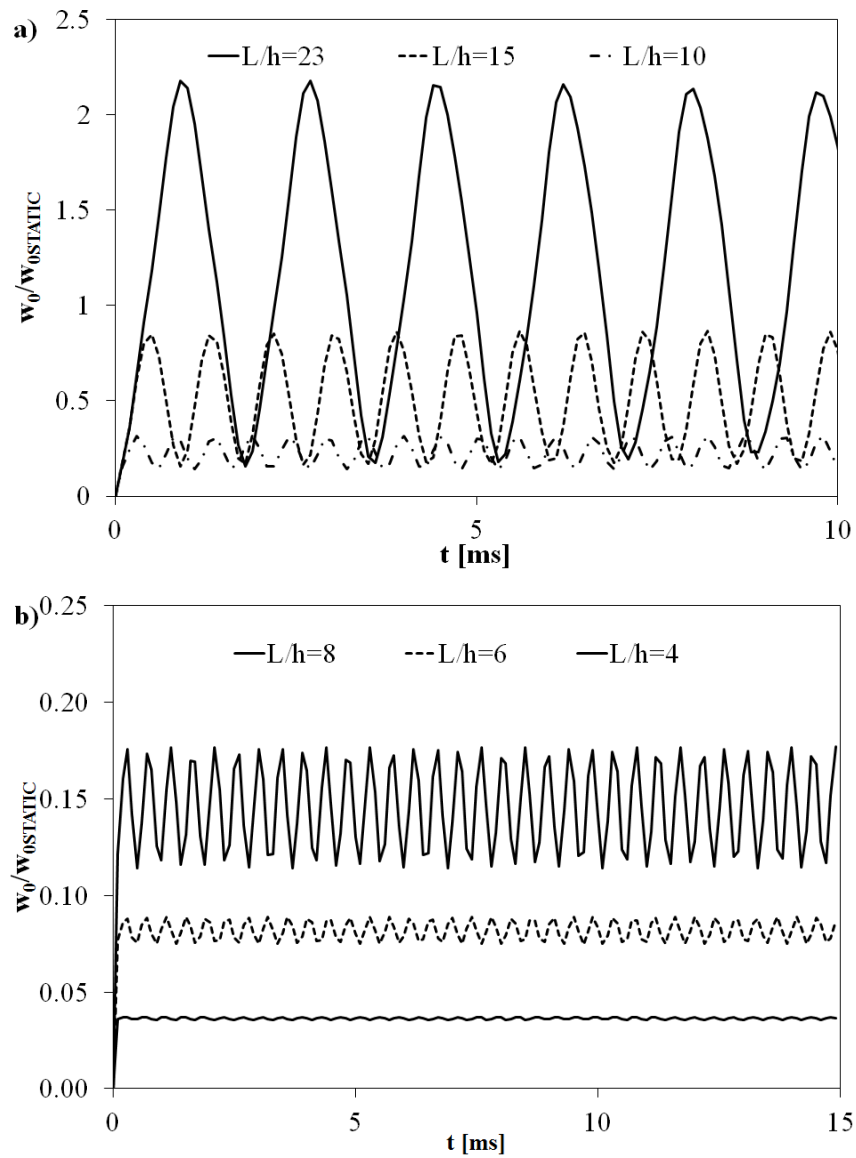
Figure 3.14 Non dimensional deflection time history for a sandwich panel with different length to thickness ratios subjected to a constant pulse loading.

Chapter 4: Study of bonded joints

In this Chapter, as an application of the AD-ZZ model to problem of practical interest, its particularization to study of bonded joints is presented. This kind of joints offers a combination of improved performances and manufacturing advantages with respect to traditional mechanical fastening, like better vibration isolation, accommodation of thermal expansion mismatch and hygrothermal swelling, better aesthetic appearance and better aerodynamic capabilities.

In particular, adhesive bonding allows for a more gradual transfer of load between the structural elements, thus achieving a more uniform stress distribution. As a direct consequence, adhesive bonding is the most suitable technique for joining components when stress concentrations due to mechanical fastening have potentially catastrophic effects on strength and fatigue life, like for composite laminates, as discussed by Her [179].

Simulating bonded joints is a rather complex matter that requires in many cases to account for geometric and material nonlinearity, to take into consideration the stress boundary conditions in a point form and to carry out the analysis with a sophisticate modelling of out-of-plane stress and strain fields. As shown by the comprehensive literature reviews by Vinson [180] and by da Silva et al. [181], many analytical, numerical and experimental studies have been published over years.

A serious design concern regarding adhesively bonded joints is the evaluation of the stress and strain fields across the joint and how they are influenced by geometry, materials, loading conditions, temperature and moisture effects. A considerable effort has been made by many researchers to fully understand the intricacies in the behaviour of bonded joints and how the stress state influences the failure modes. The analysis of bonded joints can be carried out via finite element analysis (FEA) without introducing any simplifying assumption that could limit accuracy even in the case of complex joint geometries and complex material models including nonlinear effects. However FEA requires a quite long preparation and a large computational

time. To overcome this problem, analytical models (AM) based on simplifying assumptions and finite-difference schemes are extensively adopted for studying joints. Analytical [**182**], [**183**], [**184**], [**185**], [**186**], [**187**], finite element [**188**], [**189**], [**190**], [**191**] and finite-difference [**192**] solutions show that even when the adherends and the adhesive materials are homogeneous and isotropic, stresses and deformations are complex due to the different elastic moduli of adhesive and adherends and the enforcement of the stress boundary conditions. Results of the analyses show non-uniform shear strain and stress distributions in the adhesive layer caused by the progressive reduction of the strain in the adherends along the overlap and the continuity of the adhesive/adherends interface. The out-of-plane transverse shear and normal stresses in single- (SLJ) and double-lap (DLJ) bonded joints have a peak close to the edges of the bonding layer, which can lead to the premature failure of the joint in service. The peeling stress can be larger than the shear stress, thus becoming the dominant effect at the edges, as shown, e.g., by Nemes and Lachaud [**193**]. The readers can find a comprehensive discussion and extensive assessments in the papers by da Silva et al. [**181**] and [**194**].

Most AM are stress-based models that still maintain some of the simplifying assumptions of the pioneering models (Volkersen [**195**], Goland and Reissner [**196**] and Hart-Smith [**197**]) in order to allow a fast, low cost solution in closed form. Often, shear stress is assumed constant across the thickness of the adhesive, or shear and peel stresses in the adhesive layer are calculated solving a plane strain problem. This happens because the adhesive is assumed to deform only in shear and the adherends are assumed to be rigid, though these hypotheses could be not realistic in all cases. With the advent of bonded laminated composites as primary structures in the 80's, more complex AM that consider the effects due to the deformation of the adherends and of the adhesive have been developed in order to adequately treat joints with laminated adherends. In this case, it is of primary importance to accurately account for the large variation of the transverse shear and normal stresses across the thickness that rise as a consequence of the different properties of the layers constituting the joint. However, trying to keep these improved models as simple as possible, often the stress-free boundary conditions at the ends of the overlap are still disregarded, along with the bending effect due to the eccentric load path of SLJ. Moreover, the deformability of the adherends is still accounted for with simplified techniques, as in [**196**] and [**197**]. Refined AM with improved predictive capability are reviewed by da Silva et al. [**181**], Gustafson et al. [**182**], Diaz Diaz et al. [**183**] and Radice and Vinson [**184**]. These models, depending on the complexity of their governing

differential equations, can be solved either in closed or numerical form. For examples, the models by Renton and Vinson [**198**], Srinivas [**199**] and Allman [**200**] are cited as examples that account for the transverse shear and normal deformations of adhesive and adherends, satisfy the stress-free boundary conditions ([**198**], [**199**]) and consider the effects of bending, stretching and shearing in the adherends and the tearing actions in the adhesive ([**200**]). Bonded joints with adherends made of composite materials have been recently studied by Diaz Diaz et al. [**183**] using a stress based layerwise model obtained by stacking Reissner-Mindlin plates, which requires to solve a system of 29 equations in 29 unknown parameters.

Since the assumptions of AM can affect the accuracy of results, an increasing number of 3-D FEA and of finite-difference 3-D schemes results for bonded joints have been published in the last years. The papers by Khalili et al. [**189**] and Diaz et al. [**190**] dealing with 3-D FEA of SLJ with CFRP adherends and epoxy adhesive and the paper by Andruet et al. [**188**] dealing with geometric nonlinear effects are cited as examples. Finite-difference 3-D schemes as an alternative to FEA and AM are overviewed by Xu and Li [**192**].

As discussed by Adams and Mallick [**201**], whenever a complex representation aimed at realistically simulating the stress fields is employed, a numerical scheme should be used for solving, even in the case of AM. However, this does not result disadvantageous and impractical compared to simpler AM allowing closed-form solutions, because costs are still saved with respect to 3-D FEA without significant accuracy loss. Besides, AM are not affected by stress singularities at the edge interfaces like 3-D FEA.

Geometric and material nonlinear effects and adherends with dissimilar thickness have been recently considered by Mortensen and Thomsen [**202**] using refined AM. Damage of joints under impact loading is considered by Vaidya et al. [**203**].

The Classical Laminated Plate Theory (CLPT) and the First-Order Shear Deformation Plate Theory (FSDPT) are used for analysis of bonded joints with laminated composite adherends by Mortensen and Thomsen [**202**], Wah [**204**] and Yang and Pang [**205**]. These applications shed light on whether the analysis of bonded joints can be successfully carried out with ordinary displacement-based models, which are the tools customarily employed for the analysis of laminated structures. Nevertheless the adhesive peel stress is disregarded in the constitutive equations and the transverse shear stress is neglected or assumed constant across the thickness (as a consequence, equilibrium is not satisfied at the interfaces and the stress free conditions at the end of the overlap are not met), these studies have shown that the results

of displacement-based models can be in good agreement with those of finite element models, as shown e.g. in [**205**]. Accordingly, further research is motivated in this field because even better results could be obtained without the mentioned infringements. Moreover, displacement-based AM are of interest for analysis of bonded joints because the same approach can be used across the overlap and far from it, so designers can carry out a realistic analysis of the structures in the bonded region and outside it contemporaneously and with the same tool.

As a contribution towards refinement of studies with displacement-based approaches, in this section the analysis of bonded joints with laminated adherends is carried out assuming as structural model the AD-ZZ model, which is here reformulated in order to treat bonded joints through inclusion of a variable in-plane representation. Thanks to this feature, the representation can be different in the adherends and in the overlap. Thus, the model can accurately simulate the variation of solutions across the joint and it can predict the effects of such variation on global and local behaviour, whose relevance has been shown by Gaudiello and Kolpakov [**206**] and Kolpakov [**207**].

4.1 Modelling of the problem

When adhesively bonded joints with laminated adherends are considered, the problem becomes a multiple-point boundary value problem. The boundary conditions at the edges of the adherends and of the overlap regions are satisfied finding appropriate expressions of the higher-order contributions to displacements. Since these relations are rather lengthy and tedious, here they are obtained using symbolic calculus, as already done in Chapter 2 for the development of the AD-ZZ model.

A different representation for the adherends and for the overlap area can be used, because geometry and material properties change across the joint. In this way, always appropriate expressions of the coefficients of displacements are obtained together with the possibility of refining the model in the in-plane direction.

If one assumes that no variation occurs in the transverse direction y as customarily, the transverse shear and the normal stresses should identically vanish over the free surface Ω_1 and

Ω_2 of the overlap (see Figure 4.1). Therefore, it is possible to enforce the following relations to hold in integral or point form:

$$\sigma_{xz} = 0; \quad or \quad \int_{\Omega_i} \sigma_{xz} dz = 0; \quad i=1,2$$

$$\sigma_{xx} = 0; \quad or \quad \int_{\Omega_i} \sigma_{xx} dz = 0; \quad i=1,2$$

(4.1)

The stresses are consistent with the applied loads as

$$N = \int_{\Omega_i} \sigma_{xx} dz;$$

$$M = \int_{\Omega_i} z \, \sigma_{xx} dz;$$

(4.2)

$$Q = \int_{\Omega_i} \sigma_{xz} dz;$$

N, M, Q being the in-plane, bending and shear resultants. All these conditions are used for computing an appropriate number of coefficients of displacements. Non-vanishing stresses can be enforced, because in real adhesive joints a fillet of surplus adhesive, the so-called spew-fillet can be formed at the end of overlap zone allowing transferring the shear stress.

Since the adherends may have a different number of layers, a laminated model is developed whose number of layers is different across the joint, as shown in Figure 4.1.

The middle surface Ω of the overlap is chosen as the plate reference surface. A rectangular Cartesian reference frame (*x, y, z*) with (*x, y*) in Ω and *z* normal to it is assumed as reference system. The effects of non-linear strains, which are important for SLJ and DLJ, are accounted for using the updated Lagrangian methodology, which offers an improved numerical efficiency than the standard Lagrangian approach.

Material non-linearity can be accounted for by implementing stiffness coefficients that varies with the load magnitude, as successfully done in Ref. [**122**] (See Chapter 8).
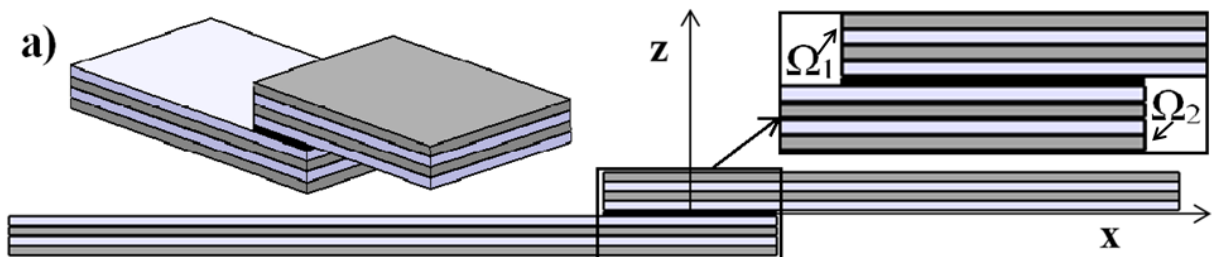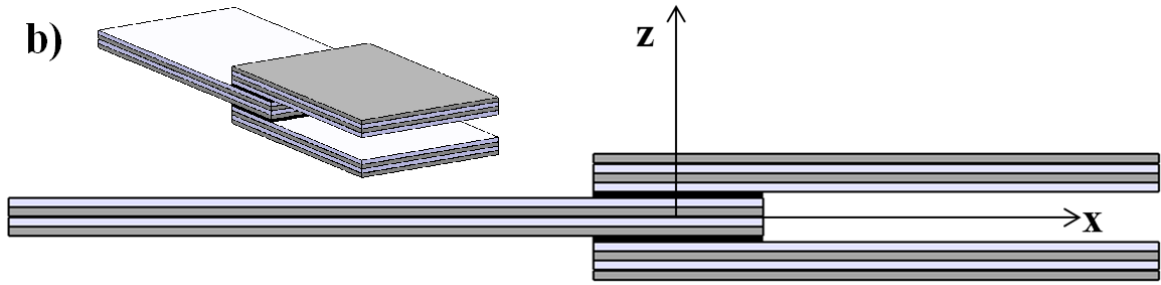
Figure 4.1 Geometry and reference system for analysis of: a) single lap joints; b) double lap joints.

The through-the-thickness variation of displacements across the thickness is postulated in the following general, piecewise form that considers four separated contributions, as indicated by the superscripts:

$$u(x,y,z) = U^0(x,y,z) + U^i(x,y,z) + U^c(x,y,z) + U^{c-ip}(x,y,z) \tag{4.3}$$

$$v(x,y,z) = V^0(x,y,z) + V^i(x,y,z) + V^c(x,y,z) + V^{c-ip}(x,y,z) \tag{4.4}$$

$$w(x,y,z) = W^0(x,y,z) + W^i(x,y,z) + W^c(x,y,z) + W^{c-ip}(x,y,z) \tag{4.5}$$

The first three contributions, $(\ )^0$, $(\ )^i$ and $(\ )^c$, are the same as in the model of Chapter 2. Instead, the new contributions with superscript $^{c-ip}$ aimed at fulfilling the continuity conditions in case of variation of the in-plane representation have the following expressions:

$$U^{c-ip}(x,y) = \Theta_x^k(x,y)(x-x_k)H_k + \Gamma_x^k(x,y)(x-x_k)^2 H_k \tag{4.6}$$

$$V^{c-ip}(x,y) = \Theta_y^k(x,y)(x-x_k)H_k + \Gamma_y^k(x,y)(x-x_k)^2 H_k \tag{4.7}$$

$$W^{c-ip}(x,y) = \left(\Theta_w^k + \Theta_{w*}^k + \chi_w^k + \chi_{w*}^k\right)(x,y)(x-x_k)H_k + \left(\Gamma_w^k + \Gamma_{w*}^k + \Lambda_w^k + \Lambda_{w*}^k\right)(x,y)(x-x_k)H_k \tag{4.8}$$

As for Eqs. (2.14), (2.15) and (2.19), H_k activates the contribution of the continuity functions starting from the variation of the in-plane representation. It could be noticed that for bonded joints this variation can happen only in one direction (x or y) and not in both at the same time. The piecewise contributions of Eqs. (4.6) – (4.8) are incorporated in order to make continuous the stresses and their gradients up the desired order at the interfaces of the regions where the in-plane representation is changed, as prescribed by the elasticity theory. Generally speaking, the summations of Eqs. (4.6) – (4.8) can have infinite terms, since from equilibrium it is possible to deduce that the continuity should hold for the stresses and their in-plane gradient of any order. By the practical viewpoint, the summations can be truncated, without significant loss of accuracy. Accordingly, in the present work the summations of Eqs. (4.6) – (4.8) are considered, without significant accuracy loss as shown by the results of the next section. In

details, the terms of first order in the in-plane coordinate are aimed at fulfilling the continuity of the stresses; those of second order are aimed at satisfying the continuity of the stress gradients.

As already done in Chapter 2, the explicit expressions of the continuity functions are evaluated in closed form using a symbolic calculus tool.

By the practical viewpoint, bonded joints are treated as laminates with variable properties across the thickness and over the in-plane direction x. In particular considering the structure of Figure 4.2, the procedure proposed splits this domain into 6 different subdomains (irrespectively of the fact that the structure is a plate or a beam) each of which can have different mechanical properties. When modelling a single lap joint (Figure 4.1a), the subdomains Adherend 2 and Adherend 4 should disappear, therefore their mechanical properties are assumed to be 0 (nearly 0 in order to avoid numerical problems) within the solving procedure. Terms 4.6 – 4.8 restore continuity of stresses and their gradients at the interfaces Ω_1 and Ω_2, while, as customarily, U^c, V^c and W^c restore continuity across the thickness, as explained in Chapter 2.
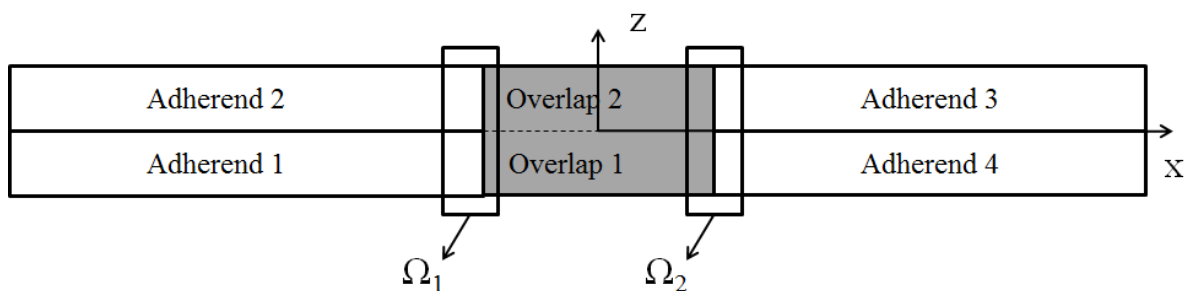
Figure 4.2 Subdomains considered for modelling single lap joint with the present procedure.

4.2 Applications to bonded joints

Sample cases of SLJ and DLJ published in the literature are retaken and analysed by the present model in order to assess whether it can be successfully employed for studying adhesively bonded joints.

In order to preliminary assess the capability of the present analytical model to treat case with in-plane discontinuity the two material wedge by Hein and Erdogan [**208**] is considered.

All the computational times provided in the following sections are obtained carrying out the analyses on a laptop computer with dual-core CPU 1.80 GHz, 64 bit operating system and 4 GB RAM.

4.2.1 Two material wedge

In order to assess the capability of the AD-ZZ model to predict continuous stresses under sudden in-plane variation of properties, first the sample case of a two-material wedge (two semi-infinite sectors under uniaxial traction) is considered (Figure 4.3). The goal is to compare the in-plane variation of the shear stress σ_{xy} across the material discontinuity to exact elasticity solution by Hein and Erdogan [**208**].

In this sample case, the variation of solutions in the transverse direction with respect to the plane *x, y* of Figure 4.3 has no relevance. Here, just the in-plane shear stress is considered, being the one with the highest singularity strength at the corner interface. A Young's modulus of 7.3 GPa and a Poisson's ratio of 0.3 are assumed for the deformable sector, while a modulus larger by a factor 100 is assumed for simulating the rigid sector.
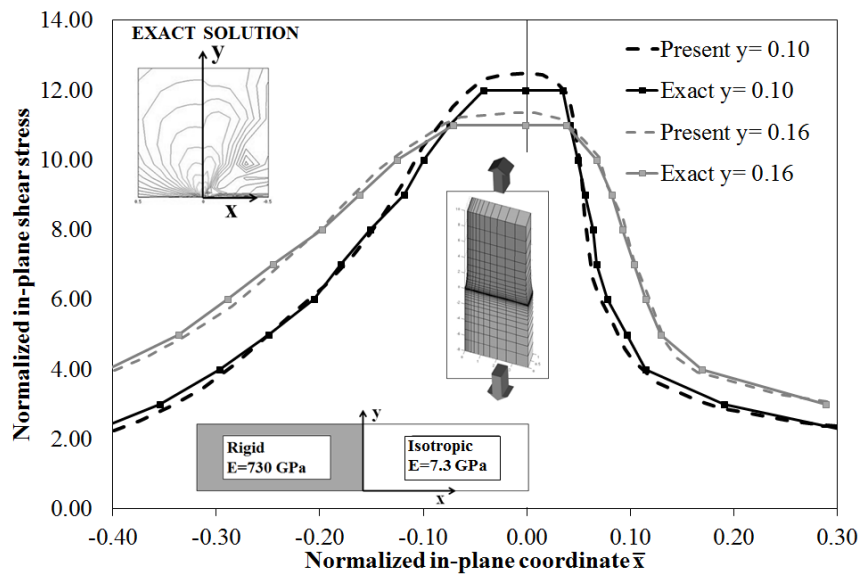
Figure 4.3 In-plane variation of the normalized in-plane shear stress for the two material wedge by the present model and exact solution [208] (inset: exact solution by Hein and Erdogan [208]).

The exact elasticity solution shows a strong stress concentration at the edge corners, which could produce a catastrophic failure in service when dissimilar materials are bonded together. Hence, the stress analysis should be carried out with the maximal accuracy at the interface of materials with dissimilar properties. Figure 4.3 reports the in-plane variation of the shear stress σ_{xy} across the material interface normalized as follows:

$$\overline{\sigma_{xy}} = \frac{\sigma_{xy}}{\sigma_{xyMAX}} \qquad\qquad (4.9)$$

The present analytical solution is obtained assuming a subdivision of the domain of the two half plates into 16x16 subdomains (see Figure 4.2) whose side length is progressively reduced close to the corner interface. Each of the two half plates has length-to-width ratio of 50. One plate is clamped, the other is stretched (with no bending) in the x direction. Within each subdomains the in-plane variation of the d.o.f is assumed parabolic in the in plane coordinates x and y. The continuity of the in-plane shear stress is enforced at the sides of subdomains by computing the appropriate expressions of the continuity functions appearing in Eqs. (4.6) – (4.8).

The results of Figure 4.3 show the capability of the AD-ZZ model to accurately reproduce the variation of the shear stress σ_{xy} across the interface even in this case. The present structural model is shown able to capture a continuous stresses with a discontinuous gradient like in the exact solution.

The strong stress concentration occurring at the interface of material with dissimilar properties shows the importance of enforcing the stress continuity under in-plane material discontinuity to accurately evaluate stresses.

4.2.2 Adhesively bonded joints

The sample cases by Diaz Diaz et al. [183], Radice and Vinson [184], Andruet et al. [188] Vaidya et al. [203] and da Silva and Adams [209] are considered in order to assess the capability of the present displacement-based multilayered plate model to describe the stress fields in adhesively bonded joints.

Case A. As first application, the sample case by Radice and Vinson [184] is considered. In this study, a single-lap joint clamped at the left edge and simply supported at the right one

undergoing an axial load with intensity 40 kN/mm is analysed. The adherends are made of an aluminium alloy (E= 70 GPa, υ=0.33), while the adhesive is made of an epoxy resin (E= 4.82 GPa, υ=0.4). The adherends are 50.8 mm long and 1.62 mm thick, the overlap length is 12.7 mm, while the adhesive thickness is 0.25 mm.

It could be remarked that the length- to-thickness ratio of the adherends is more than 30 and, in addition, they are made of isotropic material, therefore the present model does not require the computation of the continuity functions in the adherends, nor an extremely high order expansion across the thickness. Accordingly, a second order expansion is adopted both for the in-plane and the transverse displacements. Figure 4.4a shows how the shear stress σ_{xz} varies along the bond-line, whereas Figure 4.4b gives the variation of the peeling stress σ_z along the same line. According to [**184**], the variation of solutions in the transverse direction *y* is neglected. The results by the present model reported as a solid line are obtained using as trial functions in the overlap section the following ones:

$$u^0(x, y) = A^U \left[\cosh(x) - 1\right]\cos\left(\frac{\pi x}{L_x}\right)$$

$$w^0(x) = A^W \sin\left(\frac{\pi x}{L_x}\right) \tag{4.10}$$

$$\gamma_x^{\,0}(x, y) = A^{\gamma_x}\left[\cosh(x)\right]\cos\left(\frac{\pi x}{L_x}\right)$$

In this way, the problem turns into a system of three equations in the three unknown amplitude of the in-plane and transverse displacement components and of the transverse shear rotation. The solution represented as a dashed line is obtained using in the overlap section the following Fourier series expansion with 30 components:

$$u^0(x, y) = \sum_{m=1}^{M} \sum_{n=1}^{N} A_{mn} \cos\left(\frac{m\pi}{L_x} x\right) \sin\left(\frac{n\pi}{L_y} y\right)$$

$$v^0(x, y) = \sum_{m=1}^{M} \sum_{n=1}^{N} B_{mn} \sin\left(\frac{m\pi}{L_x} x\right) \cos\left(\frac{n\pi}{L_y} y\right)$$

$$w^0(x, y) = \sum_{m=1}^{M} \sum_{n=1}^{N} C_{mn} \sin\left(\frac{m\pi}{L_x} x\right) \sin\left(\frac{n\pi}{L_y} y\right) \quad\quad (4.11)$$

$$\gamma_x^{\,0}(x, y) = \sum_{m=1}^{M} \sum_{n=1}^{N} D_{mn} \cos\left(\frac{m\pi}{L_x} x\right) \sin\left(\frac{n\pi}{L_y} y\right)$$

$$\gamma_y^{\,0}(x, y) = \sum_{m=1}^{M} \sum_{n=1}^{N} E_{mn} \sin\left(\frac{m\pi}{L_x} x\right) \cos\left(\frac{n\pi}{L_y} y\right)$$

In both cases, the trial functions of the lower and upper adherends are those of Eq. (4.11) in order to respect the boundary conditions. In the former case, the problem is solved in 1.5 s, while 80 s are required in the latter one. It could be noticed that in this benchmark case the present model, thanks to its refined representation (high-order terms, transverse continuity and in-plane continuity), is proven to be able of capturing the stress fields with just one component in the series, so it appears suitable to efficiently solve the problem examined. The same consideration does not hold for lower order models such as the PWM3 of Section 2.1.3 or the PWM4 of Section 2.1.4.
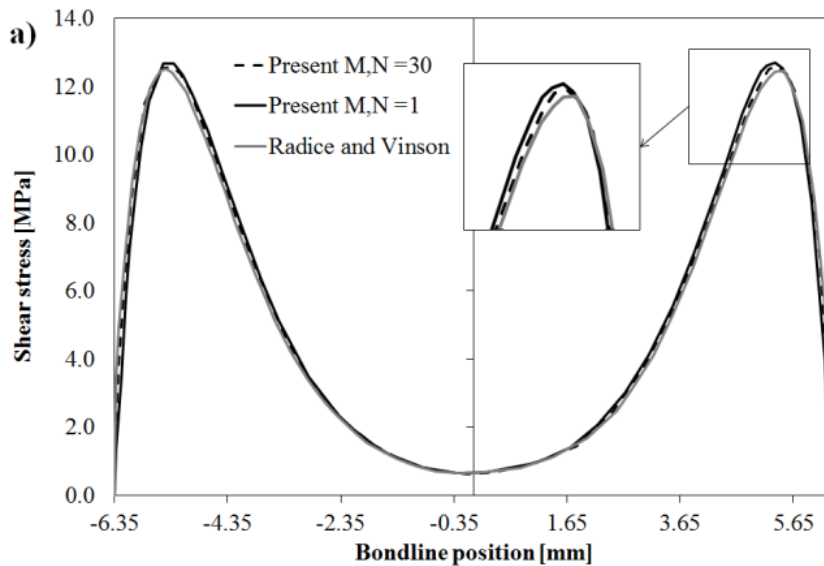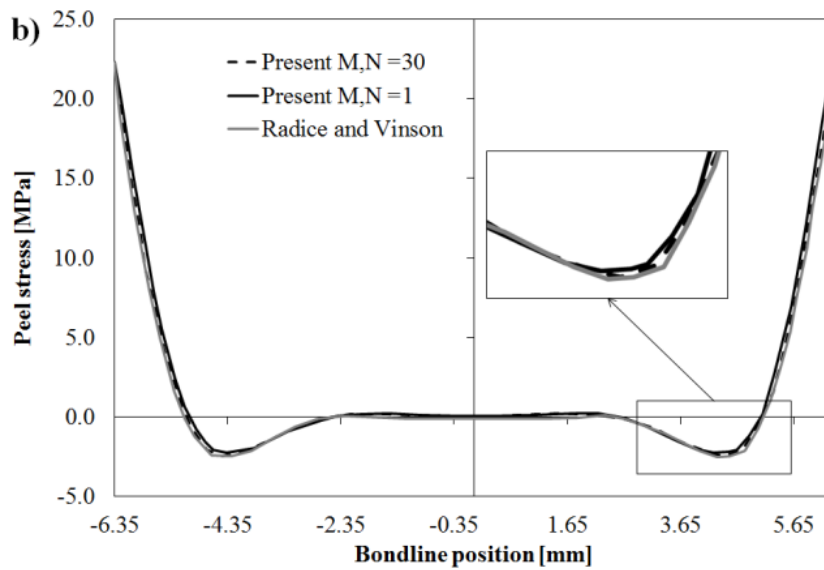
Figure 4.4 Single-lap joint with aluminium adherends. Span-wise distribution of: a) shear stress and b) peel stress at the mid-plane of the adhesive layer by Radice and Vinson's elasticity model [184] and by the present model using different shape functions.

Case B. As next case, the single-lap joint with CFRP adherends analysed by Vaidya et al. [**203**] and retaken by Khalili et al. [**189**] is considered. The mechanical properties of the adherends are: $E_1= E_2= 50$ GPa, $E_3= 7.2$ GPa, $G_{12}= 5$ GPa, $G_{13}= G_{23}=3$ GPa, $\upsilon_{12}=0.3$, $\upsilon_{13}= \upsilon_{23}=0.25$. Those of the adhesive are: $E= 2.8$ GPa, $\upsilon=0.35$. The adherends are 87.5 mm long and 3 mm thick, the adhesive thickness is 0.33 mm, while the overlap length is 25.4 mm. The lower adherend is restrained against translation but free to rotate, while the other one is simply-supported at the edge, where a uniformly distributed traction load with intensity 7500 N is applied. Figures 4.5a and 4.5b show the span-wise distributions of transverse shear stress and peel stress, as predicted by the present model and in [**203**]. Similarly to what done in the previous case, the variation of solutions in the transverse direction *y* is still neglected. Please note that the curves named BC1 are computed imposing the stress-free boundary condition at the edges of the adhesive, those referred as BC2 are instead achieved imposing the same value of the shear as Vaidya et al. [**203**] at the edge of the adhesive. This solution, even if it does not respect the condition of Eq. (4.1) is considered in order to show again that the AD-ZZ model, thanks to its variable representation, can fulfil different boundary condition, as already shown in 3.1.5. In both cases, the trial functions for the adherends are those of Eq. (4.11) while in the overlap the trial functions are those of Eq. (4.10). As far as the through-the thickness representation is concerned, in both cases a third-order representation of the in-plane

displacement and a fourth-order one for the transverse displacement is adopted. Differently to Case A, two computational layers are considered across the thickness of the adherends in order to accurately represent their stress variation. Nevertheless more computational layers are considered than in the former case, the processing time is still comparable, since just 1.7 s are required to solve the problem. Also in this case the representation with a single component gives quite accurate result with the lowest computational effort.
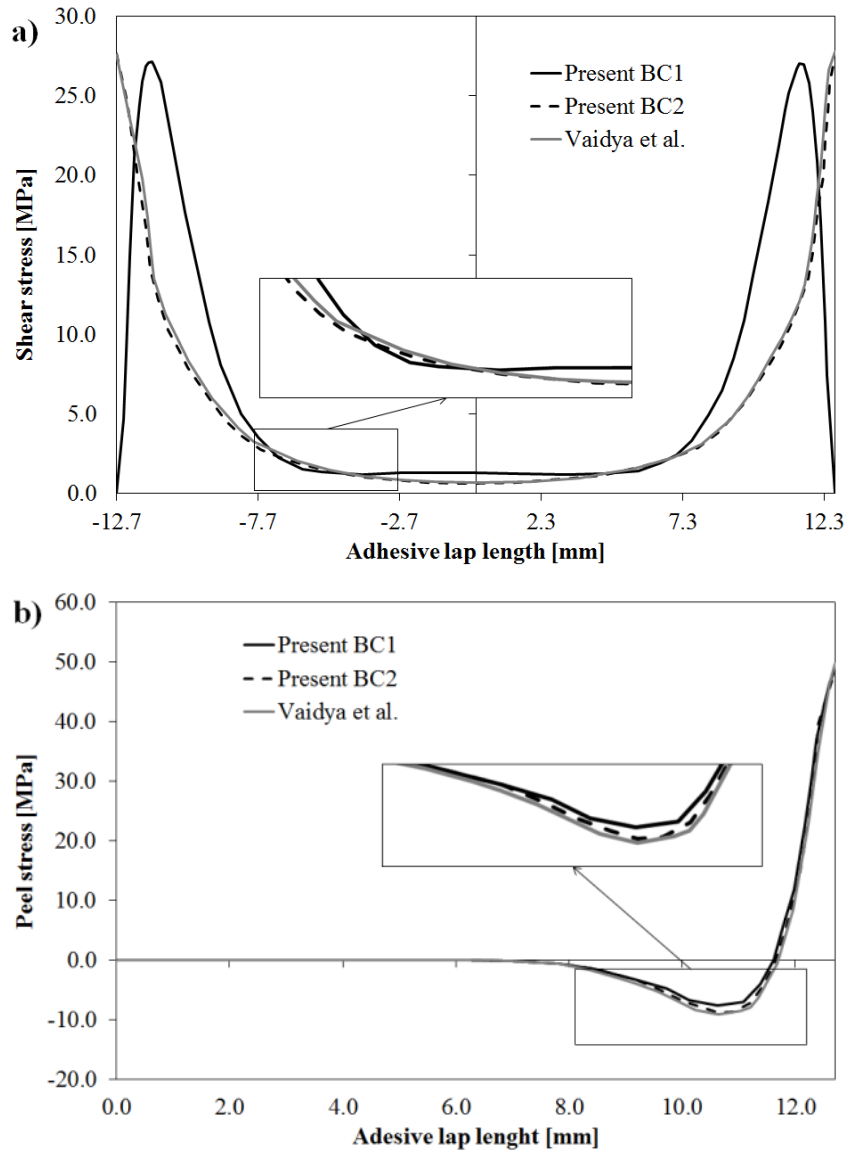
Figure 4.5 Single-lap joint with CFRP adherends. Span-wise distribution of: a) shear stress and b) peel stress by Vaidya et al. [203] (FEA) and by the present model enforcing or not the free-edge stress boundary conditions.

Case C. It is now considered the case analysed by Diaz Diaz et al. [**183**] of a double-lap joint with adherends made of different materials. The outer adherends are assumed to be made of

steel (E= 210 GPa, υ=0.3), while the inner adherend is assumed to be orthotropic (E_1= 120 GPa, E_3= 10 GPa, G_{13}= 5 GPa, υ_{13}= 0.3). The adhesive is an epoxy resin (E= 4 GPa, υ=0.3). The thickness of the adherends is 3 mm, while that of the adhesive is 0.5 mm. The overlap length is 40 mm. The joint is undergoing a traction load of 5000 N. A comparison is presented with the results by the structural model of Ref. [183] and by a finite element model therein considered for comparisons. The analysis with the present model is carried out considering a second order expansion of the in-plane displacement and a third order expansion of the transverse displacement across the thickness of the outer adherends and of the adhesive. Instead, a third order expansion of the in-plane displacement and a fourth order expansion of the transverse displacement across the thickness are adopted within the inner orthotropic adherend. As no information about the total length of the adherends and about their boundary conditions can be gathered from Diaz Diaz et al. [183], only the overlap section is simulated by the present model. Figures 4.6 shows the span-wise distribution of transverse shear and transverse normal stresses between lower outer adherend and adhesive and between inner adherend and adhesive, as predicted by the present model using the single component representation of Eq. (4.10), i.e. M,N=1, and the series expansion of Eq. (4.11) with M,N=30. As it takes only 1.3 s, obviously the first approach is dramatically faster, since 65 s are required to perform the analysis with 30 components. The comparison with the reference results shows that the fastest approach is also quite accurate and thus efficient, considering that the use of many components in the series does not produce a consistent accuracy improvement, while it considerably increases the processing time and the memory occupation.
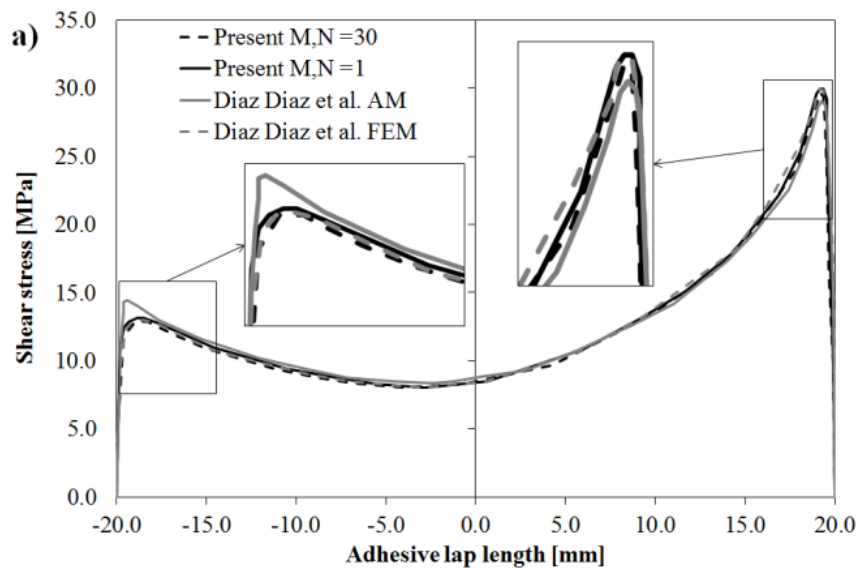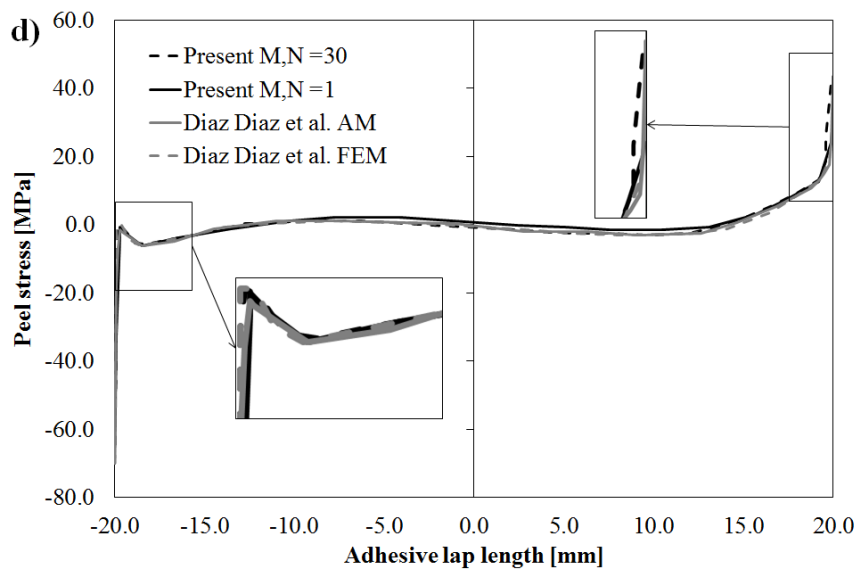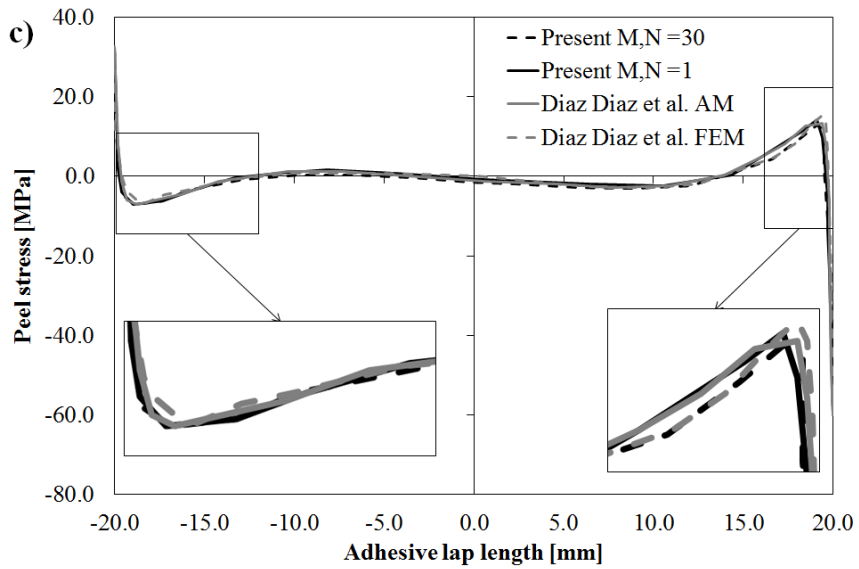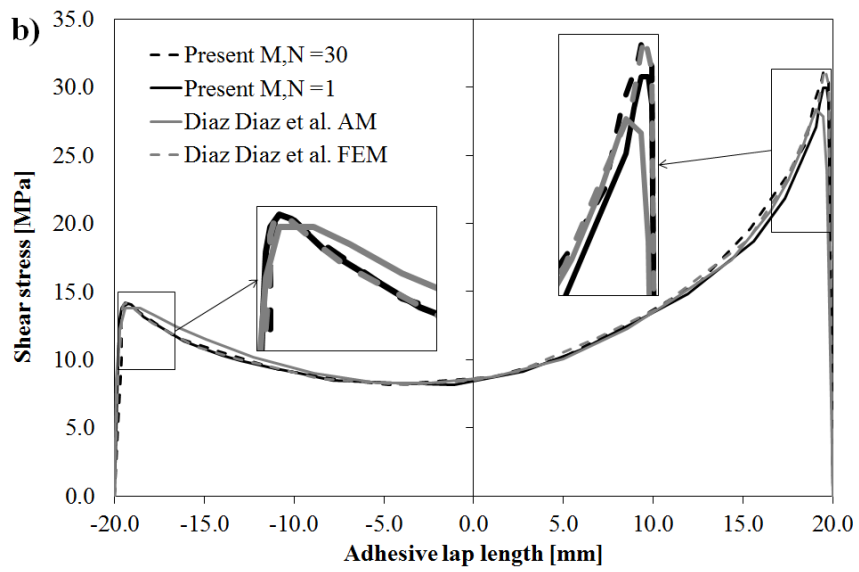
Figure 4.6 Double-lap joint with heterogeneous adherends. Span-wise distribution of shear stress between a) lower adherend and adhesive and b) inner adherend and adhesive and of peel stress between c) lower adherend and adhesive and d) inner adherend and adhesive by Diaz-Diaz et al. [183] (analytical and FEA) and by the present model using different trial functions.

Case D. In order to verify whether the method employed to model non-linearity provides accurate results, it is now considered the single-lap joint studied by Andruet et al. [**188**]. The joint has aluminium adherends (E= 68.3 GPa, υ=0.3) and epoxy resin adhesive (E= 2.5 GPa, υ=0.3); it is clamped at left edge and simply supported at the right one, where an average tensile stress with intensity 200 MPa is applied. The thickness of the adherends is 1.6 mm, that of the adhesive is 0.1 mm. The overlap length is 20 mm, while the adherends are 60 mm long.

Figure 4.7 shows the results obtained by the present variable kinematics model either imposing the boundary constraints prescribed by the theory of elasticity, which are named as BC1, or imposing the same value of the shear stress computed by Andruet et al. [**188**] at the free edge of the adhesive, here named as BC2.

In both cases, a third order piecewise variation of the in-plane displacement and a fourth order variation of the transverse displacement is chosen, using as trial functions those of Eq. (4.10). Irrespectively of the constraints imposed, the computational time is 1.5 s. As far as the in-plane representations of displacements in the adherends are concerned, the same trial functions already adopted for Case A are employed.

The results show that also in this case the present model provides predictions in very good agreement with the reference ones. This confirms the correct implementation and the effectiveness of the updated Lagrangian approach in taking into account the effects of geometric nonlinearity, as already pointed out in the literature.
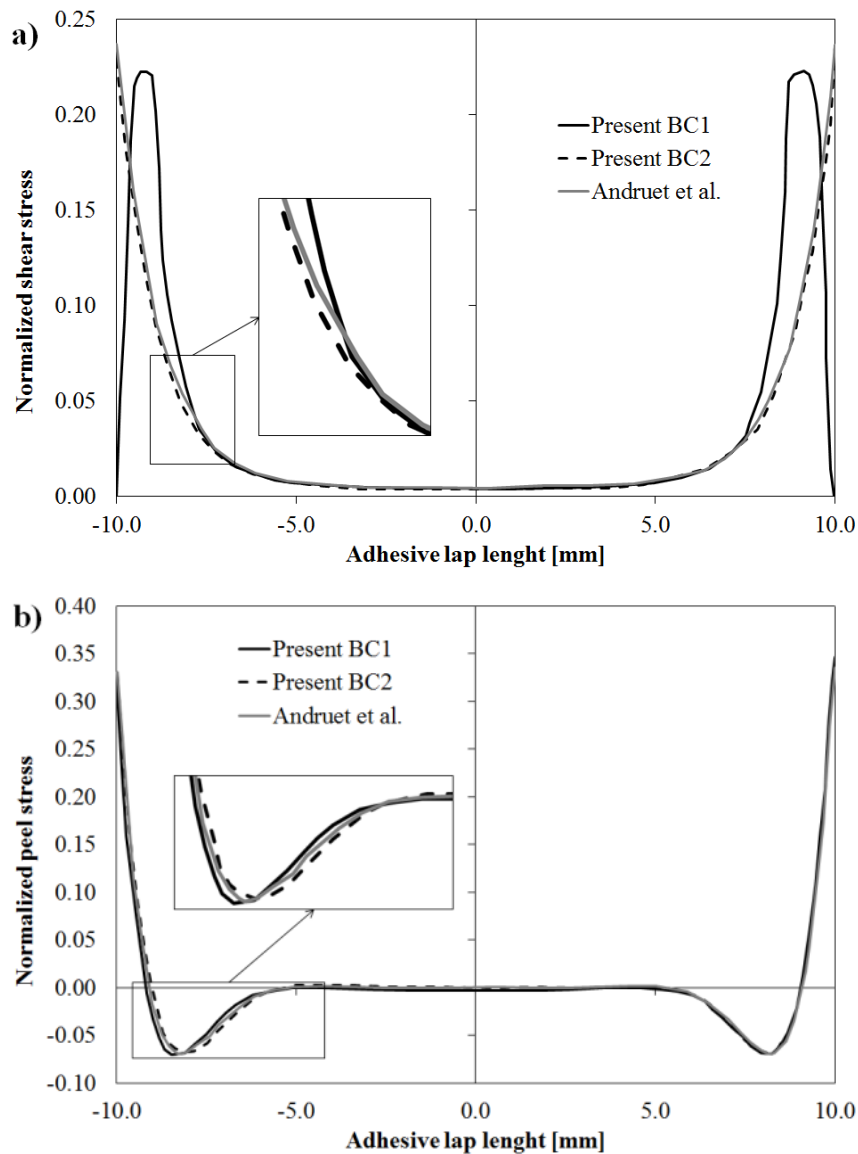
Figure 4.7 Non-linear analysis of single-lap joint. Span-wise distribution of: a) shear stress and b) peel stress by Andruet et al. [188] (FEA) and by the present model enforcing or not the free-edge stress boundary conditions.

Case E. In order to compare the numerical results of the present model to those obtained through experimental tests, the failure loads of titanium/composite double lap joints presented by da Silva and Adams [209] are considered. The adherends are made of titanium (Ti-6Al-4V) and of a 0°/90° laminate obtained by staking two plies of carbon fabric HTM552, impregnated with a BMI resin composite. According to [209], different adhesives are considered, namely Supreme 10HT or AV119. Table 4.1 reports the comparisons between experimental and numerical results obtained assuming for the d.o.f. the in-plane representation reported in Eq. (4.11) considering M= N= 35. For what concerns the

representation across the thickness, a third order piecewise variation of the in-plane displacement and a fourth order variation of the transverse displacement are chosen. The failure loads reported in Table 4.1 are computed considering the stress-based failure criteria of Refs. [**210**] and [**211**]. The good agreement shown with respect to the results of experiments [**209**] confirms that the present model accurately predicts the stresses and, besides, that stress-based criteria like [**210**] and [**211**] can be successfully used for determining the strength of bonded joints.

		Composite inner adherend	Composite outer adherend
Supreme 10HT	Ref. [**209**]	24.40	38.54 (± 1.21)
	Present (FC [**210**])	26.20	40.50
	Present (FC [**211**])	26.35	40.30
AV119	Ref. [**209**]	21.89 (± 1.11)	37.33 (± 3.93)
	Present (FC [**210**])	23.48	39.19
	Present (FC [**211**])	23.15	39.51

Table 4.1 Comparison between failure loads [kN] predicted by the present model and those experimentally measured in Ref. [209] for titanium/composites double lap joints. (FC= Failure Criterion).

Applications to linear and nonlinear benchmark test cases of joints taken from the literature presented in this section have shown that the AD-ZZ model can accurately and efficiently treat bonded joints with laminated adherends. In fact, for all the examined cases, accurate results were obtained in few seconds carrying out the analyses on a laptop computer.

Chapter 5: Variable stiffness composites and stitching

In this chapter two techniques for improving the energy absorption properties of laminated and sandwich composites are presented: variable stiffness composites and the use of textile composites. Their application is aimed at improving the structural performances of composite structures.

Indeed, the former tool acts directly on the energy contributions that rule the deformation of the structure. An energy tuning takes place, because variable stiffness composites enable to minimize the energy absorbed through unwanted modes (i.e., the ones involving interlaminar strengths and causing delamination) and maximize that absorbed through desired modes (i.e., the ones involving membrane strengths).

The appropriate in-plane distribution of plate stiffness coefficients is obtained making the strain energy contributions of interest extremal under in-plane variation of the plate stiffness properties, and enforcing proper conditions. These constraints range from the imposition of the thermodynamic constraints, to the choice of a convex or a concave shape for the stiffness coefficients (in order to minimize or maximize the energy contributions of interest), to the imposition of a mean value for these coefficients. In order to obtain these stiffness variations, in-plane fibre orientations are varied.

Therefore, the new approach VSC, based on a variable spatial distribution of stiffness properties, can limit the detrimental effects of damage and can improve the structural performances of fibre reinforced and sandwich composites by tuning their energy absorption properties. With this approach, contrasting objectives can be conjugated, like the improvement of stiffness and, contemporaneously, of delamination strength.

In this chapter, the present technique is applied to laminates or to the face sheets of sandwich composites.

For what concerns textile composites, as explained forward, the most interesting application is stitching or tufting of sandwiches, which implies the insertion of through-the-thickness reinforcements in the structure. Stitching basically involves sewing high-tensile strength yarn (e.g. glass, carbon or Kevlar), through an uncured prepreg laminate or dry fabric plies using an industrial sewing machine. Stitching of prepreg laminates is more difficult, because the tackiness of the uncured resin makes sewing difficult and some of the in-plane fibres may be broken and/or distorted. This damage can adversely affect the mechanical properties of stitched laminates. Because of this problem, stitching is mostly used with dry fabric preforms. The tufting process consists of the insertion of a threaded needle into dry fabrics or sandwich preforms, and its removal from the piece along the same trajectory. The thread remains in the place by the friction between fibre and core, creating a 3D structure.

In both cases, these reinforcements considerably enhance transverse normal strength and stiffness of sandwiches, thus reducing interlaminar stresses at critical interfaces and damage in sandwiches undergoing impact loading.

In order to get an evaluation of the effects due to transverse reinforcement on the mechanical properties of stitched sandwiches, virtual material tests using 3D finite element are performed. Then, the homogenized mechanical coefficients evaluated in this way are provided to the AD-ZZ model, which evaluates the stress and displacement fields of the structures.

Since the numerical results show that the interlaminar stresses can be consistently reduced using these techniques, keeping a high stiffness, future applications are expected, where the local effects are accounted for in a much more detailed way. In subsequent sections the features of these techniques will be briefly summarized, their implementation process discussed in detail, and the numerical applications presented.

However, first of all, the analysis of the state-of-the-art is premised in order to explore in which way the same problem has been solved in literature.

5.1 State of the art

Various techniques have been recently published in literature with the aim of preventing the damage accumulation typical of composite structures and obtaining improved structural performances.

Many authors chose to apply the Functionally Graded Materials as a promising technique for avoiding unwise stress concentrations at interfacial material discontinuities that conventional fibre reinforced and sandwich composites usually exhibit, by virtue of the gradual variation of their physical properties. Among many other authors, here the contribution of Fuchiyama and Noda [212] is reminded. It seems from the results published in [212] that the design of FGM introduces technological difficulties and their theoretical performances can differ a lot from the practical ones, observed in experimental tests.

As an alternative, an improvement in the impact and delamination resistance and in dissipation can be achieved by stacking layers with different absorption and dissipation properties, namely, plies with customary properties and viscoelastic layers, as proposed by Suzuky et al. [213]. However, since the viscoelastic layers must be as thick and numerous as the structural layers in order to achieve good performances, this method unfortunately makes the structures too flexible and it is not effective for sandwich composites, because the number of damping layers to be incorporated is lower than in laminated composites. Moreover, the stresses in the adhesive film which bonds the viscoelastic layers to the host structure could limit the strength and the service life.

Several studies dealing with methods, which seek to simultaneously improve stiffness, energy absorption and dissipation, have been recently published. Jung and Aref [214] seeks to conjugate stiffness with energy dissipation by combining different materials with different absorption and stiffness properties. Lakes [215] shows that the structural hierarchy makes possible to obtain both the desired stiffness and the damping properties.

Furthermore, McCoucheon et al. [216] shows that the energy dissipation can be increased without remarkable stiffness loss by inserting fluid filled micro-tubes into a matrix material, where the fluid flow is induced by the composite deformation. However, all these solutions introduce quite strong technological complications.

Recently, variable stiffness composites in which the orientation of the fibres minimizes the stresses have been studied, for example, by Pedersen [217] and Setoodeh et al. [218]. Moreover, other research studies by Zinoviev and Ermakov [219] and Georgi [220] investigated the effects of the fibres' orientation (constant over the plate) for finding configurations able to dissipate a large amount of the incoming energy, while keeping the wanted strength and stiffness properties unchanged.

Other authors suggested the use of advanced technological skills such as stitching, lap and T joints, or short rods in order to improve the transverse shear strength of multilayered materials and limit the detrimental effects of local damage and delamination propagation. These tools oppose cracks and sliding displacements by inducing bridging tractions, as shown by Cox [221]. As far as laminates are concerned, stitching is largely employed. Gui and Li [222] demonstrated that this technique can improve the buckling behaviour, while Mouritz [223] showed that the fracture toughness of stitched laminates is much higher than the equivalent unstitched ones. Shah Khan and Mouritz [224] reported that the translaminar strength of fibre reinforced polymer (FRP) composites can be improved considerably with a thread of carbon, glass or Kevlar.

Many approaches have been suggested for sandwiches: stitching of faces and stitching through-the-thickness (Potluri et al. [6]), integrated pile core (Judawisastra et al. [7]) and vertical composite columns, 3D pins or shear keys implanted in the core (Wang et al. [8], Vaidya et al. [9] and Nilanjan [10]) and folded core (Heimbs et al. [225]). These techniques have been proven successful in improving the performance of sandwiches under impact loading (Potluri et al. [6], Vaidya et al. [9] and Heimbs et al. [225]), the fatigue behaviour (Judawisastra et al. [7]) and the shear properties (Nilanjan [10] and Wang et al. [226]). However the Advanced Composites Technology (ACT) program proposed by NASA [227] demonstrated that stitching through-the-thickness is the most effective technical skill in reducing costs and improving damage tolerance of aircraft structures. Another available technique, which inserts reinforcement in the through-the-thickness direction, is tufting [228], whose characteristics have been discussed above.

Summarizing, among many solutions explored in literature, here the author has chosen to exploit i)the great tailoring capability, offered by fibre-reinforced composites, and the effects of varying the fibre orientation over the space and ii) the great improvement on transverse normal strength and stiffness brought by the insertion of through-the-thickness reinforcement by stiching or tufting.

5.2 Variable stiffness composites

The process has the aim of finding a proper distribution of the stiffness properties that minimises the energy absorbed through unwanted modes (e.g., modes involving interlaminar strengths) and maximises that absorbed by desired modes (e.g., modes involving membrane strengths). This distribution is determined by solving the Euler-Lagrange equations, obtained by making extremal the in-plane, bending and out-of-plane shear contributions to strain energy under spatial variation of the stiffness properties. Once the expressions of the optimal stiffness have been obtained, the in-plane variation of the fibre orientation can be computed by inverting the stress-strain relations for each lamina of arbitrary orientation.

In this way the amount of the energy stored by specific modes can be minimised, or maximised, as desired, so this technique works as an energy "*tuning*".

In order to find the stationary condition for the strain energy contributions, the first step requires writing the strain energy of the AD-ZZ model.

The procedure starts by imposing zero its first variation under variation of the functional d.o.f.; note that this constraint associated with the variation of the external work represents the equilibrium condition.

Enforcing the vanishing of the first variation of the strain energy, with the stiffness properties as primary variables, a set of governing equations is obtained, the so called Euler–Lagrange equations that represent the relations enabling the stiffness properties to make the strain energy contributions extremal. The closed form or the numerical solution of these equations gives the variable distribution of the stiffness properties.

The strain energy due to bending is the contribution by the terms that multiply w^0, while the terms that multiply γ_x^0, γ_y^0 represent the strain energy due to transverse shears. The process has the objective of finding stiffness distributions that simultaneously solve these equations. In this procedure, the in-plane contributions multiplying u^0 and v^0 are disregarded since laminated and sandwich composites have a larger strength and stiffness in the in-plane direction than in the thickness one. However, in-plane stresses should be assessed, as their excessive relaxation may cause the failure.

Generally speaking, the stationary condition for the bending energy is obtained integrating by parts the virtual variation of the strain energy under variation of the functional d.o.f. and collecting the contributions that multiply each displacement d.o.f.:

$$[MR] \begin{Bmatrix} \delta u^0 \\ \delta v^0 \\ \delta w^0 \\ \delta \gamma_x^0 \\ \delta \gamma_y^0 \end{Bmatrix} = 0 \tag{5.1}$$

Where [MR]:

$$\begin{bmatrix} \left[MR^x \right] & 0 & 0 & 0 & 0 \\ 0 & \left[MR^y \right] & 0 & 0 & 0 \\ 0 & 0 & \left[MR^z \right] & 0 & 0 \\ 0 & 0 & 0 & \left[MR^{\gamma_x} \right] & 0 \\ 0 & 0 & 0 & 0 & \left[MR^{\gamma_y} \right] \end{bmatrix} \tag{5.2}$$

Notice that the [MR^i] matrices have different dimensions, and, their expressions are as follows:

$$MR^x = -WR1$$
$$MR^y = -WR2$$
$$MR^z = -WR3 \tag{5.3}$$
$$MR^{\gamma_x} = WR4 - \frac{4}{3}WR5 + WR6 + WR7$$
$$MR^{\gamma_y} = WR8 - \frac{4}{3}WR9 + WR10 + WR11$$

Where WR are:

$$WR1 = B_{11,111} + B_{12,122} + 3B_{16,112} + B_{26,222} + 2B_{66,122}$$

$$WR2 = B_{12,112} + B_{16,111} + 3B_{26,112} + B_{22,222} + 2B_{66,112}$$

$$WR3 = D_{11,1111} + 2D_{12,1122} + 4D_{16,1112} + 4D_{26,1222} + 4D_{66,1122} + D_{22,2222}$$

$$WR4 = D_{11,111} + D_{12,122} + 3D_{16,112} + D_{26,222} + 6D_{66,122}$$

$$WR5 = \left(\frac{F_{11}}{h^2}\right)_{,111} + \left(\frac{F_{12}}{h^2}\right)_{,122} + 3\left(\frac{F_{16}}{h^2}\right)_{,112} + \left(\frac{F_{26}}{h^2}\right)_{,222} + 2\left(\frac{F_{66}}{h^2}\right)_{,221}$$

$$WR6 = D^a_{11,111} + D^a_{12,122} + 3D^a_{16,112} + D^a_{26,222} + 2D^a_{66,122}$$

$$WR7 = D^a_{12,112} + D^a_{22,222} + 3D^a_{26,122} + D^a_{16,111} + 2D^a_{66,112}$$

$$WR8 = D_{16,111} + D_{12,122} + 3D_{26,122} + D_{22,222} + 6D_{66,112}$$

$$WR9 = \left(\frac{F_{16}}{h^2}\right)_{,111} + \left(\frac{F_{22}}{h^2}\right)_{,222} + 3\left(\frac{F_{26}}{h^2}\right)_{,122} + \left(\frac{F_{12}}{h^2}\right)_{,112} + 2\left(\frac{F_{66}}{h^2}\right)_{,112}$$

$$WR10 = D^b_{16,111} + D^b_{12,112} + 3D^b_{26,122} + D^b_{22,222} + 2D^b_{66,112}$$

(5.4)

In (5.4), B_{ij} are the membrane – bending coupling stiffness coefficients of the AD-ZZ model, D_{ij} are the bending stiffness coefficients of the AD-ZZ model and F_{ij} are the higher-order stiffness coefficients of the AD-ZZ model (see the Appendix for their definition).

The stationary condition for the transverse shear energy in the plane (x, z) is obtained again integrating by parts the virtual variation of the strain energy under variation of the functional d.o.f. and collecting the contributions that multiply each displacement d.o.f. :

$$[SR]\begin{Bmatrix} \delta u^0 \\ \delta v^0 \\ \delta w^0 \\ \delta \gamma_x^0 \\ \delta \gamma_y^0 \end{Bmatrix} = 0$$

(5.5)

Where [SR]:

$$\begin{bmatrix} \left[SR^x\right] & 0 & 0 & 0 & 0 \\ 0 & \left[SR^y\right] & 0 & 0 & 0 \\ 0 & 0 & \left[SR^z\right] & 0 & 0 \\ 0 & 0 & 0 & \left[SR^{\gamma_x}\right] & 0 \\ 0 & 0 & 0 & 0 & \left[SR^{\gamma_y}\right] \end{bmatrix}$$

(5.6)

Once again, the matrices [SR^i] have different dimensions and, their expressions are as follows:

$$SR^x = XR_{R1} + XR_{R1}^a + XR_{R1}^d + XR_{R44} + XR_{R44}^a + XR_{S44}^d - \frac{4}{3h^2}\left(XR_{P1} - XR_{P6}\right) +$$

$$-\frac{1}{2h}\left(XR_{26X2} + XR_{31X2} + XR_{36X2} + XR_{41X2}\right) - \frac{2}{3h^2}\left(XR_{26X3} + XR_{31X3} + XR_{36X3} + XR_{41X3}\right)$$

$$SR^y = XR_{R2} + XR_{R2}^a + XR_{R2}^d + XR_{R55} + XR_{R55}^a + XR_{S55}^d - \frac{4}{3h^2}\left(XR_{P2} - XR_{P7}\right) +$$

$$-\frac{1}{2h}\left(XR_{27X2} + XR_{32X2} + XR_{37X2} + XR_{42X2}\right) - \frac{2}{3h^2}\left(XR_{27X3} + XR_{32X3} + XR_{37X3} + XR_{42X3}\right)$$

$$SR^z = XR_{R3} + XR_{R3}^a + XR_{R3}^d + XR_{R66} + XR_{R66}^a + XR_{S66}^d - \frac{4}{3h^2}\left(XR_{P3} - XR_{P8}\right) +$$

$$-\frac{1}{2h}\left(XR_{28X2} + XR_{33X2} + XR_{38X2} + XR_{43X2}\right) - \frac{2}{3h^2}\left(XR_{28X3} + XR_{33X3} + XR_{38X3} + XR_{43X3}\right)$$

$$SR^{\gamma_x} = 0$$

(5.7)

$$SR^{\gamma_y} = XR_{R4} + XR_{R4}^a + XR_{R4}^d + XR_{R88} + XR_{R88}^a + XR_{S88}^d - XR_{T88} - XR_{T88}^a - XR_{T88}^d +$$

$$-\frac{4}{3h^2}\left(XR_{P4} - XR_{P9}\right) + \frac{4}{h^2}XR_{RR1} - \frac{1}{2h}\left(XR_{29X2} + XR_{34X2} + XR_{39X2} + XR_{44X2}\right) +$$

$$-\frac{2}{3h^2}\left(XR_{29X3} - XR_{34X3} + XR_{30X3} + XR_{35X3} + XR_{40X3} + XR_{45X3}\right) + \frac{1}{h}\left(XR_{47X1} + XR_{49X1}\right) +$$

$$+\frac{2}{h^2}\left(XR_{47X2} + XR_{49X2}\right)$$

Where XR are:

$$XR_{R1} = B_{11,11} + B_{16,12}$$
$$XR_{R2} = B_{16,11} + B_{12,12}$$
$$XR_{R3} = D_{11,111} + 2D_{16,112} + D_{12,122}$$
$$XR_{R4} = R_{1X,11} + R_{2X,12}$$
$$XR_{R5} = R_{3X,11} + R_{4X,12}$$

(5.8a)

$$R_{1X} = D_{11} + D_{11}^a + D_{16}^d - \frac{4}{3}\frac{F_{11}}{h^2}$$

$$R_{2X} = D_{16} + D_{16}^a + D_{12}^d - \frac{4}{3}\frac{F_{16}}{h^2}$$

$$R_{3X} = D_{16} + D_{16}^b + D_{11}^c - \frac{4}{3}\frac{F_{16}}{h^2}$$

(5.8b)

$$R_{4X} = D_{12} + D_{12}^b + D_{16}^c - \frac{4}{3}\frac{F_{12}}{h^2}$$

$$XR_{R1}^a = B_{11,11}^a + B_{16,12}^a$$

$$XR_{R2}^a = B_{16,11}^a + B_{12,12}^a$$

$$XR_{R3}^a = D_{11,111}^a + 2D_{16,112}^a + D_{12,122}^a$$

(5.8c)

$$XR_{R4}^a = R_{1X,11}^a + R_{2X,12}^a$$

$$XR_{R5}^a = R_{3X,11}^a + R_{4X,12}^a$$

$$R_{1X}^a = D_{11}^a + D_{11}^{aa} + D_{16}^{ad} - \frac{4}{3}\frac{F_{11}^a}{h^2}$$

$$R_{2X}^a = D_{16}^a + D_{16}^{aa} + D_{12}^{ad} - \frac{4}{3}\frac{F_{16}^a}{h^2}$$

(5.8d)

$$R_{3X}^a = D_{16}^a + D_{16}^{ab} + D_{11}^{ac} - \frac{4}{3}\frac{F_{16}^a}{h^2}$$

$$R_{4X}^a = D_{12}^a + D_{12}^{ab} + D_{16}^{ac} - \frac{4}{3}\frac{F_{12}^a}{h^2}$$

$$XR_{R1}^d = B_{16,11}^d + B_{66,12}^d$$

$$XR_{R2}^d = B_{66,11}^d + B_{26,12}^d$$

$$XR_{R3}^d = D_{16,111}^d + 2D_{66,112}^d + D_{12,122}^d$$

(5.8e)

$$XR_{R4}^d = R_{1X,11}^d + R_{2X,12}^d$$

$$XR_{R5}^d = R_{3X,11}^d + R_{4X,12}^d$$

$$R_{1X}^d = D_{16}^d + D_{16}^{ad} + D_{66}^{dd} - \frac{4}{3}\frac{F_{11}^d}{h^2}$$

$$R_{2X}^d = D_{66}^d + D_{66}^{dd} + D_{26}^{dd} - \frac{4}{3}\frac{F_{66}^d}{h^2}$$

(5.8f)

$$R_{3X}^d = D_{66}^d + D_{66}^{bd} + D_{16}^{cd} - \frac{4}{3}\frac{F_{16}^d}{h^2}$$

$$R_{4X}^d = D_{26}^d + D_{26}^{bd} + D_{66}^{cd} - \frac{4}{3}\frac{F_{26}^d}{h^2}$$

$$XR_{R44} = B_{16,12} + B_{66,22}$$
$$XR_{R55} = B_{66,11} + B_{26,22}$$
$$XR_{R66} = D_{16,112} + 2D_{66,122} + D_{26,222} \tag{5.8g}$$
$$XR_{R88} = R_{9X,12} + R_{10X,212}$$
$$XR_{R99} = R_{11X,12} + R_{12X,22}$$

$$R_{9X} = D_{16} + D_{16}^a + D_{66}^d - \frac{4}{3}\frac{F_{16}}{h^2}$$

$$R_{10X} = D_{66} + D_{26}^a + D_{26}^d - \frac{4}{3}\frac{F_{66}}{h^2}$$
$$\tag{5.8h}$$

$$R_{11X} = D_{66} + D_{66}^b + D_{16}^c - \frac{4}{3}\frac{F_{66}}{h^2}$$

$$R_{12X} = D_{26} + D_{26}^b + D_{66}^c - \frac{4}{3}\frac{F_{26}}{h^2}$$

$$XR_{R44}^a = B_{16,12}^a + B_{66,22}^a$$
$$XR_{R55}^a = B_{66,12}^a + B_{26,22}^a$$
$$XR_{R66}^a = D_{16,112}^a + 2D_{66,122}^a + D_{26,222}^a \tag{5.8i}$$
$$XR_{R88}^a = R_{9X,12}^a + R_{10X,22}^a$$
$$XR_{R99}^a = R_{11X,12}^a + R_{12X,22}^a$$

$$R_{9X}^a = D_{16}^a + D_{16}^{aa} + D_{66}^{ad} - \frac{4}{3}\frac{F_{16}^a}{h^2}$$

$$R_{10X}^a = D_{66}^a + D_{26}^{aa} + D_{26}^{ad} - \frac{4}{3}\frac{F_{66}^a}{h^2}$$
$$\tag{5.8j}$$

$$R_{11X}^a = D_{66}^a + D_{66}^{ab} + D_{16}^{ac} - \frac{4}{3}\frac{F_{66}^a}{h^2}$$

$$R_{12X}^a = D_{26}^a + D_{26}^{ab} + D_{66}^{ac} - \frac{4}{3}\frac{F_{26}^a}{h^2}$$

$$XR_{T88} = A_{44} - 4\frac{D_{44}}{h^2} + A_{44}^a + A_{45}^d$$

$$XR_{T99} = A_{45} - 4\frac{D_{45}}{h^2} + A_{44}^c + A_{45}^b$$

$$XR_{T88}^a = A_{44}^a - 4\frac{D_{44}^a}{h^2} + A_{44}^{aa} + A_{45}^{ad}$$

$$XR_{T99}^a = A_{45}^a - 4\frac{D_{45}^a}{h^2} + A_{44}^{ac} + A_{45}^{ab}$$

(5.8k)

$$XR_{T88}^d = A_{44}^d - 4\frac{D_{44}^d}{h^2} + A_{44}^{ad} + A_{45}^{dd}$$

$$XR_{T99}^d = A_{45}^d - 4\frac{D_{45}^d}{h^2} + A_{44}^{cd} + A_{45}^{bd}$$

$$XR_{P1} = E_{11,11} + E_{16,12}$$

$$XR_{P2} = E_{16,11} + E_{12,12}$$

$$XR_{P3} = F_{11,111} + 2F_{16,112} + F_{12,122}$$ (5.8l)

$$XR_{P4} = R_{18X,11} + R_{19X,12}$$

$$XR_{P5} = R_{20X,11} + R_{21X,12}$$

$$R_{18X} = F_{11} + F_{11}^a + F_{16}^d - \frac{4}{3}\frac{H_{11}}{h^2}$$

$$R_{19X} = F_{16} + F_{16}^a + F_{12}^d - \frac{4}{3}\frac{H_{16}}{h^2}$$

(5.8m)

$$R_{20X} = F_{16} + F_{16}^b + F_{11}^c - \frac{4}{3}\frac{H_{16}}{h^2}$$

$$R_{21X} = F_{12} + F_{12}^b + F_{16}^c - \frac{4}{3}\frac{H_{12}}{h^2}$$

$$XR_{P6} = E_{16,12} + E_{66,22}$$

$$XR_{P7} = E_{66,12} + E_{26,22}$$

$$XR_{P8} = F_{16,112} + 2F_{66,122} + F_{26,222}$$ (5.8n)

$$XR_{P9} = R_{22X,12} + R_{23X,22}$$

$$XR_{P10} = R_{24X,12} + R_{25X,22}$$

$$R_{22X} = F_{16} + F_{16}^a + F_{66}^d - \frac{4}{3}\frac{H_{16}}{h^2}$$

$$R_{23X} = F_{66} + F_{66}^a + F_{26}^d - \frac{4}{3}\frac{H_{66}}{h^2}$$

$$R_{24X} = F_{66} + F_{66}^b + F_{16}^c - \frac{4}{3}\frac{H_{66}}{h^2}$$

(5.8o)

$$R_{25X} = F_{16} + F_{16}^b + F_{66}^c - \frac{4}{3}\frac{H_{26}}{h^2}$$

$$XR_{RR1X} = D_{44} + D_{44}^a + D_{44}^d - 4\frac{F_{44}}{h^2}$$

$$XR_{RR2X} = D_{45} + D_{45}^a + D_{45}^d - 4\frac{F_{45}}{h^2}$$

$$XR_{26X2} = D_{112,11}^a + D_{162,12}^a$$

$$XR_{27X2} = D_{162,11}^a + D_{122,12}^a$$

(5.8p)

$$XR_{28X2} = E_{112,111}^a + 2E_{162,112}^a + E_{122,122}^a$$

$$XR_{29X2} = R2_{R1X,11} + R2_{R2X,12}$$

$$XR_{30X2} = R2_{R3X,11} + R2_{R4X,12}$$

$$R2_{R1X} = 2D_{11}^{aa} + 2D_{16}^{ad} + 2E_{11}^a + 2E_{11}^{aa} + 2E_{16}^{ad} + 2F_{11}^a + 2F_{11}^{aa} + 2F_{16}^{ad}$$

$$R2_{R2X} = 2D_{16}^{aa} + 2D_{12}^{ad} + 2E_{16}^a + 2E_{16}^{aa} + 2E_{12}^{ad} + 2F_{16}^a + 2F_{16}^{aa} + 2F_{12}^{ad}$$

$$R2_{R3X} = 2D_{11}^{ac} + 2D_{16}^{ab} + 2E_{16}^{ab} + 2E_{16}^{ab} + 2E_{12}^{ac} + 2F_{16}^a + 2F_{11}^{ac} + 2F_{16}^{ab}$$

(5.8q)

$$R2_{R4X} = 2D_{12}^{ab} + 2D_{16}^{ac} + 2E_{12}^{ab} + 2E_{16}^{ac} + 2F_{12}^a + 2F_{16}^{ac}$$

$$XR_{31X2} = D_{112,12}^d + D_{262,22}^d$$

$$XR_{32X2} = D_{261,12}^d + D_{222,22}^d$$

$$XR_{33X2} = E_{122,112}^d + 2E_{262,122}^d + E_{222,222}^d$$

(5.8r)

$$XR_{34X2} = R2_{R5X,12} + R2_{R6X,22}$$

$$XR_{35X2} = R2_{R7X,12} + R2_{R8X,22}$$

$$R2_{R5X} = 2D_{12}^{ad} + 2D_{12}^{dd} + 2E_{12}^d + 2E_{12}^{ad} + 2E_{26}^{dd} + 2F_{12}^d + 2F_{12}^{ad} + 2F_{26}^{dd}$$

$$R2_{R6X} = 2D_{26}^{ad} + 2D_{26}^{dd} + 2E_{26}^d + 2E_{26}^{ad} + 2E_{22}^{dd} + 2F_{26}^d + 2F_{26}^{ad} + 2F_{22}^{dd}$$

$$R2_{R7X} = 2D_{12}^{cd} + 2D_{26}^{bd} + 2E_{26}^d + 2E_{26}^{bd} + 2E_{12}^{cd} + 2F_{26}^d + 2F_{12}^{cd} + 2F_{26}^{bd}$$

(5.8s)

$$R2_{R8X} = 2D_{22}^{bd} + 2D_{26}^{cd} + 2E_{22}^{bd} + 2E_{26}^{cd} + 2F_{22}^d + 2F_{26}^{cd}$$

$$XR_{37X2} = D^a_{66,12} + D^a_{262,22}$$

$$XR_{38X2} = E^a_{162,112} + 2E^a_{662,122} + E^a_{262,222}$$

$$XR_{39X2} = R2_{R10X,12} + R2_{R11X,22}$$

$$XR_{40X2} = R2_{R12X,12} + R2_{R13X,22}$$

(5.8t)

$$R2_{R10X} = 2D^{aa}_{16} + 2D^{ad}_{66} + 2E^a_{26} + 2E^{aa}_{16} + 2E^{ad}_{66} + 2F^a_{16} + 2F^{aa}_{16} + 2F^{ad}_{66}$$

$$R2_{R11X} = 2D^{ad}_{26} + 2D^{aa}_{66} + 2E^a_{66} + 2E^{ad}_{26} + 2E^{aa}_{66} + 2F^a_{66} + 2F^{ad}_{26} + 2F^{aa}_{66}$$

$$R2_{R12X} = 2D^{ac}_{16} + 2D^{ab}_{66} + 2E^a_{66} + 2E^{ac}_{16} + 2E^{ab}_{66} + 2F^a_{66} + 2F^{ac}_{16} + 2F^{ab}_{66}$$

$$R2_{R13X} = 2D^{ab}_{26} + 2D^{ac}_{66} + 2E^{ab}_{26} + 2E^{ac}_{66} + 2F^a_{26} + 2F^{ac}_{66}$$

(5.8u)

$$XR_{41X2} = D^d_{162,11} + D^d_{662,12}$$

$$XR_{42X2} = D^d_{662,11} + D^d_{262,12}$$

$$XR_{43X2} = E^a_{162,111} + 2E^d_{662,112} + E^d_{262,222}$$

$$XR_{44X2} = R2_{R14X,11} + R2_{R15X,12}$$

$$XR_{45X2} = R2_{R16X,11} + R2_{R17X,12}$$

(5.8v)

$$R2_{R14X} = 2D^{ad}_{16} + 2D^{dd}_{66} + 2E^d_{16} + 2E^{ad}_{16} + 2E^{dd}_{66} + 2F^d_{16} + 2F^{ad}_{16} + 2F^{dd}_{66}$$

$$R2_{R15X} = 2D^{dd}_{26} + 2D^{ad}_{66} + 2E^d_{66} + 2E^{dd}_{26} + 2E^{ad}_{66} + 2F^d_{66} + 2F^{dd}_{26} + 2F^{ad}_{66}$$

$$R2_{R16X} = 2D^{cd}_{16} + 2D^{bd}_{66} + 2E^d_{66} + 2E^{cd}_{16} + 2E^{bd}_{66} + 2F^d_{66} + 2F^{cd}_{16} + 2F^{bd}_{66}$$

$$R2_{R17X} = 2D^{bd}_{26} + 2D^{cd}_{66} + 2E^{bd}_{26} + 2E^{cd}_{66} + 2F^d_{26} + 2F^{cd}_{66}$$

(5.8w)

$$XR_{46X2} = 2B^a_{44} + 2B^{aa}_{44} + 2B^{ad}_{45} + 2D^{aa}_{44} + 2D^{ad}_{45} + 2E^a_{44} + 2F^{aa}_{44} + 2F^{ad}_{45}$$

$$XR_{47X2} = 2B^a_{45} + 2B^{ac}_{45} + 2B^{ad}_{45} + 2D^{ac}_{44} + 2D^{ab}_{45} + 2E^a_{45} + 2F^{ac}_{44} + 2F^{ab}_{45}$$

$$XR_{48X2} = 2B^d_{45} + 2B^{ad}_{45} + 2B^{dd}_{55} + 2D^{ad}_{45} + 2D^{dd}_{55} + 2E^d_{45} + 2F^{ad}_{45} + 2F^{dd}_{55}$$

$$XR_{49X2} = 2B^d_{55} + 2B^{cd}_{45} + 2B^{bd}_{55} + 2D^{cd}_{45} + 2D^{bd}_{55} + 2E^d_{55} + 2F^{cd}_{45} + 2F^{bd}_{55}$$

(5.8x)

In Eq. (5.8), B_{ij}, D_{ij} and F_{ij} are as explained above, while E_{ij} and H_{ij} are higher-order stiffness coefficients of the AD-ZZ model (see again the Appendix for their definitions). The quantities for the shear energy contribution in the plane (y, z) are not reported, since they are similar to those for the plane (x, z), substituting x with y.

As outlined by Eqs. (5.4) and (5.8), the terms MR_{ij} and SR_{ij} are spatial derivatives of the stiffness properties obtained after integrating by parts the derivatives of the displacement d.o.f. So Eqs. (5.1) and (5.5) represent partial differential equations.

As mentioned above, the procedure disregards the equations involving in-plane energy, since laminated and sandwich composites have weak out-of-plane properties and strong in-plane properties. Thus, considering Eqs. (5.1) and (5.5) just the lines that multiply δw^0, $\delta\gamma_x^0$ and $\delta\gamma_y^0$

require a simultaneous solution. In particular, since the extremal condition under variation of the stiffness properties yields irrespectively of the response, equations (5.1) and (5.5) can be split into a set of partial differential equations of the following form:

$$\sum MR_{3j} = 0; \sum MR_{4j} = 0; \sum MR_{5j} = 0 \tag{5.9}$$

$$\sum SR_{3j} = 0; \sum SR_{4j} = 0; \sum SR_{5j} = 0 \tag{5.10}$$

The distribution of the spatial stiffness properties that make extremal the bending and transverse shear energy contributions is obtained by the simultaneous solution of Eqs. (5.9) and (5.10). In particular, considering the coefficients defined in Eqs. (5.4) and (5.8) these equations determine a set of partial differential equations up to the fourth order in (x, y). This set of equations has to be solved simultaneously, and the solutions of the problem for the face plies are represented by exponential functions for elastic coefficients with indices 11, 12, 13, 16, 22, 23, 26, 36, 66 and constant for elastic coefficients with indices 44, 45, 55, since just first order derivatives of the stiffness properties with these indices are involved in Eqs. (5.4) and (5.8). This is physically consistent since the orientation of the fibres over the plane (x, y) does not affect the transverse shear properties of the plies.

Therefore the solution of the extremal problem is

$$C_{ij} = \sum_{p=1}^{P} \left[A_{1p}^{ij} e^{\left(px+^1\phi_n^x\right)} +^1 k_x \right] \cdot \left[A_{2i}^{ij} e^{\left(py+^1\phi_n^y\right)} +^2 k_y \right] \quad \text{i,j=1,2,3,6}$$

$$C_{44} = L \tag{5.11}$$

$$C_{45} = M$$

$$C_{55} = N$$

The appropriate amplitude, phase, mean value and period in Eq. (5.11) are determined enforcing conditions such as the stiffness at the bounds, a convex or a concave shape and thermodynamic constraints related to the conservation of energy. Also the mean values of the mechanical properties (i.e. the mean value of the functions and of their powers of various orders) of the variable stiffness ply should be imposed to be the same of that with straight fibre.

Once the stiffness coefficients C_{ij} (x, y) have been defined, the law of variation of the fibre orientation angle is obtained inverting the stress-strain relations for lamina of arbitrary orientation (see. Ref. [**133**]). As already done for the development of the AD-ZZ model, also in this case the solution to (5.9) and (5.10) is computed through symbolic calculus.

Here, the fibre paths shown in Figure 5.1 are considered, which represent a solution compatible with the governing equation (5.11): MB minimizes the bending component of the strain energy, MS minimizes the shear component of the strain energy of each ply. From the practical viewpoint, MB distribution is obtained imposing maximum bending stiffness at the centre of the ply and minimum at the edge. The in-plane variations of the most significant C_{ij} for the MB ply are reported in Figure 5.1. From this figure, it is possible to notice that MB determines a significant increase of C_{11} at the centre of the ply, and a reduction at its edges. For what concerns C_{12}, which represents the local in-plane shear stiffness, its magnitude is significantly high at bounds of the ply, while at the centre it remains almost unchanged with respect to the straight fibre case. This trend is also the same of the coefficient C_{22}. The coupled effects of the distributions of C_{11}, C_{12} and C_{22} imply, as desired, an increase of the bending stiffness at the centre of the ply and a decrease at the bounds, where the shear stiffness in the in-plane direction grows. Finally, with MB distribution, the transverse shear stiffness decreases maintaining a value almost constant.

The MS distribution is obtained imposing maximum bending stiffness at the edge of the ply and minimum at the centre, as shown by the stiffness distributions reported in Figure 5.1. This figure shows that the in-plane distribution C_{11} is higher at the bounds than at the centre of the ply, while for C_{12} and C_{22} the trend is the opposite. In fact, they have low value at bounds and high value at the centre. C_{44} remains almost constant and similar to the original value. By the practical point of view, MS distribution determines a transfer of energy from bending in the x-direction, to bending in the y-direction and to in-plane shear.
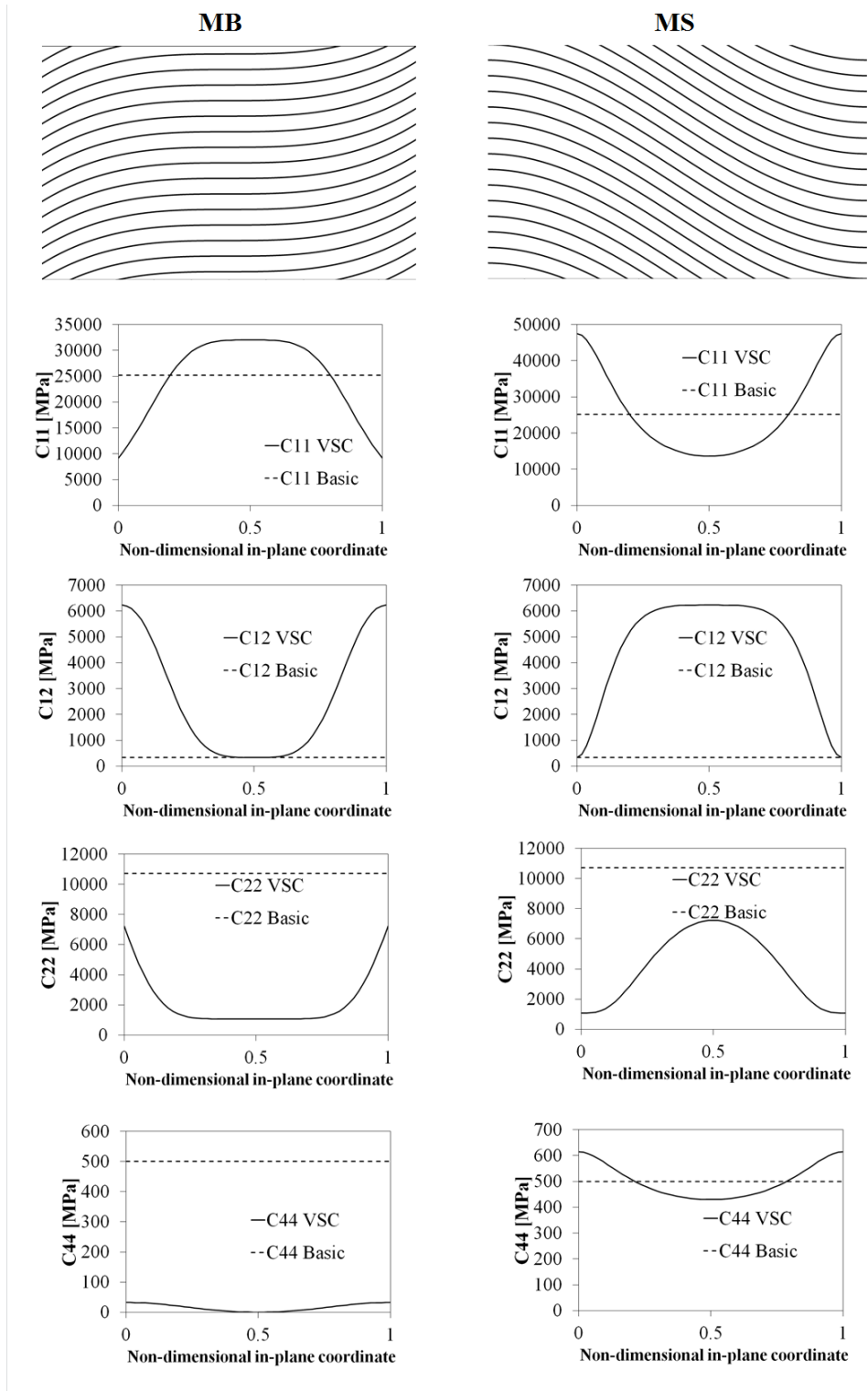
Figure 5.1 Fibre distributions and in-plane distributions of the C_{ij} for the MB and MS plies.

5.3 Stitching

The insertion of a through-the-thickness reinforcement introduces the idea of 3D material. Within this framework, several approaches, validated by comparisons with experimental results or 3D FEA, have been suggested for modelling the mechanical behaviour of this kind of materials. According to Prodromou et al. [**229**], they can be broadly classified into four classes, here referred as: i) analytical methods, ii) methods based upon inclusion method, iii) methods based upon cell method and iv) FEM methods. The analytical methods (see, e.g. [**230**] - [**231**] - [**232**]) are based on laminate theory and orientation averaging techniques. In these models, the composite is discretized into small volume elements, which can be treated as unidirectional lamina with transverse isotropic properties. Making the assumption of either iso-stress, or iso-strain, the macroscopic properties are determined by volume averaging the response of a composite representative body. These methods give an accurate prediction for in-plane on-axis moduli, while shear and out-of-plane properties could be predicted with significant errors, as outlined in [**229**] and [**233**]. Inclusion methods [**234**], [**235**] adopt a mean field approach based upon the equivalent inclusion theory [**236**], for evaluating the mechanical properties. However, comparisons with experiments showed that average errors relative to experimental results of at least 10 % can be found with this technique, as reported in [**229**].The cell method [**229**], [**237**] is based on the theory of continuum media. It firstly split the structure into representative volume elements, which repeat itself throughout the material. The following step requires defining the macroscopic average stresses and strains from the microscopic ones, next continuity of traction and displacements should be imposed at the interfaces between the constituent volumes. In the final step, the overall elasto-plastic behaviour is determined by expressing it as a constitutive relationship between the average stress, strain and plastic strain, in conjunction with the effective elastic stiffness tensor of the composite. With respect to the inclusion methods, it is possible to halve the average errors relative to experimental results, as shown in [**229**]. According to [**229**], the most accurate approach to date available is that based on material testing carried out with full scale finite element analysis (FEA), as proposed in [**238**] and [**239**]. Accordingly, here, the author has chosen to adopt this strategy to evaluate the homogenized mechanical properties of the stitched structure employed by the AD-ZZ model to compute stresses and displacements. In

particular, virtual material tests are carried out using the mixed solid element developed in Ref. [**240**].
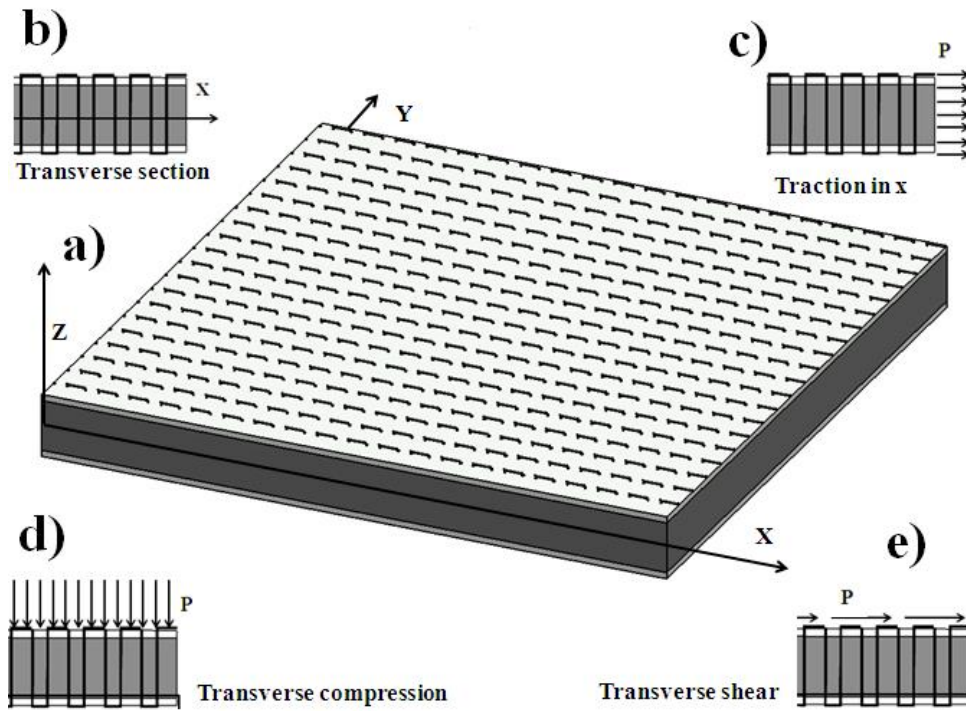
Figure 5.2 a) 3D model of stitched sandwich. b) Transverse section. Loading scheme for calculating c) in-plane moduli, d) transverse modulus and e) shear moduli with 3D FEA.

The first step is creating the geometrical model of the structure, (Figure 5.2). Once the geometrical model is created, the elastic coefficients of the structure are computed carrying out the analysis with the 3D FE model [**240**]. Its nodal d.o.f. are the three displacements and the three interlaminar stresses to meet the stress and displacements continuity requirements at the interfaces. The reason for this choice is that the computational effort required is not larger than that required by displacement-based counterpart solid elements, while accuracy and convergence are dramatically improved.

The in-plane moduli are evaluated with the loading scheme of Figure 5.2c. The loading scheme of Figure 5.2d is employed to compute the transverse modulus E_3, while that of Figure 5.2e is adopted to obtain the shear moduli G_{13} and G_{23}. Using stresses and strains computed with the FEA and the constitutive equation $\{\sigma\}=[C]\{\varepsilon\}$, the homogenized elastic properties are computed in a straightforward way [**241**]:

$$E_{11} = \frac{\sigma_{11(3DFEA)}}{\varepsilon_{11(3DFEA)}} \quad \upsilon_{12} = -\frac{\varepsilon_{22(3DFEA)}}{\varepsilon_{11(3DFEA)}} \quad \upsilon_{13} = -\frac{\varepsilon_{33(3DFEA)}}{\varepsilon_{11(3DFEA)}}$$

$$E_{22} = \frac{\sigma_{22(3DFEA)}}{\varepsilon_{22(3DFEA)}} \quad \upsilon_{23} = -\frac{\varepsilon_{33(3DFEA)}}{\varepsilon_{22(3DFEA)}} \quad \upsilon_{21} = -\frac{\varepsilon_{11(3DFEA)}}{\varepsilon_{22(3DFEA)}}$$

$$E_{33} = \frac{\sigma_{33(3DFEA)}}{\varepsilon_{33(3DFEA)}} \quad \upsilon_{31} = -\frac{\varepsilon_{11(3DFEA)}}{\varepsilon_{33(3DFEA)}} \quad \upsilon_{32} = -\frac{\varepsilon_{22(3DFEA)}}{\varepsilon_{33(3DFEA)}} \qquad (5.12)$$

$$G_{12} = \frac{\sigma_{12(3DFEA)}}{\varepsilon_{12(3DFEA)}} \quad G_{13} = \frac{\sigma_{13(3DFEA)}}{\varepsilon_{13(3DFEA)}} \quad G_{23} = \frac{\sigma_{23(3DFEA)}}{\varepsilon_{23(3DFEA)}}$$

It could be noticed that through other loading conditions all the homogenized macromechanical coefficients of [C] are evaluated.

The procedure explained is carried out using a specific value of the stitching spacing, but, as outlined in [6], this parameter plays a fundamental role in varying the stiffness of the structure. Accordingly, this effect is taken into consideration employing the rule of mixture proposed by Mori and Tanaka [234]:

$$E_{if} = E_{i\,st} + k \cdot V \left(E_{1b} - E_{i\,st} \right) \quad (i = 1,2,3)$$

$$\upsilon_{ijf} = \upsilon_{ij\,st} + k \cdot V \left(\upsilon_{12b} - \upsilon_{ij\,st} \right) \ (ij = 12,13,23) \qquad (5.13)$$

$$G_{ijf} = G_{ij\,st} + k \cdot V \left(G_{12b} - G_{ij\,st} \right) \ (ij = 12,13,23)$$

The subscripts "f", "st" and "b" refer respectively to the stitched or tufted layer, to the standard layer and to the binder. The symbol "V" corresponds to the reinforcement percentage volume in the considered layer. Thus, V allows accounting for the effects of the stitching spacing. Finally, "k" is an index that enables to vary the mechanical properties of the material constituting the binder. Please note that the relation of Eq. (5.13) represents a conservative approach with respect to the effective correlation between elastic coefficients and stitching spacing, as shown in [242]. It could be remarked that no more than 60 seconds on a laptop computers are required to carry out each analysis, while, in order to verify the accuracy of the present technique, two cases are considered for which their mechanical properties have been evaluated from experiments.

As first case, it is analysed the stitched laminate studied by Yudhanto et al. in [243], who proposed experimental evaluations of the in plane moduli for a T800SC-24kf dry preforms

with tow orientation of $[+45°/90°/-45°/0°_2/+45°/90°_2/-45°/0°]_s$, stitched with a 200 denier Vectran® thread. The preform is impregnated with epoxy resin XNR/H6813. Table 5.1 reports comparisons between the experimental results and the coefficients computed using the method explained above. From these numerical results it could be noticed that virtual material tests provide results in good agreement with experiments.

	Stitch pitch (mm)	6	3
E_x (MPa)	Experiment [243]	51.1 ± 1.9	51.7 ± 3.1
	Present	52.2	52.7
υ_{xy} (MPa)	Experiment [243]	0.314 ± 0.013	0.324 ± 0.005
	Present	0.317	0.325

Table 5.1 Comparison between the mechanical properties calculated by Yudhanto et al. [243] and the present ones.

For a further assessment, it is considered the sandwich studied by Lascoup et al. in [244]. This paper presents experimental results for a sandwich with a 20 mm polyurethane foam core and 1 mm E-glass fibre faces. Different configurations are analysed by varying the stitching spacing (i.e. three values of the stitching step in the x direction are considered) and the angle between through-the-thickness reinforcement and faces (here indicated with α). The reinforcing thread is made of 2400 TEX glass fibre (E=13.7 GPa) and its diameter is 2.7 mm. The stitching spacing in the y direction is fixed and its value is 24 mm. Accordingly to the behaviour shown in [6], reducing the stitching spacing has a significant bearing in increasing transverse and shear modulus. From Table 5.2, it could be noticed that virtual material tests provide results included in the natural dispersion of experiments, therefore the accuracy of the method proposed in this section can be considered satisfactory.

	Stitching step= 12.5 mm		
		α=45°	
E_z (MPa)	Experiment [244]	206.7 ± 13.3	
	Analytical [244]	208.1	
	Present	207.5	
G_{xz} (MPa)	Experiment [244]	28.0 ± 2.1	
	Analytical [244]	42.1	
	Present	26.4	
	Stitching step= 25 mm		
		α=45°	α=60°
E_z (MPa)	Experiment [244]	95.5 ± 2.1	133.5 ± 9.9
	Analytical [244]	93.9	149.3
	Present	96.1	134.1
G_{xz} (MPa)	Experiment [244]	19.4 ± 2.3	14.8 ± 1.7

	Analytical [**244**]	21.9	13.4
	Present	20.1	15.4
Stitching step= 50 mm			
		α=45°	
E_z (MPa)	Experiment [**244**]	57.9 ± 4.8	
	Analytical [**244**]	36.9	
	Present	59.9	
G_{xz} (MPa)	Experiment [**244**]	15.9 ± 0.7	
	Analytical [**244**]	10.9	
	Present	16.2	

Table 5.2 Comparison between the mechanical properties calculated by Lascoup et al. [244] and the present ones.

5.4 Numerical results of VSC and stitching

In this section applications of the procedures discussed in this chapter will be presented to static and dynamic analyses of laminates and sandwiches.

5.4.1 Applications to laminates and sandwiches

As first application aimed at showing the effects of variable stiffness composites on stresses, it is considered the simply-supported laminated square plate by Pagano [**145**] having a length-to-thickness ratio S of 4. Two loading conditions are analysed, namely a static one with the plate undergoing a bi-sinusoidal loading and a dynamic one with a triangular blast pulse acting on the upper face of the plate. It is reminded that this structure, already considered in Chapter 3, is made of MAT p (E_L/E_T=25; G_{LT}/E_T=0.5; G_{TT}/E_T=0.2; υ_{LT}=0.25), while the lay-up considered are reported in Figure 5.3.
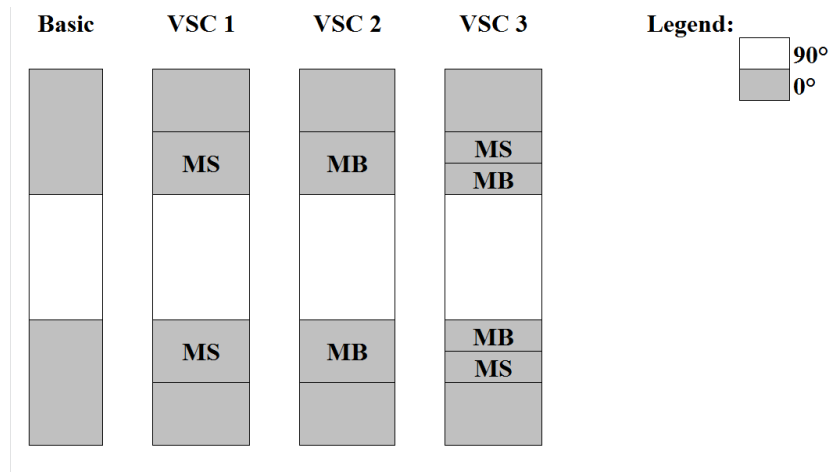
Figure 5.3. Lay-ups considered for analysis of a [0°/90°/0°] laminated plate with variable stiffness composites.

Shear stresses and the transverse displacement are reported where they assume their maximum, in the following normalized form:

$$\bar{\sigma}_{xz} = \frac{\sigma_{xz}\left(0, \frac{L_y}{2}, z\right)}{p^0 S} \quad \bar{\sigma}_{yz} = \frac{\sigma_{yz}\left(\frac{L_x}{2}, 0, z\right)}{p^0 S} \quad \bar{w} = 100 \frac{E_T w\left(\frac{L_x}{2}, \frac{L_y}{2}, z\right)}{hp^0 S^4} \quad \text{(static)}$$

$$\bar{w}(x, y, z, t) = \frac{w\left(\frac{L_x}{2}, \frac{L_y}{2}, z, t\right)}{\bar{w}(x, y, z)} \quad \text{(dynamics)}$$

(5.14)

Figure 5.4a represents the through-the-thickness variation of the shear stress $\bar{\sigma}_{xz}$ of the lay-ups considered while Figure 5.4b represents the through-the-thickness variation of the shear stress $\bar{\sigma}_{yz}$.
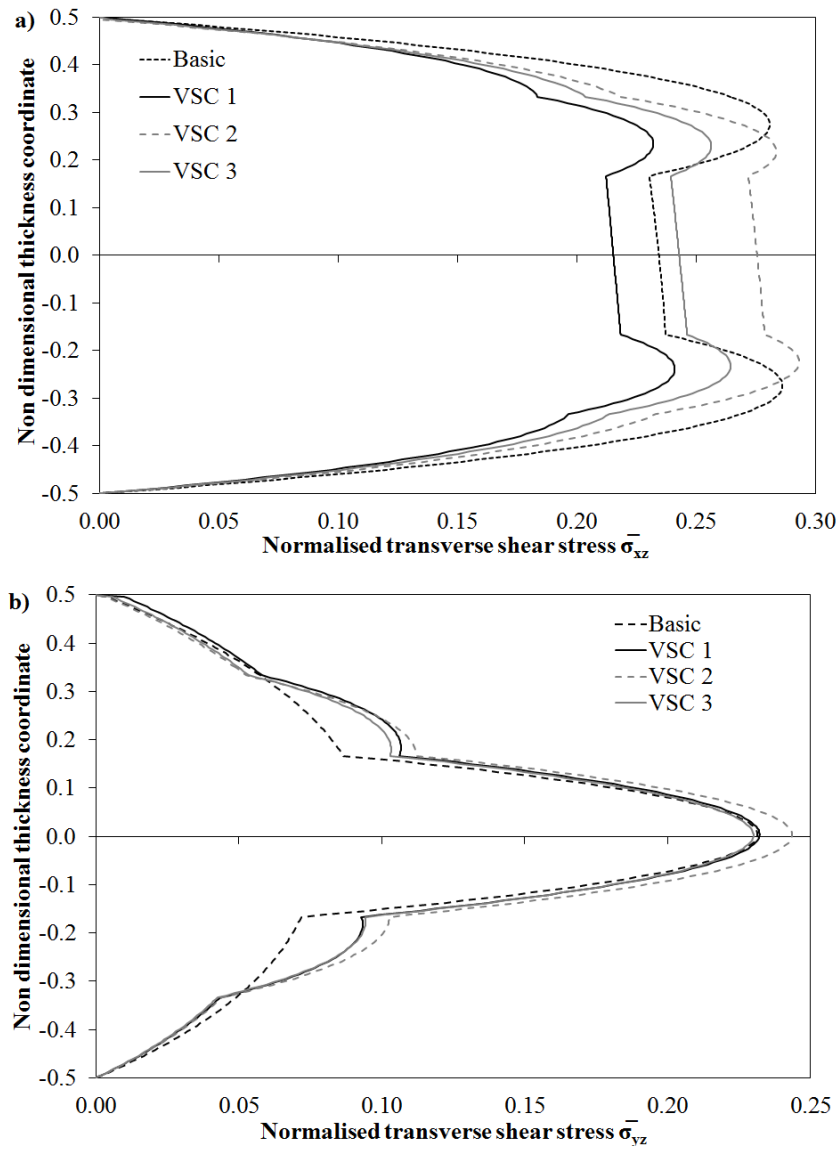
Figure 5.4 Through-the-thickness distribution of the transverse shear stresses a) $\bar{\sigma}_{xz}$ and b) $\bar{\sigma}_{yz}$ for the laminated plate with variable stiffness composites.

In Table 5.3 is reported the deflection in the centre of the plates for the considered lay-ups.

	Un Opt	VSC 1	VSC 2	VSC 3
$\bar{w}$	1.954	1.919	1.903	1.890
gain		-1.80%	-2.60%	-3.30%

Table 5.3 Deflection in the centre of the plates.

Figure 5.5 represents the central deflection of the laminated plate with variable stiffness composites under a triangular pulse loading.
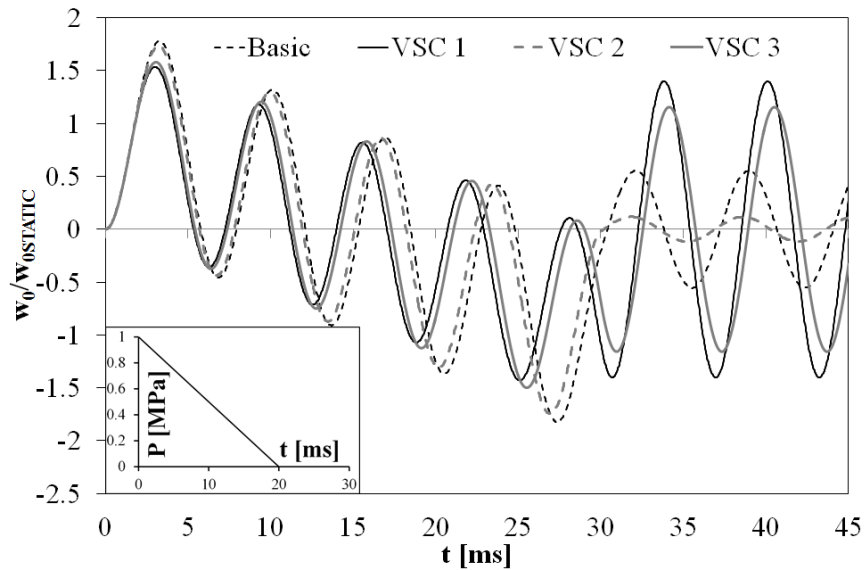
Figure 5.5 Time history for the laminated plate with variable stiffness composites undergoing triangular blast pulse loading.

From the reported results it can be noticed the effects of variable stiffness composites. Remembering that the aim of the process is the reduction of the interlaminar stresses, from this viewpoint the most efficient lay-up seems VSC 1, whose interlaminar shear stress sensibly decreases with respect to the standard case. This is physically consistent, since with this stacking sequence the difference between the material properties of adjacent plies is reduced. Instead, for what concerns results about the transverse displacement the best lay-ups is VSC 3, which is characterized by the simultaneous presence of plies that minimize the bending component of the strain energy and of plies that minimize the shear component of the strain energy.

It is now considered a sandwich with core in MAT4, while the faces are in M10. The mechanical properties of M10 are: E_1=36.23 GPa, E_3=7.21 GPa, G_{13}=5.68 GPa, υ_{13}=0.3263, ρ= 2.54 kg/dm^3. It is reminded that the mechanical properties of MAT 4 are: E_1=E_3=0.05 GPa, G_{13}=0.0217 GPa, υ_{13}=0.15, ρ= 0.166 kg/dm^3.

The thickness of the layers are (0.2 h/0.3 h)$_s$, while the length to thickness ratio (*L/h*) is 10, where *L=100 mm* and, as reported in Figure 5.6, five lay-ups are considered (VSC 1-VSC 5), by varying the position across the thickness of standard, MB and MS plies. Of course, the position of these layers across the thickness is determined directly comparing the response of all the stack-up possible options since few constituent layers are considered. As for the previous case, applications will be presented both for statics and dynamics considering the

beam undergoing a sinusoidal loading in the former case and a triangular blast pulse loading in the latter one.
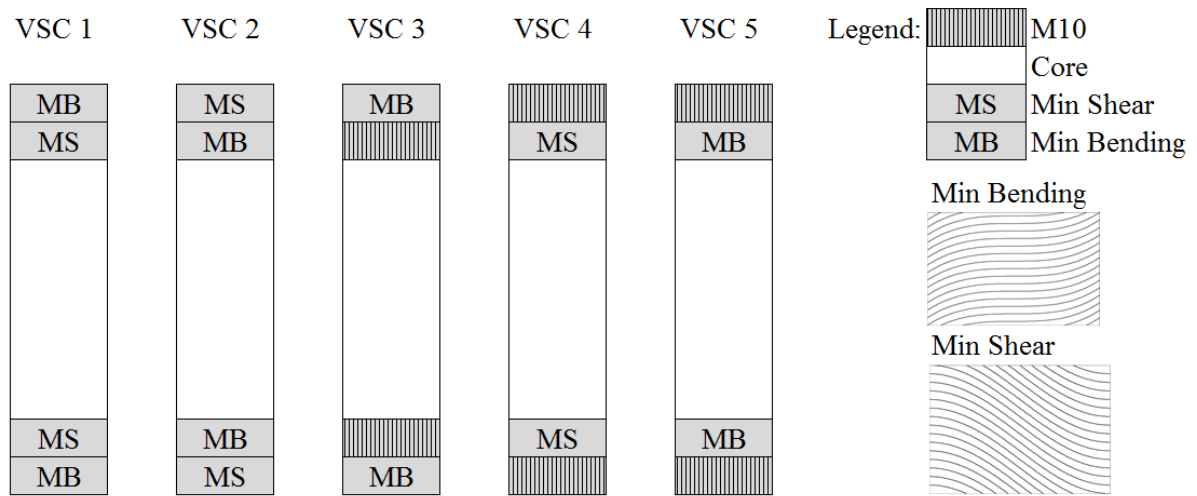
Figure 5.6 Variable stiffness plies and lay-ups considered for analysis of sandwich beam.

According to the results presented in Ref. [**245**], the choice of considering this specific value of *L/h* is done considering that for thick structures the effect of the variable stiffness composites is limited due to their high stiffness. This is also corroborated by the results of Figure 5.7, which reports the gain (gain= w_{basic}/w_{VSC2}) by VSC 2 configuration when the length-to-thickness ratio grows. On the other hand, extremely thin structures would not underline the capability of the AD-ZZ model in describing the effects of the transverse shear deformations and the out-of-plane stresses.
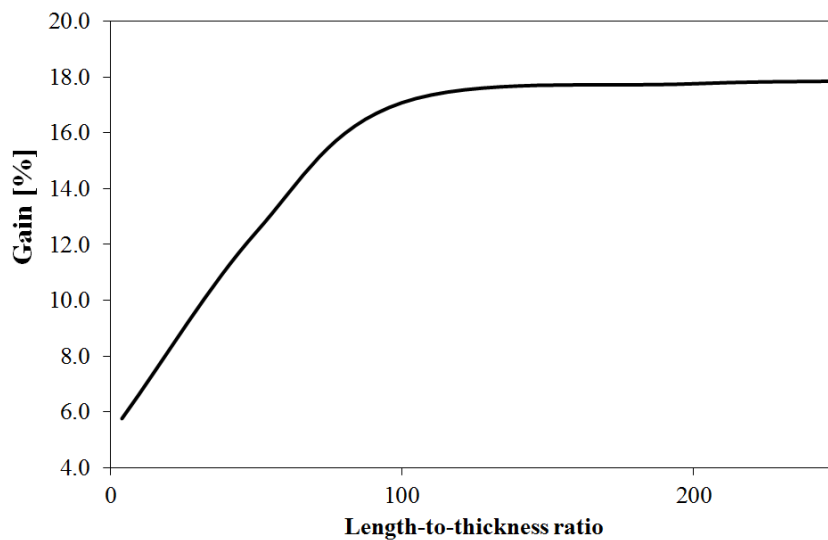
Figure 5.7 Improvement due to variable stiffness composites as function of the length-to-thickness ratio for a sandwich beam.

The numerical results of Figure 5.8 – 5.9 are normalized as follows:

$$w*(x,z) = \frac{E_2 w\left(\frac{L_x}{2},z\right)}{p^0 \cdot h} \quad \sigma*_{xz}(x,z) = \frac{\sigma_{xz}(0,z)}{p^0} \quad \text{(statics)}$$

$$\bar{w}(x,z,t) = \frac{w\left(\frac{L_x}{2},z,t\right)}{w*(x,z)} \quad \text{(dynamics)}$$

(5.15)
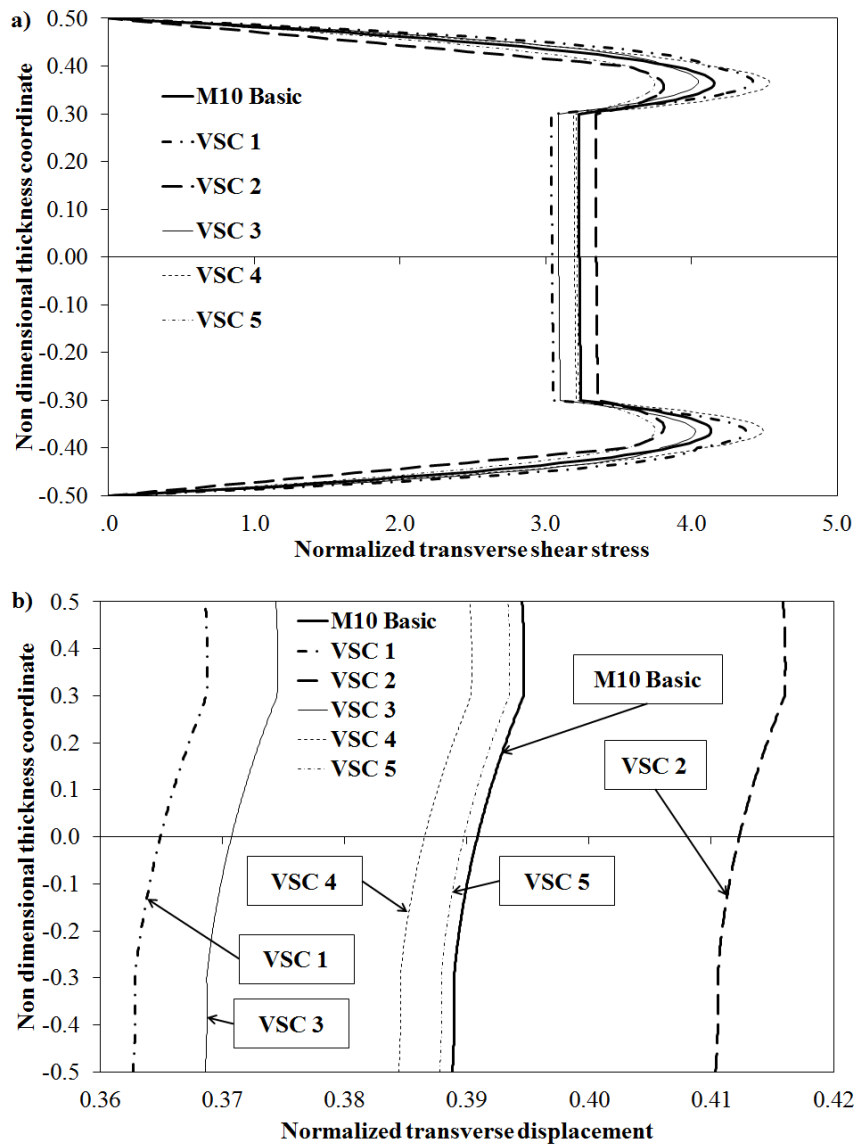
Figure 5.8 Through-the-thickness distribution of a) transverse shear stresses σ*_xz and b) transverse displacement w* for the sandwich plate with variable stiffness composites.

For what concerns shear stress, VSC 1 – 3 and 4 have similar behaviour, since all these configurations determine an increase of the stress in the faces and a reduction in the core. In particular, for VSC 1 this reduction of shear stress in the core (and at the interfaces between core and faces) is of 6%. It is reminded that core materials have in general low strengths, thus reducing stresses in this zone of the structure has a significant bearing. VSC 2 and 5, instead, determine a decrease of the shear in the faces and an increase of this quantity in the core. So they seem to be less attractive than the other configurations.

In terms of the transverse displacement, the best results are obtained by VSC 1 and 3. This is physically consistent, since these two lay-ups have the MB plies as outer layers, where the effects of bending are stronger. Accordingly, the MB fibre distribution, which minimizes the effects of bending, is more effective when placed in this position.
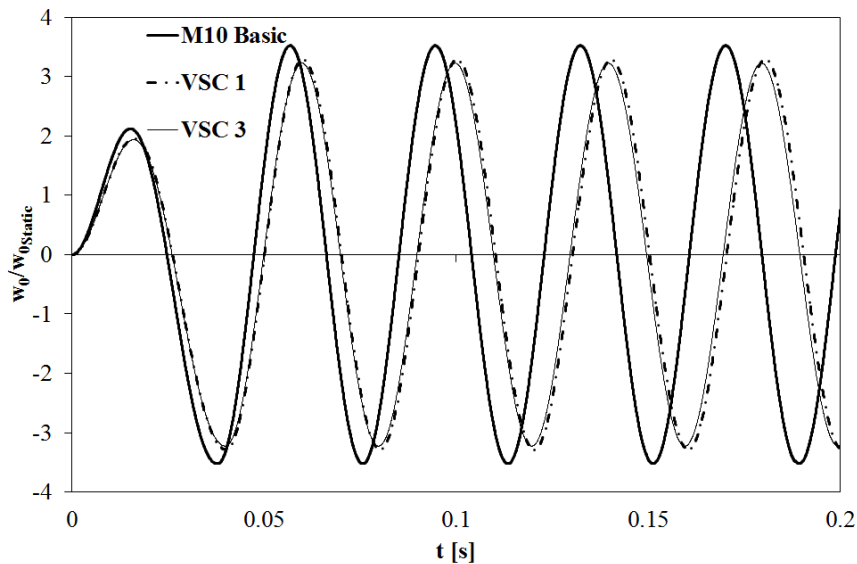
Figure 5.9 Time history for the sandwich beam with variable stiffness composites undergoing triangular blast pulse loading.

In Figure 5.9 only the results from VSC 1 and VSC 3 are reported, since the time history of the other lay-ups is not significantly different from that of the standard one. Both configurations have similar behaviour: they reduce the amplitude and the frequency of the oscillations.

Results presented in this section for laminates and sandwiches confirm that variable stiffness composites can be interesting, since they improve static and dynamic structural performances.

5.4.2 Stitching of sandwiches

Attention is now focused on evaluating whether stitching can be useful for improving strength and stiffness of sandwiches. Applications are presented to three simply supported damaged sandwich beams undergoing sinusoidal loading and then to a square plate with the same boundary conditions and bi-sinusoidal loading. The beams are characterized by a length to thickness ratio of 4, they have a (MAT 1/2/3/1/3/4)$_s$ stacking sequence and the following thickness ratios of the constituent layers (0.010/ 0.025/ 0.015/ 0.020/ 0.030/ 0.4)$_s$.

Damage is modelled using the ply-discount theory as in [107] and in Chapter 3. In particular, three cases are studied: i) the damage of the core, simulated reducing G_{13} of MAT 4 of a 10^2 factor, ii) the damage of the upper face of the structures, simulated reducing E_1 of the materials constituting the upper face of a 10^2 factor, and iii) the damage of the upper face of the structures, simulated reducing E_3 of the material constituting the upper face and the core of a 10^2 factor. Displacements and stresses are reported normalized in the following form, according to Ref. [107], where the exact solutions for cases i) and iii) have been computed:

$$\overline{\sigma}_{xz} = \frac{\sigma_{xz}(0,z)}{p^0} \quad \overline{w} = \frac{E_2 w\left(\frac{L_x}{2},z\right)}{h p^0} \quad \overline{\sigma}_x = \frac{\sigma_x\left(\frac{L_x}{2},z\right)}{p^0} \tag{5.15}$$

Stress and displacement fields are represented in Figure 5.10. Both a T300 reinforcement (mechanical properties of T300 are: E_1=139 GPa, E_3=9.4 GPa, G_{13}=4.5 GPa, υ_{13}=0.0209, ρ= 1.86 kg/dm^3) and a parametric one (different values of the index "k" (see Eq. (5.13))) have been considered. In both cases, the reinforcing thread has circular section with a 2.5 mm diameter, and the reinforcement percentage volume 'V' is 0.1.

d)

e)

f)
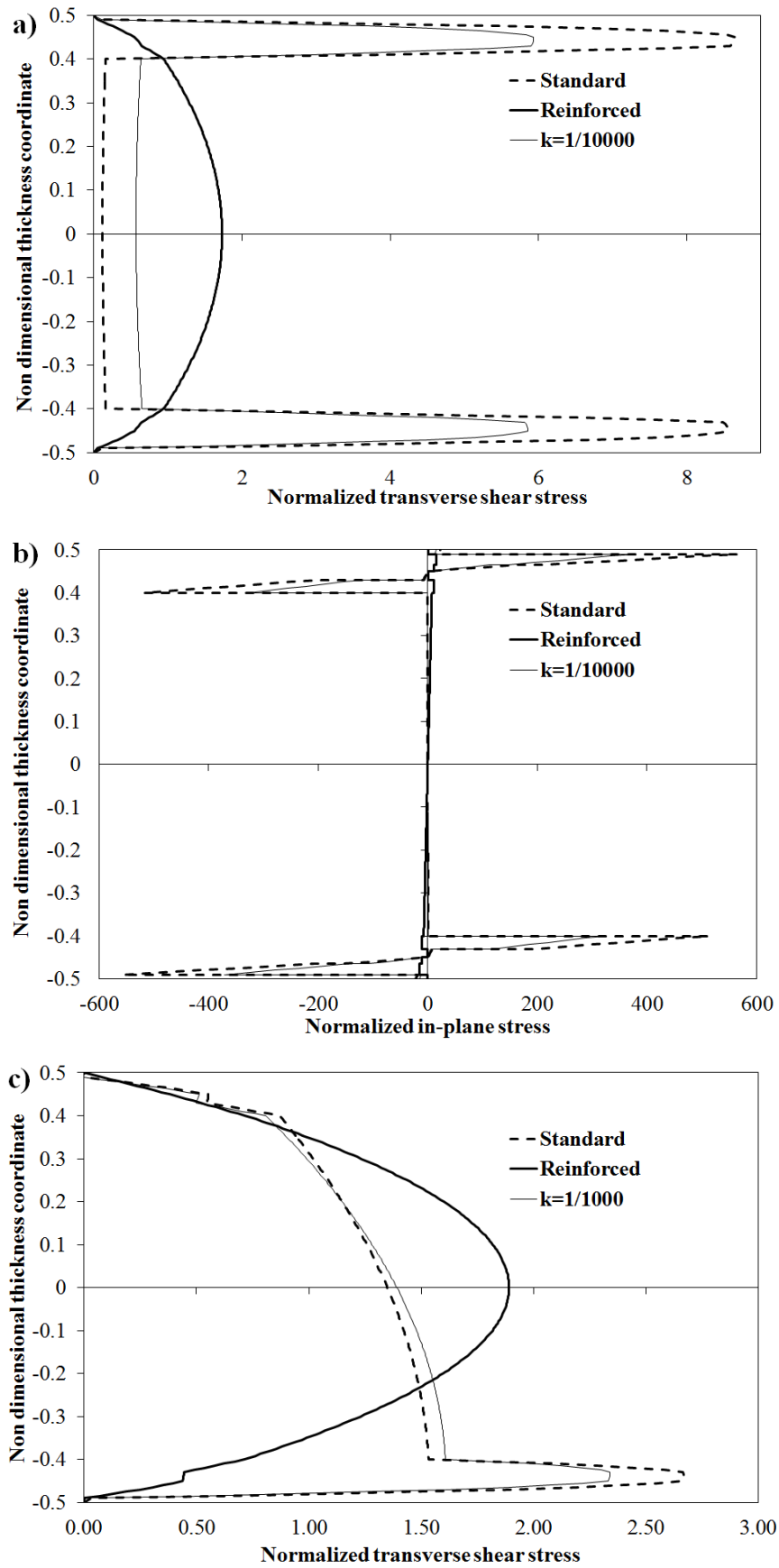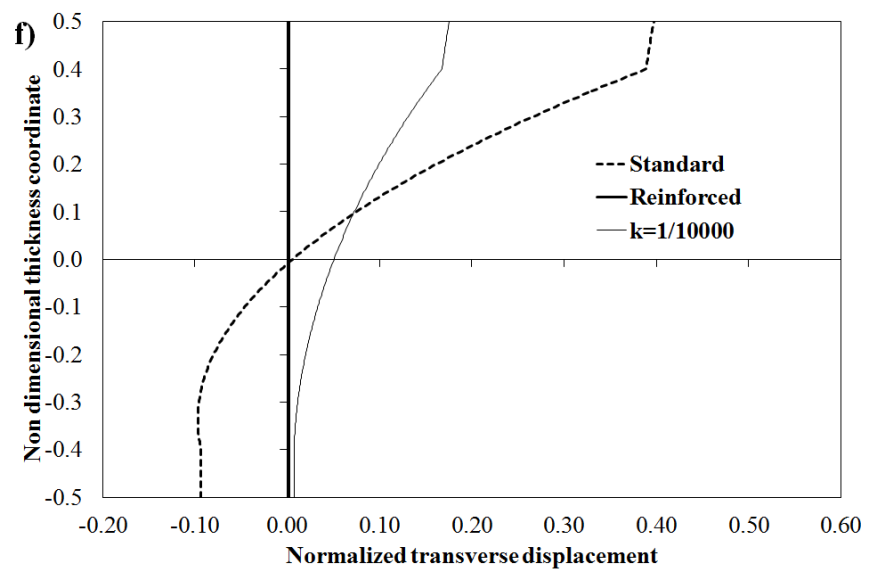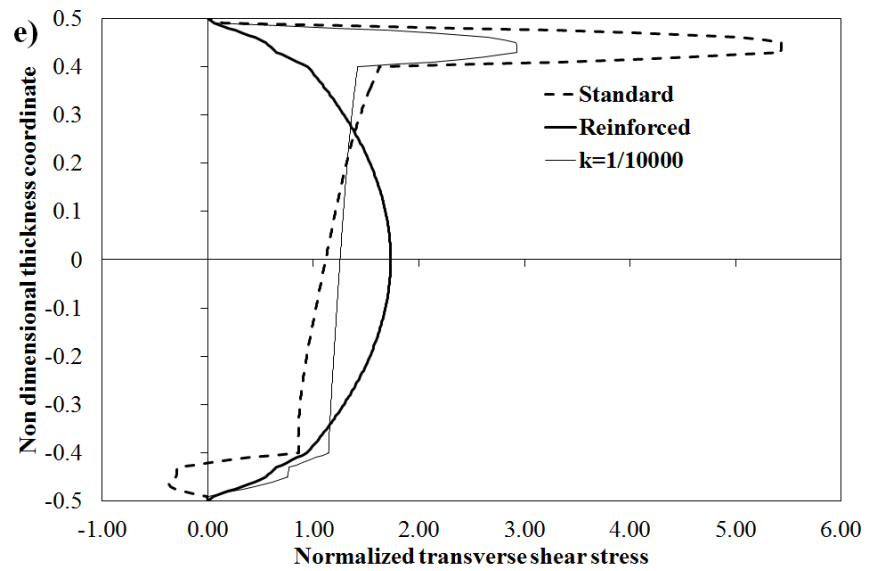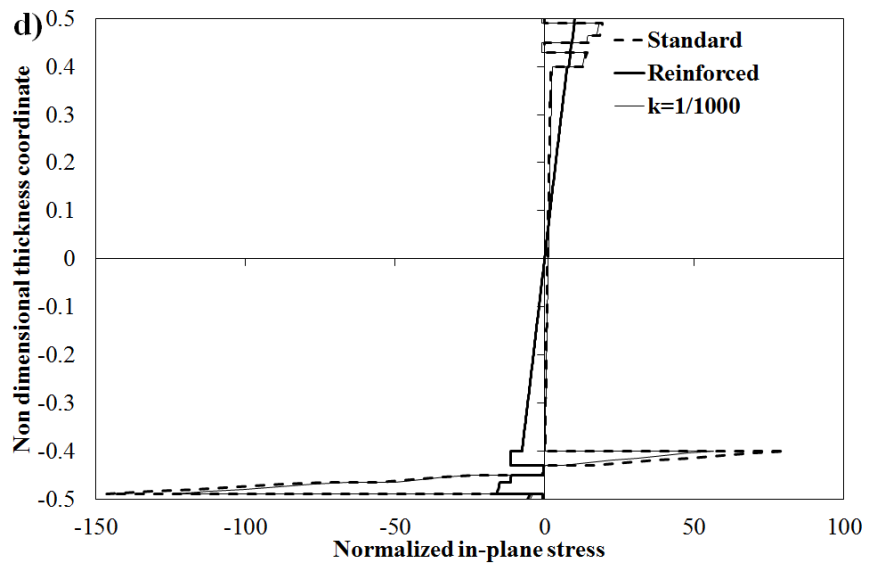
Figure 5.10 Through-the-thickness distribution of a) transverse shear stress $\bar{\sigma}_{xz}$ and b) in-plane stress $\bar{\sigma}_{xx}$ for sandwich beam with damaged core. Through-the-thickness distribution of c) transverse shear stress $\bar{\sigma}_{xz}$ and d) in-plane stress $\bar{\sigma}_{xx}$ for sandwich beam with damaged upper face (E1 degraded). Through-the-thickness distribution of d) transverse shear stress $\bar{\sigma}_{xz}$ and e) transverse displacement $\bar{w}$ for sandwich beam with damaged upper face (E_3 degraded).

Please note that in Figure 5.10 the sandwiches stitched considering k=1 are named as 'reinforced', while those with no reinforcement are named as 'standard'. Numerical results show that stitching is effective in reducing the detrimental effects of out-of-plane stresses (Fig. 5.10a, 5.10c and 5.10e) and transverse displacement (Fig. 5.10f). In particular numerical results for the case with k=1/10000 demonstrate that a great improvement of stress and displacement can also be obtained considering a reinforcing binder with very low mechanical properties. Stress recovery could also be obtained with the insertion of viscoelastic layers (see, e.g. [**213**]), although at the expense of a consistent stiffness loss, as outlined before.

The last case of analysis considers the sandwich plate examined in Ref. [**162**]. The aim is to show whether the beneficial effects of through-the-thickness reinforcement can be obtained also for sandwich plates. The mechanical properties of the Graphite/Epoxy faces are: E_1=132.38 GPa E_2=E_3=10.76 GPa, G_{13}=5.65 GPa, G_{12}=5.62 GPa, G_{23}=3.61 GPa, υ_{12}=υ_{13}=0.24, υ_{23}=0.49; the mechanical properties of the foam core are: E_1= E_2=E_3=0.035 GPa, G_{13}= G_{12}= G_{23}= 0.0123 GPa, υ_{12}=υ_{13}= υ_{23}=0.4. T300 reinforcement with circular section and 2.5 mm diameter and a reinforcement percentage volume 'V' of 0.1 have been considered. The plate is square (L_x= L_y= 1 m) and characterized by a length to thickness ratio of 10, with the following thickness ratios of the constituent layers $(0.1/0.4)_s$. Figure 5.11a represents the through-the-thickness variation of the transverse shear stress σ_{xz}, while Figure 5.11b represents the through-the-thickness variation of the transverse shear stress σ_{yz}. As in Figure 5.10 the sandwiches stitched considering k=1 are named as 'reinforced', while those with no reinforcement are named as 'standard'. From the numerical results of Figure 5.11, it could be remarked that through-the-thickness reinforcement is effective in reducing the interlaminar shear stresses also in sandwich plates.
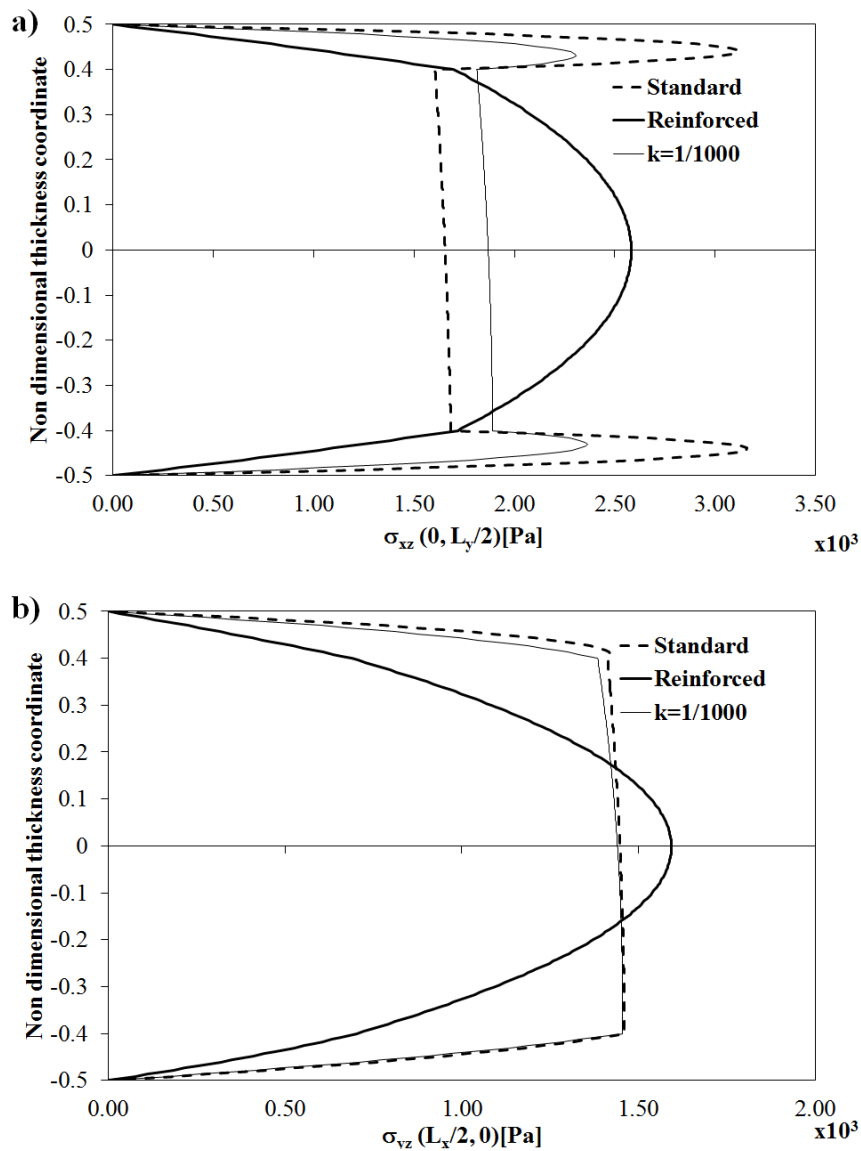
Figure 5.11. Through-the-thickness distribution of a) transverse shear stress σ$_{xz}$ and b) transverse shear stress σ$_{yz}$ for the square plate.

As general remarks, it could be outlined that stitching determines an increase of transverse shear stresses in the core, and a reduction in the faces. Since experimental results reported in [**244**] show that stitching through-the-thickness increases the strength of the structure, a great reduction of the delamination index can be obtained. This justifies the experimental results reported in [**6**] and [**228**], showing a reduced damage under impact loading.

In light of the achievements brought by variable stiffness composites and stitching, in the next section, these techniques will be applied simultaneously to improve structural performances of a sandwich plate with M10 faces.

5.4.3 Variable stiffness composites and stitching coupled

The aim of this section is to verify whether variable stiffness composites and stitching can improve performances of a sandwich with M10 faces and initially straight fibres up to those of a sandwich having T300 faces with straight fibre orientation, here named as reference case. For doing this, it is again considered the sandwich beam with M10 faces of Section 5.4.1. It is reminded that this beam has a length-to-thickness ratio of 10 and the thickness ratios of the constituent layers are $(0.2\ h/0.3\ h)_s$. The reference structure, instead, is a sandwich beam with the same geometric characteristics but with T300 faces. The lay-ups of Figure 5.6 are again considered and in particular the faces of VSC 1 and VSC 3 lay-ups are stitched using a reinforcing thread in T300. Numerical results are reposted in Figure 5.12 normalized according to Eqs. (5.15).
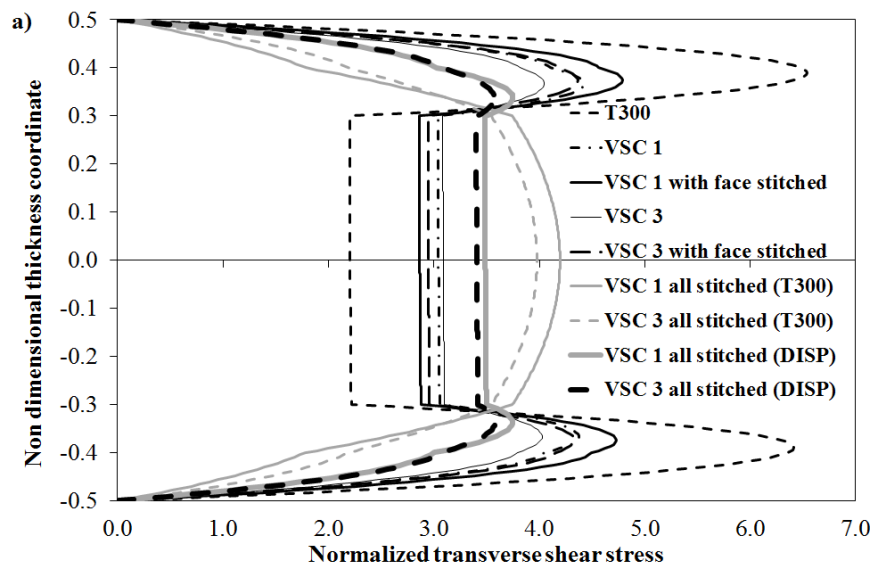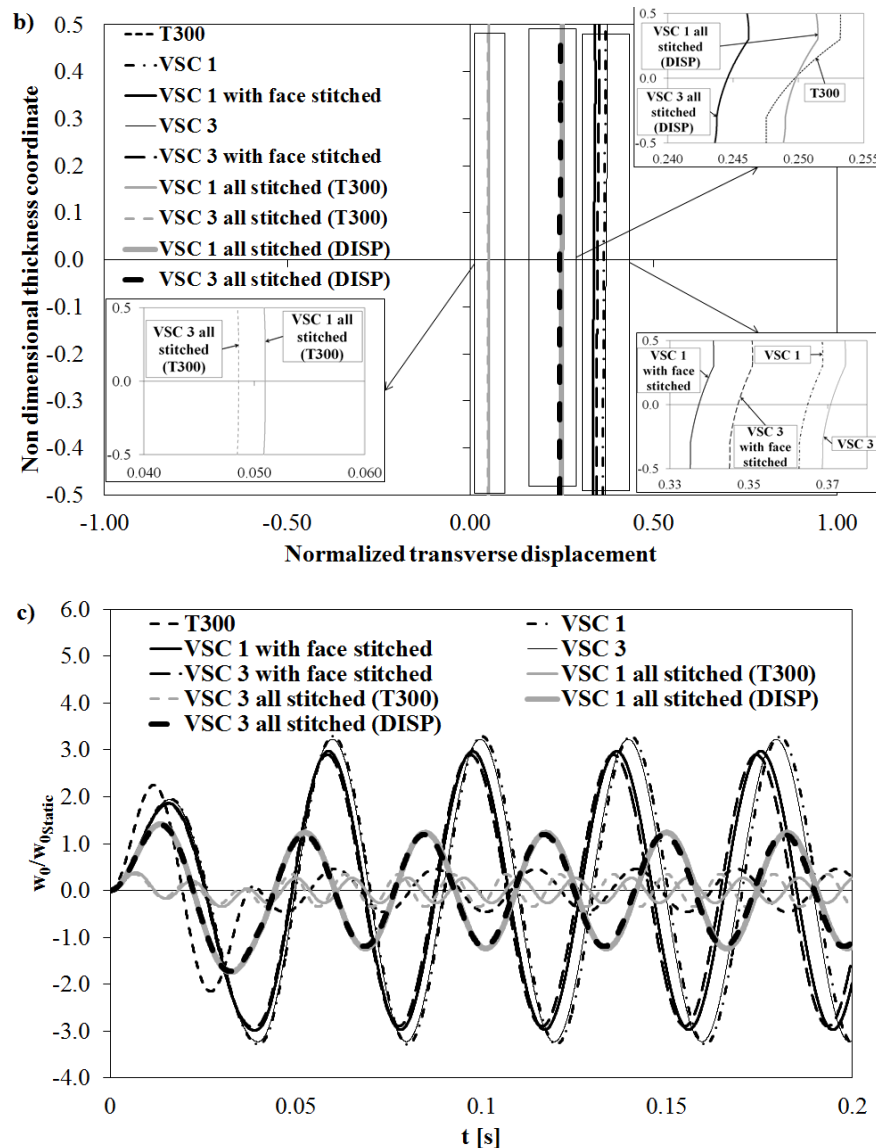
Figure 5.12 Through the thickness distribution of a) normalized transverse shear stress σ^*_{xz} and b) normalized transverse displacement w* for the lay-ups considered. c) Time history for the lay-ups considered.

This strategy improves the bending stiffness of the sandwich with M10 faces as shown in Figure 5.12b. In fact, for both the lay-ups considered, a 7% reduction of the transverse displacement is obtained with respect to the results of Figure 5.8. As it can be noticed in Figure 5.12a, the behaviour of VSC 1 and VSC 3 with stitched faces is similar: an increase of the shear stress in the faces is obtained, coupled with a reduction of its value at the face-core interface. The increase of the bending stiffness is also underlined by the time history reported in Figure 5.12c. Indeed, it could be noticed a decrease of the amplitude of the oscillations, as well as a decrease of their period.

However stitching is more effective when applied to "weak" materials such as that constituting to core of the sandwich beam. Therefore, in order to further improve the performances of the sandwich with M10 faces, it is possible to consider VSC 1 and VSC 3 stitched across all the thickness with a reinforcing thread made of T300 (named as 'VSC 1 *all stitched (T300)*' and 'VSC 3 *all stitched (T300)*').

The improvements are evident. Indeed, the transverse displacement of the sandwich with M10 faces is now considerably lower than that of the beam with T300 faces. The transverse shear stress is considerably lower in the faces, while an increase is obtained in the core. It could be noticed that, differently to the previous cases, VSC 3 lay-up obtains lower value of transverse displacement with respect to VSC 1.

The improvements in terms of stiffness are evident also for dynamic loading, as it can be noticed from Figure 5.12c. In fact, the insertion of a reinforcing binder determines a significant decrease of the amplitude of the oscillations, coupled with a decrease of their period.

Bearing in mind the effectiveness of stitching across the whole thickness of the sandwich, it is possible to consider a reinforcing thread, whose mechanical properties are lower than those of one in T300. In particular the results of Figure 5.12 named as 'VSC 1 *all stitched (DISP)*' and 'VSC 3 *all stitched (DISP)*' are obtained considering a reinforcing binder with E_1=0.72 GPa, E_3=0.21 GPa, G_{13}=0.2 GPa, υ_{13}=0.2613. With this configuration, the transverse displacement of the sandwich with M10 faces is the same than that with T300 faces. As far as the shear stress is concerned, a reduction of its value in the faces is obtained, while, an increase in the core is achieved.

The time history reported in Figure 5.12c shows that the two lay-ups have similar dynamic behaviour.

From the numerical results previously presented, it is possible to underline a consistent increase of the stiffness given by variable stiffness composites and stitching. Applying the delamination criterion of Ref. [**8**] 'VSC 1 *all stitched (DISP)*' obtains a 4% reduction of the delamination index in the faces and obtains a 7% increase of the delamination index at the face-core interface. For what concerns 'VSC *3 all stitched (DISP)*', a 6% reduction of the delamination index in the faces and a 4% increase of the delamination index at the face-core interface are obtained.

Results presented in this chapter showed that variable stiffness composites and stitching could be interesting methods aimed at improving performances and damage tolerance of laminates and sandwiches undergoing static and dynamic loads. Each technique can be applied separately from the other or alternatively they could be coupled.

Appendix: Stiffness matrices of the AD-ZZ model

Herein, the expression of the stiffness matrices of the AD-ZZ model employed in Eqs. (5.4) and (5.8) are defined.

Considering the quantities defined in Chapter 2 and Eq. (1.1) and by substituting the expressions of strains and stresses by the AD-ZZ model into (2.49) the following stiffness matrices are defined:

$$\left[A_{ij}, B_{ij}, D_{ij}, E_{ij}, F_{ij}, H_{ij} \right] = \left\langle C_{ij} \left[1, z, z^2, z^3, z^4, z^6 \right] \right\rangle \quad \text{for i,j=1,2,3,6}$$

$$\left[A_{ij}, D_{ij}, F_{ij} \right] = \left\langle C_{ij} \left[1, z^2, z^4 \right] \right\rangle \quad \text{for i,j=4,5}$$

$$\left[B_{ij}^\alpha, D_{ij}^\alpha, F_{ij}^\alpha \right] = \left\langle C_{ij} \left[1, z, z^3 \right] \sum_{k=1}^{n_l-1} \alpha_k \left(z - z_k \right) \right\rangle \quad \text{for i,j=1,2,3,6 and } \alpha\text{=a,b,c,d}$$

$$\left[A_{ij}^\alpha, D_{ij}^\alpha \right] = \left\langle C_{ij} \left[1, z^2 \right] \sum_{k=1}^{n_l-1} \alpha_k \right\rangle \quad \text{for i,j=4,5 and } \alpha\text{=a,b,c,d}$$

$$D_{ij}^{\alpha\beta} = \left\langle C_{ij} \sum_{k=1}^{n_l-1} \alpha_k \left(z - z_k \right) \sum_{k=1}^{n_l-1} \beta_k \left(z - z_k \right) \right\rangle \quad \text{for i,j=1,2,3,6 and } \alpha, \beta\text{=a,b,c,d} \qquad \text{(A.1)}$$

$$A_{ij}^{\alpha\beta} = \left\langle C_{ij} \sum_{k=1}^{n_l-1} \alpha_k \sum_{k=1}^{n_l-1} \beta_k \right\rangle \quad \text{for i,j=4,5 and } \alpha, \beta\text{=a,b,c,d}$$

$$\left[D_{ij2}^\alpha, E_{ij2}^\alpha, F_{ij2}^\alpha \right] = \left\langle C_{ij} \left[z^2, z^3, z^5 \right] \sum_{k=1}^{n_l-1} \alpha_k \right\rangle \quad \text{for i,j=1,2,3,6 and } \alpha\text{=a,b,c,d}$$

where:

$$\langle . \rangle = \int_{-\frac{h}{2}}^{\frac{h}{2}} (.) dz \qquad \text{(A.2)}$$

$$a = \Phi_x^k \quad b = \Phi_y^k \quad c = \Psi^k \quad d = \Omega^k$$

Chapter 6: Formulation of a C^0 theory

As already stated, one of the main drawbacks of the AD-ZZ model is that derivatives of various orders of the functional d.o.f. are incorporated in the displacement fields. This is due to the fact that expressions of zig-zag functions and of higher-order "adaptive" contributions are obtained once for all in a physically consistent way enforcing differential equations like the continuity of interlaminar stresses, the boundary conditions and indefinite equilibrium equations. Regrettably, derivatives are unwise contributions when finite elements are developed, since they should appear as nodal d.o.f. Consequently, computationally inefficient interpolating functions must be used. Techniques for eliminating derivatives such those proposed by Zhen and Wanji [72] and Sahoo and Singh [246] could be employed, resulting in an increase of the nodal d.o.f. Thus, using these techniques, the advantage of having just the minimal number of functional d.o.f., i.e. five, brought by the AD-ZZ model becomes merely apparent.

The aim of the present chapter is to develop and assess a technique that converts derivatives of the d.o.f. by updating the strain energy expression and the work of forces, as in [247], [248] and [249]. The objective is finding *a priori* corrections of displacements in closed form, which make the energy of the AD-ZZ model with all the derivatives neglected equivalent to that of its initial counterpart model containing all the derivatives. This idea was already successfully applied in [247] and [249], where energy updating was developed as a post-processing technique to improve the predictive capability of shear deformable commercial finite elements. Here, the same idea is used for eliminating the derivatives of the functional d.o.f. directly (i.e. in a non-iterative closed form) from the AD-ZZ model, so to obtain a C^0 equivalent model with just five d.o.f. able to account for zig-zag and layerwise effects. Differently to [247] and [249], here Hermite's polynomial representations of the d.o.f. are used over the domain, whose order depends upon the order of derivatives appearing in the

model, instead of using spline functions interpolating results of a preliminary finite element solution over a patch of elements.

In this chapter accuracy and efficiency of the updating technique will be assessed comparing the results of the model [119] to its equivalent counterpart free from derivatives, considering closed form solution of reference sample cases with intricate through-the-thickness displacement and stress distributions, for which exact elasticity solutions are available for comparisons. They are chosen because many models give poor predictions for such extreme test cases, or require a large number of variables across the thickness in order to be accurate. As already done previously, extremely thick cases are considered in order to highlight the zig-zag and layerwise effects.

6.1 Theoretical formulation

In the present section, the main steps towards development of a C^0 formulation of the AD-ZZ model are presented.

As shown by [247] and [249], it is possible to locally improve the accuracy of a finite element analysis using an iterative post-processing technique working on a spline interpolation of finite element results. Numerical results therein presented demonstrated that in the most critical regions, a solution as accurate as the one by a layerwise model can be obtained.

As outlined above, the idea of taking advantage of an energy updating process, here referred as SEUPT, can also be used for deriving a modified expression of a structural model. Indeed, differently to what proposed in [247] and [249], the corrective displacements can be found in a direct (i.e. non iterative) closed form, as outlined forward in this section.

In particular, a C^0 model can be obtained from the zig-zag model of Chapter 2 constructing energy equivalent displacement field free from derivatives of the functional d.o.f.

Closed form expressions of this displacement field are computed once for all in a straightforward way through SEUPT starting from the AD-ZZ model, hereafter referred as the original model (OM), in order to obtain the equivalent C^0 model (EM).

6.1.1 Equivalence of models

Hereon all the quantities that refer to the OM model are indicated with the superscript ^{OM}, while those referring to the EM model with the superscript ^{EM}. Accordingly, the displacement components of the AD-ZZ model constituting the OM model are indicated as u(x, y, z)^{OM}, v(x, y, z)^{OM}, w(x, y, z)^{OM} while their counterparts representing the EM model obtained by SEUPT are indicated as u(x, y, z)^{EM}, v(x, y, z)^{EM}, w(x, y, z)^{EM} or in compact form as $\forall^{OM}$ and $\forall^{EM}$, respectively. Displacements $\forall^{OM}$ are assumed as the sum of terms $\forall^{\varnothing}$ that are just functions of the d.o.f. and terms $\forall^{\cup}$ containing all the derivatives of the d.o.f.

$$\forall^{OM}(x, y, z) = \forall^{\varnothing}(x, y, z) + \forall^{\cup}(x, y, z) \tag{6.1}$$

The basic assumption of SEUPT is that each term $\forall^{\cup}$ can be removed, since its energy contributions are accounted for incorporating corrective terms free from derivatives Δu^0, Δv^0, Δw^0, $\Delta \gamma_x^{\,0}$, $\Delta \gamma_y^{\,0}$ (in compact form $\Delta \forall^{\varnothing}$):

$$\forall^{EM}(x, y, z) = \forall^{\varnothing}(x, y, z) + \Delta \forall^{\varnothing}(x, y, z) \tag{6.2}$$

The expressions of the $\Delta \forall^{\varnothing}$ terms will be derived from the energy balance, which is written in compact form as:

$$\delta \int (.)|_E = \delta \int (.)|_{Ai} - \delta \int (.)|_{Af} + \delta \int (.)|_{Am} = 0 \tag{6.3}$$

its contributions being:

$$\int (.)|_{Ai} = \frac{1}{2} \int_V \{\sigma\}^T \{\varepsilon\} dV \quad \text{the strain energy} \tag{6.4}$$

$$\int (.)|_{Af} = \int_V \{b\} \{u\} dV + \int_S \{t\} \{u\} dS \quad \text{the work of external forces} \tag{6.5}$$

$$\int (.)|_{Am} = \int_V -\rho \{\ddot{u}\} \{u\} dV \quad \text{the work of inertial forces} \tag{6.6}$$

The symbols $\{\sigma\}$ and $\{\varepsilon\}$ represent strain and stress vectors, respectively, $\{b\}$ and $\{t\}$ the body and surface forces, ρ the density and $\{u\}$ the displacements of OM or EM models. The energy balance (6.3) (for both the models) is split into five independent balance equations, one for each primary variable, using the principle of virtual work (inertial forces accounted for):

$$\left[\delta \int (.)|_E \right]^{u^0} = 0 \,;$$

$$\left[\delta\int(.)|_E\right]^{v^0}=0\,;$$

$$\left[\delta\int(.)|_E\right]^{w^0}=0\,;\tag{6.7}$$

$$\left[\delta\int(.)|_E\right]^{\gamma_x^0}=0\,;$$

$$\left[\delta\int(.)|_E\right]^{\gamma_y^0}=0\,;$$

Then, the corrective displacements Δu^0, Δv^0, Δw^0, $\Delta\gamma_x^0$, $\Delta\gamma_y^0$ appearing in each of these sub-integrals $\delta\int(.)|_E$ are computed by imposing each contribution by the OM model to be equivalent by the energy standpoint to its counterpart by the EM model:

$$\left[\delta\int(.)|_E\right]^{u^0OM}=\left[\delta\int(.)|_E\right]^{u^0EM}=0\,;$$

$$\left[\delta\int(.)|_E\right]^{v^0OM}=\left[\delta\int(.)|_E\right]^{v^0EM}=0\,;$$

$$\left[\delta\int(.)|_E\right]^{w^0OM}=\left[\delta\int(.)|_E\right]^{w^0EM}=0\,;\tag{6.8}$$

$$\left[\delta\int(.)|_E\right]^{\gamma_x^0OM}=\left[\delta\int(.)|_E\right]^{\gamma_x^0EM}=0\,;$$

$$\left[\delta\int(.)|_E\right]^{\gamma_y^0OM}=\left[\delta\int(.)|_E\right]^{\gamma_y^0EM}=0\,;$$

The volume integrals are carried out as $\int(.)=\int_0^x\int_0^y\int_0^z$ so to obtain the corrective

displacements as spatial functions. Eqs. (6.8) impose that the contributions of each d.o.f. of the EM model are equivalent by the energy standpoint to those by the OM model. Therefore, whether the consistent displacement field by the OM model satisfies the energy balance, the modified displacements by the EM model satisfy it too. Thus, they represent an admissible solution, as explained next. Please, note that previous Eqs. (6.8) can be written since OM and EM models have the same functional d.o.f.

Depending on whether the structural problem is solved in closed form, or via a finite element discretization, $\forall^{OM}$ and $\forall^{EM}$ will contain either unknown amplitudes of trial functions or nodal quantities. Through symbolic calculus, the corrective displacements, whose expressions hold for any set of loading and boundary conditions, lay-up and geometry, are obtained in closed form as functions of these unknowns in a straightforward way.

Numerical results will show that this technique is potentially useful for the development of a C^0 finite element.
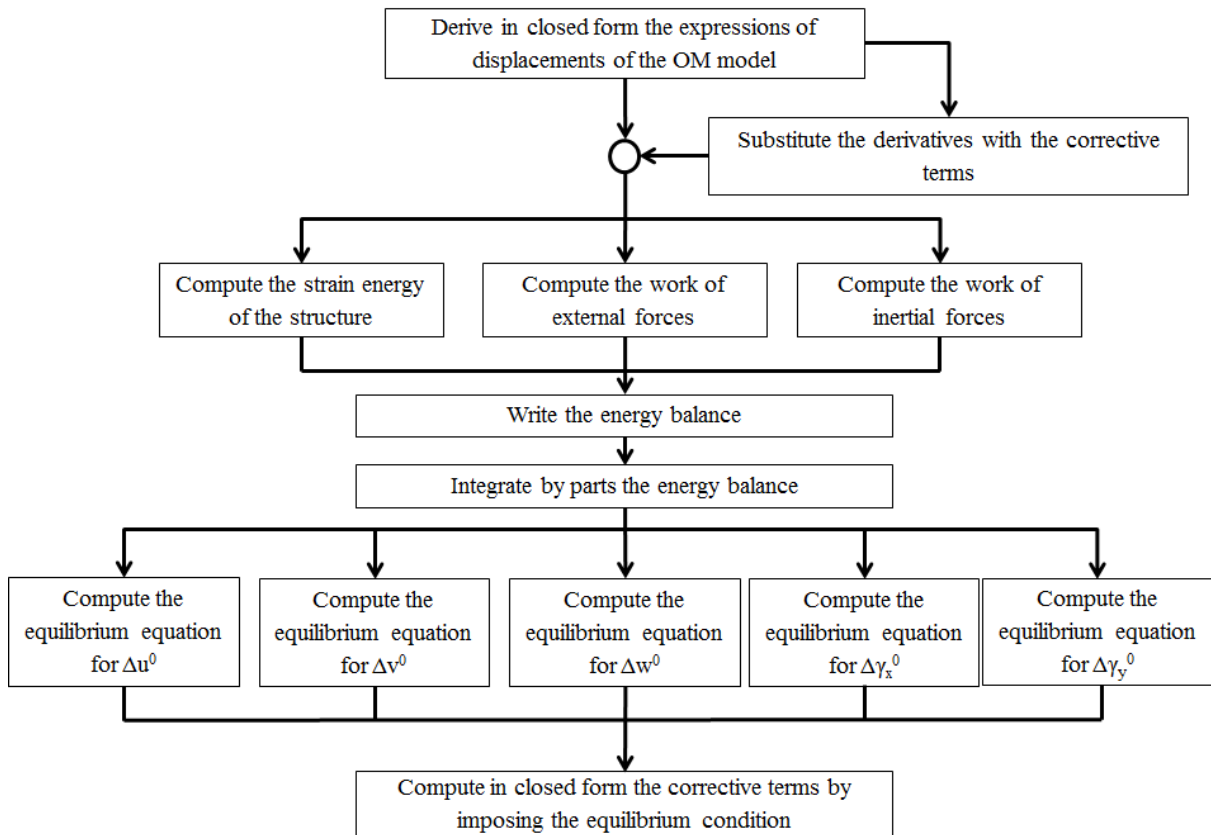
Figure 6.1 Stages of the procedure employed to obtain the equivalent C⁰ model

6.1.2 Steps for deriving the equivalent C^0 EM model

The steps for obtaining the model EM from the model OM are the following ones (see the flow chart of Figure 6.1 for a synthesis).

First, in order to obtain closed form expressions of corrective displacements Δu^0, Δv^0, Δw^0, $\Delta \gamma_x^0$, $\Delta \gamma_y^0$ of general validity from Eqs. (6.8), appropriate spatial distributions of displacements under the same loading and boundary conditions should be postulated. Instead of assuming a spline interpolation of nodal results as in the former applications of SEUPT (see e.g. Icardi [247] and [249]), here an analytical solution is assumed that admits a direct solution in closed form. In this form, besides to be useful for solving Eqs. (6.8), it will speed up computations.

Assume that the domain Ω (i.e. the analysed structure) is decomposed into subdomains, irrespectively of whether the problem will be solved by an analytic approach or via finite elements, and consider a generic subdomain Ω^* inside it. The d.o.f. variation inside Ω^* is expressed through Hermite's polynomials, since they represent the interpolation scheme for developing a conforming element from the OM model. In particular, it is reminded that the conditions (2.6), (2.7) and (2.22) imposed to define higher-order terms and continuity functions of the AD-ZZ model involve derivatives of the functional d.o.f. up to the third order. Therefore, in order to respect the conformity conditions (see [**250**], [**251**]), as interpolation functions at least products of 5th order Hermite polynomials in x and y should be assumed. This interpolation makes continuous the d.o.f. and their derivatives at the bounds of Ω^*. According to this, each d.o.f. of the OM model, here represented in compact form by the symbol $\wp$, is expanded as the sum of Hermite's polynomials $^\rho H_i$ (the superscript ρ refers to the interpolated quantity, the index i is used for indicating the values assumed at the vertices of the square sub-region Ω^*) in x and y as follows:

$$\wp = \sum_{i=1}^{4} {}^{\wp}H_i \wp_i + \sum_{i=1}^{4} {}^{\wp_{,x}}H_i \wp_{i,x} + \sum_{i=1}^{4} {}^{\wp_{,y}}H_i \wp_{i,y} + \sum_{i=1}^{4} {}^{\wp_{,xx}}H_i \wp_{i,xx} + \sum_{i=1}^{4} {}^{\wp_{,xy}}H_i \wp_{i,xy} + \sum_{i=1}^{4} {}^{\wp_{,yy}}H_i \wp_{i,yy} + ... \qquad (6.9)$$

. Terms have been reported only up to the second order of derivation, but additional similar terms can be included for obtaining the continuity also of higher-order derivatives. The purpose of SEUPT is finding a C^0 formulation represented by the equivalent EM model that allows for a computationally efficient Lagrangian representation. This solution is obtained from Eqs. (6.8) assuming the Hermitian representation (6.9) for the OM model and the Lagrangian representation for the EM model. Since the continuity of displacement derivatives and stresses at nodes and sides is an essential requirement that cannot be satisfied by the Lagrangian interpolation, it should be preliminary enforced in the OM model by computing terms Δ^{c-ip} of Eqs (4.6), (4.7) and (4.8).

Once solved Eqs. (6.8), the EM model is made equivalent in terms of energy to the OM model. This means that the two models determine the same results for deflections, buckling loads, free vibration frequencies and whenever the solution is just related to the energy. However, the OM model could be unable to satisfy all the boundary constraints on stresses, which require imposing equivalence between the two models in a point form. Hence, all the quantities containing derivatives of the d.o.f. (i.e. strains and stresses) should be determined

by substituting the closed form expressions of the d.o.f. of the EM model into the analytic OM expressions obtained through symbolic calculus. Explicit expressions being rather lengthy, this is represented in compact form as:

$$\{\sigma\}^{EM} \equiv \{\sigma\}^{OM}$$
$$\{\varepsilon\}^{EM} \equiv \{\varepsilon\}^{OM}$$

(6.10)

These operations that are crucial for obtaining accurate stress predictions by the EM model are inexpensive, since they require a little fraction of time, because it is just required a substitution of data into analytic expressions provided once for all by symbolic calculus. Note that this procedure is similar to what happens for displacement-based finite elements, where the solution provides the nodal values of variables, which are then put into constitutive relations to find stresses.

6.1.3 Application to simple models

Hereafter it is shown how SEUPT can improve the accuracy of a model up to that of another one. To this purpose, two rather simple models for which results can be easily obtained by hands are considered in order to illustrate the procedure. The first model is the FSDPT, whose displacement field is as follows:

$$U(x,y,z) = u^0(x,y) + z\left[\gamma_x^0(x,y) - w^0_{,x}(x,y)\right]$$

$$V(x,y,z) = v^0(x,y) + z\left[\gamma_y^0(x,y) - w^0_{,y}(x,y)\right]$$

(6.11)

$$W(x,y,z) = w^0(x,y)$$

The model (6.11) is updated by using SEUPT up to that of the following cubic model:

$$U(x,y,z) = u^0(x,y) + z\left[\gamma_x^0(x,y) - w^0_{,x}(x,y)\right] + C_x(x,y)z + D_x(x,y)z^3$$

$$V(x,y,z) = v^0(x,y) + z\left[\gamma_y^0(x,y) - w^0_{,y}(x,y)\right] + D_y(x,y)z^3$$

(6.12)

$$W(x,y,z) = w^0(x,y)$$

here named R-HSDPT. Eqs. (6.12) are based on the HSDPT model by Reddy [13], with the addiction of the term linear in z (i.e. C_xz). The unknowns D_x and D_y are computed by imposing the boundary conditions for shear stresses (i.e., Eqs 2.6), while C_x is added in order

to show the capability of the present approach to treat different boundary conditions. Consider a plate clamped in x=0. In order to satisfy the equilibrium at this point one should impose:

$$\int_{-\frac{h}{2}}^{\frac{h}{2}} \sigma_{xz} dz = R_v \qquad (6.13)$$

Where R_v is the constraint force at the clamped edge. From Eq. (6.13) it is possible to easily obtain:

$$C_x = \frac{R_v}{Q_{44} h} \qquad (6.14)$$

It could be noticed that this term, not depending on the functional d.o.f., allows fulfilling the constraints on the clamped edge even if at his point all the functional d.o.f. vanish. Successful applications of this idea are presented in Icardi and Sola [**120**].

For what concerns SEUPT, two corrective terms $\Delta\gamma_x$ and $\Delta\gamma_y$ are now searched in order to make the strain energy of the FSDPT model (6.11) equivalent to that of the R-HSDPT (6.12). Therefore, considering the strain energy of the two confronted model, Eqs. (6.8) turn into:

$$\left[\delta \int (.)|_E \right]^{\gamma_x^0 FSDPT} = \left[\delta \int (.)|_E \right]^{\gamma_x^0 R-HSDPT} = 0$$
$$\left[\delta \int (.)|_E \right]^{\gamma_y^0 FSDPT} = \left[\delta \int (.)|_E \right]^{\gamma_y^0 R-HSDPT} = 0 \qquad (6.15)$$

Note that in Eqs. (6.15) only contributions that depend on the functional d.o.f. are included, therefore the terms (6.14) is not considered in this system. The corrective terms $\Delta\gamma_x$ and $\Delta\gamma_y$ are obtained in a straightforward way, by solving Eqs. (6.15):

$$\Delta\gamma_x(x,y) = -\frac{4}{3h^2} z^2 \gamma_x(x,y)$$
$$\Delta\gamma_y(x,y) = -\frac{4}{3h^2} z^2 \gamma_y(x,y) \qquad (6.16)$$

Note that, these expressions hold for any set of loading and boundary conditions, lay-up and geometry, but, above all, they do not imply the introduction of new d.o.f. In addition, these computations could be performed numerically when solving the static or dynamic problem or when developing finite elements using symbolic calculus. As explained above, this second approach has been adopted here since it allows doing these computations only once, thus dramatically improving efficiency. Finally, it is underlined that Eqs. (6.16) impose

equivalence between the two models only in terms of energy, thus, the updated model is unable to satisfy the boundary constraint fulfilled by the terms (6.14). To overcome this problem, as mentioned above, it is necessary to impose equivalence between the two models in a point form as in Eqs. (6.10).

Once solved these last equations, the two models considered are coincident. .

6.2 Numerical applications of SEUPT

Numerical assessments will be presented with the aim of showing whether the present version of SEUPT provides an effective way for obtaining the EM C^0 equivalent version of the zig-zag model OM [**119**], without losing accuracy. It is reminded that in Chapter 3 this model has been already proven to be accurate and computationally efficient when closed form solutions are considered, since it achieves the accuracy of layerwise models with just five d.o.f. Therefore, the aim of present numerical results is to assess the accuracy of the C^0 equivalent EM model comparing its predictions to those of the OM model.

To reach this goal, as benchmark test cases, multi-layered beams with simply-supported edges in cylindrical bending under sinusoidal transverse distributed loading are considered, which simulate laminated and sandwich beams with laminated faces. These apparently quite unrealistic test cases, owing to their loading and boundary conditions, are considered because the exact 3D elasticity solution is available, so it can be used as a reliable reference solution for comparing the predictions of EM and OM models. To this reason, these test cases are often considered in literature by researchers who assess the accuracy of available theories. Therefore, in addition to exact results, also a large amount of approximate results by a variety of models is available for comparisons. Interest to these cases is also due to the possibility of obtaining results in closed form by the EM and OM models as Navier's solutions, which do not suffer from round-off and discretization errors intrinsic of numerical solutions like those by finite elements. It could be observed that when analytical solutions can be found, as for the test cases here considered, there is no need of C^0 models because the derivatives of the d.o.f. do not represent a drawback for this type of solution, while they are for finite elements. Therefore, analytical results by the EM model seem apparently meaningless, but instead they represent a necessary preliminary stage because, before developing finite elements, since the

capability of the EM equivalent C^0 model of preserving features and advantages of the OM model should be assessed.

The comparison between EM and OM models is extended also to damaged sandwich beams. The damage is simulated reducing the elastic moduli, according to the ply discount theory, as already done previously. Simply-supported, sandwich beams with damaged faces and/or core, undergoing sinusoidal transverse loading are considered and, in addition, the damage is assumed to be distributed over the entire length, because in this case the exact elasticity solution can be still found [107] and used for comparisons. As stated above, owing to the reduction of elastic moduli used for simulating the damage rise, intricate through-the-thickness distributions of out-of-plane stresses take place as a consequence of asymmetric, distinctly different properties, which make the samples considered a very severe test case for the models.
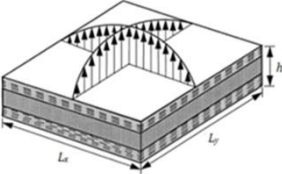
As further assessment, the case of a cantilever beam will be considered in order to show whether the EM model likewise the OM model can treat boundary conditions of practical interest that are difficult to satisfy.

6.2.1 Simply-supported edges and sinusoidal loading

Symmetrical cross-ply plate - As a preliminary assessment, it is considered the simply supported [0°/90°/0°] laminated square plate analysed in [145] and [246] and customarily considered as benchmark by many researchers. The constituent material is mat-p (E_L/E_T=25; G_{LT}/E_T=0.5; G_{TT}/E_T=0.2; υ_{LT}=0.25) and each layer has the thickness equal to h/3. Different length to thickness ratios are considered in Table 6.1 where the stress field and the transverse displacement are reported normalized as follows:

$$\overline{\sigma}_{xx} = \sigma_{xx}\left(\frac{L_x}{2},\frac{L_y}{2},\frac{h}{2}\right)\frac{h^2}{L_x^2\,p^0} \quad \overline{\sigma}_{yy} = \sigma_{yy}\left(\frac{L_x}{2},\frac{L_y}{2},\frac{h}{6}\right)\frac{h^2}{L_x^2\,p^0} \quad \overline{\sigma}_{xy} = \sigma_{xy}\left(0,0,\frac{h}{2}\right)\frac{h^2}{L_x^2\,p^0}$$

$$\overline{\sigma}_{xz} = \sigma_{xz}\left(0,\frac{L_y}{2},0\right)\frac{h}{L_x\,p^0} \quad \overline{\sigma}_{yz} = \sigma_{yz}\left(\frac{L_x}{2},0,0\right)\frac{h}{L_x\,p^0} \quad \overline{w} = w\left(\frac{L_x}{2},\frac{L_y}{2},0\right)\frac{100E_T h^3}{L_x^4 p^0} \qquad (6.17)$$

The numerical results of Table 6.1 show that the OM model is accurate and it does not suffer from locking, since always accurate results are obtained.

L_x/h	Model	$\overline{w}$	$\overline{\sigma}_{xx}$	$\overline{\sigma}_{yy}$	$\overline{\sigma}_{xy}$	$\overline{\sigma}_{xz}$	$\overline{\sigma}_{yz}$
4	Exact [145]	2.006	0.755	0.556	0.0505	0.2560	0.216
	Ref. [246]	1.9597	0.7819	0.5195	0.051	0.2335	0.1885
	OM present	1.9988	0.761	0.549	0.0508	0.2573	0.219
10	Exact [145]	0.7405	0.59	0.288	0.0289	0.357	0.123
	Ref. [246]	0.7316	0.596	0.2792	0.0288	0.3094	0.107
	OM present	0.7402	0.591	0.285	0.0289	0.359	0.120
20	Exact [145]	-	0.552	0.2115	0.0234	0.385	0.094
	Ref. [246]	0.5098	0.558	0.2088	0.0234	0.3286	0.084
	OM present	0.5105	0.553	0.2110	0.0234	0.382	0.090
50	Exact [145]	-	0.541	0.185	0.0216	0.393	0.084
	Ref. [246]	0.4439	0.5465	0.186	0.0218	0.3347	0.0766
	OM present	0.4451	0.542	0.185	0.0216	0.390	0.085
100	Exact [145]	0.4347	0.539	0.181	0.0213	0.3947	0.083
	Ref. [246]	0.4343	0.5448	0.182	0.0215	0.3355	0.0755
	OM present	0.4346	0.538	0.181	0.0213	0.3949	0.083

Table 6.1 Non-dimensional deflection and stresses of simply supported laminated [0•/90•/0•] plate under bi-sinusoidal loading.

Asymmetrical cross-ply beam - As a subsequent test, it is considered the [0°/90°/0°/90°] asymmetrical cross-ply beam formerly analysed in [72] having 4 layers in mat-p of equal thickness (0.25h/0.25h/ 0.25h/0.25h). Because the lay-up is asymmetrical, this sample case is suitable to investigate whether the EM model provides accurate results, the stress fields being strongly asymmetrical too.

As already mentioned above, these results refer to an extremely thick case with a length-to-thickness ratio ($L_x/h=S$) of 4 and simply-supported edges, undergoing a sinusoidal distributed transverse loading

$$p^0(x) = \sum_{m=1}^{M} P_m \sin\left(\frac{m\pi}{L_x}x\right) \tag{6.18}$$

Like in [72], in the present case just a single component, i.e. M=1, is considered. Solution to this case is assumed as a series expansion as follow:

$$u^0(x,y)=\sum_{m=1}^{M}A_m\cos\left(\frac{m\pi}{L_x}x\right) \quad w^0(x,y)=\sum_{m=1}^{M}C_m\sin\left(\frac{m\pi}{L_x}x\right) \quad \gamma_x^{\ 0}(x,y)=\sum_{m=1}^{M}D_m\cos\left(\frac{m\pi}{L_x}x\right) \tag{6.19}$$

The trigonometric functions (6.19) are chosen because they satisfy the simply-supported kinematic boundary constraint conditions $w^0 = w_{,x}^0 = 0$, whereas A_m, C_m and D_m constitute the unknown amplitudes. Once substituted in the governing equations, obtained applying the Rayleigh-Ritz method in standard form, the unknown amplitudes are computed in a straightforward way solving an algebraic problem. The results of Figure 6.2 have been computed considering M=1 in Eqs. (6.19) and choosing a third order expansion of the in-plane displacement, a fourth-order expansion of the transverse displacement and a single computational layer for discretizing each physical layer. It is reminded that, nevertheless four different computational layers are considered, the number of functional d.o.f of the OM model does not increase. In the present case they are just three, like for the FSDPT model, since no variation rise in the *y* direction. Of course, the overall number of d.o.f., i.e. the dimension of the algebraic system depends upon the expansion order chosen in Eq. (6.19). In the present case it corresponds to a 3x3 system.

The results of Figure 6.2 are reported in the following normalized form:

$$\overline{\sigma}_{xz}=\frac{\sigma_{xz}(0,z)}{p^0} \quad \overline{\sigma}_{xx}=\frac{\sigma_{xx}\left(\frac{L_x}{2},z\right)}{p^0} \quad \overline{\sigma}_{zz}=\frac{\sigma_{xx}\left(\frac{L_x}{2},z\right)}{p^0} \quad \overline{u}=\frac{E_2u(0,z)}{hp^0} \quad \overline{w}=\frac{E_2w\left(\frac{L_x}{2},z\right)}{hp^0} \tag{6.20}$$

Figure 6.2a represents the through-the-thickness variation of the shear stress $\overline{\sigma}_{xz}$ predicted by the AD-ZZ model (OM model) and by its equivalent C^0 counterpart EM, compared to the exact solution found in [**72**] applying the Pagano's method [**144**]. Figure 6.2b represents the through-the-thickness variation of the in-plane displacement $\overline{u}$ by the OM, by the EM models, and by the exact solution [**72**]. These results show that the predictions of models OM and EM are in good agreement with each other and with the exact solution thus demonstrating the effectiveness of the present technique in obtaining an equivalent C^0 model. It should be observed that the results of Figure 6.2a are obtained directly from constitutive equations. Thus, as already shown in Chapter 3, no post-processing techniques are required to obtain accurate results, as confirmed by the correct variation of the displacements of Figure 6.2b.
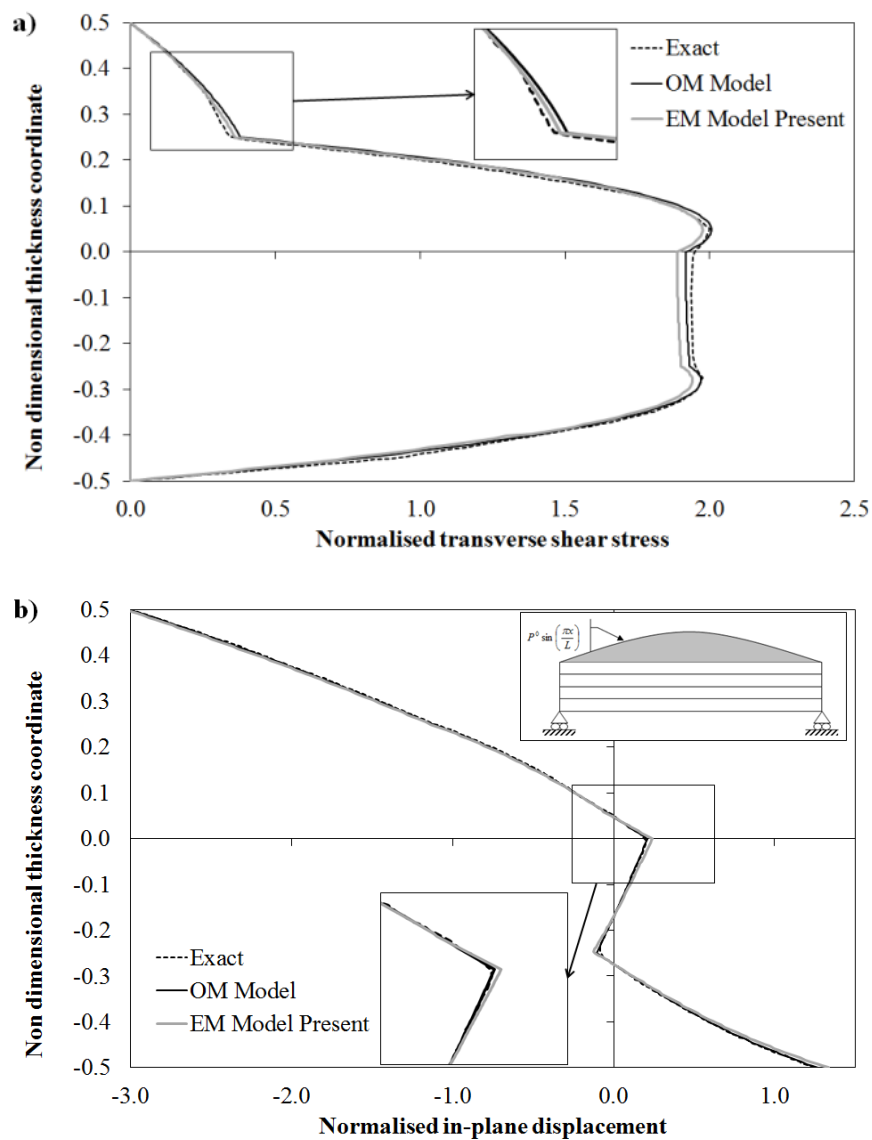
Figure 6.2 Exact solution and through-the-thickness distribution of: a) normalized transverse shear stress; b) normalized in-plane displacement by the OM Model [119] and by the present EM Model for a laminated [0°/90°/0°/90°] beam.

Sandwich beam - Now the sample case of a sandwich beam with asymmetrical properties is considered in order to assess the quality of results provided by the EM model when the properties of the constituent layers are distinctly different.

It is here retaken the same sample case already considered in Chapter 3, for which the exact 3D elasticity solution was obtained again applying the technique [**144**]. It is reminded that the face layers are made of materials MAT1 to MAT3, while the core is made of material MAT4 (MAT 1: $E_1=E_3=1$ GPa, $G_{13}=0.2$ GPa, $\upsilon_{13}=0.25$; MAT 2: $E_1=33$ GPa, $E_3=1$ GPa, $G_{13}=0.8$ GPa, $\upsilon_{13}=0.25$; MAT 3: $E_1=25$ GPa, $E_3=1$ GPa, $G_{13}=0.5$ GPa, $\upsilon_{13}=0.25$; MAT 4: $E_1=E_3=0.05$

151

GPa, G_{13}=0.0217 GPa, υ_{13}=0.15), the lay-up sequence being chosen as (MAT 1/2/3/1/3/4)$_s$, with the following thickness ratios of the constituent layers (0.010/0.025 /0.015/0.020/0.030/0.4)$_s$. Also in this case, a length-to-thickness ratio ($L_x/h=S$) of 4 is considered.

The loading and boundary conditions, the series expansion used for representing the displacements (6.19) and the normalisation (6.20) are still used.

It can be seen from the results of Figure 6.3 that the equivalent C^0 EM model gives as accurate results as the OM model also for this case. In particular, both models are shown to accurately predict the interlaminar stresses directly from constitutive equations even when the variations are rather intricate. The success of the EM model shows that a C^0 equivalent formulation can be obtained by SEUPT in order to eliminate the derivatives of the d.o.f. that follows from the enforcements of the physical constraints inside any physically-based zig-zag model.
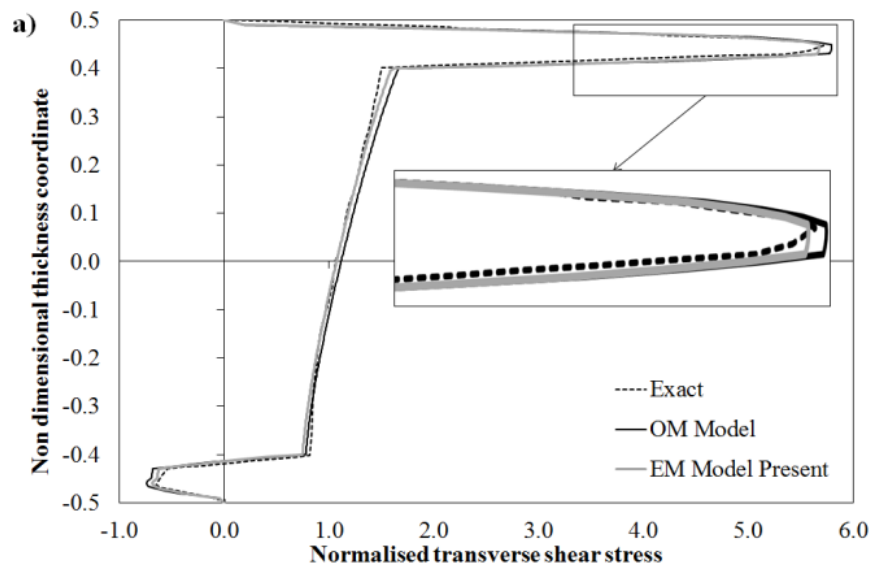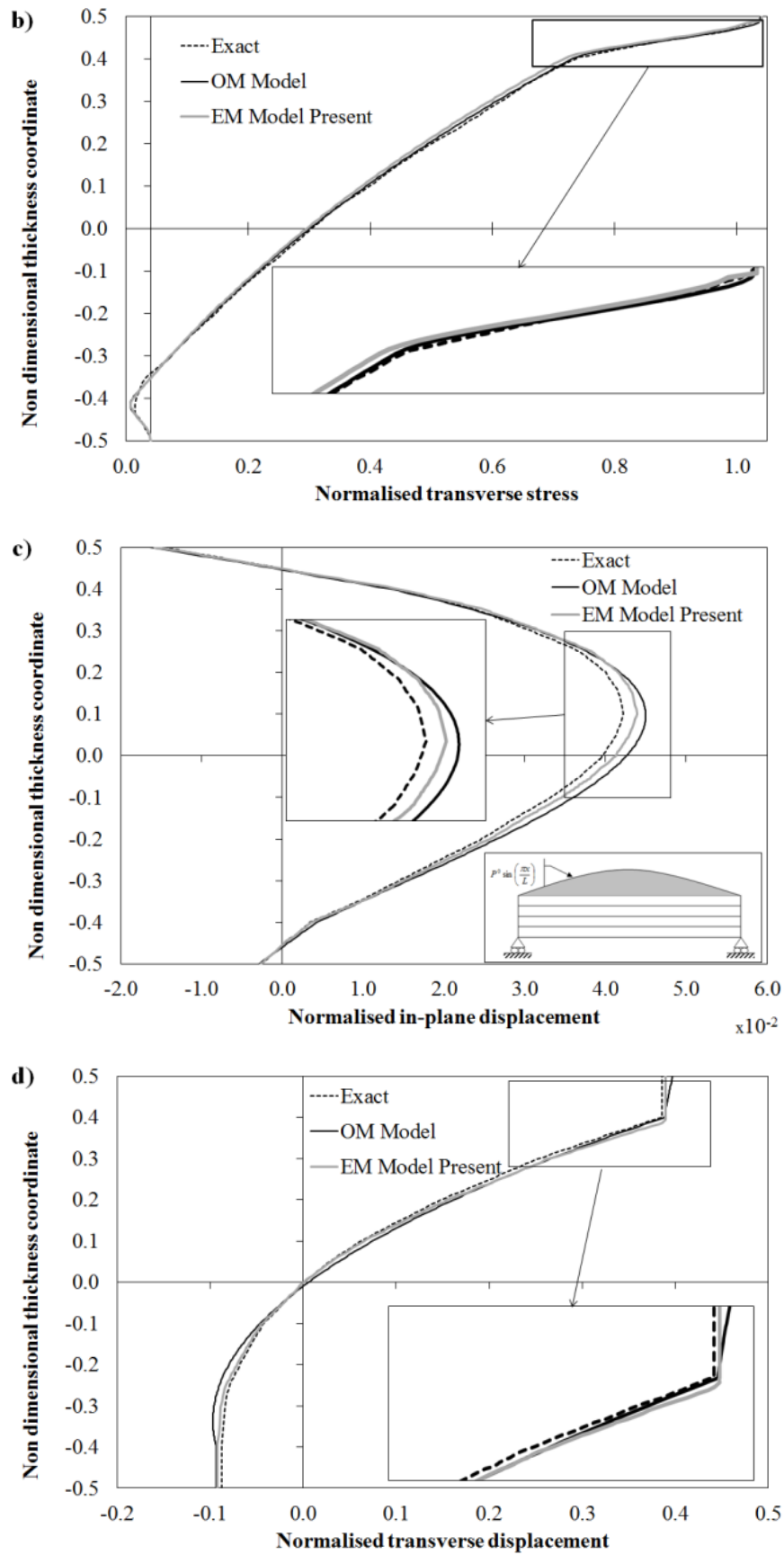
Figure 6.3 Exact solution and through-the-thickness distribution of: a) normalized transverse shear stress; b) normalized transverse stress; c) normalized in-plane displacement; d) normalized transverse displacement by the OM Model [119] and by the present EM model for a sandwich beam with damaged upper face.

6.2.2 Clamped edges

Since a distinctive feature of the OM model consists in the possibility of enforcing a non-vanishing transverse shear stress at clamped edges, where the mid-plane displacements and shear rotations must vanish, it should be tested whether this capability is preserved by the EM equivalent model. As already mentioned, it is reminded that once displacements and shear rotations are enforced to vanish within conventional models having the mid-plane displacements and shear rotations as functional d.o.f., a vanishing transverse shear is obtained that gives rise to poor results. On the contrary, the OM model can correctly enforce these boundary conditions because high-order contributions can be determined by enforcing any desired set of boundary conditions, the coefficients appearing in these terms being computed through the enforcement of the desired conditions.

In order to assess whether the equivalent C^0 EM model can accurately describe the stress field with clamped edges, the cantilever sandwich beam subjected to a uniform transverse loading of Ref. [**129**] is again considered. It is reminded that the structure has the faces in unidirectional Carbon-Epoxy laminates (E_1= 157.9 GPa, E_2=E_3= 9.584 GPa, G_{12}= G_{13}= 5.930 GPa, G_{23}= 3.277 GPa, ν_{12}= ν_{13}= 0.32, ν_{23}= 0.49) and a PVC foam core (E= 0.1040 GPa, ν= 0.3). It has a length-to-thickness ratio of 10 and the thickness ratios of the constituent layers are [0.1h/0.8h/0.1h].

As already done in Chapter 3, according to [**129**], the trial functions for the displacement d.o.f. are represented as products of orthogonal one-dimensional Gram–Schmidt polynomial in the *x* and *y* directions.

Figure 6.3 reports the through-the-thickness distribution of the transverse shear stress, which is normalized as follows:

$$\overline{\sigma}_{xz} = \frac{h}{L_x p^0} \sigma_{xz}\left(\frac{L_x}{5}, \frac{L_y}{2}, z\right) \tag{6.21}$$

The results show that the EM model accurately predicts the through-the-thickness variation of the transverse shear stress at clamped edges. Being in good agreement with the results given

in [**129**], the equivalent EM model is still shown successful.
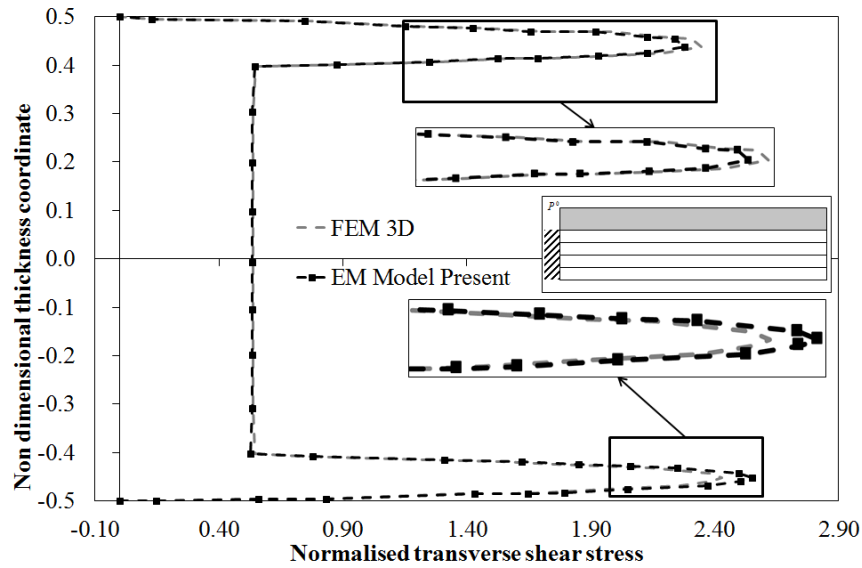
***Figure 6.4 Normalized transverse shear stress by the present EM Model and by the 3D FEM [129]
for a cantilever sandwich beam.***

Results presented in this section have demonstrated that through SEUPT a C^0 formulation of the AD-ZZ model can be easily obtained preserving its accuracy. For what concerns efficiency, the application of SEUPT claims for nearly 630 s when the symbolic calculus has to be carried out to compute the closed form expressions of the d.o.f. of the EM model. Instead, if the closed form expressions of the EM d.o.f. are already known the computational times of the analysis are the 10% higher than those of the AD-ZZ model. These times refer to analyses performed on a laptop computer with a 1.80 GHz double-core processor and 4 GB RAM.

The next chapter focuses the attention on the formulation of finite elements of class C^0 based on the AD-ZZ model, taking advantage of SEUPT.

Chapter 7: Finite element implementations

In the previous chapter the effectiveness of SEUPT in obtaining a C^0 formulation of the AD-ZZ model without prejudicing its accuracy has been demonstrated. As stated above, the following step implies developing finite elements taking advantage of this technique.

7.1 C^0 displacement based finite element

In the present Section, the main steps towards the development of a displacement based finite element of class C^0 will be summarized and its accuracy will be assessed.

7.1.1 Formulation

Because no derivatives are involved as nodal d.o.f., serendipity interpolation functions can be used. Thus, the vector of nodal unknowns can be assumed as:

$$\{Q\} = \left\{ \left[u_1^0, v_1^0, w_1^0, \gamma_{x1}^0, \gamma_{y1}^0 \right] *, \ldots, \left[u_8^0, v_8^0, w_8^0, \gamma_{x8}^0, \gamma_{y8}^0 \right] * \right\}^T \tag{7.1}$$

(see Figure 7.1).
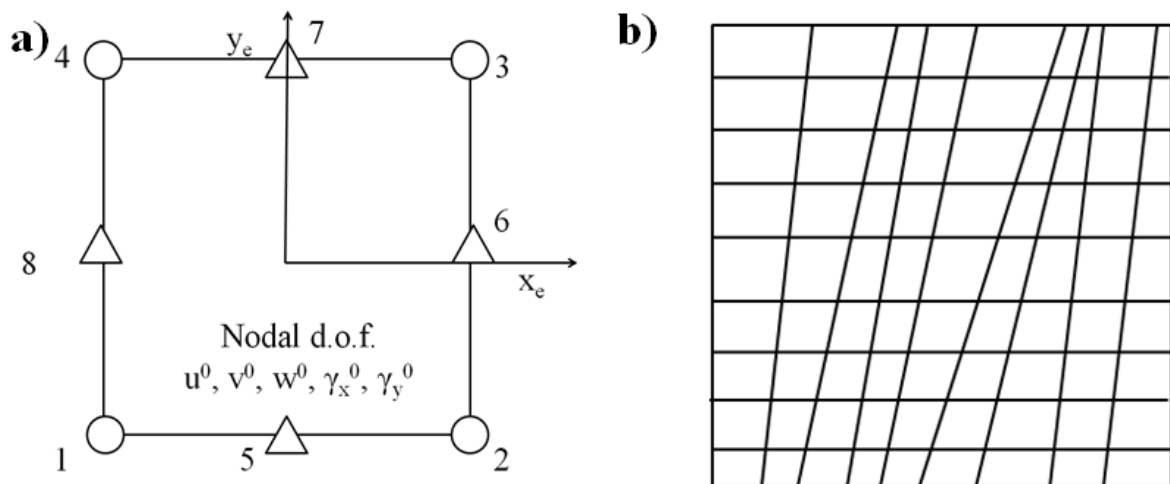
Figure 7.1 a) Reference system for the element in the natural plane; b) the distorted meshing used in Table 7.2 .

Such a parabolic representation is not chosen to integrate local equilibrium equations for predicting interlaminar stresses like for the standard shear deformable elements. Instead, it is just chosen in order to obtain accurate results with a relatively coarse meshing. Indeed, as shown by the numerical results given previously, either the AD-ZZ model or its equivalent C^0 counterpart obtained through SEUPT accurately predict stresses from constitutive equations, with no need of any post-processing operation like integration. It is well known that the accuracy of isoparametric elements can be improved by computing stresses at selected points inside elements and by altering the elastic coefficients for transverse shear (see Cook et al. [252]). This is unnecessary for the present element because the consistency of the discretized strain fields is guaranteed by the AD-ZZ model used for computing them. Another reason that justifies the choice of considering an eight node element is that accuracy of isoparametric quadrilateral element is too poor, as shown in the literature. As a general remark, it is also underlined that parabolic interpolation allows the edges to be curved, though this feature is not exploited here.

Since a separate representation of w^{0*}, γ_x^{0*}, γ_y^{0*} is chosen, the element does not suffer from shear locking, as shown forward by numerical results for thin laminates. Indeed, as indicated by Prathap [250], this separate representation prevents from loss of the consistent relation between shear forces and bending moments of elements.

The variation of a generic variable q inside the element is represented as customarily by:

$$\{q\} = [N]\{Q\} \tag{7.2}$$

$[N]$ being the matrix of shape functions. At corners nodes (i=1, 2, 3, 4) they are expressed by:

$$N_i = \frac{1}{4}(1 + \xi\xi_i)(1 + \eta\eta_i)(\xi\xi_i + \eta\eta_i - 1) \tag{7.3}$$

while at mid-side nodes they are:

$$N_i = \frac{1}{2}(1 - \xi^2)(1 + \eta\eta_i) \text{ for (i= 5, 7)} \tag{7.4}$$

$$N_i = \frac{1}{2}(1 - \eta^2)(1 + \xi\xi_i) \text{ for (i= 6, 8)} \tag{7.5}$$

Where ξ_i and η_i can assume the value $\pm$ 1.

To standardize the computation of integrals, mapping is used for obtaining a square element with unit sides from any quadrilateral element in the physical plane

$$x = \sum_{i=1}^{8} x_i N_i \text{ and } y = \sum_{i=1}^{8} y_i N_i \tag{7.6}$$

An isoparametric formulation is chosen in order to efficiently compute the Jacobian matrix

$$[J] = \begin{bmatrix} \dfrac{\partial x}{\partial \xi} & \dfrac{\partial y}{\partial \xi} \\ \dfrac{\partial x}{\partial \eta} & \dfrac{\partial y}{\partial \eta} \end{bmatrix} \tag{7.7}$$

So to obtain the physical derivatives $\dfrac{\partial}{\partial x}$, $\dfrac{\partial}{\partial y}$ from the derivatives $\dfrac{\partial}{\partial \xi}$, $\dfrac{\partial}{\partial \eta}$ over the natural plane

$$\begin{Bmatrix} \dfrac{\partial}{\partial x} \\ \dfrac{\partial}{\partial y} \end{Bmatrix} = [J]^{-1} \begin{Bmatrix} \dfrac{\partial}{\partial \xi} \\ \dfrac{\partial}{\partial \eta} \end{Bmatrix} \tag{7.8}$$

The strains are expressed as:

$$\{\varepsilon\} = [B]\{Q\} \tag{7.9}$$

(herein just infinitesimal strains are considered) and the stresses as:

$$\{\sigma\} = [D][B]\{Q\} \tag{7.10}$$

[D] being the matrix of 3D elastic coefficients. Using previous definitions, the stiffness matrix is obtained from the strain energy functional as:

$$[K] = \int_{Ve} [B]^T [D][B] dV \tag{7.11}$$

V_e being the volume of the element, while the mass matrix is obtained from the kinetic energy functional as:

$$[M] = \int_{Ve} \rho[N]^T [N] dV \tag{7.12}$$

ρ being the density. The vector of nodal loads is obtained from the expression of the work of external forces as:

$$\{Fe\} = \int_{Ve} [N]^T \{\overline{X}\} dV - \int_{Se} [N]^T \{\bar{f}\} dS - [N]^T \{\widetilde{F}\} \tag{7.13}$$

$\{\overline{X}\}$ being the vector of body forces, $\{\bar{f}\}$ the vector of surface forces applied on the surface S_e and $\{\widetilde{F}\}$ the point forces. Then, equilibrium equation is obtained (Zienkiewicz and Taylor [**251**]):

$$[K]\{Q\} + [M]\{\ddot{Q}\} = \{Fe\} \tag{7.14}$$

The computation of integrals involved in the former relations is carried out using a 3x3 Gaussian integrations scheme. Selective reduced integration is unnecessary because locking is avoided. In multilayered structures, the integrals are carried out summing the contributions layer-by-layer.

7.1.2 Applications

The accuracy of the displacement-based finite element will be assessed by comparing its results with exact solutions of sample test cases available in the literature and to the results by the AD-ZZ model in closed form.

Lay-up, loading and boundary conditions traditionally used by researchers for assessing the accuracy of models are considered. All the computational times reported in this section are obtained performing the analyses on a laptop computer with a 1.80 GHz double-core processor and 4 GB RAM.

Case A. First, the classical sample test case of a simply supported, unsymmetrical [0°/90°] laminated square plate undergoing bisinusoidal loading is analysed. The exact solution for this sample case recently retaken by Thai and Choi [**253**] to test their model was provided by Pagano [**145**].

The two constituent layers are in MAT p (E_L/E_T=25; G_{LT}/E_T=0.5; G_{TT}/E_T=0.2; υ_{LT}=0.25) and each has thickness equal to the laminate half thickness (h/2). Different length to thickness ratios are considered in Table 7.1 where the transverse displacement is reported normalized as follows:

$$\bar{w} = w\left(\frac{L_x}{2},\frac{L_y}{2},0\right)\frac{100E_2 h^3}{L_x^4 p^0} \tag{7.15}$$

The numbers in square brackets in Table 7.1 are the computational time required by the AD-ZZ model and by the present implementation (superscript F). Due to the symmetry of the problem just a quarter of the plate is discretized considering a 9x9 meshing. Results of Table 7.1 confirm that the present finite element does not suffer from locking and it is as accurate as the AD-ZZ model.

L/h	Exact [145]	Thai and Choi [253]	AD-ZZ model [119]	Present
2 [1.20 s;3.05^F s]	4.9362	5.4059	5.0536	5.0735
5 [0.89 s;2.62^F s]	1.7287	1.7584	1.7299	1.7315
10 [0.78 s;1.93^F s]	1.2318	1.2373	1.2325	1.2336
20 [0.65 s;1.45^F s]	1.1060	1.1070	1.1065	1.1065
100 [0.51 s;1.35^F s]	1.0742	1.0636	1.0743	1.0743

Table 7.1 Transverse displacement for a simply supported [0°/90°] laminated plate, as predicted by: present element, AD-ZZ model (Icardi and Sola [119]) and exact solutions.

Case B. Now it is considered a sandwich plate subjected to doubly sinusoidal transverse loading, whose exact solution was derived by Zhen and Wanji [**72**]. The mechanical properties of face plies, made of a high modulus graphite/epoxy composite, are: E_1=172.4 GPa, E_2=E_3=6.89 GPa, G_{12}=G_{13}=3.45 GPa, G_{23}=1.378 GPa, υ_{12}=υ_{12}=υ_{23}=0.25, while those of the foam core are: E_1=E_2=0.276 GPa, E_3=345GPa, G_{13}=G_{23}=0.414 GPa, G_{12}=0.1104 GPa, υ_{12}=υ_{13}=υ_{23}=0.25. The thickness of the face sheets at the upper and the lower surfaces are equal to 0.1h, whereas the thickness of core is of 0.8h. In Table 7.2, stresses and displacements for different length-to-thickness ratios (L/h) are reported normalized as follows:

$$\overline{\sigma}^{\,u}_{\,xx} = \frac{\sigma_{xx}\left(0,0,\dfrac{h}{2}\right)h^2}{q^0 L_x^2}$$

$$\overline{\sigma}^{\,l}_{\,xx} = \frac{\sigma_{xx}\left(0,0,-\dfrac{h}{2}\right)h^2}{q^0 L_x^2}$$

$$\overline{\sigma}_{\,xz} = \frac{\sigma_{xz}\left(\dfrac{L_x}{2},0,0\right)h}{q^0 L_x}$$

$$\overline{\sigma}_{\,yz} = \frac{\sigma_{yz}\left(0,\dfrac{L_y}{2},0\right)h}{q^0 L_x}$$

(7.16)

The results of Table 7.2 show again that the finite element obtains accurate results both for thick and thin structures with low computational cost. Thus, it is still shown that the finite element model gives results having the same accuracy as those predicted in closed form by the OM model over which it is based.

Convergence tests reported in Table 7.2 show the capability of the element to accurately predict the out-of-plane critical stresses with a rather coarse discretization. Progressively refined results are obtained from a 3x3 to a 9x9 meshing on a quarter of the plate, due to symmetry of the problem, as reported in Table 7.2 along with computational times (number in square brackets). Results regarding analyses with distorted meshing (results with superscript D) are also reported in Table 7.2.

L/h		$\overline{\sigma}^{\,u}_{\,xx}$	$\overline{\sigma}^{\,l}_{\,xx}$	$\overline{\sigma}_{\,xz}$	$\overline{\sigma}_{\,yz}$
4	Zhen and Wanji [72]	1.5622	-1.5622	0.1505	0.1325
	AD-ZZ Model [1.15 s]	1.5622	-1.5300	0.1505	0.1363
	Present (3x3) [1.88 s]	1.7030	-1.6857	0.1326	0.1243
	Present (5x5) [2.22 s]	1.5779	-1.5986	0.1370	0.1317
	Present (9x9) [2.88 s]	1.5622	-1.5250	0.1505	0.1375
	Present (9x9) [D] [2.89 s]	1.6403	-1.6088	0.1594	0.1442
10	Zhen and Wanji [72]	1.1686	-1.1686	0.2957	0.0506
	AD-ZZ Model [1 s]	1.1686	-1.1650	0.2957	0.0506
	Present (3x3) [1.66 s]	1.1983	-1.1855	0.2605	0.0456
	Present (5x5) [1.98 s]	1.1722	-1.1621	0.2898	0.0493
	Present (9x9) [2.2 s]	1.1686	-1.1599	0.2957	0.0506
	Present (9x9) [D] [2.24 s]	1.1856	-1.176	0.3015	0.0515
20	Zhen and Wanji [72]	1.1101	-1.1101	0.3174	0.0360

AD-ZZ Model [0.66 s]	1.1101	-1.1101	0.3174	0.0360
Present (3x3) [0.92 s]	1.1105	-1.1105	0.3180	0.0356
Present (5x5) [1.23 s]	1.1103	-1.1103	0.3177	0.0359
Present (9x9) [1.66 s]	1.1101	-1.1101	0.3174	0.0360
Present (9x9) [D] [1.68 s]	1.1106	1.1106	0.3178	0.0362

Table 7.2 Stress field for a simply supported sandwich plate, as predicted by: present element, AD-ZZ model (Icardi and Sola [119]) and exact solutions. [Superscript D stands for distorted mesh (see Figure 7.1)].

Case C. The next case considers the square sandwich plate studied by Sahoo and Singh [**246**]. The structure is clamped on all the four sides and it is undergoing a bisinusoidal distributed load of intensity q^0. The faces are realized in MAT p (E_L/E_T=25; G_{LT}/E_T=0.5; G_{TT}/E_T=0.2; υ_{LT}=0.25). The mechanical properties of the foam material constituting the core are: E_1/E_{TF} =E_2/E_{TF} =0.04, E_3/E_{TF} =0.5, G_{13}/E_{TF} =G_{23}/E_{TF} =0.06, G_{12}/E_{TF} =0.016, υ_{12}=υ_{13}=υ_{23}=0.25. The thickness distribution of the layers is [0.1h/0.8h/0.1h]; where h is the overall thickness of the plate. Table 7.3 reports displacements and stresses for different length-to-thickness ratios, normalized as follows:

$$\overline{w} = w\left(\frac{L_x}{2},\frac{L_y}{2},0\right)\frac{100E_{2_f}h^3}{L_y^4 p^0}$$

$$\left\{\overline{\sigma}_{xx},\overline{\sigma}_{yy},\overline{\sigma}_{xy}\right\} = \left\{\sigma_{xx}\left(\frac{L_x}{2},\frac{L_y}{2},\frac{h}{2}\right),\sigma_{yy}\left(\frac{L_x}{2},\frac{L_y}{2},\frac{h}{2}\right),\sigma_{xy}\left(0,0,\frac{h}{2}\right)\right\}\frac{h^2}{q^0 L_y^2} \qquad (7.17)$$

$$\overline{\sigma}_{xz} = \frac{\sigma_{xz}\left(0,\frac{L_y}{2},0\right)h}{q^0 L_y}$$

Due to the symmetry of the problem, also in this case just a quarter of the plate is discretized considering a 9x9 meshing. As previously, the numbers reported in square brackets still represent the computational times required by the AD-ZZ model and by the FEM model (superscript F) to perform the analyses.

The numerical results of Table 7.3 show that the present element can accurately treat also structures with clamped edges.

L/h		$\overline{w}$	$\overline{\sigma}_{xx}$	$\overline{\sigma}_{yy}$	$\overline{\sigma}_{xy}$	$\overline{\sigma}_{xz}$
	Sahoo and Singh [**246**]	17.3124	2.2047	0.2366	0.0868	0.1061
2 [1.45 s;3.6 [F] s]	AD-ZZ Model	17.3125	2.2047	0.2366	0.0868	0.1061
	Present	17.3125	2.2048	0.2366	0.0868	0.1065

	Sahoo and Singh [246]	3.9718	0.7798	0.1506	0.0493	0.1962
5 [1.30 s;3.25 ^{F} s]	AD-ZZ Model	3.9719	0.7798	0.1506	0.0493	0.1963
	Present	3.9719	0.7798	0.1506	0.0493	0.1964
	Sahoo and Singh [246]	1.4269	0.5184	0.0774	0.0300	0.2719
10 [1.13 s;2.98 ^{F} s]	AD-ZZ Model	1.4269	0.5184	0.0774	0.0300	0.2719
	Present	1.4269	0.5184	0.0774	0.0300	0.2719

Table 7.3 Stress and displacement fields for a clamped sandwich plate, as predicted by: present element, OM model (Icardi and Sola [119]) and exact solutions.

Case D. Aiming at verifying the accuracy of the present element also for angle-ply structures a four-layered antisymmetric [30°/-30°/30°/-30°] square plate is analysed. The constituent layers, each having thickness h/4, are in mat p (E_L/E_T=25; G_{LT}/E_T=0.5; G_{TT}/E_T=0.2; υ_{LT}=0.25). The plate is simply supported, it has a length-to-thickness ratio (L/h) of 4 and it is undergoing a bi-sinusoidal loading. According to Savoia and Reddy [254], who provides the exact 3D solution for this case, the quantities reported in Figure 7.2 are normalized as follows:

$$\left\{ \overline{\sigma}_{xz} ; \overline{\sigma}_{yz} \right\} = \left\{ \sigma_{xz}\left(0,\frac{L_y}{2}\right); \sigma_{yz}\left(\frac{L_x}{2};0\right) \right\} \frac{h}{q^0 L_x}$$

$$\left\{ \overline{u} ; \overline{v} \right\} = \left\{ u\left(0,\frac{L_y}{2}\right); v\left(\frac{L_x}{2};0\right) \right\} \frac{E_2 h}{q^0 L_x^2}$$

(7.18)

As a general remark to the results of Figure 7.2, it could be noticed that considering the interfaces between the layers 1-2 and 3-4 the through-the-thickness distributions of in-plane displacements have a slope, which varies, but without reversing as postulated by geometrically-based zig-zag function (1.8). For what concerns the accuracy of the present model, the results of Figure 7.2 confirm it for this case, even for the completely antisymmetric distribution of the transverse shear stress $\overline{\sigma}_{yz}$. Computations have been carried out considering 225 elements on a quarter of the plate (inset in Figure 7.2) and they take 10 s to be performed.
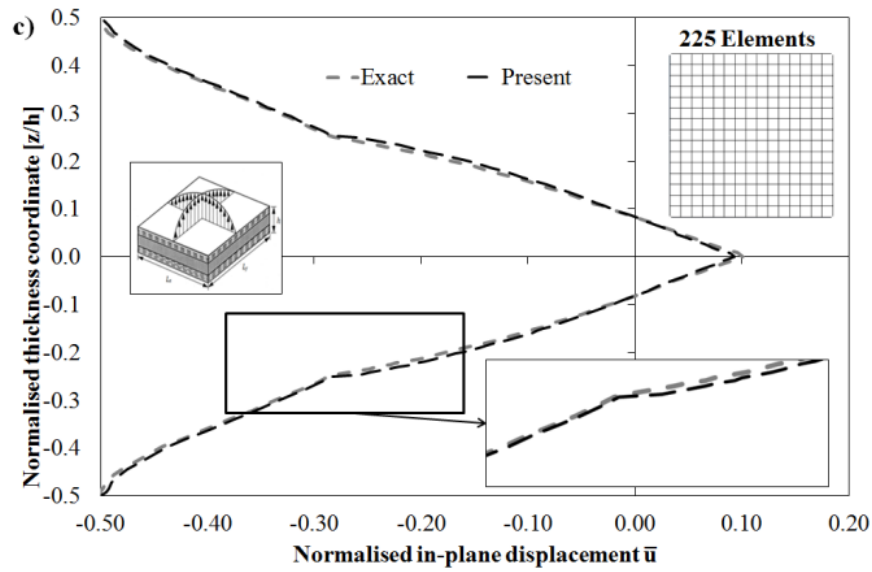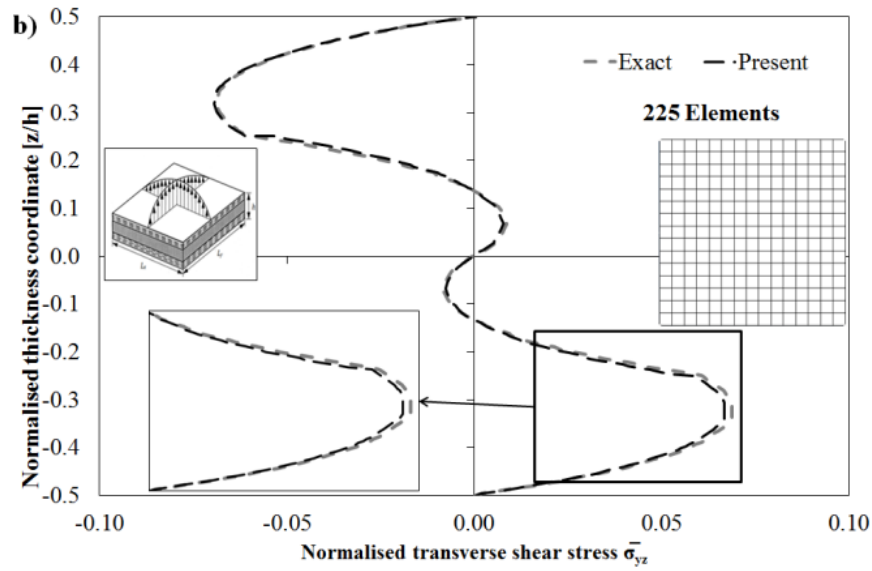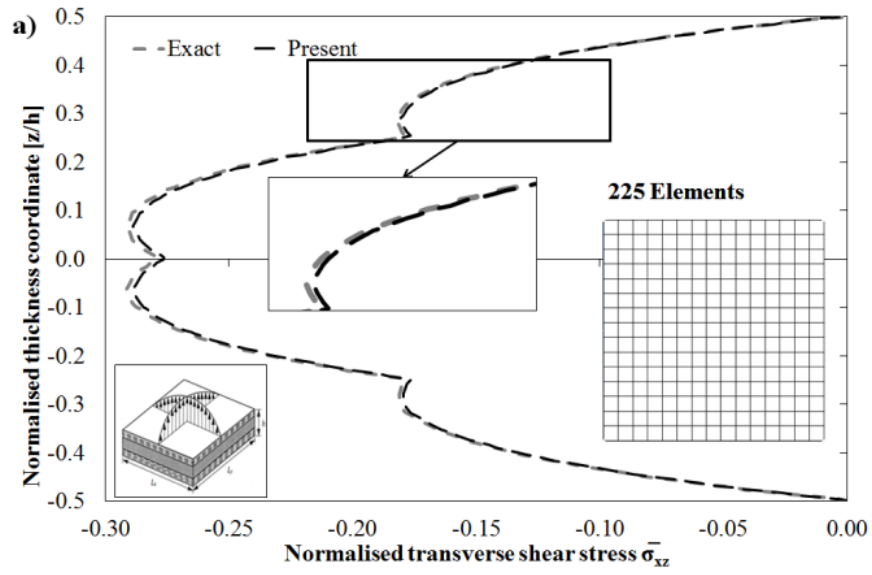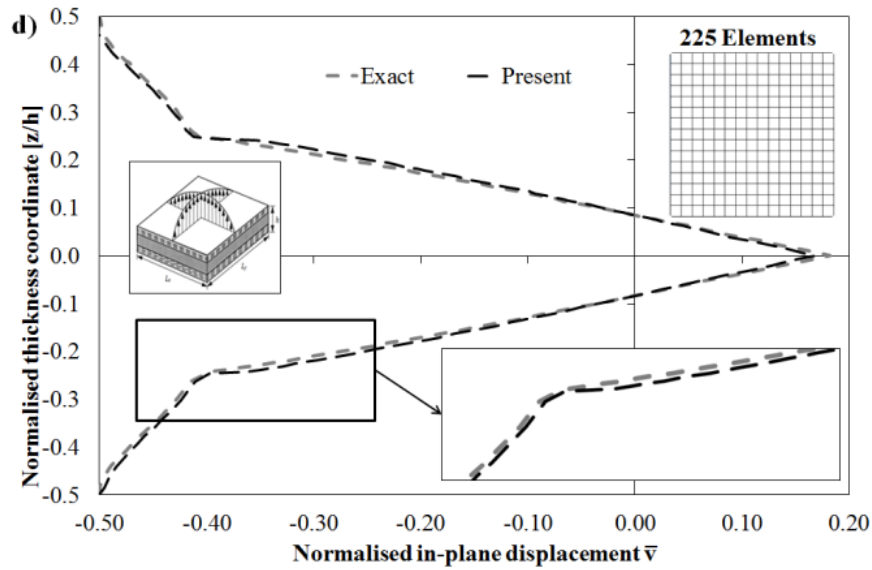
Figure 7.2 (a and b) Normalized transverse shear stresses; (c and d) in-plane displacements by Savoia and Reddy [254] (exact 3D solution) and by the present element for an angle-ply [30°/−30°/30°/−30°] laminated plate

Case E. The natural frequencies of the simply-supported laminate analysed by Mantari at al. [255] and by Noor [256] that provides the exact solution, are computed with those computed by the present element. Different E_1/E_2 ratios are considered, while the other mechanical properties are: $E_3/E_2=1$, $G_{12}/E_2= G_{13}/E_2=0.6$, $G_{23}/E_2=0.5$, $v_{12}=v_{13}=v_{23}=0.25$, $\rho=1$. The length-to-thickness ratio is 5, the stacking sequence is $[0°/90°/90°/0°]$ and the thickness of the layers is [0.25h/ 0.25h/ 0.25h/ 0.25h]. According to Mantari at al. [255], the results reported in Table 7.4 are normalized as follows:

$$\overline{f} = f \frac{L_x^2}{h} \sqrt{\frac{\rho}{E_2}} \tag{7.19}$$

The numbers in square brackets reported in Table 7.4 represent the computational times (in seconds) required by the present finite element implementation to perform the analysis. The results by the present model given in Table 7.4 have been obtained considering a 9x9 meshing within a quarter of the laminate. As a general remark to the results of Table 7.4, it could be noticed that the frequencies are higher as the E_1/E_2 ratio grows, according to the fact that they are proportional to the stiffness. For what concerns the present element, all the natural frequencies are evaluated with the due accuracy even when the constituent material is strongly directional. Also in this case, few seconds are required to perform all the analyses, showing again the efficiency of the present element.

E_1/E_2	$\bar{f}$ Exact [256]	$\bar{f}$ [255]	$\bar{f}$ Present
3 [3.5]	6.618	6.565	6.599
10 [4.26]	8.210	8.286	8.225
20 [5.65]	9.560	9.552	9.558
30 [6.98]	10.272	10.305	10.275
40 [8.03]	10.752	10.826	10.751

Table 7.4 Comparison between the frequencies of a multilayered composite plate computed by Noor [256] (exact solution), Mantari el al. [255] and by the present finite element implementation.

Case G. As a further assessment of the present element for static analyses, the simply supported sandwich beam (i.e. plate in cylindrical bending) with damaged core of Chapter 3 is considered. It is reminded that the beam has a (MAT 1/2/3/1/3/4)s lay-up with the following thickness ratios of layers (0.010/0.025/0.015/0.020/0.030/0.4)s., while the constituent material have the following mechanical properties MAT 1: $E_1=E_3=1$ GPa, $G_{13}=0.2$ GPa, $\upsilon_{13}=0.25$; MAT 2: $E_1=33$ GPa, $E_3=1$ GPa, $G_{13}=0.8$ GPa, $\upsilon_{13}=0.25$; MAT 3: $E_1=25$ GPa, $E_3=1$ GPa, $G_{13}=0.5$ GPa, $\upsilon_{13}=0.25$; MAT 4: $E_1=E_3=0.05$ GPa, $G_{13}=0.0217$ GPa, $\upsilon_{13}=0.15$. Note that in order to study a beam with plate elements, the structure is modelled as a rectangular plate with the $L_x \gg L_y$ (see inset in Figure 7.3). In addition, as shown in (7.20) results are evaluated at the center of the structure, where free edge effects are not present.

The G_{13} modulus of MAT4 is reduced by a factor 10^2 for simulating the complete failure of the core under transverse shear and the damage is assumed to be spread over the entire length of the sandwich beam.

Figure 7.3 reports the comparison between the exact solution [107] and the results by the present element, normalized as follows:

$$\bar{\sigma}_{xz} = \frac{\sigma_{xz}\left(0, \frac{L_y}{2}, z\right)}{p^0}$$

$$\bar{\sigma}_z = \frac{\sigma_z\left(\frac{L_x}{2}, \frac{L_y}{2}, z\right)}{p^0} \tag{7.20}$$

$$\bar{u} = 100 \frac{E_2 u\left(0, \frac{L_y}{2}, z\right)}{hp^0}$$

As evidenced by the numerical results, the present finite element implementation provides results in good agreement with the exact 3D solution also for this case.

a)

b)

c)
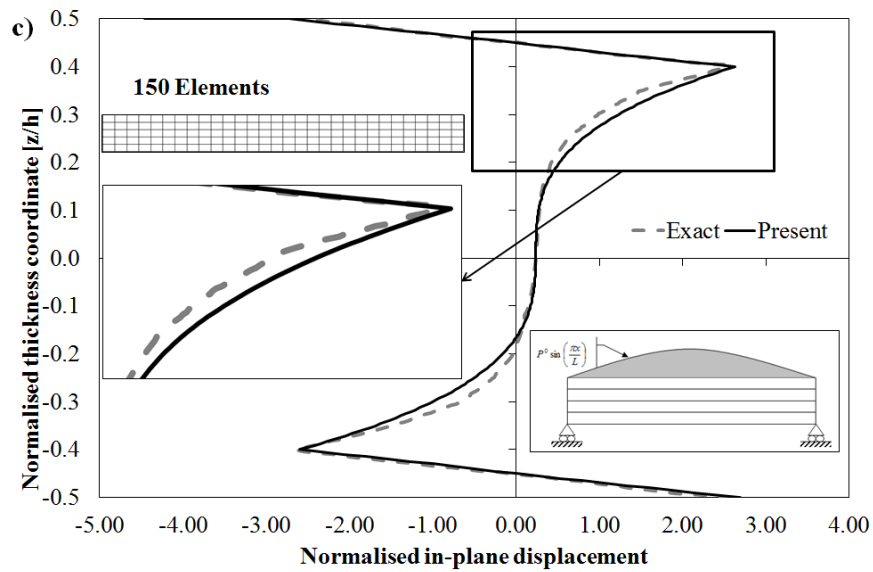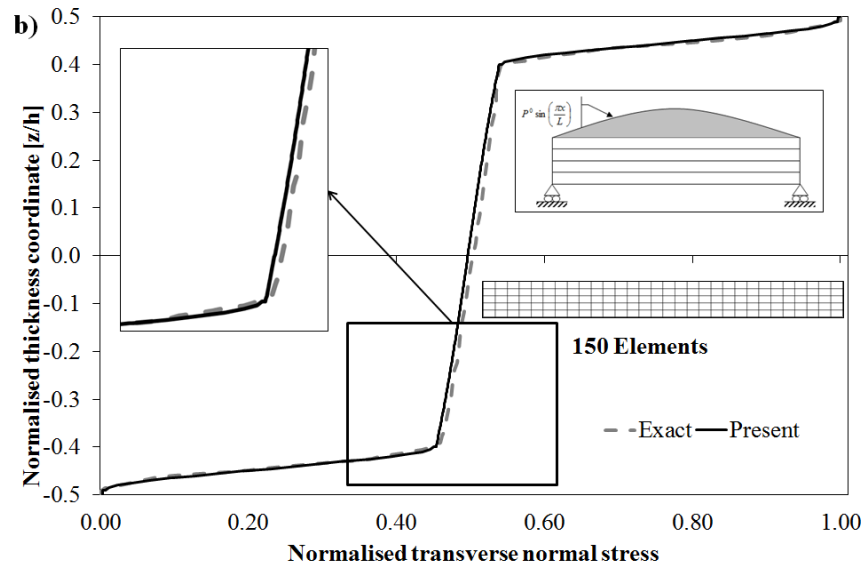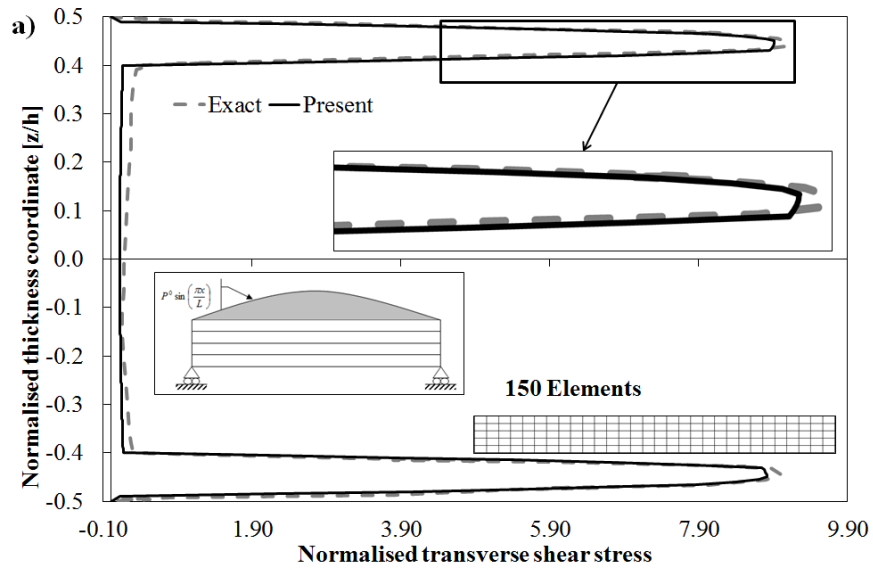
Figure 7.3 Comparison between exact solution [107] and solution by the present element for a sandwich beam with damaged core: a) normalized transverse shear stress; b) normalized transverse normal stress; c) normalized in-plane displacement.

Applications presented in this section have shown that the finite element developed through SEUPT obtains accurate results requiring low computational times in a variety of cases. Therefore, the present energy updating technique and finite element appear as a good alternative to those to date available for developing finite elements from zig-zag models. Indeed, it uses a standard interpolating scheme and it offers a great accuracy with the minimal number of unknown nodal variables at an affordable processing cost.

7.2 C^0 mixed finite element

In the present Section the main steps towards the development of a mixed finite element of class C^0 will be summarized and its accuracy will be assessed.

7.2.1 Formulation

Based on the SEUPT technique discussed above, an eight-node mixed plate element with standard Lagrangian interpolating functions is developed. According to [**257**], here the term mixed is used for indicating that the only fields to be varied in the sense of Variational Calculus (i.e. master fields) are internal fields (i.e. defined inside the volume of the domain). As nodal d.o.f., the nodal components of displacements $u(x, y, z)^{EM}$, $v(x, y, z)^{EM}$, $w(x, y, z)^{EM}$ and the stresses σ_{xz}^{J}, σ_{yz}^{J}, σ_{zz}^{J} at the reference middle plane are assumed (see Figure 7.4). With this choice of the nodal d.o.f., only the continuity conditions on σ_{xz}, σ_{yz}, σ_{zz} are met, while that on $\sigma_{zz,z}$ is disregarded.
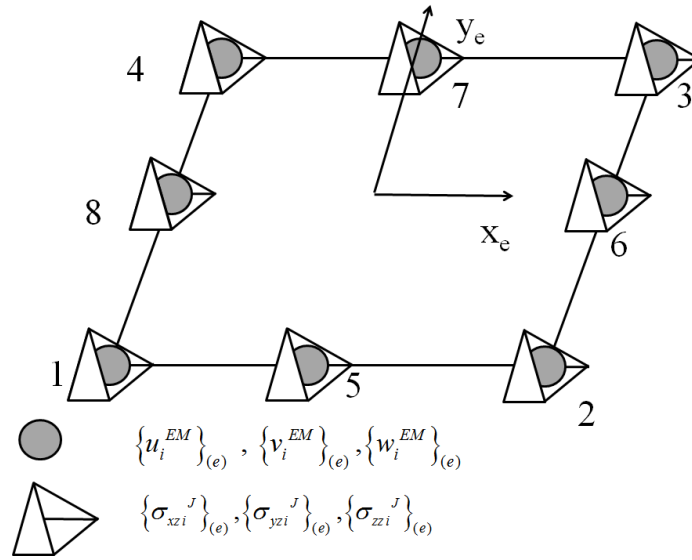
Figure 7.4 Reference system for the element in the natural plane.

Since stresses and displacements can be varied separately, the Hellinger-Reissner multi-field principle is the governing functional:

$$\delta \Pi_{HR} = \delta \int_V \sigma_{ij} \varepsilon_{ij}^u - \frac{1}{2} \sigma_{ij} S_{ijkl} \sigma_{kl} dV - \delta \left(\int_V b_i u_i dV + \int_S t_i u_i dS \right) = \delta U_{HR} - \delta W_{HR} \qquad (7.21)$$

The symbol S_{ijkl} represent the components of the elastic compliance tensor (i.e., the inverse of the elastic stiffness tensor C_{ijkl}) so that $S_{ijkl} \sigma_{kl} = \varepsilon_{ij}^\sigma$ represents the strains obtained from the stress-strain relations

Accordingly, ½ $\sigma_{ij} S_{ijkl} \sigma_{kl}$ is the complementary energy density in term of the master stress field. The slave fields are the strains ε_{ij}^σ and ε_{ij}^u:

$$\varepsilon_{ij}^\sigma = C_{ijkl} \sigma_{kl}; \quad \varepsilon_{ij}^u = \frac{1}{2} \left(u_{i,j} + u_{j,i} \right) \qquad (7.22)$$

The vector of the nodal d.o.f. for the generic element (e) in its natural reference system J is thus represented by:

$$\{q_e\}^T = \left\{ \left\{ u_i^{EM} \right\}_{(e)}, \left\{ v_i^{EM} \right\}_{(e)}, \left\{ w_i^{EM} \right\}_{(e)}, \left\{ \sigma_{xzi}^J \right\}_{(e)}, \left\{ \sigma_{yzi}^J \right\}_{(e)}, \left\{ \sigma_{zzi}^J \right\}_{(e)} \right\}^T \qquad (7.23)$$

where i is the node number (i=1, 8).

Nevertheless the transverse normal stress gradient is not assumed as a functional d.o.f., in order to avoid stress derivatives as nodal d.o.f., the numerical results will show that the boundary conditions (2.22) will be spontaneously satisfied, as already shown by Icardi [109] and Icardi and Atzori [240] using layerwise plate elements and solid ones, respectively.

Therein, accurate solutions were obtained either for regular problem involving laminates and sandwiches (even when they are thick and the properties of their constituent layers are distinctly different), or singular problems like the case of a two material wedge with certain side angles and materials with dissimilar properties. Even no cases were found where the lack of the enforcement of continuity of the transverse normal stress gradient gives incorrect results.

Hereon the basic steps towards derivation of the present element will be summarized. Details concerning standard aspects will be omitted, being explained in common textbooks. The displacements, represented in synthetic form as D and the interlaminar stresses as S, are interpolated separately as:

$$D = \sum_1^8 D^e N^e_{disp}; \quad S = \sum_1^8 S^e N^e_{stress} \tag{7.24}$$

Generally speaking, in order to fulfil the equilibrium conditions in point-wise form (i.e. self-equilibrating elements), the order of N^e_{stress} should be higher than that of N^e_{disp}. However, here, differently to customary mixed elements the nodal stresses are not required to be represented in a point-wise self-equilibrating form, since, similarly to what happens for displacement based elements, the basic assumption is that the intra-element equilibrium conditions are met in an approximate integral form (i.e. through energy balance), as postulated by Zienkiewicz and Taylor [**251**]. Accordingly, the same inner representation in (x, y) can be assumed both for displacements and stresses, i.e. $N^e_{disp} = N^e_{stress} = N$. In the present case, the shape functions of Eqs. (7.3) − (7.5) are chosen. Thus no derivatives of the d.o.f should be chosen as nodal quantities. Consequently, C^1 or higher-order interpolating functions are unnecessary.

The option of using the same representation for displacements and stresses is chosen because it makes easier the development of mixed elements without compromising accuracy, as shown since the pioneering paper by Loubignac et al. [**258**]. In addition, an identical interpolation for displacements and stresses is acceptable by the viewpoint of numerical stability of mixed elements, as discussed forward.

Representations (7.3) - (7.5) meet the compatibility condition, as the displacements and the interlaminar stresses being nodal d.o.f. and having the same representation for adjacent elements are continuous inside and at the edges of the elements. Consistency is also ensured at the through-the-thickness interfaces, being the present element based on the AD-ZZ model.

However, since the membrane stresses are not assumed as nodal d.o.f., they could be discontinuous between adjacent elements, as for classical displacement based elements with Lagrangian shape functions.. With these assumptions, the stresses within the finite element are represented as:

$$\{\sigma\} = \begin{bmatrix} & & & \left[\hat{D}\right] & & \\ \{0\} & \{0\} & \{0\} & \{N_{stress}\} & \{0\} & \{0\} \\ \{0\} & \{0\} & \{0\} & \{0\} & \{N_{stress}\} & \{0\} \\ \{0\} & \{0\} & \{0\} & \{0\} & \{0\} & \{N_{stress}\} \end{bmatrix} \{q_{(e)}\}$$ (7.25)

$[\hat{D}]$ being the matrix that defines the in-plane stress components

$$\{\sigma_{xx} \ \sigma_{yy} \ \sigma_{xy}\}^T = [S*][B]\{q_{(e)}\} = \left[\hat{D}\right]\{q_{(e)}\}$$ (7.26)

$[S*]$ being the related elastic coefficients and $[B]$ the derivatives of the shape functions.

The "stiffness" matrix is derived in a straightforward, standard way from the internal energy functional U_{HR} substituting the discretized displacements and stresses:

$$\{q_{(e)}\}^T \left[\hat{K}\right]^e \{q_{(e)}\} = \{q_{(e)}\}^T \int_V \left[\hat{C}\right]^T [B] - \frac{1}{2}\left[\hat{C}\right]^T [S]\left[\hat{C}\right] dV \{q_{(e)}\}$$ (7.27)

while the vector of generalized nodal forces is obtained from the work of forces W_{HR} substituting the finite element discretization of displacements. Assembly of the stiffness matrix and of the vector of nodal forces is carried out with the standard techniques.

The integrals defining the stiffness matrix and the nodal force vector are computed either in exact form using symbolic calculus, so to avoid numerical instabilities, or through Gaussian integration, because a reduced integration scheme could be used (even if it was never applied for obtaining the numerical results given next).

To standardize the computation of integrals, as customarily, a topological transformation is carried out from the physical plane (x, y) to the natural plane (η, θ) similarly to what done in Eqs. (7.6) – (7.8).

As well known, stability, solvability and locking phenomena of mixed elements are governed by rather complex mathematical relations (see, Babuska [259] and Brezzi [260]). In particular, certain choices of the shape functions could not give meaningful results. A necessary condition for solvability, which in most cases suffices for acceptability of mixed elements, is that the number of displacement d.o.f. n_u must be equal (like in the present element), or larger than the number of stress d.o.f. n_σ. Sufficient conditions for solvability (see, Olson [261]) are

that for a single element that is free of boundary conditions i) the number of zero eigenvalues of $[\hat{K}]^e$ is equal to the number of rigid body modes, ii) the total number of positive eigenvalues is equal to the number of stress d.o.f., iii) the total number of zero and negative eigenvalues is equal to the number of displacement d.o.f. However, even when these admissibility tests are passed, erroneous, highly oscillating results could be obtained. For homogeneous, isotropic materials this problem is usually overcome by relaxing the stress continuity impositions, but in laminated and sandwich composites the interfacial stress continuity conditions cannot be skipped, otherwise the physical meaning of solution is lost. The opposite possibility is that nevertheless these tests are failed, mixed elements could be effective for solving regular problems. Accordingly, mixed elements should be tested considering sample cases with the same features of the practical cases to be solved, whose solution in exact or approximate numerical form is available for comparisons.

In the forthcoming section, solvability, convergence and accuracy tests of the element will be presented, considering laminates and sandwiches for which either exact solution in closed-form or in numerical form are available in the literature for comparison.

7.2.2 Applications

First of all, an eigenvalue solvability test is presented. In accordance with Olson [261], this test is carried out over a single finite element in the shape of a square plate with sides of unit length and free of boundary conditions (thickness should be sufficiently small to have a plane-stress, plane-strain problem). The same isotropic material analysed by Mijuca [262] in a similar test is here considered with the following mechanical properties $E_1 (= E_2 = E_3) =1$ and $\upsilon=0.3$. The results of this test are reported in Table 7.5.

According to the rules discussed above, the finite element shows a number of zero eigenvalues (6) equal to the number of rigid body modes. At the same time, the total number of positive eigenvalues (24) is the same as the number of generalized stress d.o.f. and the total number of zero and negative eigenvalues (24) is equal to the number of generalized displacement d.o.f. These conditions being satisfied in the test, the sufficient condition for solvability is passed by the present mixed element. Thus, it can be applied to solution of other sample cases in order to verify its behaviour in problems of practical interest.

Mode	Eigenvalue	Mode	Eigenvalue	Mode	Eigenvalue	Mode	Eigenvalue	Mode	Eigenvalue	Mode	Eigenvalue
1	0.58	2	0.27	3	0.28	4	0.19	5	0.19	6	0.10
7	0.08	8	0.07	9	0.062	10	0.062	11	0.054	12	0.054
13	0.049	14	0.022	15	0.022	16	0.018	17	0.018	18	0.018
19	0.017	20	0.016	21	0.016	22	0.006	23	0.006	24	0.005
25	0	26	0	27	0	28	0	29	0	30	0
31	−0.022	32	−0.022	33	−0.027	34	−0.059	35	−0.059	36	−0.073
37	−0.073	38	−0.082	39	−0.11	40	−0.11	41	−0.138	42	−0.155
43	−0.192	44	−0.21	45	−0.21	46	−0.23	47	−0.38	48	−0.69

Table 7.5 Solvability test for an isotropic material.

Aiming at verifying the convergence rate of the present element, the sample case analysed by Zhen et al. [35] is considered, with a length-to thickness ratio of 4. The analysis is carried out for a plate that undergoes a bisinusoidal loading and is simply supported at the edges. The constituent material is mat p (E_L/E_T=25; G_{LT}/E_T=0.5; G_{TT}/E_T=0.2; υ_{LT}=0.25) and the stacking sequence is [15°/-15°]. Table 7.6 reports the through-the-thickness variation of the in-plane stress for different meshing schemes by the present element and by Zhen et al. [35], normalized as follows:

$$\overline{\sigma}_x = \frac{\sigma_x\left(\dfrac{L_x}{2},\dfrac{L_y}{2},z\right)h^2}{p^0 L_x^2} \tag{7.28}$$

The results of Table 7.6 show that the present element is as accurate as the 3D solutions reported in Ref. [35], and even with rather coarse meshing the accuracy is satisfactory. This confirms that mixed elements are accurate without requiring a very fine discretization as already underlined in the literature.

z/h	-0.5	-0.2	0.0⁻	0.0⁺	0.2	1
3D [35]	-0.9960	-0.0373	0.4526	-0.4719	0.0260	1.0446
Zhen et al. [35] 4x4	-1.0292	-0.0371	0.4719	-0.4926	0.0240	1.0812
Present 4x4 [2.33]	-1.0291	-0.0371	0.4721	-0.4924	0.0250	1.0791
Zhen et al. [35] 8x8	-0.9992	-0.0356	0.4582	-0.4771	0.0235	1.0481
Present 8x8 [8.51]	-0.9991	-0.0362	0.438	-0.4751	0.0239	1.0465
Zhen et al. [35] 12x12	-0.9925	-0.0353	0.4552	-0.4738	0.0234	1.0411
Present 12x12 [17.1]	-0.0995	-0.0372	0.4531	-0.4729	0.0249	1.0451
Zhen et al. [35] 14x14	-0.9910	-0.0353	0.4546	-0.4732	0.0234	1.0396
Present 14x14 [20.2]	-0.9961	0.0374	0.4525	-0.4718	0.0261	1.0446

Table 7.6 Normalized in plane stress for a [15°/-15°] square plate by Zhen et al. [35] and by the present mixed element with progressively refining meshing.

As a further assessment of the convergence rate, the laminated [0°/90°/0°] plate for which Vel and Batra computed the exact 3D solution in Ref. [**167**] is considered. The plate is square and has a length to thickness ratio (L_x/h) of 5. The constituent material is again MAT p (E_L/E_T=25; G_{LT}/E_T=0.5; G_{TT}/E_T=0.2; υ_{LT}=0.25), and for what concerns boundary and loading conditions, the plate is simply supported on two opposite edges, clamped on the other two and it is undergoing a bi-sinusoidal normal load with intensity p^0 on the upper face, whereas the bottom one is traction free. The results of Table 7.6 report the transverse displacement component at the centre of the plate $\bar{w}$ and the transverse shear stress $\bar{\sigma}_{xz}$ near the clamped edge normalized according to [**167**] as:

$$\bar{\sigma}_{xz} = \frac{10 \cdot h \cdot \sigma_{xz}\left(\dfrac{L_x}{8},\dfrac{L_y}{2},z\right)}{p^0 L_x}; \quad \bar{w} = \frac{100 E_T \cdot h^3}{p^0 L_x^4} w\left(\dfrac{L_x}{2},\dfrac{L_y}{2},z\right) \tag{7.29}$$

Like in the previous case, the numbers in square brackets represent the computational time required to perform the analysis on a laptop computer with an 1.80 GHz double-core processor and 4 GB RAM. The numerical results show that the present finite element provides very accurate results as compared to the exact 3D solution. Also in this case it is shown that even with a rather coarse discretization the accuracy is good.

	z/h	-0.50	-0.40	-0.30	-0.20	-0.10	0.00	0.10	0.20	0.30	0.40	0.50
$\bar{\sigma}_{xz}$	Ref. [42]	0.000	2.609	3.227	2.643	2.113	2.093	2.100	2.668	3.340	2.734	0.000
	Present (3x3) [1.97]	0.000	2.720	3.830	2.949	2.450	2.360	2.450	2.950	3.950	2.920	0.000
	Present (5x5) [2.70]	0.000	2.650	3.450	2.734	2.325	2.248	2.299	2.750	3.430	2.805	0.000
	Present (9x9) [9.26]	0.000	2.607	3.227	2.643	2.114	2.094	2.099	2.668	3.340	2.735	0.000
$\bar{w}$	Ref. [42]	1.152	1.158	1.162	1.167	1.173	1.180	1.188	1.198	1.208	1.218	1.227
	Present (3x3)	1.613	1.545	1.450	1.406	1.375	1.340	1.333	1.388	1.398	1.415	1.443
	Present (5x5)	1.234	1.288	1.291	1.299	1.304	1.306	1.309	1.295	1.299	1.305	1.312
	Present (9x9)	1.153	1.158	1.161	1.168	1.172	1.180	1.188	1.197	1.207	1.217	1.228

Table 7.7 Normalized shear stress and transverse displacement for a [0°/90°/0°] square plate by Vel and Batra [167] (exact 3D solution) and by the present mixed element with progressively refining meshing.

With the goal of verifying the accuracy of the present mixed element for structure with abruptly changing material properties and general boundary conditions, the cantilever piezoactuated beam studied by Robbins and Reddy [**263**] is considered. As already done in

Section 7.2.2, in order to study a beam with plate elements, the structure is modelled as a rectangular plate with the Lx >> Ly (see inset in Figure 7.5). The structure is made of an underlying aluminium beam substructure (thickness 15.2 mm), an adhesive film (thickness 0.254 mm) and a piezoactuator (thickness 1.52) bonded on the upper face. The mechanical properties of the constituent materials are: E_{alum}=69 GPa, G_{alum}=27.5 GPa, υ_{alum}=0.25; E_{ad}=6.9 GPa, G_{ad}=2.5 GPa, υ_{ad}=0.4; E_{1piezo}=69 GPa, E_{3piezo}=48 GPa, G_{piezo}=21 GPa, $\upsilon_{13piezo}$=0.25, $\upsilon_{31piezo}$=0.175. Piezoactuator, adhesive and aluminium substructure form an unsymmetrical three material laminate that exhibits bending/extension coupling. The only acting loads for this case are the self-equilibrating loads induced by the piezoactuator. According to Robbins and Reddy [263], a bending deformation is provided by applying an uniform actuation strain of 0.001 to the piezoelectric layer via an applied electric field. Thus, at each node of the structure is applied a displacement in the x direction obtained integrating the actuated strain over the section of the beam. The length of the beam is 152 mm.

Figure 7.5a shows the spanwise variation of membrane, transverse shear and transverse normal stresses near the top of the aluminium substrate (z1= 6.61 mm) and at the centre of the adhesive layer (z2= 6.84 mm), while Figure 7.5b represents the stress fields across the thickness close to the free edge. The stress distributions are presented in the following normalized form, according to [263], where the exact solution for this case is presented:

$$
\begin{aligned}
\overline{\sigma}_x &= \frac{A_{tot} \cdot \sigma_x \cdot 10^3}{\left(E_1 A\right)_{alum} + \left(E_1 A\right)_{ad} + \left(E_1 A\right)_{piezo}}; \\[2mm]
\overline{\sigma}_z &= \frac{A_{tot} \cdot \sigma_z \cdot 10^3}{\left(E_3 A\right)_{alum} + \left(E_3 A\right)_{ad} + \left(E_3 A\right)_{piezo}}; \\[2mm]
\overline{\sigma}_{xz} &= \frac{A_{tot} \cdot \sigma_{xz} \cdot 10^3}{\left(G_{13} A\right)_{alum} + \left(G_{13} A\right)_{ad} + \left(G_{13} A\right)_{piezo}};
\end{aligned}
\tag{7.30}
$$

The subscripts alum, ad, piezo and tot being used for indicating the cross sectional area and the elastic moduli of the substrate structure, of the adhesive and of the piezoactuator layer, respectively, which are considered as isotropic materials.

The results of Figure 7.5 show that the present mixed element is accurate also for this case in which a singular-like stress field arises. In details, in Figure 7.5a it can be noticed that the element accurately describes the unwanted dangerous stress concentrations that appear at the free end of the beam without showing erroneous oscillating results close to the edge. Also the through-the-thickness distribution of the stresses is well described as shown in Figure 7.5b, in

particular the mixed element is capable of capturing the sharp variation of the bending stress that can be seen near the bonding layer also in this case with a reasonably refined meshing. For this case of analysis the present element required 47 s.
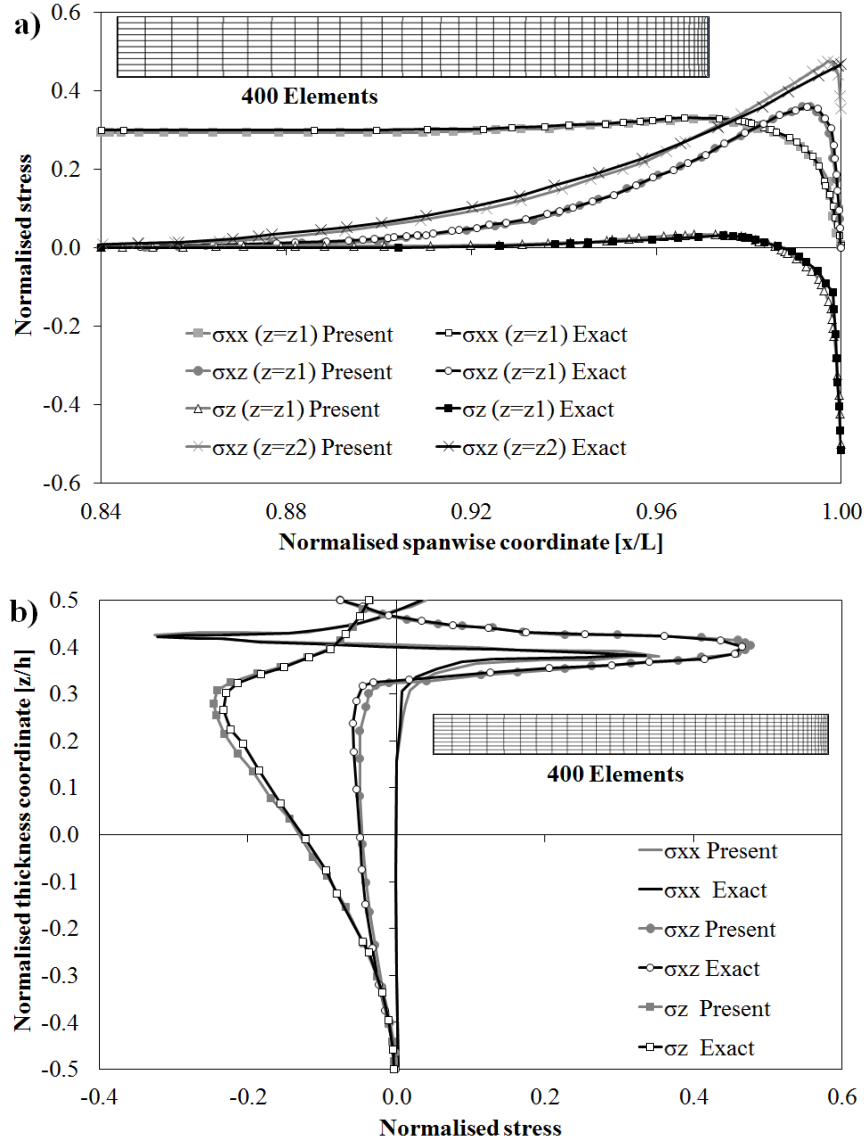
Figure 7.5 Normalized variation of the stress field for a cantilever piezoactuated beam a) along the span and b) across the thickness (inset meshing scheme adopted).

Numerical results presented in this section have shown that the mixed finite element developed obtains accurate results requiring low computational times in a variety of cases. Also solvability and convergence have been demonstrated.

Chapter 8: Applications to impact studies

As already stated above, composite materials can suffer from layerwise effects that are responsible of local micro-failures and, consequently, of relevant loss of strength and stiffness. As the damaged area may increase in size under loading in service till causing a premature failure, the basic requirement is that composites must carry the ultimate design load even when they are damaged. Therefore, accurate numerical simulations are required to understand whether the service life of composite structures may be hampered by the rise and growth of damage in service and whether and when the damaged structure needs repair or substitution.

Within this framework, manufacturers have found a high susceptibility to impact damage from dropped tools, vehicular collisions and to damage caused by drilling. A critical case for aircraft structures is impact from crushed stones during taxiing manoeuvres and take-off. The readers are referred to the papers by Richardson and Wisheart [264], Morinière et al. [265] and by Abrate [266] - [267] for a comprehensive review of low-velocity impact studies on laminates. Methods for predicting delamination induced by low-velocity impacts are discussed by Elder et al. [268]. A review of numerical and experimental impact studies on sandwich panels, a discussion of their damage mechanisms and of failure criteria used in the simulations are given by Chai and Zhu [269]. An overview of damage models is also given by Garnich and Akula Venkata [270], Liu and Zheng [271] and Corigliano [272]. The damage analysis of honeycomb sandwich panels carried out by Horrigan and Staal [273] is cited as a further study in this field. A comparison between simulations and experiments is given by Salerno et al. [274]. The effects of stacking sequence on the impact and post-impact behaviour are shown by Aktas et al. [275], those of the impactor shape are studied by Mitrevski et al. [276]. Multiple impacts are investigated by Damanpack et al. [277] and Chakraborty [278]. The impact behaviour of different honeycomb core cells is shown by Yamashita and Gotoh [279].

Structural models play a central role in the simulation procedure since they should accurately describe the behaviour of composites, but, in light of the iterations required to solve the impact problem, they should also require low computational time.

Studies by Oñate et al. [**48**] - [**49**], Icardi and Ferrero [**114**], Palazotto et al. [**280**], Kärger et al. [**281**] and Diaz Diaz et al. [**282**] have shown that ZZ-F and even equivalent single layer models (ESL) can be can be successfully adopted for impact and damage analyses in order to save costs. Accordingly, in the present chapter, a simulation procedure (IMPSIM) based on the AD-ZZ model of Chapter 2 is developed.

In particular, the progressive damage analysis is carried out at each time step using stress-based criteria, extending a pre-existing damaged area at the previous iteration to the points where the ultimate condition is reached at the next one, as customarily. The residual properties of the damaged area are determined using the continuum damage mesomechanic model by Ladevèze et al. [**283**], [**284**] that accounts for the effects of hard discontinuities in homogenized form through a modified version of the strain energy of the structure. The transverse cracking rate and the delamination ratios are computed using stress-based criteria at each time-step, then the homogenized energy that accounts for the damage is computed and used for evaluating stresses at each point.

For what concerns contact, IMPSIM adopts the modified Hertzian contact law of [**114**] to compute the contact force for laminates. Instead, the refined contact model by Palazotto et al. [**280**] that forces the target to conform to the shape of the impactor is employed to compute the contact radius when sandwiches are analysed.

Hertzian contact is chosen being proven to be accurate by a plenty of studies (see, e.g. Yigit and Christoforou [**285**] for laminates and Choi [**286**] for sandwiches), nevertheless it is developed for isotropic media. A different alternative approach accounting for the heterogeneous nature of composites is developed by Chao and Tu [**287**]. In this case, the contact stresses are derived via an energy variational approach, accounting for three-dimensional boundary conditions and interlaminar continuity. Another alternative approach is developed by Zhou and Stronge [**288**], where the load- indentation law of sandwiches is obtained via FEA (ABAQUS/Explicit) assuming elastic the face sheets and rigid-perfectly plastic the core. Application of these more advanced contact models is left to a future study.

The Newmark's implicit time integration scheme is used by IMPSIM for solving transient dynamic equations, despite experiments have shown that low-velocity impact studies could be

carried out also in static form (see, Li et al. [**289**]). This choice is enabled by the computational efficiency of the AD-ZZ model, which allows carrying out dynamic analyses with low costs.

Differently to [**114**], where non-linear strains of von Karman type are adopted, here, the updated Lagrangian approach is chosen to efficiently account for geometric nonlinearity. Accordingly, the deformations at each new time step are obtained from the geometry of the structure at the previous step, not from the initial unloaded configuration.

Since core crushing is governed by the properties of the cellular structure of honeycomb, it cannot be appropriately accounted for by the present multi-layered AD-ZZ model that describes the core as a thick layer with homogenized properties, even if it adopts a high-order piecewise representation of the transverse displacement. Therefore, the variable, apparent elastic moduli of the core while it collapses/buckles under transverse compressive loading are computed apart, once for all, through a detailed three-dimensional finite element analysis and provided to the AD-ZZ as variable properties at each load level.
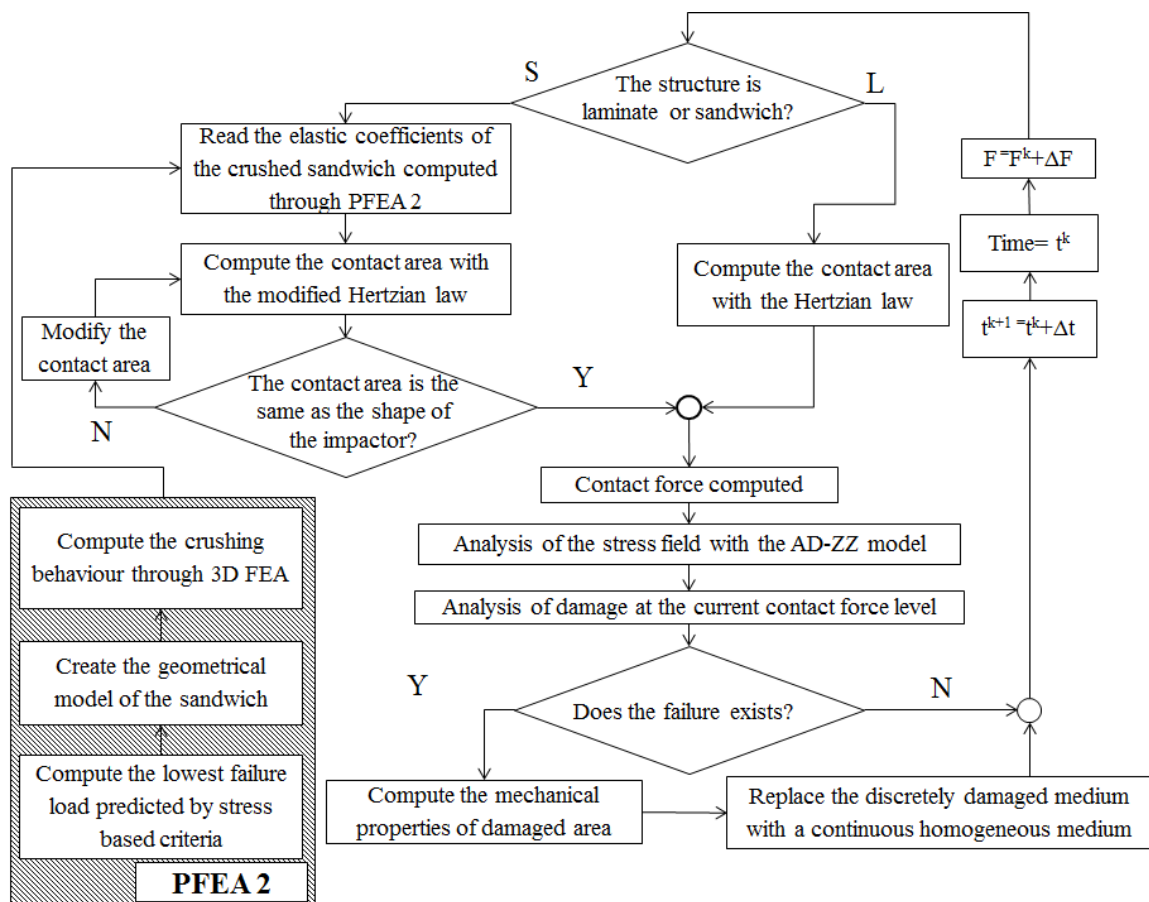
Figure 8.1 Stages of IMPSIM

8.1 Contact force modelling

Since, in the literature, the contact pressure profile is shown to be less important than the load and the area over which it acts, the contact stress is assumed to be distributed according to the Hertzian law, like in homogeneous isotropic materials:

$$\sigma(r) = \sigma(0)\sqrt{1 - \left(r^2 / R^2_{contact}\right)} \quad (\sigma(r) = 0 \text{ if } r > R_{contact}) \tag{8.1}$$

In the former equation, $R_{contact}$ is the radius of the contact area, while $\sigma(r)$, $\sigma(0)$ are the Hertzian stress intensity at a distance r from the centre and at the centre, respectively. The impactor is assumed to be spherical, because no details regarding the real shape of the contact area and the real distribution of the force acting on it are available for other impactor shapes. The analysis of laminates is carried out assuming $R_{contact}$ as a fixed variable, while for sandwiches it is computed at each step by forcing the target to conform to the shape of the impactor.

8.1.1 Laminates

In the loading phase, the contact force F is related to the indentation depth α through the contact stiffness K_c in standard form as:

$$F = K_c(R_{contact})\alpha^{\upsilon} \tag{8.2}$$

A 3D Finite element analysis, here referred as PFEA-1 is performed apart once for all as a virtual material test (VMT) for determining $R_{contact}$. A non-linear model (RADIOSS -MAT25) is adopted to account for the failures occurring in the target structure, as described next. The exponent υ is set in agreement with experiments in the literature. In the unloading phase

$$F = F_m\left(\frac{\alpha - \alpha_0}{\alpha_m - \alpha_0}\right)^q \tag{8.3}$$

and the exponent q is set according to experiments. In the previous equation, F_m is the maximum of the contact force, α_m is the relative indentation depth at each loading step and α_0 is the permanent indentation. In case of bounces, the following reloading law is assumed:

$$F = k^{'}(\alpha - \alpha_0)^p \tag{8.4}$$

Again, the contact stiffness k' is computed through VMT accounting for contact stiffness degradation due to the damage arose in the loading phase. The exponent p is still set

according to experiments. Literature shows that $\upsilon= p= 1.5$ and $q= 2.5$ are the appropriate choices for laminates.

8.1.2 Sandwiches

A constant contact radius is inappropriate when analysing sandwich panels with lightweight soft core. Thus, the iterative algorithm by Palazotto et al. [280] is applied that forces the impact area to conform to the shape of the impactor at any load increment to compute the contact radius. Since the solution depends both on the current configuration and the previous history and local deformations can be quite large, the problem is solved using a modified version of the Newton-Raphson method:

$$\delta^i = \left[\mathbf{K}\left(d^{(i-1)}\right) \right]_S d^{(i-1)} - \mathbf{F}_c^{(i-1)} \neq 0 \tag{8.5}$$

The secant stiffness matrix $[K(d)]_S$ is computed using the AD-ZZ model of Chapter 2. The symbols $d^{(i-1)}$ and δ^i represent the converged solution at the previous load increment $\mathbf{F}_c^{(i-1)}$ and the residual force, respectively. The displacement amplitude vector $d^{(i-1)}$ is updated by Δd^i in order to make the structure in equilibrium with $\mathbf{F}_c^i$. Displacements are applied during iterations till the impactor and the indentation radii conform:

$$\left[\mathbf{K}\left(d^{(i-1)}\right) \right]_T \Delta d^i = \delta^i \tag{8.6}$$

$[K(d)]_T$ being the tangent stiffness matrix computed using the AD-ZZ model. The updated vector of displacement d.o.f. d^i is computed as:

$$d^i = d^{(i-1)} + \Delta d^i \tag{8.7}$$

The process is repeated till the convergence tolerance is reached. Namely, the convergence tolerance is compared with the percentage of variation of the solution, from the current to the previous iteration using the norm of displacements

$$\bar{d}^i = \sqrt{\sum_n \left(d_j^n\right)^2} \tag{8.8}$$

to compute

$$D = \frac{\left[\bar{d}^{i+1} - \bar{d}^i \right]}{\bar{d}^i} \tag{8.9}$$

The iterative process is stopped when $D \leq 1\%$. Once a converged solution is obtained, the simulation procedure goes on.

8.2 Damage and post-damage modelling

The failure analysis of composites is a topic still open to discussion. As already reminded, the characteristic feature of composites is to absorb the incoming energy through a complex interaction of local failures in their microstructure. For example, carbon epoxy composites often fail by matrix or fibre failure, while glass-fibre-reinforced composites often fail by a fibre-matrix interaction. The fibres can fail by traction, shear, compressive instability, or brittle failure. The matrix can fail by apparently ductile shear, brittle fracture, or by microcracks parallel to fibres caused by transverse-tension loading. Since all these failure modes influence each other, they should not be assessed independently. Sandwich composites fails either by general and local instability modes (i.e. rippling, face damping), core failure, skin indentation, debonding, wrinkling, etc., or as a consequence of fibres and matrix failure or delamination of skin layers like in laminated composites.

Since an accumulation of damage in service can adversely affect the structural performances, obviously, an accurate assessment of the local damage mechanisms and of the post-failure behaviour is mandatory within the framework of the damage tolerance design. This calls for sophisticated computational models and suitable stress decomposition techniques, which accurately capture the three-dimensional stress fields at the level of constituents and, evidently, for accurate failure models at the microstructure level.

Forty years of extensive studies have progressed significantly the knowledge. Bibliographical review papers, papers where the accuracy of criteria is assessed and monographs dealing with the failure mechanisms of composites are available in the specialized literature. Recent papers in which a comprehensive bibliographical review is provided, are Rowlands [290], Nahas [291], Echaabi and Trochu [292], Paris [293], Tennyson and Wharam [294] and Tong [295].

Nevertheless a variety of failure criteria based on various approaches are available, an efficient stresses and damage computation suitable for designers still remains under discussion. Being outside the aims of the present work a comprehensive review of failure

criteria and damage models, in the present section, just the failure criteria and the damage model assumed within IMPSIM are recalled.

8.2.1 Stress based failure criteria.

The 3-D Hashin and Rotem's criterion [**296**] with in-situ strengths is used for predicting the fibre and matrix's failures. Tensile failure is ruled by:

$$\left(\frac{\sigma_{11}}{X^t}\right)^2 + \frac{1}{S_{12=13}{}^2}\left(\tau_{12}{}^2 + \tau_{13}{}^2\right) = 1, \ (\sigma_{11} > 0) \tag{8.10}$$

X^t being the tensile strength of fibres, $S_{12=13}$ the in-situ shear strength of the matrix resin and σ_{11}, τ_{12} and τ_{13} the tensile and shear stresses acting on the fibres. Compressive failure is predicted by:

$$\sigma_{11} = -X^c, \ (\sigma_{11} < 0) \tag{8.11}$$

X^c being the compressive strength of fibres. Matrix failure under traction is described by:

$$\left(\frac{\sigma_{22}+\sigma_{33}}{Y^t}\right)^2 + \frac{1}{S_{23}{}^2}(\tau_{23}{}^2 - \sigma_{22}\sigma_{33}) + \left(\frac{\tau_{12}}{S_{12=13}}\right)^2 + \left(\frac{\tau_{13}}{S_{12=13}}\right)^2 = 1 \ (\sigma_{22}+\sigma_{33} > 0) \tag{8.12}$$

while under compression it is described by:

$$\frac{1}{Y^c}\left[\left(\frac{Y^c}{2S_{23}}\right)^2 - 1\right](\sigma_{22}+\sigma_{33}) + \frac{(\sigma_{22}+\sigma_{33})^2}{4S_{23}{}^2} + \frac{(\tau_{23}{}^2 - \sigma_{22}\sigma_{33})}{S_{23}{}^2} + \frac{(\tau_{12}{}^2 + \tau_{13}{}^2)}{S_{12=13}{}^2} = 1 \tag{8.13}$$

$(\sigma_{22} + \sigma_{33} < 0)$

Delamination failure is predicted using the Choi-Chang's criterion [**297**]:

$$e_d^2 = D_a\left[\frac{\overline{\sigma}_{yz}^n}{S_i^n} + \frac{\overline{\sigma}_{xz}^{n+1}}{S_i^{n+1}} + \frac{\overline{\sigma}_{yy}^{n+1}}{Y_i^{n+1}}\right]^2 > 1 \tag{8.14}$$

where $Y^{n+1} = Y_t{}^{n+1}$ if $\overline{\sigma}_{yy} > 0$, or $Y^{n+1} = Y_c{}^{n+1}$ if $\overline{\sigma}_{yy} < 0$, D_a is an empirical constant that is set after consideration of the material properties, $\overline{\sigma}_{ij}$ is the average stress at the interface between the nth ply and the $n+1^{th}$ ply:

$$\overline{\sigma}_{ij}^{n+1} = \frac{1}{h_{n+1}}\int_{t_{n-1}}^{t_n}\sigma_{ij}dt \tag{8.15}$$

The symbol *'i'* stands for *in situ*, while *'t'* and *'c'* stand for traction and compression, respectively. This criterion is chosen because numerical tests in literature have shown its accuracy for laminates undergoing low velocity impact loading.

The failure of honeycomb core under compression and transverse shear is predicted using the criterion by Besant et al. [**298**]:

$$\left(\frac{\sigma_{zz}}{\sigma_{cu}}\right)^n + \left(\frac{\sigma_{xz}}{\sigma_{lu}}\right)^n + \left(\frac{\sigma_{yz}}{\sigma_{lu}}\right)^n = e_{core} \quad (e_{core} > 1) \tag{8.16}$$

σ_{cu} and τ_{lu} being the core strengths in compression and transverse shear. It is assumed n = 1.5, since numerical tests in literature have shown that results with this choice are quite accurate. However, results do not considerably vary changing the exponent from 1 to 2.

The failure of foam core is estimated according to the rule suggested by Evonik for Rohacell core ([**299**], [**300**]), using as safety factor R_{11}/σ_v :

$$\sigma_v = \frac{\sqrt{(12a_2 + 12a1 + 12)I_2 + [4a_2^2 + (4a_1 + 4)a_2 + a_1^2]I_1^2} + a_1 I_1}{2a_2 + 2a_1 + 2} \tag{8.17}$$

where $I_1 = \sigma_{11} + \sigma_{22} + \sigma_{33}$ and $I_2 = \frac{1}{3}\left[\sum_{i=1}^{3}\sigma_{ii}^2 - \sigma_{11}\sigma_{22} - \sigma_{11}\sigma_{33} - \sigma_{22}\sigma_{33} + 3\sum_{ij=12,13,23}\sigma_{ij}^2\right]$

Parameters $a_1 = k^2(d-1)/d$, $d = R_{11}^-/R_{11}^+$, $a_2 = (k^2/d) - 1$ and $k = \sqrt{3}R_{12}/R_{11}^+$ are determined from experiments, while R_{11}^+, R_{11}^- and R_{12} represent the strengths of the foam under traction compression and shear, respectively.

Core crushing failure under out-of-plane normal and shear stresses is also predicted using the criterion by Lee and Tsotsis [**301**]

$$\frac{\sigma_{zz}}{Z^c} = 1 \ , \quad \frac{\sigma_{xz}}{S^x} = 1 \ , \quad \frac{\sigma_{yz}}{S^y} = 1 \tag{8.18}$$

Z^c, S^x, S^y being the compressive yield strength and the out-of-plane shear strengths, respectively. As both criteria (8.16) and (8.18) refer to honeycomb failure, the failed region is computed as the envelope of failures predicted by each of these two criteria. Strengths and material properties assumed in sections 8.5 and 8.6 are taken from material databases and from experiments published in the literature.

8.2.2 Mesoscale damage model.

In order to account for the effects of hard discontinuities in homogenized form, the mesoscale damage model (DML) by Ladevèze et al. [283], [284] is used. It provides a modified strain energy expression from which stresses are computed, considering materials damaged as in the reality by the standpoint of energy functionals. Therefore, no factors are guessed to modify the initially health properties in the failed regions adopting this damage model.

DML replaces the discretely damaged medium containing matrix cracks, delaminations and fibres failures with a continuous homogeneous medium, equivalent from an energy standpoint, whose strain energy expression incorporates damage indicators computed as the homogenized result of damage micromodels. Micro-meso relations, representing the homogenized result of micromodels, are derived from damage variables and associated forces. Displacement, strain and stress fields on the microscale are denoted as U^m, ε^m and σ^m, respectively. These quantities are expressed as the sum of the solution of a problem $\tilde{P}$ in which damage is removed and the solution of a residual problem $\bar{P}$ where a residual stress is applied around the damaged area. The homogenized potential energy density of the generic ply is expressed as ([283], [284]):

$$\frac{2E_p^S}{|S|} = [\pi\bar{\varepsilon}\pi]^t[\bar{M}_1(\bar{I}_{22},\bar{I}_{12})][\pi\bar{\varepsilon}\pi] + \tilde{\sigma}_{33}[\bar{M}_2(\bar{I}_{22},\bar{I}_{12})]\tilde{\sigma}_{33} +$$

$$+\tilde{\sigma}_{33}[\bar{M}_3(\bar{I}_{22},\bar{I}_{12})][\pi\bar{\varepsilon}\pi] - \frac{(1+\bar{I}_{23})\tilde{\sigma}_{23}^2}{\tilde{G}_{23}} - \frac{(1+\bar{I}_{13})\tilde{\sigma}_{13}^2}{\tilde{G}_{13}} - \frac{(1+\bar{I}_{33})<\tilde{\sigma}_{33}^2>_+^2}{\tilde{E}_3}$$

(8.19)

The meaning of symbols is as follows: $\bar{I}_{22}$, $\bar{I}_{12}$, $\bar{I}_{23}$, $\bar{I}_{13}$ and $\bar{I}_{33}$ are the damage indicators, each defined as the integral of the strain energy of the elementary cell for each basic residual problem under the five possible elementary loads in the directions 22, 12, 23, 13, 33; $[\bar{M}_1]$, $[\bar{M}_2]$, $[\bar{M}_3]$ are operators that depend on the material properties, $|S|$ is the deformation, $<.>_+$ represents the positive part operator. The homogenized potential energy density of the generic interface is expressed as ([283], [284]):

$$\frac{2E_p^j}{|\gamma_j|} = -\frac{(1+\bar{I}^1)\tilde{\sigma}_{13}}{\tilde{k}_1} - \frac{(1+\bar{I}^2)\tilde{\sigma}_{23}}{\tilde{k}_2} - \frac{(1+\bar{I}^3)\tilde{\sigma}_{33}}{\tilde{k}_3}$$

(8.20)

$\tilde{k}_1$, $\tilde{k}_2$ and $\tilde{k}_3$ being the elastic stiffness coefficients of the interface, $\bar{I}^1$, $\bar{I}^2$ and $\bar{I}^3$ the three damage indicators and γ_j the deformation. The coefficients of stresses in equations (8.19) and (8.20) represent the elastic properties of the homogenized model equivalent to the discretely

damaged real model. The damage is quantified in terms of cracking rate $\Re = \overset{..}{L} \Big/ \overset{..}{h}$ and

delamination ratio $\Im = \overset{..}{E} \Big/ \overset{..}{h}$, which are damage variables that links the damage state to the loss

of stiffness of the damage mesoconstituent, $\overset{..}{L}$ being the distance between two adjacent cracks,

$\overset{..}{h}$ being the length of the crack across the thickness and $\overset{..}{E}$ being the length of the

microcrack. Experiments show that the range of practical interest for $\Re$ is [0; 0.7] and for $\Im$

is [0; 0.4].

In the present procedure, the damage indicators are determined numerically through 3-D FEA

VMT (PFEA-3). The elementary cell is discretized by 3-D elements once for all outside the

time-loop cycle, considering discrete values of fibre failure and matrix cracking rates and

delamination ratios of the elementary cell obtained at various load levels applying criteria

(8.10) to (8.14).

The modified elastic properties by the mesoscale model are provided to the AD-ZZ model

that is used for carrying out the analysis. The progressive failure analysis is performed at each

time step applying criteria (8.10)-(8.18) under the forces provided by the contact model (8.1)-

(8.9) and the modified elastic coefficients of the mesoscale model (8.19)-(8.20). The damage

computed at the previous step by the criteria (8.10)-(8.18) is extended at the next step to the

points where the ultimate stress is reached. Instead of carrying out the analysis at an infinite

number of points, a discrete representation is used that identifies small square damaged cells

of the domain over which the ultimate stress is reached or just passed (up to an assumed

magnitude tolerance, see Fig. 8.13), in a fashion similar to that of finite elements.

Accordingly, the domain is subdivided into fictitious small square cells, whose damage state

computed at the central point is assumed constant over the area of the cell. A layer loop

computes the stresses across the thickness at the central point of each cell, which is used for

carrying out the damage analysis. Obviously, the smaller is the dimension of cells, the better

is accuracy and the larger is the computational effort.

8.3 Core crushing simulation

The behaviour of the "soft" material constituting the core needs to be accurately described, because a large amount of energy is absorbed through various folds and failure modes of the core structure. Thus, a discrete modelling is required for simulating with the due accuracy the effects that local phenomena have upon energy absorption mechanisms, which are strongly affected by the through-the-thickness properties.

As shown in many works taken from literature (see, e.g. [302] and [303]), honeycomb core behaves linearly at low strains, buckles and then undergoes progressive folding, finally followed by densification. Indeed, depending on the nature of the wall material, cells collapse by elastic buckling, plastic yielding, creep or brittle fracture. Collapse ends once the opposite cell walls come in contact.

Being non-uniform and complex, deformation patterns and stress distributions of honeycomb require a constitutive description under multi-axial conditions. In particular, shear stress has considerable influence on the crush behaviour, since the energy absorption rate is largely influenced by the ratio between the shear stress and the other stresses. The ratio of skin thickness to side length and honeycomb relative density have also a large influence. The inner cells deform completely in the axial collapse model under transverse loading with respect to the plane of the panel, while the outer cells along the sides exhibit collapse patterns with shear. Compared to metallic core, Nomex^{TM} honeycomb is relatively brittle, as it starts to fracture after reaching a critical loading. Accordingly, in metallic honeycomb the collapse mechanism is plastic and starts after buckling, while Nomex^{TM} honeycomb undergoes buckling of cells, followed by debonding failure at the cell interfaces and fracture.

Homogenized models cannot properly treat crushing of honeycomb, as it highly depends on geometry and material properties. Therefore, micromechanical approaches giving a detailed representation of the real geometry, which explicitly models core using shell elements, are required. In addition, a self-contact algorithm should be used for preventing from interpenetration between the folds in the cell walls. Modelling of foam core needs use of 3-D solid elements and appropriate homogenized material properties that are determined from experiments.

At the peak load, the elastic properties of core should be very accurately computed, appropriately reducing the properties of the failed regions, otherwise the peak is lower and

wider than in the reality [**303**]. Numerical tests show that if properties are inappropriately progressively reduced, the assumption of an elastic-plastic model can lead to an underestimated load peak.

As microbuckling and local failure of core are highly mesh sensitive [**303**], a very refined meshing is required. Indeed, a coarse discretization causes a higher initial load peak and higher load in the densification regime. However, very small elements are inappropriate if their dimension is not larger than the thickness of the honeycomb foil. Using reasonable meshing, the influence of cell size can be accurately predicted in the 3D finite element analysis with an affordable computational effort and then it can be used for designing honeycomb cores with desired energy absorption properties and given crush loads.

A more advanced option is using a homogenized discrete/finite model used in a semi-adaptive coupling technique, as discussed by Aktay et al. [**303**], since the discrete particles describe very accurately the crushing behaviour with a low cost. With this technique, elimination of elements that failed under contact compression stresses is avoided, so the contact force information is not lost.

Here a detailed, preliminary finite element analysis (PFEA-2) is carried apart once for all in order to compute the apparent elastic moduli of the core while it collapses/buckles under transverse compressive loading. The reason of this choice is that a discrete modelling of honeycomb may determine overloading computations when simulating structures of industrial complexity.

According to what discussed above, in the PFEA-2 phase, a detailed representation of the honeycomb structure is adopted to compute the tangent moduli of the core while it crushes. Shell elements with elastic-plastic isotropic material are used for discretizing core, paying attention to employ a self-contact algorithm. Please consider that the relatively brittle behaviour of Nomex ^{TM} is simulated through the failure criteria. The cell walls bonded together are modelled using double shell elements. Instead, foam core is discretized by solid elements with nonlinear material behaviour derived from experiments. Specifically, the hardening curve of foam core is obtained by curve-fitting the results of numerical compression tests.

The variable, apparent elastic moduli of the core are determined as the tangent moduli at each load level computed from the average ratio of stresses and strains. These moduli are determined in any sub-region in which the area around the contact point is ideally subdivided

and then they are provided to the AD-ZZ model for the analysis. Despite the core is apparently treated as a homogeneous material by the AD-ZZ model, the effects of crushing are accounted for locally, assuming elastic properties variable with position. Even if, here the solving procedure is analytical, elastic properties variable with position can be treated splitting the analysed structure into different subdomains (i.e. one for each variation of the mechanical properties), similarly to what done in Chapter 4, in order to treat joints. At the in-plane interfaces between these subdomains the AD-ZZ model through terms (4.6) − (4.8) restores in-plane continuity of stresses and gradients.

Even though the AD-ZZ model is based on infinitesimal strain-displacement relations, the nonlinear effects, considered when computing the apparent, variable elastic properties of the core, are also taken into consideration when the structural analysis with the AD-ZZ model is carried out, because the updated Lagrangian methodology is used. This approach evaluates the deformations at each new time step from the geometry of the structure at the previous step, not from the initial unloaded configuration.

PFEA-2 is started below the lowest failure load predicted by the criteria of Besant et al. [**298**] and Lee and Tsotsis [**301**].

In order to assess the accuracy of the simulation procedure, the experimental crushing behaviour obtained by Aminanda et al [**302**] and Flores-Johnson et al. [**304**] for honeycomb and foam cores are compared with those obtained using the PFEA-2.

Figure 8.2a reports the force-displacement curve for the Aluminium alloy honeycomb, analysed by Aminanda et al. [**302**]. It has cell size of 6 mm and cell wall thickness of 0.12 mm. The analysis is carried out applying quasi-static load in the thickness direction on a 25x25 mm plate. In agreement to what expected, the curve shows an initial linear elastic and stiff response, then, once reached the maximum value of the force, the curve presents a sharp drop due to the beginning of the vertical edge deformation. During this phase the force reaches a plateau, and finally the diagram shows the condensation phase. As it can be seen, numerical results behave in accordance with experiments.

Figure 8.2b reports the strain-stress behaviour for foam cores with different density, under uniaxial compression test. The analyses are carried out considering two cubes with 100 mm edges made with Rohacell 51WF and 110WF foams. According to Flores-Johnson et al. [**304**], the compressive load is applied in quasi-static conditions.

As for the honeycomb core the numerical results are in good agreement with the experimental ones. Both cores initially show linear elastic and stiff response, followed by elastic-plastic behaviour, without work hardening. After this phase, the material cannot absorb further energy, thus stress rises sharply without significant increase of the strain.
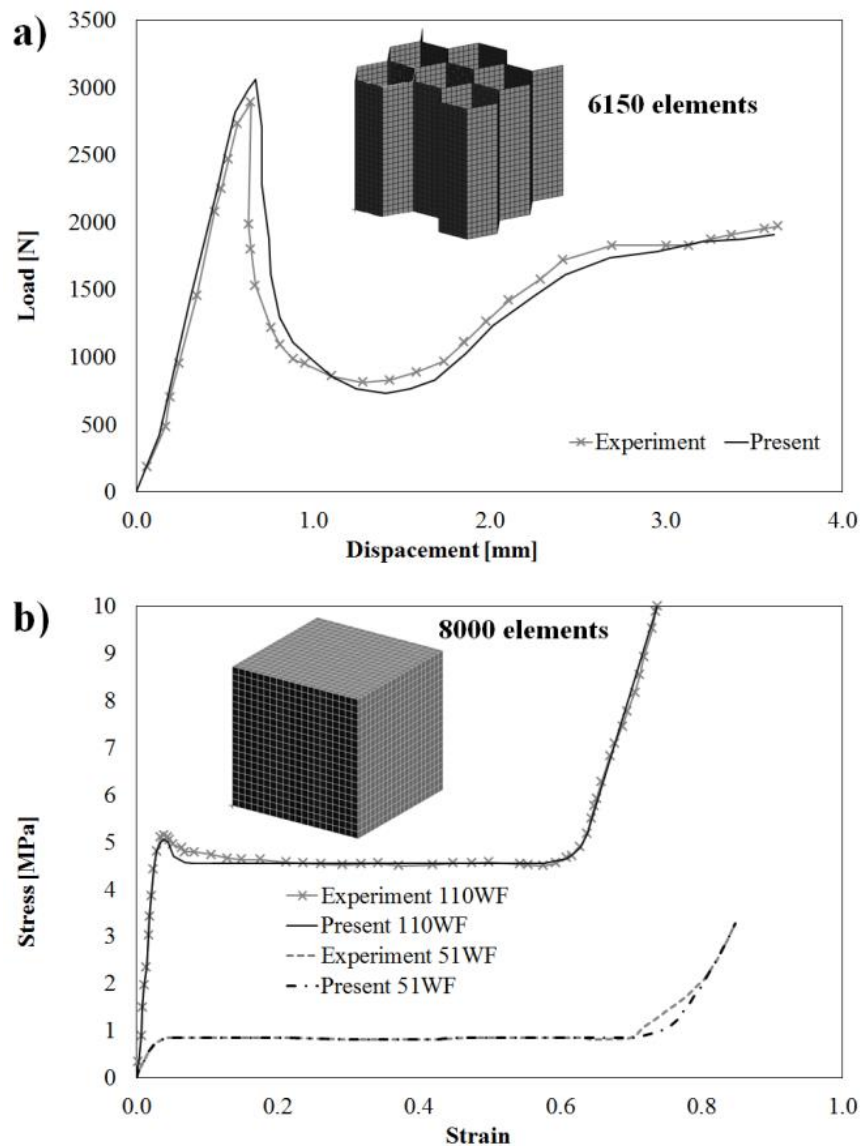
Figure 8.2 Crushing behaviour detected by the present simulation procedure and a) by Aminanda et al [302] for sandwich with honeycomb core, b) by Flores-Johnson et al. [304] for sandwiches with foam core.

8.4 Solution of the structural problem

The problem is solved adopting the AD-ZZ model assuming the through-the-thickness variation of the displacement field as postulated by Eqs. (4.3) – (4.5)

Solution is found in closed form at each time step within the framework of the Rayleigh-Ritz's method, assuming the in-plane variation of functional degrees of freedom u^0, v^0, w^0, γ_x^0 and γ_y^0 expressed as:

$$u^0(x,y,t) = \sum_{m=1,2,3}^{M} \sum_{n=1,,2,3}^{N} A_{mn}(t) \ \sin\left(\frac{m\pi}{L_x}x\right)\sin\left(\frac{n\pi}{L_y}y\right);$$

$$v^0(x,y,t) = \sum_{m=1,2,3}^{M} \sum_{n=1,2,3}^{N} B_{mn}(t) \ \sin\left(\frac{m\pi}{L_x}x\right)\sin\left(\frac{n\pi}{L_y}y\right);$$

$$w^0(x,y,t) = \sum_{m=2,4}^{M} \sum_{n=2,4}^{N} C_{mn}(t) \ \left[\cos\left(\frac{m\pi}{L_x}x\right)-(-1)^{m/2}\right]\left[\cos\left(\frac{n\pi}{L_y}y\right)-(-1)^{n/2}\right]; \qquad (8.21)$$

$$\gamma_x^0(x,y,t) = \sum_{m=1,2,3}^{M} \sum_{n=1,2,3}^{N} D_{mn}(t) \ \sin\left(\frac{m\pi}{L_x}x\right)\sin\left(\frac{n\pi}{L_y}y\right);$$

$$\gamma_y^0(x,y,t) = \sum_{m=1,2,3}^{M} \sum_{n=1,2,3}^{N} E_{mn}(t) \ \sin\left(\frac{m\pi}{L_x}x\right)\sin\left(\frac{n\pi}{L_y}y\right);$$

for clamped edges, or as:

$$u^0(x,y,t) = \sum_{m=1}^{M}\sum_{n=1}^{N} A_{mn}(t) \ \sin\left(\frac{m\pi}{L_x}x\right)\cos\left(\frac{n\pi}{L_y}y\right);$$

$$v^0(x,y,t) = \sum_{m=1}^{M}\sum_{n=1}^{N} B_{mn}(t) \ \cos\left(\frac{m\pi}{L_x}x\right)\sin\left(\frac{n\pi}{L_y}y\right);$$

$$w^0(x,y,t) = \sum_{m=1}^{M}\sum_{n=1}^{N} C_{mn}(t) \ \sin\left(\frac{m\pi}{L_x}x\right)\sin\left(\frac{n\pi}{L_y}y\right); \qquad (8.22)$$

$$\gamma_x^0(x,y,t) = \sum_{m=1}^{M}\sum_{n=1}^{N} D_{mn}(t) \ \sin\left(\frac{m\pi}{L_x}x\right)\cos\left(\frac{n\pi}{L_y}y\right);$$

$$\gamma_y^0(x,y,t) = \sum_{m=1}^{M}\sum_{n=1}^{N} E_{mn}(t) \ \cos\left(\frac{m\pi}{L_x}x\right)\sin\left(\frac{n\pi}{L_y}y\right);$$

for edges that are freely movable in the in-plane directions.

At clamped edges, the mechanical boundary conditions

$$Q_x = \int_\Gamma \sigma_{xz} dz dy \quad ; \quad Q_y = \int_\Gamma \sigma_{yz} dz dx \qquad\qquad (8.23)$$

are satisfied by an appropriate choice of the higher order terms of the AD-ZZ model, Γ being the contour of the plate. Q_x, Q_y are assumed to be uniformly distributed over Γ when the edges are sufficiently far from the impact point located at the centre of the plate. This assumption is valid for large length side-to-thickness ratios.

Application of the Rayleigh-Ritz method for studying impact, which is a non-conservative problem, is allowed since IMPSIM studies this problem as a sequence of conservatives problems (one for each time-step) in which the contact force and the stiffness coefficients are fixed.

The dynamic governing equations in matrix form are obtained from (8.21) or (8.22), then they are solved using Newmark's time integration scheme. Once unknown amplitudes A_{mn}, ..., E_{mn} are computed at each time step, stresses are calculated and the damage analysis is carried out.

The expressions of linear, secant and tangent stiffness matrices of the AD-ZZ model are deduced from (8.21) or (8.22), once they are substituted in (4.3), (4.4) and (4.5) according to [**251**]. The consistent mass matrix of the AD-ZZ is computed considering the inertia contributions within governing functionals, like the dynamic version of the principle of virtual work.

8.5 Application to indentation of sandwiches

As a preliminary application of the simulation procedure described above, in this section numerical results dealing with indentation of sandwiches are compared to experiments taken from literature (see Figure 8.3 for a simplified representation of the loading scheme). Please note that all the computational times reported in this section refer to analyses carried out on a laptop computer with dual-core CPU 1.80 GHz, 64 bit operating system and 4 GB RAM.
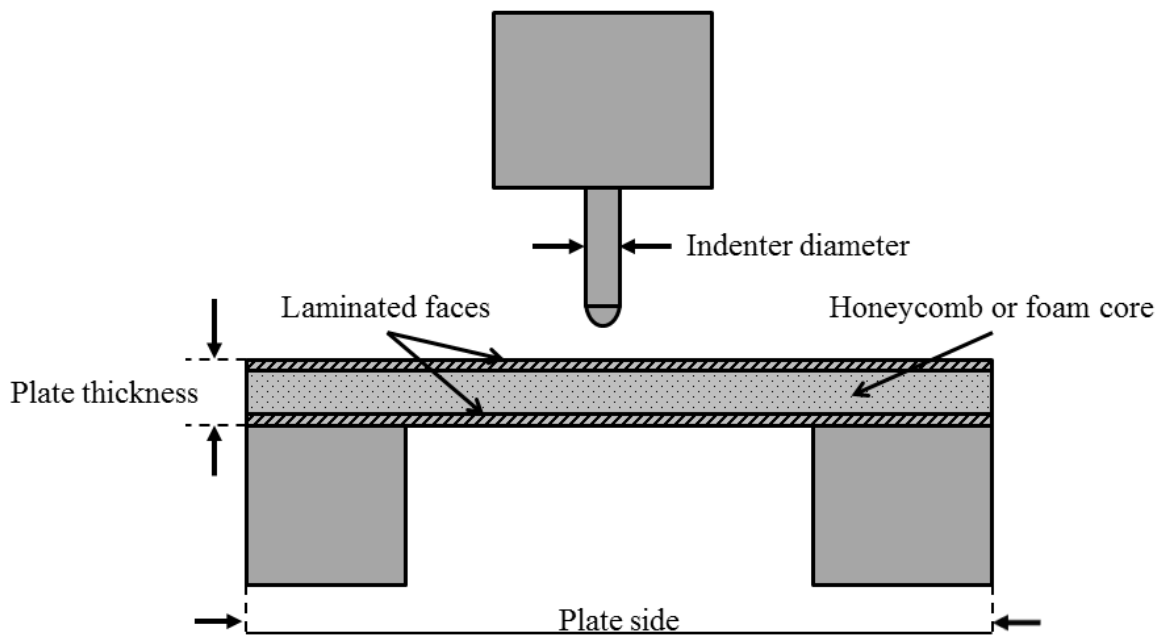
Figure 8.3 Schematic representation of the loading conditions for indentation.

8.5.1 Panels with Rohacell foam core

As first case, let us consider the sandwich plate analysed by Flores-Johnson and Li [**305**] with sides 100 x 100 mm. The faces are in Toho Tenax carbon fibre HTA plain weave fabric 5131, whose mechanical properties are $E_{11}= E_{22}=33.38$ GPa, $\upsilon_{12}=0.051$, $\sigma_{1T}= \sigma_{2T}=124$ MPa, $\sigma_{1T}= \sigma_{2T}=684$ MPa. The faces have a stacking sequence [0°/90°].

Different Rohacell foam cores have been considered. In details, the foams used are 51WF, 71WF, 110WF and 200WF. The mechanical properties of the foams are chosen according to the indication of the manufacturer and they are summarized in Table 8.1. The thickness of the faces is 0.416 mm, while the thickness of the core is 10 mm. The indentation is carried out considering a hemi-spherical indenter with 20 mm diameter.

Properties	51WF	71WF	110WF	200WF
Density [kg/m^3]	52	75	110	205
Compressive strength [MPa]	0.8	1.7	3.6	9
Tensile strength [MPa]	1.6	2.2	3.7	6.8
Flexural strength [MPa]	1.6	2.9	5.2	12
Shear strength [MPa]	0.8	1.3	2.4	5

| Elastic modulus [MPa] | 75 | 105 | 180 | 350 |
| Shear modulus [MPa] | 24 | 42 | 70 | 150 |

Table 8.1 Mechanical properties of Rohacell foams ([299]- [305]).

The results presented in Figure 8.4 are in good agreement with the experiments by Flores-Johnson and Li [**305**]. It could be noticed that, except that for the 110 WF, all the force-indentation curves present a typical behaviour: an initial part where force and displacement grow, then the force reaches a peak, drops down and raises again. These phenomena are accurately described by the present simulation procedure. Please note that in this case 15 elements across the thickness have been considered during the PFEA-2, while the mesoscale model determines a reduction of the mechanical properties that is strongly influenced by the foam constituting the core. Indeed, for the sandwich with 51 WF core the mechanical properties of the upper face are reduced of 40% and those of the core of 50%. Instead, the panel with 71 WF core requires a 40% reduction of the mechanical properties of the upper faces and 35% reduction of the mechanical properties of the core. In the analysis of the plate with 110 WF core the degraded mechanical properties are 30% and 35% lower than the undamaged ones of the core and the upper face respectively. Finally the last case needs a 20% decrease of the mechanical properties of the 200 WF core and 25% reduction of those of the upper face. The computational times are similar for the four cases considered, and they vary from 427 s for the sandwiches with 51 WF core and 431 s for the sandwich with 200 WF core.

For all the cases considered in Figure 8.4, it is reported as an inset the comparison between the damage predicted by the present simulation procedure and that experimentally detected in [**305**]. Note that the results by the present analytical procedure are obtained applying the stress-based criteria in a grid of points. If in a generic point the failure criteria predicts the damage, a small square area (fictitious) is considered damaged, as explained in Section 8.2.2. The damage reported in Figure 8.4 is the envelop of all the damaged areas computed by the procedure. A more detailed application of this procedure is presented in Section 8.6.3.

As a general remark, it could be observed that in all these cases the present simulation procedure provides results in good agreement with the experimental ones. In details, as also outlined in [**305**], it can be seen that the damage is more localised for sandwiches with greater

core density due to the increase of stiffness, which enhances the local effect of the indentation.
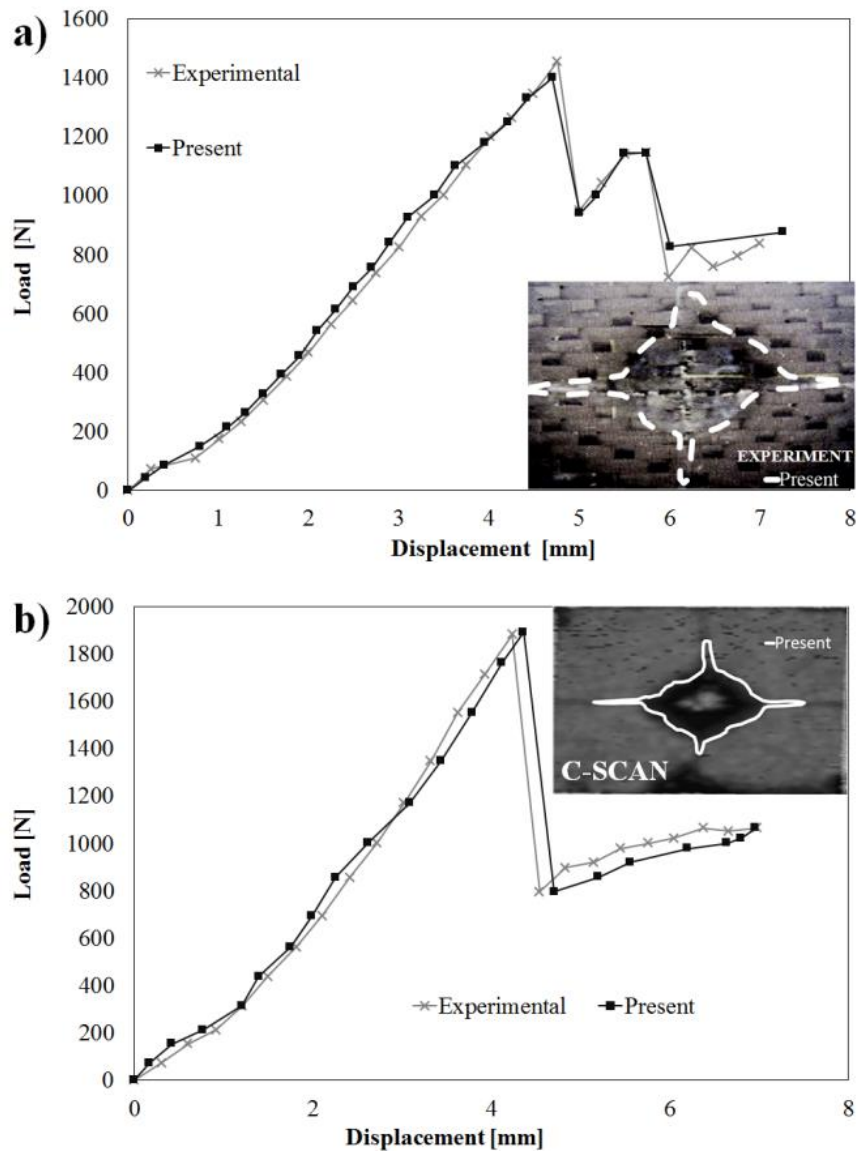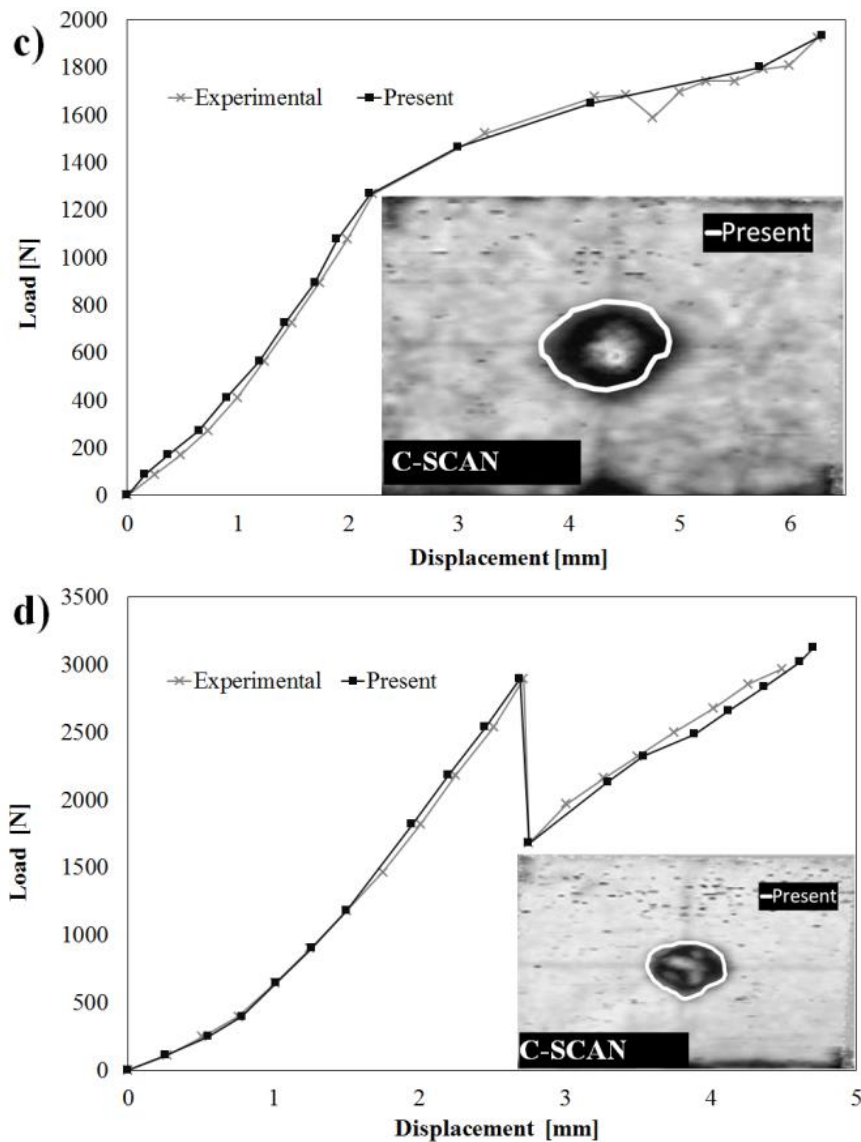
Figure 8.4 Comparison between experimental [305] and present numerical force–indentation curves for sandwich panels with a) 51WF foam core, b) 71WF foam core, c) 110WF foam core and d) 200WF foam core.

Flores-Johnson and Li in [**305**] presents also experimental results for the indentation of a 100 x 100 mm sandwich plate loaded by hemi-spherical indenter with different diameter, indenter A has 16 mm diameter, indenter B has 20 mm diameter, indenter C has 25 mm diameter. The plate has Toho Tenax carbon fibre HTA plain weave fabric 5131 faces and Rohacell 51WF core. Once again, the faces have a stacking sequence [0°/90°], the thickness of the faces is 0.416 mm, while the thickness of the core is 10 mm.

Numerical results reported in Figure 8.5 are in good agreement with the experimental ones. Also in this case during the PFEA-2 15 elements have been considered across the thickness of

the core, while the indenter diameter has an influence on the results by the mesoscale model. Specifically, with indenter A the mechanical properties of the upper face are degraded of 70% while those of the core of 65%. The results by the indenter B are the same described above, while those by indenter C are a 25% reduction of the mechanical properties of the core and a 32% of those of the upper face. As far as computational times are concerned, 361 s are required to carry out the analysis when indenter A is considered, 427 s when indenter B is considered and 525 s when indenter C is considered.
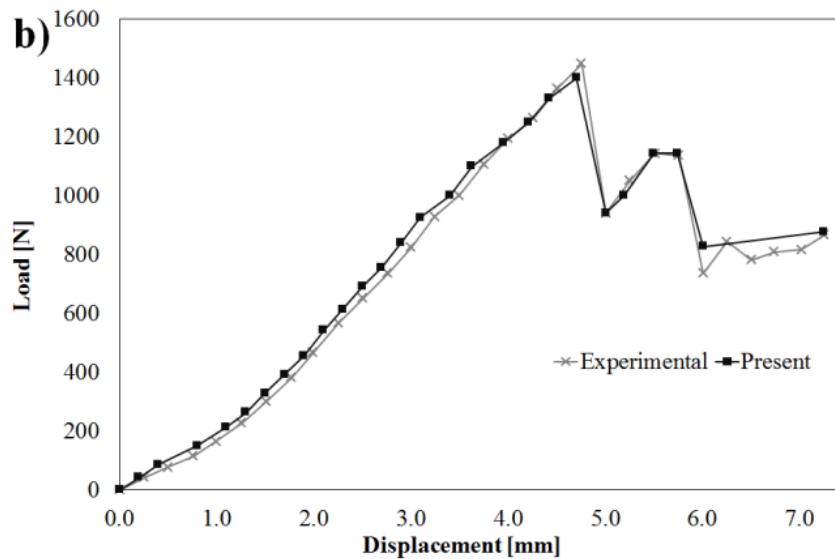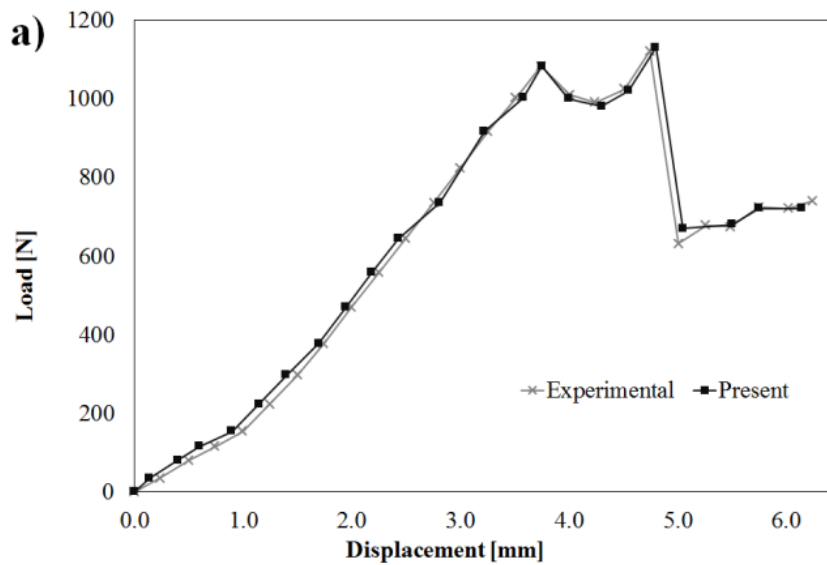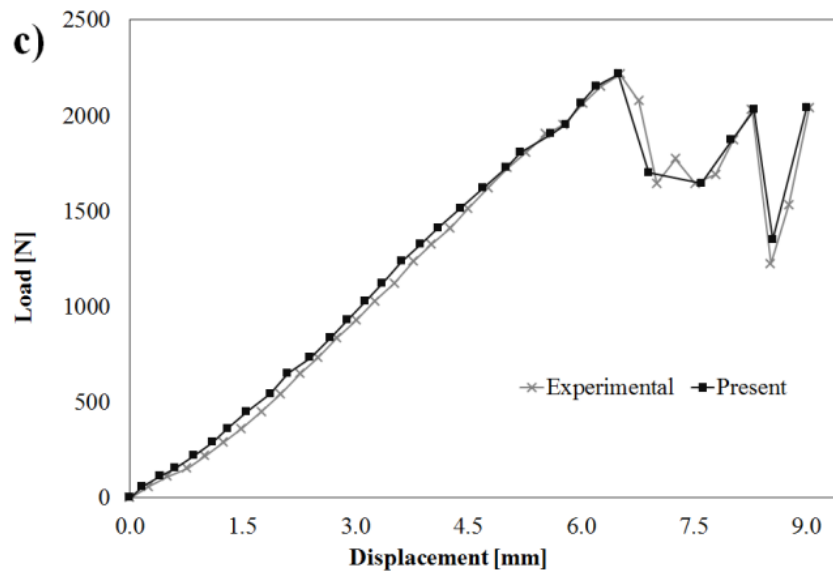
Figure 8.5 Comparison between experimental [305] and present numerical force–indentation curves for 51WF foam cored sandwich panels with a) indenter A, b) indenter B and c) indenter C.

8.5.2 Panels with honeycomb core

Consider the 152.4x152.4 mm sandwich plates with honeycomb core analysed by McQuigg [**306**]. The skins of the sandwich construction are obtained using two plies of style 7781 plain woven E-glass fabric with 40% epoxy resin content, whose strength and modulus in the warp and fill direction are 413.6 MPa and 20.7 GPa, respectively, for compressive loading, and 372.3 MPa and 20.7 GPa, respectively, for tensile loading. The in-plane shear strength and modulus are 88.6 MPa and 2.76 GPa, respectively. The in-plane Poisson's ratio is 0.14 and the interlaminar shear strength is 24.13 MPa. The plies are directionally aligned in the 0° direction and the thickness of the skins is 0.508 mm. The Nomex^{TM} honeycomb core has a 25.4 mm thickness, with 3.175 mm cell size, 0.018 mm foil gauge, and a density of 48.1 kg/m^3.

The indentation is carried out using a hemi-spherical indenter with 12.7 mm diameter acting at 0.75 L_x and 0.25 L_y, being L_x and L_y the size of the panel in the x and y direction, respectively. The panel is clamped on all four edges.

The results for this case reported in Figure 8.6 are still in accordance with the experimental ones. As far as PFEA-2 is concerned, 30 elements have been considered across the thickness of the honeycomb, while the mesoscale model calls for a 38% reduction of the mechanical

properties of the upper face and a 34% reduction of those of the core. In this case, the analysis takes 295 s.

Figure 8.6 Comparison between experimental force-indentation curves by McQuigg [306] and those obtained using the present simulation procedure.

As explained above, the core density has a significant bearing in determining the energy absorption of the structure. Accordingly, attention is now focused on the experimental indentations of 139.7x139.7 mm sandwich panels with honeycomb core with different densities, carried out by McQuigg [306]. The panel named as 3 PCF-XX has Nomex[TM] honeycomb core with density of 48.1 kg/m^3, 3.175 mm nominal cell size and 0.018 mm foil thickness, while that named 6 PCF-XX has Nomex[TM] honeycomb core with density of 96.11 kg/m^3, 3.175 mm nominal cell size and 0.038 mm foil thickness. In both cases the cores are 12.7 mm thick.

The skins of both the 3PCF-XX and the 6PCF-XX panels are made of two plies each of style 6781 woven S2-glass fabric cloth with 35% epoxy resin content. The resin is MTM45-1, while the thickness of the faces is 0.508 mm and their stacking sequence is [0°/45°]. According to [306], the warp direction strength and moduli are 561.65 MPa and 29 GPa, respectively, for tensile loading, and 575.23 MPa and 29 GPa, respectively, for compressive loading. The fill direction strength and moduli are 555 MPa and 28 GPa, respectively, for compressive loading, and 476.22 MPa and 27.7 GPa, respectively, for tensile loading. The in-plane shear strength and modulus are 37.58 MPa and 3.79 GPa, respectively. The in-plane Poisson's ratio is 0.138. The indentation is carried out using a hemi-spherical indenter with

12.7 mm diameter and the panels are clamped on all four edges. In these cases, the PFEA-2 is carried out considering a discretization with 15 elements across the thickness of the honeycomb, while the results by the mesoscale model are influenced by the honeycomb density. In details, for the 3PCF-XX plate a 33% reduction of the mechanical properties of the core and a 36% reduction of the properties of the upper faces are required, while for the 6PCF-XX sandwich these values decrease to 27% and 30% for the core and the upper face, respectively. The computational costs are no longer affected by the honeycomb density; indeed, the analysis on the 3PCF-XX panel requires 558 s, while that on the 6PCF-XX panel takes 561 s. As for the former cases, the numerical results in Figure 8.7 are in good agreement with the experimental ones. It could be noticed that, an increasing of the core density determines a growth of the peak in the force value.

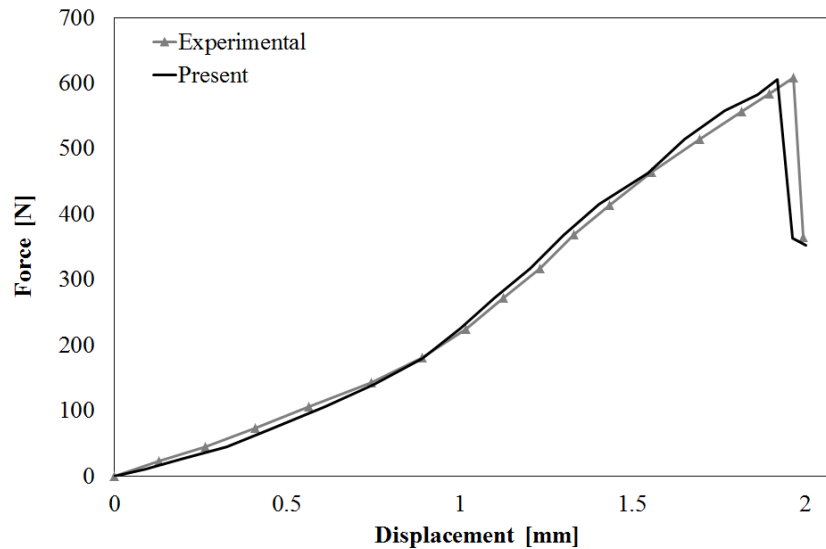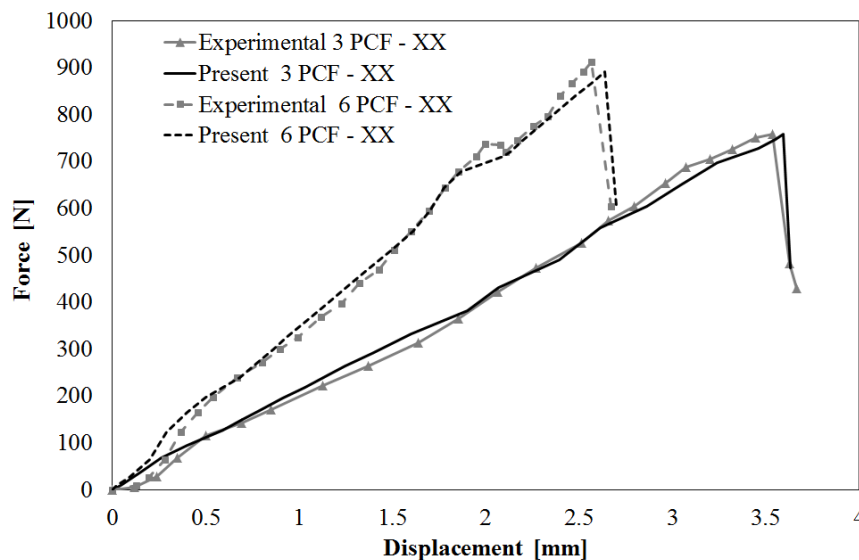***Figure 8.7 Comparison between experimental force-indentation curves by McQuigg [306] and those obtained using the present simulation procedure.***

8.6 Application to impact studies

In light of the accurate results obtained by IMPSIM for the indentation of sandwiches, in the next sections, contact force and damage evaluation of laminates and sandwiches subjected to impact are presented.

8.6.1 Contact force of laminates

First, the sample case of a 230x 127 laminated plate with a $[45°/0°/-45°/90°]_{2s}$ lamination scheme and with all the edges clamped tested by the author is presented. The plate is subjected to the impact of a steel hemispherical nose of 1.15 kg at different levels of energy (1.5 J and 2.5 J). Each of its 16 layers is made of AS4/3502 Graphite-Epoxy and its total thickness is 2.48 ± 0.0254 mm.

The acceleration time-history is detected through an accelerometer mounted on the impactor nose and connected to a data acquisition system. The contact force time-history is obtained multiplying the impactor mass by the measured acceleration. Since the arm carrying the impactor nose follows a circular trajectory, attention has been paid to assure that the impact force is perpendicular to the impacted panel, as assumed in numerical simulations. A sampling frequency of 10^5 Hz is used.

The results of Figures 8.8 and 8.9 show the numerical simulation to be appropriate, its results being in good agreement with experiments. It is worthwhile to note that just 350 s are required to carry out the analysis on a laptop computer, thus the efficiency of IMPSIM is still proven. The results with and without enforcement of the target to conform the shape of the impactor are shown to be equivalent for this case. Thus, the iterative algorithm of Section 8.1.2 is reputed unnecessary when laminates are analysed.
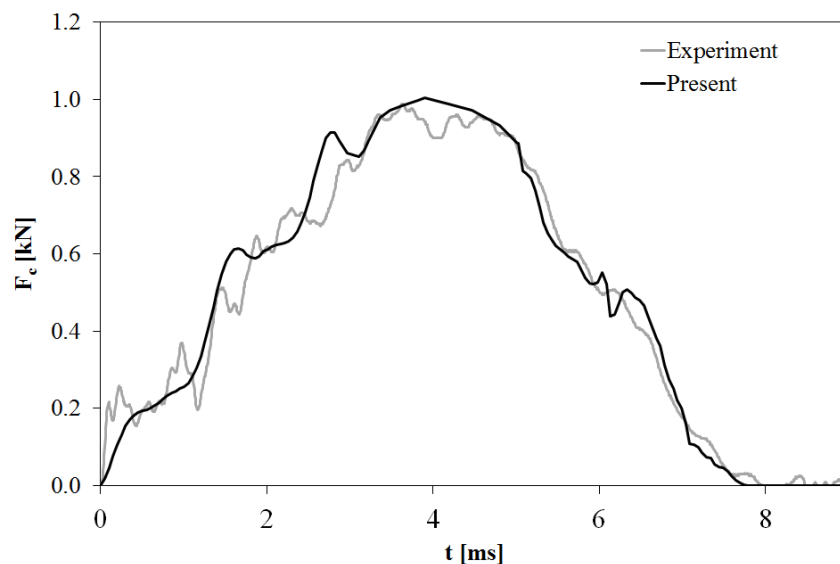
Figure 8.8 Comparison between simulated and experimental contact force for a laminated [45°/0°/-45°/90°]$_{2s}$ plate impacted at 1.5 J.
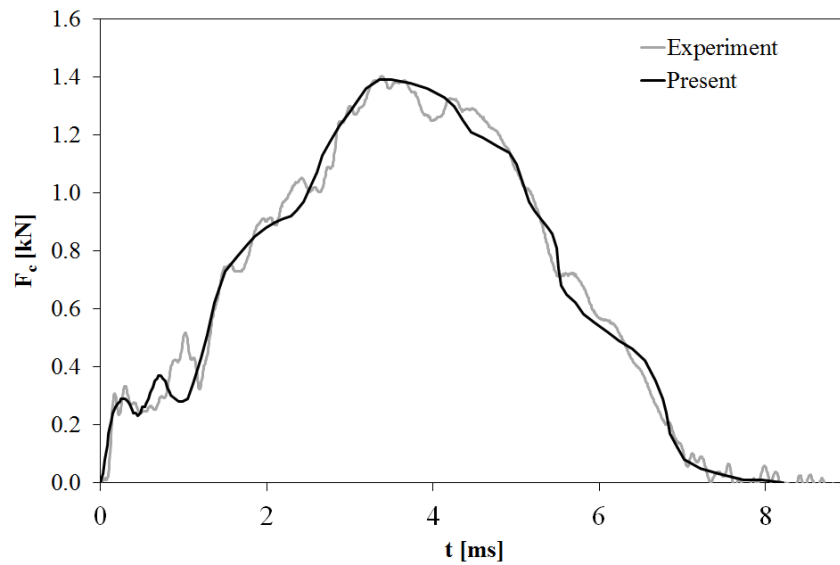
Figure 8.9 Comparison between simulated and experimental contact force for a laminated [45•/0•/-45•/90•]₂ₛ plate impacted at 2.5 J

8.6.2 Contact force of sandwiches

The experimental contact force time history detected by Kärger et al. [**281**] is compared to that predicted by IMPSIM, with and without enforcing the panel to conform to the shape of the impactor in order to show that soft media requires the application of algorithm of Section 8.1.2.

The thin top face sheet (thickness = 0.633 mm) is made of   Cytec 977-2/ HTA. The thick bottom face sheet (thickness = 2.7 mm) is made of CFRP fabric plies and UD tapes, with a $[(0°_2/45°/90°/-45°)_s]_s$ lay-up. The core, which is 28 mm thick, is made of NOMEX 4.8-48 honeycomb. This sandwich panel is completely supported at the edges and it is impacted by a steel sphere with energy of 8 J, having a diameter of 25.4 mm carried by an impactor with a mass of 1.10 kg

The results of simulations reported in Figure 8.10 show that a quite accurate prediction of the contact force is obtained at each instant of time only if: (i) the iterative algorithm of Section 8.1.2 is considered that computes the contact radius at each step; and if (ii) PFEA-2, i.e. the detailed FEA representation of the real geometry of core is carried apart in order to account for the buckling of cell walls under transverse compressive loading, as described in Section 8.3, which provides apparent elastic moduli of the core at each time step in accordance with the applied load. The fundamental role played in this simulation by the core crushing

behaviour is clearly shown, because, disregarding it, totally wrong results are obtained. So, the homogenized model can be used for successfully carrying out the progressive damage analysis only if appropriate apparent properties are provided at each load level, as obtained apart by PFEA-2.
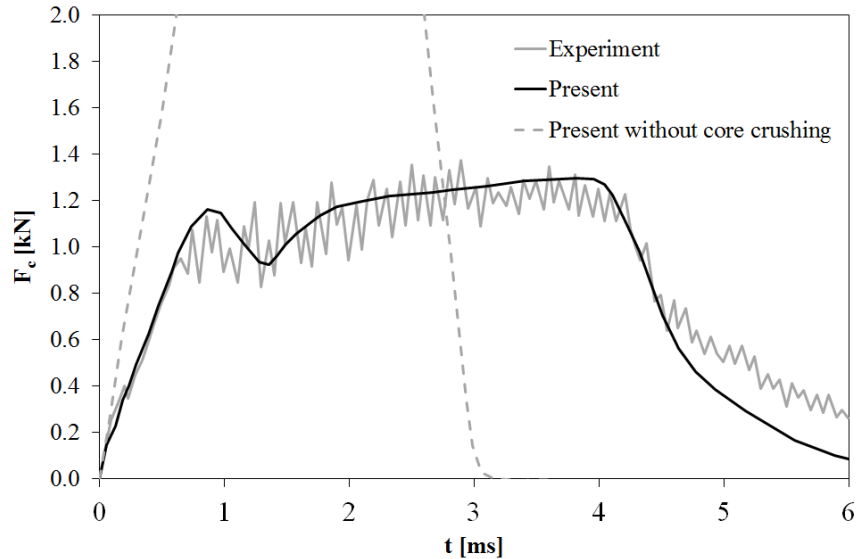
Figure 8.10 Contact force for a sandwich plate impacted at 8 J by experiment [281] and the present simulation procedure.

As in this case the algorithm that accounts for the core crushing behaviour is activated, the computations at each time step are a little bit slower than in previous cases where a laminate was considered. However, just 550 s are required to compute the contact force time history, hence the simulation procedure is still proven to be accurate and cost-effective.

In order to evaluate whether accurate predictions of the contact force of sandwiches can be obtained at different levels of energy, attention is now focused on the sandwich panel with PVC foam core (Divinycell H250) and laminated carbon fabric/epoxy faces (AGP370-5H/ 3501-6S) studied by Schubel et al. [**307**], for impact energies ranging from 7.75 to 108 J. A sphere with a radius of 12.7 cm mounted on an impactor with a mass of 6.22 kg is left to fall onto the panel. Increasing the heights of the mass drop, the above mentioned impact energies are obtained. The sandwich plate has sides of 27.9 cm, thickness of 2.82 cm and it is simply supported. The core is 25.4 mm thick, while the laminated face sheets are obtained stacking four plies of prepreg for a total thickness of 1.37 mm. According to [**307**], the mechanical properties of the faces are: ρ= 1600 kg/m^3, E_1= 77 GPa, E_2= 75 GPa, G_{12}= 6.5 GPa, G_{13}= 5.1 GPa, G_{23}= 4.1 GPa, υ_{12} = 0.07.

Figure 8.11 shows the comparison between the experiments of Ref. [**307**] and the contact force time histories predicted by IMPSIM at the three energy levels of 7.75, 41.1 and 108 J. It is seen that the present simulation obtains accurate contact force time histories in all three cases. No increasing errors are seen increasing the impact energy. Thus, it is reputed that the present modelling approach can be successfully used in the practical applications, at least for energies up to a hundred of J.
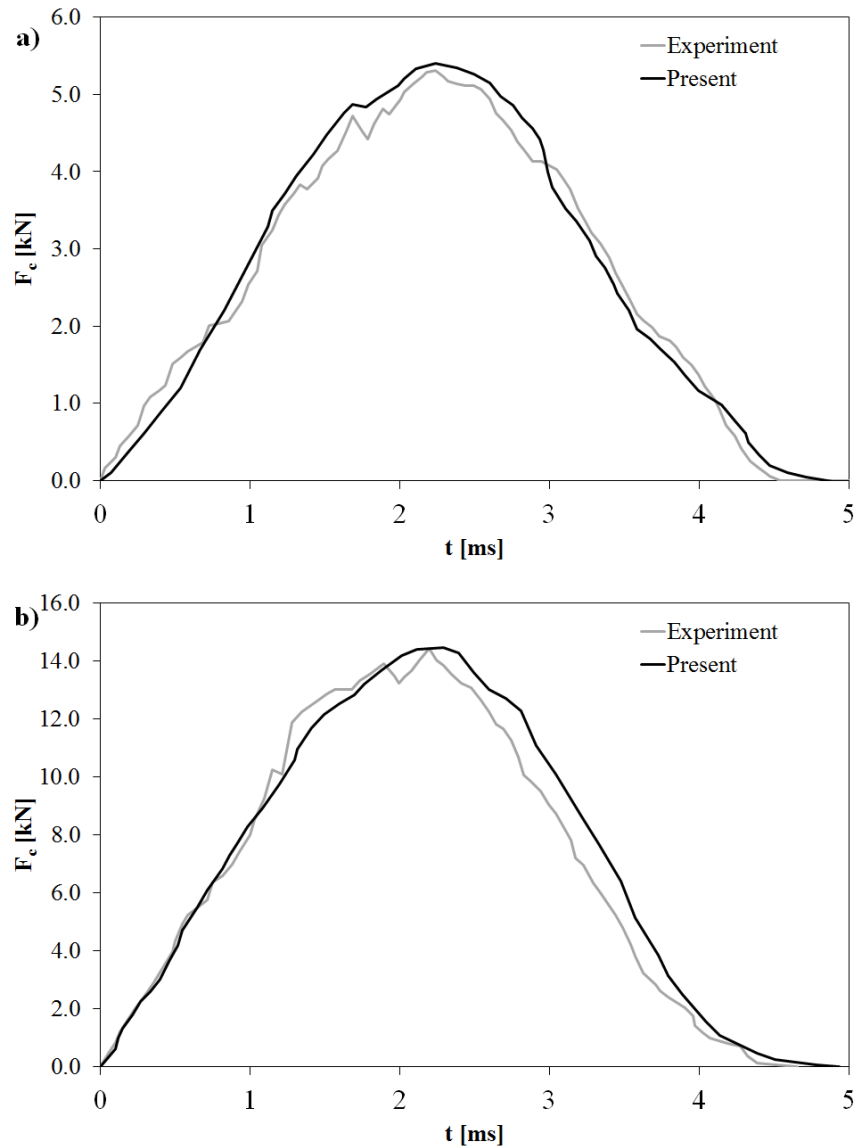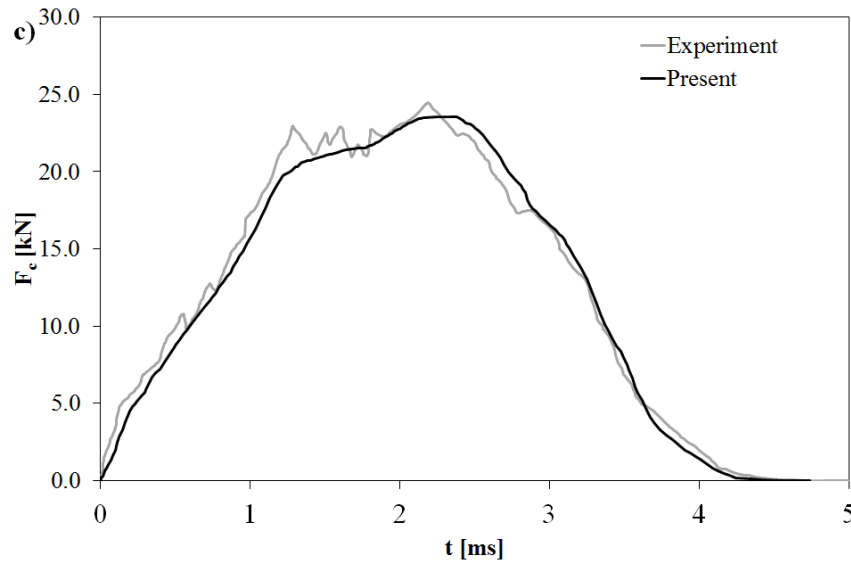
Figure 8.11 Comparisons between experimental [307] and numerical contact forces for a sandwich plate with foam core considering an impact energy of a) 7.75 J, b) 41.1 J and c) 108 J.

In the next section, the damage predicted by the present simulations is compared to that detected via ultrasonic cartography.

8.6.3 Damage evaluation

A composite panel with I stiffeners having a length of 800 mm (L_x), a width of 330 mm (L_y) and a skin thickness (t) of 3 mm formerly tested by Icardi and Zardo [**308**] is now considered. The panel is clamped at the short sides and is kept free at the long sides. It is impacted at the centre with impact energy of 40 J (mass of the impactor 5.45 kg, velocity 3.83 m/s). The skin layers are 0.25 mm thick, they are stacked with a [45°/-45°/0°/0°/45°/-45°/-45°/45°/0°/0°/-45°/45] sequence and have the following mechanical properties: E_1= 130 GPa, E_2= 8 GPa, G_{12}= 5 GPa, G_{13}= 5 GPa, G_{23}= 2.5 GPa, v_{12}= 0.3, ρ= 1557 kg/m^3. The strengths are: S_{t11}= 1.67 GPa, S_{t22}= 0.06 GPa, S_{c11}= 1.08 GPa, S_{c22}= 0.17 GPa, S_{12}= S_{13}= S_{23}= 0.07 GPa, where S_{tii} represents the strength to traction in directions i, S_{cii} represents the strength to compression in directions i while S_{ij} represents the shear strength over the plane ij. The impactor is made of steel (E= 210 GPa, v= 0.3) and has a nose sphere with a diameter of 25.4 mm.

The comparison of the contact force predicted by the simulation to that experimentally detected presented in Figure 8.12 shows again the high predictive capability achieved by IMPSIM.
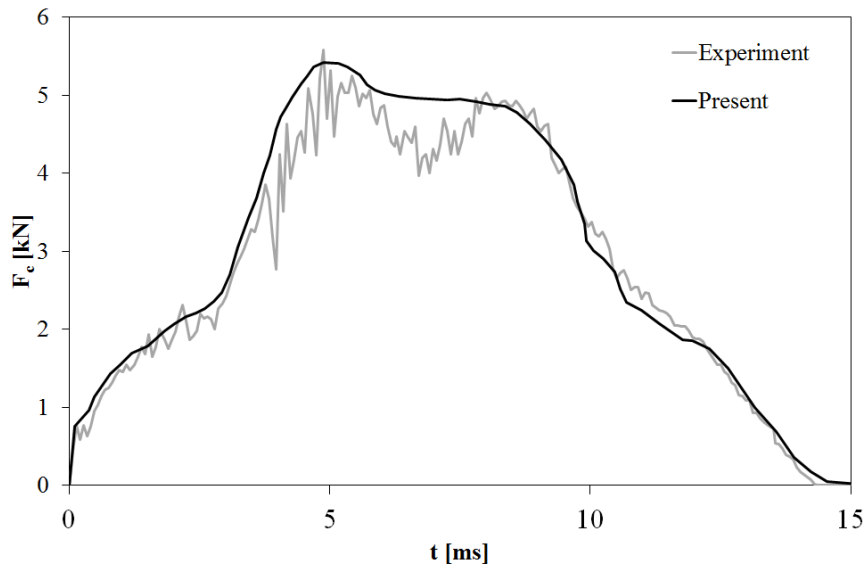
***Figure 8.12 Comparison between the experimental contact force [308] and that computed with the
present procedure for a laminate with I stiffeners.***

Instead, for what concerns the damage analysis, Figure 8.13 shows the comparison of the overlapped damaged area measured through C-SCAN (dashed line) [**308**], and that predicted by the present simulation with (light-grey regions) or without (dark-grey regions) in-plane stress continuity (4.6) – (4.8). Since ultrasonic scanning detects delaminations from the waves that reflect back, just delamination damage is reported in Figure 8.13. The results of this figure show that a correct prediction of the overlap damage is obtained in any case, but much accurate results are obtained if in-plane stress continuity is considered. Thus, this further continuity condition is shown to have a significant bearing in improving results and it does not merely represent a theoretical achievement. As an elapsed time of 490 s is required to complete the analysis, in-plane continuity does not adversely affect computational costs.

For what concerns the simulation procedure, it could be noted that the centre of each arbitrarily chosen sub-region for damage analysis corresponds to a point p_i where the damage criteria of Section 8.2.1 are applied in order to determine whether or not materials are failed. If in p_i one of the damage criteria predicts failure, the corresponding sub-region is considered damaged and therefore it is coloured in grey. Stresses in p_i are determined assuming the modified expression of the strain energy resulting by the damage mesoscale model (8.2.2) with the damage indicators computed by PFEA-3.
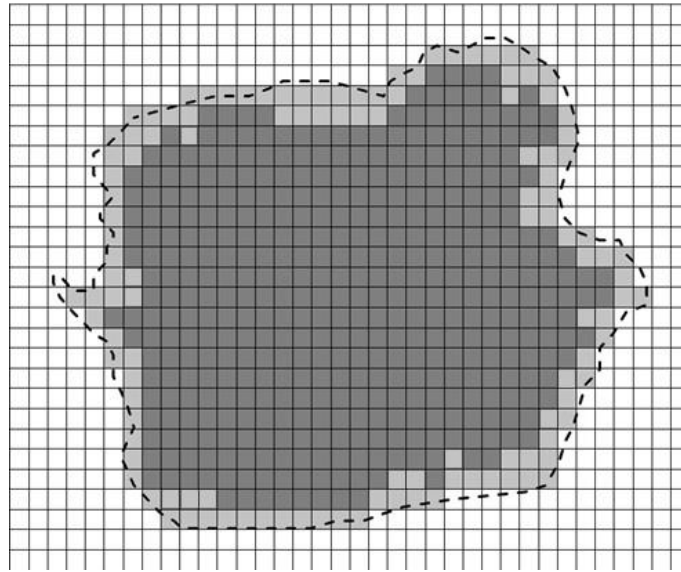
***Figure 8.13 Overlap induced damage for a laminate with I stiffeners by: C-SCAN [308] (dashed
line), present procedure without considering in-plane continuity (dark-grey square sub-regions) or
considering it (light-grey square sub-regions).***

Table 8.2 shows the extension of the delaminated area at each interface, as measured in [**308**]
and as computed by the present simulation procedure. These results confirm the accuracy of
IMPSIM, as the damage predicted at each interface is always in good agreement with
experimental results.

	Physical interface	Experimental [**308**]	Present
	1st	960	950
	2nd	790	758
	3rd	430	400
Delaminated area [mm^2]	4th	310	250
	5th	160	115
	6th	135	102
	7th	95	75
	8th	50	44

***Table 8.2 Delaminated area [mm^2] at the interfaces for a laminate with I stiffeners by the present
procedure and by experiment [308].***

The comparisons of numerical results with experiments presented in this chapter showed the
superior predictive capability of the present simulation procedure.

Accordingly, all non-classical contributions considered within it (i.e. the piecewise variable high order representation of the transverse displacement, the transverse normal stress and stress gradient continuity at the layer interfaces and the fulfilment of the stress compatibility under sudden in-plane variation of properties) are important for improving accuracy of displacement, stress and strain energy density fields, as they determine more accurate results. It is important to underline that such a high level of accuracy is achieved with a computational effort comparable to that of equivalent single layer theories, thus with no increased costs.

Conclusions

The research work presented in this Thesis is devoted to the development and assessment of accurate and computationally efficient theories and numerical tools for describing stress and displacement fields of composites structures and for increasing their structural performances. The basis and the starting point of the activity was the AD-ZZ model presented in Chapter 2. It is a recently developed 3D multilayered plate model with variable zig-zag representation of displacements, which can adapt itself to the variation of solution. It has a fixed number of functional d.o.f. and it constitutes a reformulation of a previous "adaptive model" aimed at reducing processing time. Thanks to the incorporation of physically-based zig-zag functions and high-order terms, the AD-ZZ model is able to fulfil the conditions on stresses prescribed by the elasticity theory and the equilibrium conditions across the thickness of the structure. In addition, the through-the-thickness representation can be refined where stress field has steep gradients. With the goal of reducing computational times, a symbolic calculus tool is employed for determining the expressions of the displacements' coefficients in closed form once at a time. Since these computations are carried apart, the processing time of the present model is of up 15 times lower than that required by the model from which it derives. In order to make clearer the motivations and the ideas that played a central role in the development of the AD-ZZ model, a briefly overview of the recent approaches adopted in literature for modelling composite structures was premised in Chapter 1. In particular, attention was focused on theories that adopt physically-based or cinematically-based zig-zag functions. The former approach was shown to be preferable as its hypotheses are of more general validity. Therefore the brief overview of Chapter 1 was mainly earmarked to global-local model, sublaminate approach, Refined Zig-Zag Theory by Tessler and co-workers and their applications to problem of practical interest. The basic concepts adopted by these theories for improving accuracy are substantially two: adding new unknowns that are calculated by imposing to fulfil specific conditions prescribed by the elasticity theory or refining the

interpolation in the area where the stress field has steep gradients. The development of the AD-ZZ model has taken inspiration by these two cornerstones.

The analytical results presented in Chapter 3 were devoted to investigate the AD-ZZ model prediction capabilities over a wide range of problems mainly concerning laminated and sandwich structures subjected to several boundary and load conditions (either static or dynamic). Though unrealistic for engineering applications, all the structures considered were characterized by extremely low length-to-thickness ratios in order to enhance the zig-zag and layerwise effects, thus making these cases more severe for the model. Numerical results confirmed the predictive capabilities of the AD-ZZ model, which is able to find directly from constitutive equations results as accurate as the exact solutions for the majority of the cases analysed even with strongly asymmetric structures. The problems solved in Chapter 3 constituted also the occasion to compare the accuracy of the AD-ZZ model to that of the main approaches overviewed in Chapter 1.

As an application of the AD-ZZ model to problem of practical interest, in Chapter 4, new terms were added to the displacement field postulated in Chapter 2 in order to treat under a unified approach bonded joints and laminated structures. Formally, these contributions are similar to the zig-zag functions of the AD-ZZ model, but they act in the in-plane direction. The closed form expressions of in-plane continuity are calculated through symbolic calculus, thus computational effort is not increased, since the number of functional d.o.f. does not vary. Applications to linear and nonlinear benchmark test cases of joints taken from the literature were presented. Numerical results showed that the AD-ZZ model can accurately and efficiently treat bonded joints with laminated adherends. Indeed, for all the examined cases, accurate results were obtained in few seconds carrying out the analyses on a laptop computer.

As a result of the enforcement of physical constraints, such as the stress continuity at the interfaces, the AD-ZZ model contains derivatives of the d.o.f., which make unwise the direct implementation of a finite element based on it. Accordingly, in the present research work a technique was proposed with the aim of obtaining a C0 model from a variable kinematics zig-zag one. The objective was finding a priori corrections of displacements in closed form, which make the energy of the C0 model with all the derivatives neglected equivalent to that of the initial model containing all the derivatives of the functional d.o.f. In order to describe the in-plane variation of displacements, Hermite's polynomial representations of the d.o.f. were used, whose order depends upon the order of derivatives appearing in the model. From these

polynomials, the modified expressions of displacements were computed a priori in closed form using symbolic calculus. Numerical results presented in Chapter 6 confirmed the validity of the updating technique, as it preserves the accuracy of the equivalent model though keeping fixed the number of functional d.o.f. and thus requiring a low computational effort.

From the equivalent C0 model an eight-node multi-layered isoparametric plate element with standard d.o.f. and interpolating scheme was developed. In addition, taking advantage of the strain energy updating technique, also a quadrilateral, eight-node, mixed plate element was presented. It has displacements and interlaminar stresses at the reference mid-plane as nodal d.o.f. For both the elements introduced in Chapter 7, accuracy, solvability and convergence were assessed considering multi-layered monolithic structures with cross-ply and angle-ply lay-up and sandwich-like structures with different loading and boundary conditions, for which exact solutions are available in the literature. In all the cases, accurate results were obtained, requiring low computational costs.

The application of variable stiffness composites and the stitching of sandwiches, discussed in Chapter 5, demonstrated to be effective methods for improving structural performances. The basic idea of variable stiffness composites is to minimize the energy absorbed through unwanted modes (i.e., involving interlaminar strengths) and maximize that absorbed through desired modes (i.e., involving membrane strengths), by finding a suitable in-plane variable distribution of stiffness properties. This distribution is found making extremal the energy contributions of interest under the properties spatial variation. Therefore, this new tailoring concept requires the orientation of the reinforcement fibres to be varied. As a result, an energy transfer takes place from bending to in-plane and out-of-plane shears energy modes, or vice versa, with respect to layers with customary properties. The variable stiffness distribution is obtained enforcing conditions, which range from the imposition of thermodynamic constraints, to the choice of a convex or a concave shape (in order to make minimum or maximum the energy contributions of interest), to the imposition of their mean value. The numerical applications here presented dealing with laminates and sandwiches subjected to static or blast pulse loading, showed that variable stiffness composites can consistently reduce the through-the-thickness interlaminar stress concentrations and they can keep substantially unchanged the bending stiffness (or even increasing it), when appropriately positioned across the thickness. Instead, for what concerns analysis of stitched structures with a smeared model such as the AD-ZZ, the main modelling problem is the evaluation of the homogenized

mechanical properties due to the contribution of the through-the-thickness reinforcement. For doing this, virtual material testing performed with mixed solid element was carried out, then, in order to quantify the effect of the stitching spacing the rule of mixture was adopted. Once the homogenized properties of the stitched structures have been evaluated, they are used by the AD-ZZ model for performing the analysis. Numerical applications showed, first of all, the effectiveness of this technique for evaluating the mechanical properties of stitched structures. In addition, applications to stitched structures demonstrated that also stitching is a powerful method for improving structural performances.

Finally, in Chapter 8, a simulation procedure based on the AD-ZZ model has been proposed to study of low velocity impacts on laminated and sandwich composites, with honeycomb or foam core. The contact radius and force were computed assuming the stress distribution to be Hertzian and forcing the impacted surface to conform to the impactor shape by an iterative procedure. In details, for sandwich composites that are rather deformable at the impact point, the crushing behaviour was evaluated apart through a preliminary finite element analysis. Fibre and matrix failure and delamination were simulated using simple stress-based criteria; the post-failure degradation was obtained reducing the elastic properties according to the mesoscale damage model. Sample cases were considered for which experimental results are available. The comparisons of the present simulations with these experiments showed that the present computational model is rather accurate in all the cases considered, although it requires a low computational effort.

Concluding, the research activity presented, supported by the numerical results, encourages the adoption of the theories and numerical tools herein developed for laminated and sandwich structures. In particular, the work identifies in the AD-ZZ model and the subsequent theoretical developments that originate from it (SEUPT - IMPSIM), very appealing numerical tools by virtue of their accuracy and efficiency. In addition, variable stiffness composites and stitching of sandwiches presented in this research work demonstrate to be effective method for improving structural performances of composites, being easy to produce with the current manufacturing techniques.

References

[1] J Sliseris and K Rocens, "Optimal design of composite plates with discrete variable stiffness," *Composite Structures*, vol. 98, pp. 15 - 23, 2013.

[2] A Khani , M M Abdalla, and Z Gürdal, "Circumferential stiffness tailoring of general cross section cylinders for maximum buckling load with strength constraints," *Composite Structures*, vol. 94, pp. 2851 - 2860, 2012.

[3] M A Nik, K Fayazbakhsh, D Pasini, and L Lessard, "Optimization of variable stiffness composites with embedded defects induced by Automated Fiber Placement," *Composite Structures*, vol. 107, pp. 160 - 166, 2014.

[4] P F Liu and M M Islam, "A nonlinear cohesive model for mixed-mode delamination of composite laminates," *Composite Structures*, vol. 106, pp. 47 - 56, 2013.

[5] P L Vachon, V Brailovski, and P Terriault, "Prediction of the propagation of impact-induced delamination in carbon/epoxy laminates," *Composite Structures*, vol. 95, pp. 227 - 235, 2013.

[6] P Potluri, E Kusak, and T Y Reddy, "Novel stitch-bonded sandwich composite structures," *Composite Structures*, vol. 59, pp. 251-259, 2003.

[7] H Judawisastra, J Ivens, and I Verpoest , "The fatigue behaviour and damage development of 3D woven sandwich composites," *Composite Structures*, vol. 43, pp. 35-45, 1998.

[8] B Wang et al., "Experimental investigation of 3D sandwich structure with core reinforced by composite columns," *Materials & Design*, vol. 31, pp. 158-165, 2010.

[9] U K Vaidya, S Nelson, B Sinn, and B Mathew, "Processing and high strain rate impact response of multifunctional sandwiches composites," *Composite Structures*, vol. 52,

pp. 429-440, 2001.

[10] M Nilanjan, "A methodology for improving shear performance of marine grade sandwich composites: sandwich composite panel with shear key," *Composite Structures*, vol. 92, pp. 1065-1072, 2010.

[11] B N Cox and G Flanagan, "Handbook of analytical methods for textile composites," NASA, CR-4750, 1997.

[12] J M Whitney and N J Pagano, "Shear deformation in heterogeneous anisotropic plates," *ASME J. Appl. Mech.*, vol. 37, pp. 1031-1036, 1970.

[13] J N Reddy, "A simple higher-order theory for laminated composite plates," *ASME J. Appl. Mech.*, vol. 51, pp. 745-752, 1984.

[14] J N Reddy, "Survey of recent research in the analysis of composite plates," *Composites Technology Review*, vol. 4, pp. 101 - 104, 1982.

[15] C W Bert, "A critical review of new plate theories applied to laminated composites," *Composite Structures*, vol. 2, pp. 329 - 347, 1984.

[16] A K Noor and W S Burton, "Assessment of shear deformation theories for multilayered composite plates," *Appl. Mech. Rev.*, vol. 42, pp. 1 - 9, 1989.

[17] J N Reddy, "A review of refined theories of laminated composite plates," *Shock and Vibration Digest*, vol. 22, pp. 3 - 17, 1990.

[18] J N Reddy and D H Robbins Jr., "Theories and computational models for composite laminates," *Appl. Mech. Rev.*, vol. 47, pp. 147 - 169, 1994.

[19] W S Burton and A K Noor , "Assessment of computational models for sandwich panels and shells," *Comput. Meth. Appl. Mech.*, vol. 123, pp. 125 - 151, 1995.

[20] A K Noor, W S Burton, and C W Bert, "Computational models for sandwich panels and shells," *Appl. Mech. Rev.*, vol. 49, pp. 155 - 199, 1996.

[21] A Chakrabarti, H D Chalak, M A Iqbal, and A H Sheikh, "A new FE model based on higher order zig-zag theory for the analysis of laminated sandwich beam soft core," *Composite Structures*, vol. 93, pp. 271 - 279, 2011.

[22] H Matsunaga, "A comparison between 2-D single-layer and 3-D layerwise theories for computing interlaminar stresses of laminated composite and sandwich plates subjected

to thermal loadings," *Composite Structures*, vol. 64, pp. 161 - 177, 2004.

[23] W J Chen and Z Wu, "A selective review on recent development of displacement-based laminated plate theories," *Recent Pat. Mech. Eng.*, vol. 1, pp. 29 - 44, 2008.

[24] I Kreja, "A literature review on computational models for laminated composite and sandwich panels," *Central European Journal of Engineering*, vol. 1, pp. 59 - 80, 2011.

[25] M Tahani, "Analysis of laminated composite beams using layerwise displacement theories," *Composite Structures*, vol. 79, pp. 535 - 547, 2007.

[26] A K Noor and M Malik, "An assessment of modelling approaches for thermo-mechanical stress analysis of laminated composite panels," *Comput. Mech.*, vol. 25, pp. 43 - 58, 2000.

[27] E Carrera, "Historical review of zig-zag theories for multilayered plates and shells," *Appl. Mech. Rev.*, vol. 56, pp. 287 - 308, 2003.

[28] C W To and M L Liu, "Geometrically nonlinear analysis of layerwise anisotropic shell structures by hybrid strain based lower order elements," *Finite Elements in Analysis & Design*, vol. 37, pp. 1 - 34, 2001.

[29] Y M Desai , G S Ramtekkar, and A H Shah, "Dynamic analysis of laminated composite plates using a layer-wise mixed finite element model," *Composite Structures*, vol. 59, pp. 237 - 249, 2003.

[30] G S Ramtekkar, Y M Desai, and A H Shah, "Application of a three-dimensional mixed finite element model to the flexure of sandwich plate," *Computers & Structures*, vol. 81, pp. 2183 - 2198, 2003.

[31] F Dau, O Polit , and M Touratier, "C1 plate and shell elements for geometrically nonlinear analysis of multi-layered structures," *Composite Structures*, vol. 84, pp. 1264 - 1274, 2006.

[32] E Carrera, F Miglioretti, and M Petrolo , "Accuracy of refined finite elements for laminated plate analysis," *Composite Structures*, vol. 93, pp. 1311 - 1327, 2011.

[33] R P Shimpi and A V Ainapure, "A beam finite element based on layerwise trigonometric shear deformation theory," *Composite Structures*, vol. 53, pp. 153 - 162, 2011.

[34] D Elmalich and O Rabinovitch, "A higher-order finite element for dynamic analysis of

soft-core sandwich plates," *Journal of Sand. Structures and Materials*, vol. 14, pp. 525-555, 2012.

[35] W Zhen, S H Lo, K Y Sze, and C Wanji , "A higher order finite element including transverse normal strain for linear elastic composite plates with general lamination configurations," *Finite Elements in Analysis & Design*, vol. 48, pp. 1346-1357, 2012.

[36] C Cao, A Yu , and Q H Qin , "A novel hybrid finite element model for modelling anisotropic composites," *Finite Elements in Analysis & Design*, vol. 64, pp. 36 - 47, 2013.

[37] P Dey, A H Sheikh , and D Sengupta, "A new element for analysis of composite plates," *Finite Elements in Analysis & Design*, vol. 82, pp. 62 - 71, 2014.

[38] H Matsunaga, "Vibration and buckling of cross-ply laminated composite circular cylindrical shells according to a global higher-order theory," *International Journal of Mech. Sci.*, vol. 49, pp. 1060 - 1075, 2007.

[39] H Matsunaga, "Assessment of a global higher-order deformation theory for laminated composite and sandwich plates," *Composite Structures*, vol. 56, pp. 279 – 291, 2002.

[40] H Matsunaga, "Thermal buckling of cross-ply laminated composite and sandwich plates according to a global higher-order deformation theory," *Composite Structures*, vol. 68, pp. 439 - 454, 2005.

[41] H Matsunaga, "Thermal buckling of angle-ply laminated composite and sandwich plates according to a global higher-order deformation theory," *Composite Structures*, vol. 72, pp. 177 – 192, 2006.

[42] H Matsunaga, "Free vibration and stability of angle-ply laminated composite and sandwich plates under thermal loading," *Composite Structures*, vol. 77, pp. 249 - 262, 2007.

[43] H M Mourad, T O Williams, and F L Addessio, "Finite element analysis of inelastic laminated plates using a global–local formulation with delamination," *Comput. Methods Appl. Mech. Eng.*, vol. 198, pp. 542 - 554, 2008.

[44] D Versino, H M Mourad , and T O Williams, "A global–local discontinuous Galerkin shell finite element for small-deformation analysis of multi-layered composites," *Comput. Methods Appl. Mech. Eng.*, vol. 271, pp. 269 - 295, 2014.

[45] H Hu, S Belouettar, M Potier-Ferry, and A Makradi, "A novel finite element for global and local buckling analysis of sandwich beams," *Composite Structures*, vol. 90, pp. 270 - 278, 2009.

[46] S Kapuria and J K Nath, "On the accuracy of recent global–local theories for bending and vibration of laminated plates," *Composite Structures*, vol. 95, pp. 163 - 172, 2013.

[47] E Oñate, A Eijo, and S Oller, "Simple and accurate two-noded beam element for composite laminated beams using a refined zigzag theory," *Comput. Meth. Appl. Mech. Eng.*, vol. 213, pp. 362 – 382, 2012.

[48] E Oñate, A Eijo, and S Oller, "A numerical model of delamination in composite laminated beams using the LRZ beam element based on the refined zigzag theory," *Composite Structures*, vol. 104, pp. 270 – 280, 2012.

[49] E Oñate, A Eijo, and S Oller, "Delamination in laminated plates using the 4-noded quadrilateral QLRZ plate element based on the refined zigzag theory," *Composite Structures*, vol. 108, pp. 456 - 471, 2012.

[50] P Vidal and O Polit, "A refined sinus plate finite element for laminated and sandwich structures under mechanical and thermomechanical loads," *Comput. Methods Appl. Mech. Eng.*, vol. 253, pp. 396 - 412, 2013.

[51] D S Mashat, E Carrera, A M Zenkour, and S A Al Khateeb, "Axiomatic/asymptotic evaluation of multilayered plate theories by using single and multi-points error criteria," *Composite Structures*, vol. 106, pp. 393 - 406, 2013.

[52] E Carrera, M Maiarú, and M Petrolo, "Component-wise analysis of laminated anisotropic composites," *International Journal of Solids and Structures*, vol. 49, pp. 1839 - 1851, 2012.

[53] E Carrera and A Ciuffreda, "A unified formulation to assess theories of multilayered plates for various bending problems," *Composite Structures*, vol. 69, pp. 271 - 293, 2005.

[54] E Carrera and A Ciuffreda, "Bending of composites and sandwich plates subjected to localized lateral loadings: a comparison of various theories," *Composite Structures*, vol. 68, pp. 185 - 202, 2005.

[55] L Dozio and E Carrera, "Ritz analysis of vibrating rectangular and skew multilayered

plates based on advanced variable-kinematic models," *Composite Structures*, vol. 94, pp. 2118 - 2128, 2012.

[56] A Pagani, E Carrera , M Boscolo, and J R Banerjee, "Refined dynamic stiffness elements applied to free vibration analysis of generally laminated composite beams with arbitrary boundary conditions," *Composite Structures*, vol. 110, pp. 305 - 316, 2014.

[57] F A Fazzolari and E Carrera, "Advances in the Ritz formulation for free vibration response of doubly-curved anisotropic laminated composite shallow and deep shells," *Composite Structures*, vol. 101, pp. 111 - 128, 2013.

[58] J N Reddy, "On refined computational models of composite laminates," *Int. J. for Num. Meth. in Eng.*, vol. 27, pp. 361 - 382, 1989.

[59] M Yaqoob Yasin and S Kapuria, "An efficient layerwise finite element for shallow composite and sandwich shells," *Composite Structures*, vol. 98, pp. 202 - 214, 2013.

[60] Y Frostig, "Classical and higher-order computational models in the analysis of modern sandwich panels," *Composites PartB: Engineering*, vol. 34, pp. 83 - 100, 2003.

[61] T S Plagianakos and D A Saravanos, "Higher-order layerwise mechanics and finite element for the damped characteristics of sandwich composite beams," *International Journal of Solids and Structures*, vol. 41, pp. 6853 - 6871, 2004.

[62] M Di Sciuva, "A refinement of the transverse shear deformation theory for multilayered orthotropic plates," *L'Aerotecnica Missili e Spazio*, vol. 62, pp. 84 - 92, 1984.

[63] G Giunta, A Catapano, and S Belouettar, "Failure indentation analysis of sandwich plates via hierarchical models," *Journal of Sand. Structures and Materials*, vol. 15, pp. 45-70, 2012.

[64] P Vidal, L Gallimard, and O Polit, "Explicit solutions for the modelling of laminated composite plates with arbitrary stacking sequences," *Composites PartB: Engineering*, vol. 60, pp. 697 - 706, 2014.

[65] M Shariyat, "Non-linear dynamic thermo-mechanical buckling analysis of the imperfect sandwich plates based on a generalized three-dimensional high-order global–local plate theory," *Composite Structures*, vol. 92, pp. 72 - 85, 2010.

[66] S H Lo, W Zhen, K Y Sze, and C Wanji, "An improved in-plane displacement model for the stability analysis of laminated composites with general lamination configurations," *Composite Structures*, vol. 93, pp. 1584 - 1594, 2011.

[67] L Jun, W Zhen, K Xiangshao, L Xiaobin, and W Weiguo, "Comparison of various shear deformation theories for free vibration of laminated composite beams with general lay-ups," *Composite Structures*, vol. 108, pp. 767 - 778, 2014.

[68] W Zhen and C Wanji, "Free vibration of laminated composite and sandwich plates using global–local higher-order theory," *Journal of Sound and Vibration*, vol. 298, pp. 333 - 349, 2006.

[69] W Zhen and C Wanji, "An efficient higher-order theory and finite element for laminated plates subjected to thermal loading," *Composite Structures*, vol. 73, pp. 99 - 109, 2006.

[70] W Zhen and C Wanji, "A study of global–local higher-order theories for laminated composite plates," *Composite Structures*, vol. 79, pp. 44 - 54, 2007.

[71] W Zhen and C Wanji, "A quadrilateral element based on refined global-local higher-order theory for coupling bending and extension thermo-elastic multilayered plates," *International Journal of Solids and Structures*, vol. 44, pp. 3187 - 3217, 2007.

[72] W Zhen and C Wanji, "A C0-type higher-order theory for bending analysis of laminated composite and sandwich plates," *Composite Structures*, vol. 92, pp. 653-661, 2010.

[73] C Wanji, Y K Cheung, and W Zhen, "Augmented higher order global–local theory and refined triangular element for laminated composite plates," *Composite Structures*, vol. 81, pp. 341 - 352, 2007.

[74] W Zhen, C Wanji, and R Xiaohui, "Refined global–local higher-order theory for angle-ply laminated plates under thermo-mechanical loads and finite element model," *Composite Structures*, vol. 88, pp. 643 - 658, 2009.

[75] M Di Sciuva, "A refined transverse shear deformation theory for multilayered anisotropic plates," *Atti Accademia delle Scienze di Torino*, vol. 118, pp. 279 - 295, 1984.

[76] M Di Sciuva, "Development of an anisotropic, multilayered, shear-deformable

rectangular plate element," *Composite Structures*, vol. 21, pp. 789 - 796, 1985.

[77] M Di Sciuva, "Bending, vibration and buckling of simply supported thick multilayered orthotropic plates: an evaluation of a new displacement model," *Journal of Sound and Vibration*, vol. 105, pp. 425 - 442, 1986.

[78] M Di Sciuva, "A third-order triangular multilayered plate finite element with continuous interlaminar stresses," *Int. J. for Num. Meth. in Eng.*, vol. 38, pp. 1 - 26, 1995.

[79] M Di Sciuva, "An improved shear-deformation theory for moderately thick multilayered anisotropic shells and plates," *ASME J. Appl. Mech.*, vol. 54, pp. 589 - 596, 1987.

[80] M Di Sciuva, "Further refinement in the transverse shear deformation theory for multilayered composite plates," *Atti Accademia delle Scienze di Torino*, vol. 124, pp. 248 - 268, 1990.

[81] M Di Sciuva, "Multilayered anisotropic plate models with continuous interlaminar stresses," *Composite Structures*, vol. 22, pp. 149 - 167, 1992.

[82] M Cho and R R Parmerter, "Efficient higher order composite plate theory for general lamination configurations," *AIAA J.*, vol. 31, pp. 1299 - 1309, 1993.

[83] M Cho, K O Kim, and M H Kim, "Efficient higher-order shell theory for laminated composites," *Composite Structures*, vol. 34, pp. 197 - 212, 1996.

[84] M Cho and J H Kim , "Postprocess method using displacement field of higher order laminated composite plate theory," *AIAA J.*, vol. 34, pp. 362 - 368, 1996.

[85] M Cho and J S Kim, "Four-noded finite element post-process method using a displacement field of higher-order laminated composite plate theory," *Composite Structures*, vol. 61, pp. 283 - 290, 1996.

[86] M Cho and J S Kim, "Improved Mindlin plate stress analysis for laminated composites in finite element method," *AIAA J.*, vol. 35, pp. 587 - 590, 1997.

[87] M Cho and J S Kim, "Enhanced First-Order Shear Deformation Theory for laminated and sandwich plates," *ASME J. Appl. Mech.*, vol. 72, pp. 809 - 817, 2005.

[88] M Cho and Y J Choi, "A new postprocessing method for laminated composites of general laminations configurations," *Composite Structures*, vol. 54, pp. 397 - 406,

2001.

[89] J Oh, M Cho, and J S Kim, "Enhanced lower-order shear deformation theory for fully coupled electro-thermomechanical smart laminated plates," *Smart Mat. Str.*, vol. 16, pp. 2229 - 2241, 2007.

[90] J S Kim, J Oh , and M Cho, "Efficient analysis of laminated composite and sandwich plates with interfacial imperfections," *Composites PartB: Engineering*, vol. 42, pp. 1066 - 1075, 2011.

[91] K H Lee, N R Senthilnathan, S P Lim, and S T Chow, "An improved zigzag model for the bending of laminated composites plates," *Composite Structures*, no. 15, pp. 137 - 148, 1990.

[92] S Kapuria, P C Dumir, and N K Jain, "Assessment of zigzag theory for static loading, buckling, free and forced response of composite and sandwich beams," *Composite Structures*, vol. 64, pp. 317 - 327, 2004.

[93] S Kapuria, A Ahmed, and P C Dumir, "Static and dynamic thermo- electro-mechanical analysis of angle-ply hybrid piezoelectric beams using an efficient coupled zigzag theory," *Composites Science & Technology*, vol. 64, pp. 2463 - 2475, 2004.

[94] S Kapuria, M Bhattacharyya, and A N Kumar, "Assessment of coupled 1D models for hybrid piezoelectric layered functionally graded beams," *Composite Structures*, vol. 72, pp. 455 - 468, 2006.

[95] S Kapuria and S D Kulkarni, "An efficient quadrilateral element based on improved zigzag theory for dynamic analysis of hybrid plates with electroded piezoelectric actuators and sensors," *Journal of Sound and Vibration*, vol. 315, pp. 118 - 145, 2008.

[96] X Y Li and D Liu, "Generalized laminate theories based on double superposition hypothesis," *Int. J. for Num. Meth. in Eng.*, vol. 40, pp. 1197 - 1212, 1997.

[97] W Zhen and C Wanji, "An assessment of several displacement-based theories for the vibration and stability analysis of laminated composites and sandwich beams," *Composite Structures*, vol. 84, pp. 337 - 349, 2008.

[98] M Di Sciuva and U Icardi, "Numerical assessment of the core deformability effect on the behaviour of sandwich beams," *Composite Structures*, vol. 52, pp. 41 - 53, 2001.

[99] M Gherlone and M Di Sciuva, "Thermo-mechanics of undamaged and damaged

multilayered composite plates: a sub-laminates finite approach," *Computers & Structures*, vol. 81, pp. 125 - 136, 2007.

[100] M Di Sciuva, M Gherlone, and L Librescu, "Implications of damaged interfaces and of other non-classical effects on the load carrying capacity of multilayered composite shallow shells," *Int. J. Nonlin. Mech.*, vol. 37, pp. 851 - 867, 2002.

[101] R C Averill, "Static and dynamic response of moderately thick laminated beams with damage," *Composites Eng.*, vol. 4, pp. 381 - 395, 1994.

[102] R C Averill and Y C Yip, "Development of simple, robust finite elements based on refined theories for thick laminated beams," *Computers & Structures*, vol. 59, pp. 529 - 546, 1996.

[103] V R Aitharaju and R C Averill, "C0 zig-zag finite element for analysis of laminated composites beams," *Journal of Eng. Mech.*, vol. 125, pp. 323-330, 1999.

[104] D Eby and R C Averill, "Zig-zag sublaminate model for nonlinear analysis of laminated panels," *Journal of Aerospace Eng.*, vol. 13, pp. 100 - 109, 2000.

[105] Y C Yip and R C Averill, "Three-dimensional laminated plate finite element with higher-order zig-zag sublaminate approximations," *Int. J. of Comput. Eng. Sci.*, vol. 2, pp. 137 - 180, 2001.

[106] U Icardi, "C0 plate element based on strain energy updating and spline interpolation, for analysis of impact damage in laminated composites," *International Journal of Impact Engineering*, vol. 34, pp. 1835-1868, 2007.

[107] U Icardi, "Higher-order zig-zag model for analysis of thick composite beams with inclusion of transverse normal stress and sublaminates approximations," *Composites PartB: Engineering*, vol. 32, pp. 343-354, 2001.

[108] U Icardi, "Application of zig-zag theories to sandwich beams," *Mechanics of Advanced Materials and Structures*, vol. 10, pp. 77 - 97, 2003.

[109] U Icardi, "Layerwise mixed element with sublaminates approximation and 3D zig-zag field, for analysis of local effects in laminated and sandwich composites," *Int. J. for Num. Meth. in Eng.*, vol. 70, pp. 94-125, 2007.

[110] U Icardi and R Ruotolo, "Laminated shell model with second-order expansion of the reciprocals of Lamé coefficients Hα, Hβ and interlayer continuities fulfilment,"

Composite Structures, vol. 56, pp. 293 - 313, 2002.

[111] U Icardi, M Di Sciuva, and L Librescu, "Dynamic response of adaptive cross-ply cantilevers featuring interlaminar bonding imperfections," *AIAA J.*, vol. 28, pp. 499 - 506, 2000.

[112] U Icardi and M Di Sciuva, "Large-deflection and stress analysis of multilayered plates with induced-strain actuators," *Smart Mat. Str.*, vol. 5, pp. 140 - 164, 1996.

[113] U Icardi and L Ferrero, "Multilayered shell model with variable representation of the displacements across the thickness," *Composites PartB: Engineering*, vol. 42, pp. 18-26, 2011.

[114] U Icardi and L Ferrero, "Impact analysis of sandwich composites based on a refined plate element with strain energy updating," *Composite Structures*, vol. 89, pp. 35 - 51, 2009.

[115] U Icardi and L Ferrero, "Optimisation of sandwich panels with functionally graded core and faces," *Composites Science & Technology*, vol. 69, pp. 575 - 585, 2009.

[116] U Icardi and L Ferrero, "Layerwise zig-zag model with selective refinement across the thickness," *Int. J. for Num. Meth. in Eng.*, vol. 84, pp. 1085 - 1114, 2010.

[117] U Icardi and L Ferrero, "Laminated and sandwich panels subject to blast pulse loading," *J. Mech. Mat. & Struct.*, vol. 4, pp. 1573 - 1594, 2009.

[118] U Icardi and L Ferrero, "A comparison among several recent criteria for the failure analysis of composites," *J. of Adv. Mat.*, vol. 40, pp. 73 - 111, 2008.

[119] U Icardi and F Sola, "Development of an efficient zig-zag model with variable representation of displacement across the thickness," *Journal of Eng. Mech.*, vol. 140, pp. 531-541, 2014.

[120] U Icardi and F Sola, "Analysis of bonded joints with laminated adherends by a variable kinematics layerwise model," *International Journal of Adhesion and Adhesives*, vol. 50, pp. 244 - 254, 2014.

[121] U Icardi and F Sola, "Response of sandwiches undergoing static and blast pulse loading with tailoring optimization and stitching," *Aerospace Sci. & Tech.*, vol. 32, pp. 293 - 301, 2014.

[122] U Icardi and F Sola, "Indentation of sandwiches using a plate model with variable

kinematics and fixed degrees of freedom," *Thin-Walled Structures*, vol. 86, pp. 24 - 34, 2015.

[123] U Icardi and F Sola, "Recovering critical stresses in sandwiches using through-the-thickness reinforcement," *Composites PartB: Engineering*, vol. 54, pp. 269 - 277, 2013.

[124] A Tessler, M Di Sciuva, and M Gherlone, "Refinement of Timoshenko Beam Theory for composite and sandwich beams using zigzag kinematics," NASA, TP-2007-215086, 2007.

[125] A Tessler, M Di Sciuva, and M Gherlone, "A refined zigzag beam theory for composite and sandwich beams," *Journal of Composite Materials*, vol. 43, pp. 1051 - 1081, 2009.

[126] A Tessler, M Di Sciuva, and M Gherlone, "A consistent refinement of First-order Shear-Deformation Theory for laminated composite and sandwich plates using improved zigzag kinematics," *J. Mech. Mat. & Str.*, vol. 5, pp. 341 - 367, 2010.

[127] A Tessler, M Di Sciuva, and M Gherlone, "Refined zigzag theory for homogeneous, laminated composite, and sandwich plates: a homogeneous- limit methodology for zigzag function selection," NASA, TP-2010-216214, 2010.

[128] A Tessler, M Di Sciuva, and M Gherlone, "A homogeneous limit methodology and refinements of computationally efficient zigzag theory for homogeneous, laminated composite, and sandwich plates," *Num. Meth. Part. Diff. Eqs.*, vol. 27, pp. 208 - 229, 2011.

[129] A Tessler, M Di Sciuva, and M Gherlone, "Refined zig-zag theory for laminated composite and sandwich plates," NASA, TP-2009-215561, 2009.

[130] M Gherlone, A Tessler, and M Di Sciuva, "C0 beam elements based on the Refined Zigzag Theory for multilayered composite and sandwich laminates," *Composite Structures*, vol. 93, pp. 2882 - 2894, 2011.

[131] D Versino, M Mattone, M Gherlone, A Tessler, and M Di Sciuva, "C0 triangular elements based on the Refined Zigzag Theory for multilayer composite and sandwich plates," *Composites PartB: Engineering*, vol. 44, pp. 218 - 230, 2013.

[132] F Azhari, B Boroomand, and M Shahbazi, "Exponential basis functions in the solution

of laminated plates using a higher-order Zig–Zag theory," *Composite Structures*, vol. 105, pp. 398 - 407, 2013.

[133] R M Jones, *Mechanics of composite materials*. Philadelphia: Taylor & Francis, 1999.

[134] M Di Sciuva and U Icardi, "Discrete-layer models for multilayered shells accounting for interlayer continuity," *Meccanica*, vol. 28, pp. 281 - 291, 1993.

[135] U Icardi, "Cylindrical bending of laminated cylindrical shells using a modified zig-zag theory," *Struct. Eng. and Mech.*, vol. 6, pp. 497 - 516, 1998.

[136] H Murakami, "Laminated composite plate theory with improved in-plane responses," *ASME J. Appl. Mech.*, vol. 53, pp. 661-666, 1986.

[137] M Gherlone, "On the use of zigzag functions in equivalent single layer theories for laminated composite and sandwich beams: a comparative study and some observations on external weak layers," *ASME J. Appl. Mech.*, vol. 80, pp. 061004-1-061004-19, 2013.

[138] L Librescu and R Schmidt, "A general linear theory of laminated composite shells featuring interlaminar imperfections," *International Journal of Solids and Structures*, vol. 38, pp. 3355 - 3375, 2001.

[139] R B Hetnarski and R Eslami, *Thermal stresses – advanced theory and applications.* Berlin, Germany: Springer, 2009.

[140] N J Pagano and S R Soni, "Global-local laminate variational model," *International Journal of Solids and Structures*, vol. 19, pp. 207 - 228, 1983.

[141] U Icardi, "Eight-noded zig-zag element for deflection and stress analysis of plates with general lay-up," *Composites PartB: Engineering*, vol. 29, pp. 425-441, 1998.

[142] R Barboni and P Gudenzi, "A class of C0 finite elements for the static and dynamic analysis of laminated plates," *Computers & Structures*, vol. 44, pp. 1169 - 1178, 1992.

[143] P Gaudenzi, R Barboni, and A Manini, "A finite element evaluation of single-layer and multi-layer theories for the analysis of laminated plates," *Composite Structures*, vol. 30, pp. 427 - 440, 1995.

[144] N J Pagano, "Exact solutions for composite laminates in cylindrical bending," *Journal of Composite Materials*, vol. 3, pp. 398-411, 1969.

[145] N J Pagano, "Exact solutions for rectangular bidirectional composites and sandwich plates," *Journal of Composite Materials*, vol. 4, pp. 20-34, 1970.

[146] P Vidal and O Polit, "A sine finite element using zig-zag functions for the analysis of laminated composite beams," *Composites PartB: Engineering*, vol. 42, pp. 1671 - 1682, 2011.

[147] M Touratier, "A generalization of shear deformation theories for axisymmetric multilayered shells," *International Journal of Solids and Structures*, vol. 29, pp. 1379 - 1399, 1992.

[148] P Vidal and O Polit, "A refined sine-based finite element with transverse normal deformation for the analysis of laminated beams under thermo-mechanical loads," *J. of Mech. Mat. & Struct.*, vol. 4, pp. 1127 - 1155, 2009.

[149] M Di Sciuva and M Gherlone, "A global/local third-order Hermitian displacement field with damaged interfaces and transverse extensibility: analytical formulation," *Composite Structures*, vol. 59, pp. 419 - 431, 2003.

[150] V R Aitharaju and R C Averill, "C0 zigzag kinematic displacement models for the analysis of laminated composites," *Mech. Compos. Mater. Struct.*, vol. 6, pp. 31 - 56, 1999.

[151] G M Cook and A Tessler, "A

[152] M Di Sciuva, M Gherlone, and M Mattone, "Anisotropic cubic hermitian polynomials and their use in the theory of laminated plates," *Composite Structures*, vol. 88, pp. 304 - 311, 2009.

[153] S Kapuria, P C Dumir, and A Ahmed, "An efficient higher order zigzag theory for composite and sandwich beams subjected to thermal loading," *International Journal of Solids and Structures*, vol. 40, pp. 6613 - 6631, 2003.

[154] J Oh and M Cho, "A finite element based on cubic zig-zag plate theory for the prediction of thermo-electric-mechanical behaviours," *International Journal of Solids and Structures*, vol. 41, pp. 1357 - 1375, 2004.

[155] L Iurlaro, M Gherlone, M Di Sciuva, and A Tessler, "Assessment of the Refined Zigzag Theory for bending, vibrations, and buckling of sandwich plates: a comparative study of different theories," *Composite Structures*, vol. 106, pp. 777 - 792, 2013.

[156] M Di Sciuva and M Gherlone, "Quasi-3D static and dynamic analysis of undamaged and damaged sandwich beams," *Journal of Sand. Structures and Materials*, vol. 7, pp. 31 - 52, 2005.

[157] M Di Sciuva, M Gherlone, and D Lomario, "Multi-constrained optimization of laminated and sandwich plates using evolutionary algorithms and higher-order theories," *Composite Structures*, vol. 59, pp. 149 - 154, 2003.

[158] J S Kim and M Cho, "Enhanced first-order theory based on mixed formulation and transverse normal effect," *International Journal of Solids and Structures*, vol. 44, pp. 1256 - 1276, 2007.

[159] L Iurlaro, M Gherlone, and M Di Sciuva, "A mixed cubic zigzag model for multilayered composite and sandwich plates including transverse normal deformability," in *Proc. 11th World Conference on Computational Methods*, Barcelona, 2014, pp. 3614 - 3625.

[160] F Auricchio and E Sacco, "Refined first-order shear deformation theory models for composite laminates," *ASME J. Appl. Mech.*, vol. 70, pp. 381 - 390, 2003.

[161] A Barut, E Madenci, and A Tessler, "C0-continuous triangular plate element for laminated composite and sandwich plates using the

[162] T S Plagianakos and D A Saravanos, "Higher-order layerwise laminate theory for the prediction of interlaminar shear stresses in thick composite and sandwich composite plates," *Composite Structures*, vol. 87, pp. 23-35, 2009.

[163] R A Moreira and J D Rodrigues , "A layerwise model for thin soft core sandwich plates," *Computers & Structures*, vol. 84, pp. 1256-1263, 2006.

[164] N A Chrysochoidis and D A Saravanos, "Generalized layerwise mechanics for the static and modal response of delaminated composite beams with active piezoelectric sensors," *International Journal of Solids and Structures*, vol. 44, pp. 8751-8768, 2007.

[165] J Hohe and L Librescu, "Recent results on the effect of the transverse core compressibility on the static and dynamic response of sandwich structures," *Composites PartB: Engineering*, vol. 39, pp. 108-119, 2008.

[166] M Shariyat, "A generalized high-order global-local plate theory for nonlinear bending and buckling analyses of imperfect sandwich plates subjected to thermo-mechanical

loads," *Composite Structures*, vol. 92, pp. 130-143, 2010.

[167] S S Vel and R C Batra, "Analytical solution for rectangular thick laminated plates subjected to arbitrary boundary conditions," *AIAA J.*, vol. 11, pp. 1464-1473, 1999.

[168] S Brischetto, E Carrera, and L Demasi, "Improved response of asymmetrically laminated sandwich plates by using Zig-Zag functions," *Journal of Sand. Structures and Materials*, vol. 11, pp. 257-267, 2009.

[169] L Librescu, S Y Oh, and J Hohe, "Linear and non-linear dynamic response of sandwich panels to blast loading," *Composites PartB: Engineering*, vol. 35, pp. 673-683, 2004.

[170] L Librescu, S Na, P Marzocca, C Chung, and M K Kwak, "Active aeroelastic control of 2-D wing-flap systems operating in an incompressible flowfield and impacted by a blast pulse," *Journal of Sound and Vibration*, vol. 283, pp. 685-706, 2005.

[171] L Librescu, S Y Oh, and J Hohe, "Dynamic response of anisotropic sandwich flat panels to underwater and in-air explosions," *International Journal of Solids and Structures*, vol. 43, pp. 3794-3816, 2006.

[172] T Hause and L Librescu, "Dynamic response of anisotropic sandwich flat panels to explosive pressure pulses," *International Journal of Impact Engineering*, vol. 31, pp. 607-628, 2005.

[173] T Hause and L Librescu, "Dynamic response of doubly-curved anisotropic sandwich panels impacted by blast loadings," *International Journal of Solids and Structures*, vol. 44, pp. 6678-6700, 2007.

[174] A D Gupta, "Dynamic analysis of a flat plate subjected to an explosive blast," in *Proc. of the ASME International Computers in Engineering Conference and Exhibition*, Boston, 1985, pp. 491-496.

[175] A D Gupta, F H Gregory, and R L Bitting , "Dynamic response of a simply-supported rectangular plate to an explosive blast," in *Proc. of SECTAM XIII: the South-eastern Conference on Theoretical and Applied Mechanics*, Columbia, 1986, pp. 385-390.

[176] O Song, J S Ju, and L Librescu, "Dynamic response of anisotropic thin-walled beams to blast and harmonically oscillating loads," *International Journal of Impact Engineering*, vol. 21, pp. 663-682, 1998.

[177] D K Kim and J H Han, "Establishment of gun blast wave model and structural analysis

for blast load," *J. Aircraft*, vol. 43, pp. 1159-1168, 2006.

[178] K J Bathe, *Finite element procedures*. Englewood Cliffs: Prentice-Hall, 1996.

[179] S C Her, "Stress analysis of adhesively-bonded lap joints," *Composite Structures*, vol. 47, pp. 673-678, 1999.

[180] J R Vinson, "Adhesive bonding of polymer composites," *Polym. Eng. Sci.*, vol. 29, pp. 1325-1331, 1989.

[181] L F da Silva , P J das Neves, R D Adams, and J K Spelt, "Analytical models of adhesively bonded joints-part I: literature survey," *International Journal of Adhesion and Adhesives*, vol. 29, pp. 319-330, 2009.

[182] P A Gustafson, A Bizard, and A M Waas, "Dimensionless parameters in symmetric double lap joints: an orthotropic solution for thermo-mechanical loading," *International Journal of Solids and Structures*, vol. 44, pp. 5774-5795, 2007.

[183] A Diaz Diaz, R Hadj-Ahmed, G Foret, and A Ehrlache, "Stress analysis in a classical double-lap, adhesively bonded joint with a layerwise model," *International Journal of Adhesion and Adhesives*, vol. 29, pp. 67-76, 2009.

[184] J J Radice and J R Vinson, "On the analysis of adhesively bonded structures: a higher order semi-elastic adhesive layer model," *Composites Science & Technology*, vol. 68, pp. 376-386, 2008.

[185] X F Wu and R A Jenson, "Stress-function variational method for stress analysis of bonded joints under mechanical and thermal loads," *Int. J. of Eng. Sci.*, vol. 49, pp. 279-294, 2011.

[186] C N Duong, "A unified approach to geometrically nonlinear analysis of tapered bonded joints and doublers," *International Journal of Solids and Structures*, vol. 43, pp. 3498-3526, 2006.

[187] P Schmidt, "Modelling of adhesively bonded joints by an asymptotic method," *Int. J. of Eng. Sci.*, vol. 46, pp. 1291-1324, 2008.

[188] R H Andruet, D A Dillard, and S M Holzer, "Two- and three-dimensional geometrical nonlinear finite elements for analysis of adhesive joints," *International Journal of Adhesion and Adhesives*, vol. 21, pp. 17-34, 2001.

[189] S M Khalili, S Khalili, M R Pirouzhashemi, A Shokuhfar, and R K Mittal, "Numerical

study of lap joints with composite adhesives and composite adherents subjected to in-plane and transverse loads," *International Journal of Adhesion and Adhesives*, vol. 28, pp. 411-418, 2008.

[190] J Diaz, L Romera, S Hernàndez, and A Baldomir, "Benchmarking of three-dimensional finite element models of CFRP single-lap bonded joints," *International Journal of Adhesion and Adhesives*, vol. 30, pp. 178-189, 2010.

[191] B Kilic , E Madenci, and D R Ambur, "Influence of adhesive spew in bonded single lap joints," *Engineering Fracture Mechanics*, vol. 73, pp. 1472-1490, 2006.

[192] W Xu and G Li, "Finite difference three-dimensional solution of stresses in adhesively bonded composite tubular joints subjected to torsion," *International Journal of Adhesion and Adhesives*, vol. 30, pp. 191-199, 2010.

[193] O Nemes and F Lachaud, "Double-lap adhesive bonded-joints assemblies modelling," *International Journal of Adhesion and Adhesives*, vol. 30, pp. 288-297, 2010.

[194] L F da Silva, P J das Neves, R D Adams, and J K Spelt , "Analytical models of adhesively bonded joints-part II: comparative study," *International Journal of Adhesion and Adhesives*, vol. 29, pp. 331-341, 2009.

[195] O Volkersen, "Die nietkraftverteilung in zugbeanspruchten nietverbindungen mit konstanten laschenquerschnitten," *Luftfahrtforschung*, vol. 35, pp. 4-47, 1938.

[196] M Goland and E Reissner, "The stresses in cemented joints," *Journal of Applied Mechanics*, vol. A1, pp. 17-27, 1944.

[197] L J Hart-Smith, "Adhesive-bonded single-lap joints," NASA, Technical report CR 112236, 1973.

[198] W J Renton and J R Vinson , "The efficient design of adhesive bonded joints," *Int. J. Adhesion*, vol. 7, pp. 175-193, 1975.

[199] S Srinivas, "Analysis of bonded joints," NASA, TN D-7855, 1975.

[200] D J Allman, "A theory for elastic stresses in adhesive bonded lap joints," *Quart. J. Mech. & Appl. Math.*, vol. 30, pp. 415-436, 1977.

[201] R D Adams and V Mallick, "A method for the stress analysis of lap joints," *Int. J. Adhesion*, vol. 38, pp. 199-217, 1992.

[202] F Mortensen and O T Thomsen, "Analysis of adhesive bonded joints: a unified approach," *Composites Science & Technology*, vol. 62, pp. 1011-1031, 2002.

[203] U K Vaidya, A R Gautam, M Hosur, and P Dutta , "Experimental-numerical studies of transverse impact response of adhesively bonded lap joints in composite structures," *International Journal of Adhesion and Adhesives*, vol. 26, pp. 184-198, 2006.

[204] T Wah, "Stress distribution in a bonded anisotropic lap joint," *ASME J. Eng. Mater. Technol.*, vol. 95, pp. 174-181, 1973.

[205] C Yang and S S Pang, "Stress analysis of single-lap composite joints under tension," *ASME J. Eng. Mater. Technol.*, vol. 118, pp. 247-255, 1996.

[206] A Gaudiello and A G Kolpakov, "Influence of non-degenerated joint on the global and local behaviour of joined rods," *Int. J. of Eng. Sci.*, vol. 49, pp. 295-309, 2011.

[207] A G Kolpakov, "Influence of non-degenerated joint on the global and local behaviour of joined plates," *Int. J. of Eng. Sci.*, vol. 49, pp. 1216-1231, 2011.

[208] V L Hein and F Erdogan, "Stress singularities in a two-material wedge," *Int. J. of Fract. Mech.*, vol. 7, pp. 317-330, 1971.

[209] L F da Silva and R D Adams, "Techniques to reduce the peel stresses in adhesive joints with composites," *International Journal of Adhesion and Adhesives*, vol. 27, pp. 227-235, 2007.

[210] A Rotem and Z Hashin, "Failure modes of angle-ply laminates," *Journal of Composite Materials*, vol. 9, pp. 191-206, 1975.

[211] A Puck and H Shurmann, "Failure analysis of FRP laminates by means of physically based phenomenological models," *Composites Science & Technology*, vol. 58, pp. 1045-1067, 1998.

[212] T Fuchiyama and N Noda, "Analysis of thermal stress in a plate of functionally gradient material.," *JSAE Review*, vol. 6, pp. 263-268, 1995.

[213] K Suzuky, K Kageyama, I Kimpara, and S Hotta, "Vibration and damping prediction of laminates with constrained viscoelastic layers," *Mechanics of Advanced Materials and Structures*, vol. 10, pp. 43-73, 2003.

[214] W Y Jung and A J Aref, "A combined honeycomb and solid viscoelastic material for structural damping applications," *Mechanics of Materials*, vol. 35, pp. 831-844, 2003.

[215] R S Lakes, "High damping composite materials: effect of structural hierarchy," *Journal of Composite Materials*, vol. 36, pp. 287-297, 2002.

[216] D M McCutcheon, J N Reddy, M J O'Brien, T S Creasy, and G F Hawkins, "Damping composite materials by machine augmentation," *Journal of Sound and Vibration*, vol. 294, pp. 828-840, 2006.

[217] P Pedersen, "A note on design of fiber-nets for maximum stiffness," *Journal of Elasticity*, vol. 73, 127-145 2003.

[218] S Setoodeh, M M Abdalla, and Z Gurdal, "Design of variable-stiffness composite laminates using lamination parameters," *Composites PartB: Engineering*, vol. 37, pp. 301-309, 2006.

[219] P A Zinoviev and Y N Ermakov, *Energy dissipation in composite materials*. Lancaster, USA: Technomic Pub. Co., 1994.

[220] H Georgi, "Dynamic damping investigations on composites," in *Proc. of 8th Meeting AGAD*, Williamsbourg, 1979, pp. 9.1-9.20.

[221] B N Cox, "Constitutive model for a fiber tow bridging a delamination crack," *Mechanics of Advanced Materials and Structures*, vol. 6, pp. 117-151, 1999.

[222] L Gui and Z Li, "Delamination buckling of stitched laminates," *Composites Science & Technology*, vol. 61, pp. 629-636, 2001.

[223] A P Mouritz, "Ballistic impact and explosive blast resistance of stitched laminates," *Composites PartB: Engineering*, vol. 32, pp. 431-439, 2001.

[224] M Z Shah Khan and A P Mouritz, "Fatigue behaviour of stitched GRP laminates," *Composites Science & Technology*, vol. 56, pp. 695-701, 1998.

[225] S Heimbs, J Cichosz, M Klaus, S Kilchert, and A F Johnson, "Sandwich structures with textile-reinforced composite foldcores under impact loads," *Composite Structures*, vol. 92, pp. 1485-1497, 2010.

[226] C Y Wang and C H Yew, "Impact damage in composite laminates," *Computers & Structures*, vol. 37, pp. 967-982, 1990.

[227] M B Dow and H B Dexter , "Development of stitched, braided and woven composite structures in the ACT program and at Langley research center (1985–1997)," NASA, TP-206234, 1997.

[228] A Henao, M Carrera, A Miravete, and L Castejón, "Mechanical performance of through-thickness tufted sandwich structures," *Composite Structures*, vol. 92, pp. 2052-2059, 2010.

[229] A G Prodromou, S V Lomov, and I Verpoest, "The method of cells and the mechanical properties of textile composites," *Composite Structures*, vol. 93, pp. 1290-1299, 2001.

[230] T Ishikawa and T W Chou, "Stiffness and strength behaviour of woven fabric composites," *Journal of Materials Science*, vol. 17, pp. 3211-3220, 1982.

[231] F K Ko and T W Chou, *Composite materials series – textile structural composites*. Amsterdam, Holland: Elsevier Science, 1989.

[232] N K Naik and V K Ganesh, "An analytical method for plain weave fabric composites," *Composites*, vol. 26, pp. 281-289, 1995.

[233] M Ansar, W Xinwei, and Z Chouwei, "Modelling strategies of 3D woven composites: a review," *Composite Structures*, vol. 93, pp. 1947-1963, 2011.

[234] T Mori and K Tanaka, "Average stress in matrix and average elastic energy of materials with misfitting inclusions," *Acta Metall. Mater.*, vol. 21, pp. 571-574, 1973.

[235] G Huysmans, I Verpoest, and P Van Houtte, "A poly-inclusion approach for the elastic modelling of knitted fabric composites," *Acta Mater.*, vol. 46, pp. 3003-3013, 1998.

[236] J D Eshelby, "The determination of the elastic field of an ellipsoidal inclusion and related problems," *Proc. Roy. Soc.*, vol. A241, pp. 376-396, 1957.

[237] J Aboudi, "Meso-mechanical analysis of composites by the method of cells," *Appl. Mech. Rev.*, vol. 42, pp. 193-221, 1989.

[238] S J Kim, K H Ji, and S H Paik, "Numerical simulation of mechanical behaviour of composite structures by supercomputing technology," *Adv. Compos. Mater.*, vol. 17, pp. 373-407, 2008.

[239] C S Lee, S W Chung, H Shin, and S J Kim, "Virtual material characterization of 3D orthogonal woven composite materials by large-scale computing," *Journal of Composite Materials*, vol. 39, pp. 851-863, 2005.

[240] U Icardi and A Atzori, "Simple, efficient mixed solid element for accurate analysis of local effects in laminated and sandwich composites," *Adv. in Eng. Soft.*, vol. 32, pp. 843-849, 2004.

[241] M I Okereke and A I Akpoyomare, "A virtual framework for prediction of full-field elastic response of unidirectional composites," *Computational Materials Science*, vol. 70, pp. 82-99, 2013.

[242] P Wang, Y Lei, and Z Yue, "Experimental and numerical evaluation of flexural properties of stitched foam core sandwich structure," *Composite Structures*, vol. 100, pp. 243-248, 2013.

[243] A Yudhanto, N Watanabe, Y Iwahori, and H Hoshi, "Effect of stitch density on tensile properties and damage mechanism of stitched carbon/epoxy composites," *Composites PartB: Engineering*, vol. 46, pp. 151-165, 2013.

[244] B Lascoup, Z Aboura, K Khellil, and M Benzeggagh, "Prediction of out-of-plane behaviour of stitched sandwich structure," *Composites PartB: Engineering*, vol. 43, pp. 2915-2920, 2012.

[245] U Icardi, "Extension of a new tailoring optimisation technique to sandwich shells with laminated faces," *Struct. Eng. and Mech.*, vol. 43, pp. 739-759, 2012.

[246] R Sahoo and B N Singh, "A new shear deformation theory for the static analysis of laminated composite and sandwich plates," *International Journal of Mech. Sci.*, vol. 75, pp. 324-336, 2013.

[247] U Icardi, "C0 plate element for global/local analysis of multilayered composites, based on a 3D zig-zag model and strain energy updating," *International Journal of Mech. Sci.*, vol. 47, pp. 1561-1594, 2005.

[248] J. S. Kim and M. Cho, "Enhanced modeling of laminated and sandwich plates via strain energy transformation," *Composites Science & Technology*, vol. 66, pp. 1575 – 1587, 2006.

[249] U Icardi, "Extension of the Strain Energy Updating Technique to a multilayered shell model with adaptive displacements and fixed DOF," *Journal of Aerospace Eng.*, vol. 26, pp. 842-854, 2013.

[250] G Prathap, "The displacement-type finite element approach—from art to science," *Prog. Aerospace Sci.*, vol. 10, pp. 295 - 405, 1994.

[251] O C Zienkiewicz and R L Taylor, *The finite element method*. Oxford, England: Butterworth-Heinemann, 2000.

[252] R D Cook, D S Malkus, M E Plesha, and R J Witt, *Concepts and applications of finite element analysis*, IV ed.: Wiley, 2002.

[253] H T Thai and D H Choi, "A simple First-order Shear Deformation Theory for laminated composite plates," *Composite Structures*, vol. 106, pp. 754-763, 2013.

[254] M Savoia and J N Reddy, "A variational approach to three-dimensional elasticity solutions of laminated composite plates," *Trans. ASME J. Appl. Mech.*, vol. 59, pp. 166-175, 1992.

[255] J L Mantari, A S Oktem, and C Guedes Soares, "Static and dynamic analysis of laminated composite and sandwich plates and shells by using a new higher-order shear deformation theory," *Composite Structures*, vol. 94, pp. 37-49, 2011.

[256] A K Noor, "Free vibrations of multilayered composite plates," *AIAA J.*, vol. 11, pp. 1038-1039, 1972.

[257] C A Felippa. Web Site Department of Aerospace Engineering Sciences. [Online]. http://www.colorado.edu/engineering/CAS/courses.d/AVMM.d/AVMM.Ch07.d/AVMM.Ch07.pdf

[258] C Loubignac, C Cantin, and C Touzot, "Continuous stress fields in finite element analysis," *AIAA J.*, vol. 15, pp. 1645-1647, 1978.

[259] I Babuska, "The finite element method with Lagrange multipliers," *Numerical Mathematics*, vol. 20, pp. 173-192, 1973.

[260] F Brezzi, "On the existence, uniqueness and approximation of saddle point problems arising from Lagrangian multipliers," *Revue Francaise D'Automatique, Informatique, Recherche Operationelle, Analyse Numerique*, vol. 8, pp. 129-151, 1974.

[261] M D Olson, "The mixed finite element method in elasticity and elastic contact problems," in *Hybrid and mixed finite element methods*. New York, USA: John Wiley & Sons, 1983, pp. 19-49.

[262] D Mijuca, "A new primal-mixed 3D finite element," *The Scientific Journal Facta Universitatis, Mechanics, Automatic, Control and Robotics*, vol. 3, pp. 167-178, 2001.

[263] D H Robbins and J N Reddy , "Analysis of piezoelectrically actuated beams using a layer-wise displacement theory," *Computers & Structures*, vol. 41, pp. 265-279, 1991.

[264] M O Richardson and M J Wisheart, "Review of low-velocity impact properties of

composite materials," *Composites PartA: Applied Science and Manufacturing*, vol. 27, pp. 1123 - 1131, 1999.

[265] F D Morinière, R C Alderliesten, and R Benedictus, "Modelling of impact damage and dynamics in fibre-metal laminates - A review," *International Journal of Impact Engineering*, vol. 67, pp. 27 - 38, 2014.

[266] S Abrate, "Modeling of impacts on composite structures," *Composite Structures*, vol. 51, pp. 129 - 138, 2001.

[267] S Abrate, "Impact on composite plates in contact with water," *Procedia Engineering*, vol. 88, pp. 2 - 9, 2014.

[268] D J Elder, R S Thomson, M Q Nguyen, and L Scott, "Review of delamination predictive methods for low speed impact of composite laminates," *Composite Structures*, vol. 66, pp. 677 - 683, 2004.

[269] G B Chai and S Zhu, "A review of low-velocity impact on sandwich structures," *Journal of Materials: Design & Applications*, vol. 225, pp. 207 - 230, 2011.

[270] M R Garnich and M K Akula Venkata, "Review of degradation models for progressive failure analysis of fiber reinforced polymer composites," *Appl. Mech. Rev.*, vol. 62, pp. 1 - 35, 2009.

[271] P F Liu and J Y Zheng, "Review on methodologies of progressive failure analysis of composite laminates," in *Continuum mechanics*. New York, U.S.A.: Nova Science Publishers, 2009.

[272] A Corigliano, "Damage and fracture mechanics techniques for composite structures," in *Comprehensive Structural Integrity*. Amsterdam: Elsevier Science, 2003.

[273] D P Horrigan and R A Staal, "Predicting failure loads of impact damaged honeycomb sandwich panels- A refined model," *Journal of Sand. Structures and Materials*, vol. 13, pp. 111 - 133, 2011.

[274] G Salerno et al., "Experimental-numerical assessment of impact-induced damage in cross-ply laminates," *Advanced Structured Materials*, vol. 1, pp. 493 - 504, 2012.

[275] A Aktas, M Aktas, and F Turan, "The effect of stacking sequence on the impact and post-impact behaviour of woven/knit glass/epoxy hybrid composites," *Composite Structures*, vol. 103, pp. 119 - 135, 2013.

[276] T Mitrevski, I H Marshall, R Thomson, R Jones, and B Whittingham, "The effect of impactor shape on the impact response of composite laminates," *Composite Structures*, vol. 67, pp. 139 - 148, 2005.

[277] A R Damanpack, M Shakeri, and M M Aghdam, "A new finite element model for low-velocity impact analysis of sandwich beams subjected to multiple projectiles," *Composite Structures*, vol. 104, pp. 21 - 33, 2013.

[278] D Chakraborty, "Delamination of Laminated Fiber Reinforced Plastic Composites Under Multiple Cylindrical Impact," *Materials & Design*, vol. 28, pp. 1142 - 1153, 2007.

[279] M Yamashita and M Gotoh, "Impact behavior of honeycomb structures with various cell specifications—numerical simulation and experiment," *International Journal of Impact Engineering*, vol. 32, pp. 618 - 630, 2005.

[280] A N Palazotto, E J Herup, and L N Gummadi, "Finite element analysis of low- velocity impact on composite sandwich plates," *Composite Structures*, vol. 49, pp. 209 - 227, 2000.

[281] L Kärger, J Baaran, and J Teßmer, "Rapid simulation of impacts on composite sandwich panels inducing barely visible damage," *Composite Structures*, vol. 79, pp. 527 - 534, 2007.

[282] A Diaz Diaz, J J Caron, and A Ehrlacher, "Analytical determination of the modes I, II and III energy release rates in a delaminated laminate and validation of a delamination criterion," *Composite Structures*, vol. 78, pp. 424 - 432, 2007.

[283] P Ladevèze and G Lubineau , "On a damage mesomodel for laminates: micromechanics basis and improvement," *Mechanics of Materials*, vol. 35, pp. 763-775, 2003.

[284] P Ladevèze, G Lubineau, and D Marsal, "Towards a bridge between the micro- and mesomechanics of delamination for laminated composites," *Composites Science & Technology*, vol. 66, pp. 698-712, 2006.

[285] A S Yigit and A P Christoforou, "On the impact between a rigid sphere and a thin composite laminate supported by a rigid substrate," *Composite Structures*, vol. 30, pp. 169 - 177, 1995.

[286] I H Choi, "Contact force history analysis of composite sandwich plates subjected to low-velocity impact," *Composite Structures*, vol. 75, pp. 582 - 586, 2006.

[287] C C Chao and C Y Tu, "Three-dimensional contact dynamics of laminated plates: Part 1. Normal impact," *Composites PartB: Engineering*, vol. 30, pp. 9 - 22, 1999.

[288] D W Zhou and W J Stronge, "Low velocity impact denting of HSSA lightweight sandwich panel," *International Journal of Mech. Sci.*, vol. 48, pp. 1031 - 1045, 2006.

[289] Y Li, A Xuefeng, and Y Xiaosu, "Comparison with low-velocity impact and quasi-static indentation testing of foam core sandwich composites," *International Journal of Applied Physics and Mathematics*, vol. 2, pp. 58 - 62, 2012.

[290] R E Rowlands, "Strength (failure) theories and their experimental correlations.," *Handbook of Composites; Elsevier Science Publ*, vol. 3, pp. 71-125, 1985.

[291] M N Nahas, "Survey of failure and post-failure theories of laminated fibre reinforced composites," *Journal of Composite Technology & Research*, vol. 8, pp. 138-153, 1986.

[292] J F Echaabi and F Trochu, "Review of failure criteria of fibrous composite materials," *Polymer Composites*, vol. 17, pp. 786-798, 1996.

[293] F Paris, "A study of failure criteria of fibrous composite materials," NASA, CR-2001-210661, 2001.

[294] R C Tennyson and G E Wharam, "Evaluation of failure criterion for graphite-epoxy," NASA, CR-172547, 1985.

[295] L Tong, "An assessment of failure criteria to predict the strength of adhesively bonded composite double lap joints," *Journal of Reinforced Plastics and Composites*, vol. 16, pp. 698-713, 1997.

[296] Z Hashin and A Rotem, "A fatigue failure criterion for fiber reinforced materials," *Journal of Composite Materials*, vol. 7, pp. 448-464, 1973.

[297] H Y Choi and F K Chang, "A model for predicting damage in graphite/epoxy laminated composites resulting from low-velocity point impact," *Journal of Composite Materials*, vol. 26, pp. 2134-2169, 1992.

[298] T Besant, G A Davies, and D Hitchings, "Finite element modelling of low velocity impact of composite sandwich panels," *Composites PartA: Applied Science and Manufacturing*, vol. 32, pp. 1189-1196, 2001.

[299] Evonik Röhm GmbH, "ROHACELL WF: Product Information," 2011.

[300] Q M Li, R A Mines, and R S Birch, "The crush behaviour of Rohacell-51WF structural foam," *International Journal of Solids and Structures*, vol. 37, pp. 6321-6341, 2000.

[301] S M Lee and T K Tsotsis, "Indentation failure behaviour of honeycomb sandwich panels," *Composites Science & Technology*, vol. 60, pp. 1147-1159, 2000.

[302] Y Aminanda, B Castaniè, J J Barrau, and P Thevenet, "Experimental analysis and modeling of the crushing of honeycomb cores," *Appl. Compos. Mater.*, vol. 12, pp. 213 - 227, 2005.

[303] L Aktay, A F Johnson, and B Kröplin, "Numerical modeling of honeycomb core crush behavior," *Engineering Fracture Mechanics*, vol. 75, pp. 2616 - 2630, 2008.

[304] E A Flores-Johnson, Q M Li, and R A Mines, "Degradation of elastic modulus of progressively crushable foams in uniaxial compression," *J. of Cellular Plastics*, vol. 44, pp. 415 - 434, 2008.

[305] E A Flores-Johnson and Q M Li, "Experimental study of the indentation of sandwich panels with carbon fibre-reinforced polymer face sheets and polymeric foam core," *Composites PartB: Engineering*, vol. 42, pp. 1212-1219, 2011.

[306] T D McQuigg, "Compression After Impact experiments and analysis on honeycomb core sandwich panels with thin face sheets," NASA, /CR–2011-217157, 2011.

[307] P M Schubel, J J Luo, and I M Daniel, "Low velocity impact behavior of composite sandwich panels," *Composites PartA: Applied Science and Manufacturing*, vol. 36, pp. 1389 - 1396, 2005.

[308] U Icardi and G Zardo, "C0 plate element for delamination damage analysis, based on a zig-zag model and strain energy updating," *International Journal of Impact Engineering*, vol. 31, pp. 579 - 606, 2005.